Centre Énergie Matériaux Télécommunications

DEVELOPMENT OF A SCANLESS TERAHERTZ TIME-DOMAIN IMAGING SYSTEM

Par

Luca Zanotto

Thèse présentée pour l'obtention du grade de

Philosophiae Doctor (Ph.D.)

en sciences de l'énergie et des matériaux

Jury d'évaluation

Président du jury et examinateur interne	Jinyang Liang INRS – ÉMT
Examinateur externe	François Blanchard ÉTS
Examinateur externe	Matthew Reid University of Northern British Columbia
Directeur de recherche	Luca Razzari INRS – ÉMT

AKNOWLEDGMENTS

I would like to thank all the people that have accompanied me throughout this PhD journey.

My supervisor, Prof. Luca Razzari, who has been supportive, encouraged me in pursuing my objectives, and helped me improve my approach to the research work, with constructive advice and open discussion.

My postdocs and friends, Riccardo and Giacomo, who have been always there to help me during the long hours in the lab, as well as to go out and have a beer together after work.

All of the other members of the research group, with whom I shared short or long periods of time, exchanged ideas, advice, or just a laugh when things wouldn't work the way we expected.

All the friends and colleagues at INRS, who I crossed paths with along the years, had countless coffee breaks or just a chat in the corridor, and organized plenty of activities within the student association.

I also would like to thank all the other friends I met here, who made Montreal feel like a second home. In particular, I want to remember Andrea, with whom I shared countless adventures, concerts, and bike rides.

A big thank goes to Sophia, who has been at my side all along the drafting of this thesis.

A special thank, then, goes to my mom and dad, my brother, my sister, and my grandmother, who have constantly supported me from across the Ocean. And all my friends spread in different parts of the world, who have been present at all times despite the distance.

RÉSUMÉ

Au cours des vingt dernières années, l'imagerie térahertz basée sur la spectroscopie dans le domaine temporel provoque un intérêt croissant grâce à ses capacités particulières d'étudier les caractéristiques spectrales des produits chimiques, d'extraire l'indice de réfraction et l'absorption des matériaux, ainsi que de révéler la structure interne d'objets complexes. Cependant, son utilisation répandue a été entravée par le temps d'acquisition chronophage généralement nécessaire pour balayer spatialement l'objet et, pour chaque point spatial, enregistrer le champ dans le domaine temporel via une ligne à retard. Dans ce projet de recherche, nous avons abordé cet obstacle fondamental en utilisant deux approches complémentaires. Tout d'abord, nous avons mis en œuvre une configuration d'imagerie à « pixel unique » dans le domaine temporel, qui permet d'éviter le balayage spatial et d'utiliser une reconstruction de détection compressée. Nous avons démontré l'extraction cohérente des formes d'onde temporelles térahertz d'une façon indirecte, à chaque position spatiale d'un objet via l'imagerie à « pixel unique ». Cette stratégie permet ainsi de préserver les capacités de sonder les propriétés des matériaux, offertes par la spectroscopie dans le domaine temporel, tout en permettant une réduction du temps d'acquisition. Dans la deuxième partie, nous avons davantage amélioré l'arrangement d'imagerie en utilisant un schéma de détection sans balayage. En exploitant correctement la diffraction naturelle des ondes, un cartographie temps-espace appliquée à la détection de point térahertz permet une acquisition quasi instantanée des formes d'onde térahertz. La combinaison de ces deux approches permet une réduction significative de la complexité du système et du temps d'acquisition, et constitue ainsi une solution prometteuse pour le développement d'imageurs térahertz rapides et compacts de nouvelle génération.

Mots clés : Rayonnement térahertz ; Spectroscopie dans le domaine temporel ; Imagerie à « pixel unique » ; Détection compressée ; Détection « seul coup »

ABSTRACT

In the last twenty years, terahertz imaging based on time-domain spectroscopy, has attracted increasingly growing attention thanks to its peculiar abilities to study spectral features of chemicals, extracting the refractive index and absorption of materials, as well as revealing the inner structure of complex objects. However, its widespread use has been hampered by the very long acquisition time typically required to perform a pixel-by-pixel scan of the object and, for each spatial point, record the field in time via a delay line. In this research project, we aimed to address this fundamental bottleneck by using two complementary approaches. First, we implemented a time-domain single-pixel imaging configuration, which avoids the spatial scan and makes it possible to use a compressed sensing reconstruction. We demonstrated the indirect coherent extraction of terahertz temporal waveforms at each spatial position of an object via single-pixel imaging. This strategy preserves the capabilities of probing material properties, offered by time-domain spectroscopy, while enabling a reduction of the acquisition time. In the second part, we further improved the imaging arrangement employing a scanless terahertz waveform detection scheme. By properly exploiting natural wave diffraction, a time-to-space encoding applied to terahertz point detection allows for an almost instantaneous capture of the terahertz waveforms. The combination of these two approaches leads to a significant reduction of both system complexity and acquisition time, and thus is a promising solution for the development of next-generation fast and compact terahertz imagers.

Keywords: Terahertz radiation; Time-domain spectroscopy; Single-pixel imaging; Compressed sensing; Single-shot detection;

TABLE OF CONTENTS

LIST OF FIGURES

LIST OF TABLES

LIST OF PUBLICATIONS

1. R. Piccoli, A. Rovere, YG. Jeong, Y. Jia, L. Zanotto, F. Légaré, B.E. Schmidt, R. Morandotti, and L. Razzari, *Extremely broadband terahertz generation via pulse compression of an Ytterbium laser amplifier*, Opt. Express **27**, 32659-32665 (2019)
2. L. Zanotto, R. Piccoli, J. Dong, D. Caraffini, R. Morandotti, and L. Razzari, *Time-domain terahertz compressive imaging*, Opt. Express **28**, 3795-3802 (2020)
3. L. Zanotto, R. Piccoli, J. Dong, R. Morandotti, and L. Razzari, *Single-pixel terahertz imaging: a review,* Opto-Electronic Advances, 3(9): 09200012 (2020)
4. R. Piccoli, J.M. Brown, YG. Jeong, A. Rovere, L. Zanotto, M.B. Gaarde, F. Légaré, A. Couairon, J.C. Travers, R. Morandotti, B.E. Schmidt, and L. Razzari, *Intense few-cycle visible pulses directly generated via nonlinear fibre mode mixing,* Nat. Photon. **15,** 884–889 (2021)
5. L. Zanotto, G. Balistreri, A. Rovere, O-P. Kwon, R. Morandotti, R. Piccoli, and L. Razzari, *Terahertz scanless hypertemporal imaging,* arXiv:2209.11646 (2022)

PATENTS

R. Piccoli, L. Razzari, L. Zanotto, J. Dong, R. Morandotti, *Real-Time Multidimensional Terahertz Imaging System and Method*, US 2021/0096066 - patent pending (2021)

LIST OF CONTRIBUTIONS TO INTERNATIONAL CONFERENCES

1. L. Zanotto, R. Piccoli, J. Dong, H. Breitenborn, R. Naccache, R. Morandotti, and L. Razzari, *Single-pixel terahertz imaging using a time-domain spectroscopy setup,* Photonics North (PN) (2018)
2. YG. Jeong, R. Piccoli, A. Rovere, L. Zanotto, G. Tempea, D. Wilson, M. Ivanov, A. Ramirez, R. Morandotti, F. Légaré, L. Razzari, and B.E. Schmidt, *Guiding of laser pulses at the theoretical limit – 97% throughput hollow-core fibers,* International Conference on Ultrafast Phenomena (2020) - *postdeadline contribution*
3. L. Zanotto, R. Piccoli, J. Dong, D. Caraffini, R. Morandotti, and L. Razzari, *Terahertz compressive imaging directly in the time domain,* Conference on Lasers and Electro-Optics (CLEO) (2020)
4. L. Zanotto, R. Piccoli, J. Dong, D. Caraffini, R. Morandotti, and L. Razzari, *Terahertz single-pixel imaging in the time domain,* Photonics North (PN) (2020)
5. R. Piccoli, A. Rovere, YG. Jeong, Y. Jia, L. Zanotto, F. Légaré, B.E. Schmidt, R. Morandotti, and L. Razzari, *Ultrafast phenomena in hollow-core fibers*, Photonics North (PN) (2020)
6. L. Zanotto, R. Piccoli, J. Dong, D. Caraffini, R. Morandotti, and L. Razzari, *Time-domain terahertz single-pixel imaging,* SPIE Photonics West (2021)
7. YG. Jeong, R. Piccoli, A. Rovere, L. Zanotto, G. Tempea, D. Wilson, M. Ivanov, A. Ramirez, R. Morandotti, F. Légaré, L. Razzari, and B.E. Schmidt, *Guiding of laser pulses at the theoretical limit – 97% throughput hollow-core fibers,* Laser Congress (2021)
8. YG. Jeong, R. Piccoli, A. Rovere, L. Zanotto, G. Tempea, D. Wilson, M. Ivanov, A. Ramirez, R. Morandotti, F. Légaré, L. Razzari, and B.E. Schmidt, *Guiding of laser pulses at the theoretical limit – 97% throughput hollow-core fibers,* Conference on Lasers and Electro-Optics (CLEO) (2021)
9. YG. Jeong, R. Piccoli, A. Rovere, L. Zanotto, G. Tempea, D. Wilson, M. Ivanov, A. Ramirez, R. Morandotti, F. Légaré, L. Razzari, and B.E. Schmidt, *Guiding of laser pulses at the theoretical limit – 97% throughput hollow-core fibers,* The European Conference on Lasers and Electro-Optics (CLEO Europe) (2021)
10. R. Piccoli, J.M. Brown, YG. Jeong, A. Rovere, L. Zanotto, M.B. Gaarde, F. Légaré, A. Couairon, J.C. Travers, R. Morandotti, B.E. Schmidt, and L. Razzari, *Few-cycle visible light generation in a hollow-core fiber,* Frontiers in Optics/Laser Science (2021) - *postdeadline contribution*
11. R. Piccoli, J.M. Brown, YG. Jeong, A. Rovere, L. Zanotto, M.B. Gaarde, F. Légaré, A. Couairon, J.C. Travers, R. Morandotti, B.E. Schmidt, and L. Razzari, *4-GW Few-Cycle Visible Pulse Generation via Fiber Mode Mixing,* Conference on Lasers and Electro-Optics (CLEO) (2022)

12. R. Piccoli, J.M. Brown, YG. Jeong, A. Rovere, L. Zanotto, M.B. Gaarde, F. Légaré, A. Couairon, J.C. Travers, R. Morandotti, B.E. Schmidt, and L. Razzari, *Multimodal hollow-core fibers: a new route for few-cycle visible pulse generation,* SPIE Photonics Europe (2022)

1 INTRODUCTION

1.1 Introduction to terahertz waves

The electromagnetic (EM) force is the underlying interaction at the basis of many natural phenomena. The atomic structure (as we observe it) is the result of the EM interaction between a positively charged nucleus and negatively charged electrons, somehow distributed in the space surrounding the former. All more complex structures arising from the association of multiple atoms, from molecules to living creatures, are ultimately different manifestations of how nuclei and electrons interact through the EM force.

Several scientists in the XIX century, Maxwell in particular, provided a theoretical framework through which it is possible to describe fundamental EM interactions, in terms of electric and magnetic fields (Maxwell, 1865). EM fields propagate in both space and time, thereby transferring energy and information. When propagating, these fields behave like oscillating waves, and can be mathematically described through wave equations (Jackson, 1999). One of the fundamental features of EM waves is their frequency, which gives a quantitative information on how fast a wave oscillates in time. Curiously enough, phenomena seemingly very different, like radio waves used for cellphone communications, the light emitted by a bulb, or the heat we feel when exposed to sunlight, can all be traced back to EM waves, the only difference being the frequency at which they oscillate.

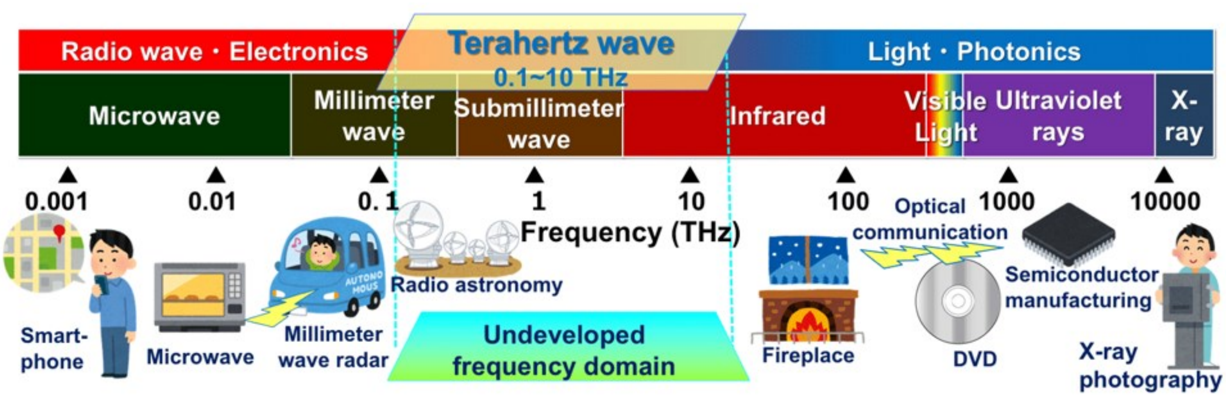

Figure 1.1 | The terahertz frequency range. *Reprinted from National Institute of Information and Communications Technology*

The portion of the EM spectrum of interest for this doctoral thesis is the one with frequencies ranging from 0.1 to 10 THz (Fig. 1.1), and commonly referred to as “terahertz (THz) radiation”. On the longer wavelengths side of this band are microwaves that can be generated and detected by oscillating charges in regular antennas, while on the shorter wavelength side lie infrared (IR) and then visible light, the generation and detection of which is typically performed with excitation of electronic transitions (e.g., in semiconductors). Even though the first attempt to measure a THz transient dates back to the 60s (Zernike & Berman, 1966), the scientific history of THz is relatively short. A key challenge has long been the lack of an efficient technology for generating and detecting this type of radiation. As a direct consequence, the scientific community started to speak about a "THz gap" to refer to such lack of technology. This hindrance was progressively overcome with the development of ultrafast optoelectronics (Auston, 1975; C. H. Lee, 1977), resulting in the measurement of the first THz transient fields (Auston et al., 1980; Mourou et al., 1981) at the beginning of the 80s. The subsequent development of laser systems capable of emitting ultrashort pulses in the femtosecond time scale further boosted THz research, eventually leading to the development of the first ultrafast THz spectroscopy systems (Gao et al., 1995; Van Exter et al., 1989).

The availability of sources and detectors of THz radiation soon prompted an interest in further exploring its peculiar properties and potentially exploiting them for practical real-world applications. For example, most non-conductive materials (such as semiconductors, plastics and papers), as well as non-polar liquids, are transparent to THz waves. This makes them useful, for instance, for the non-invasive inspection of multi-component systems (Stoik et al., 2008). Moreover, many gases (Jacobsen et al., 1996), inorganic (Grischkowsky et al., 1990) and organic compounds (Parrott & Zeitler, 2015), as well as biological molecules (Baxter & Guglietta, 2011) exhibit specific spectral "fingerprints" at THz frequencies, because of the presence of collective excitations (e.g., phonons), or rotational/vibrational modes in this spectral range. This makes it possible to use THz for sensing of substances, like explosives (Y. C. Shen et al., 2005). Furthermore, thanks to its low photon energy (~meV), THz radiation is practically non-ionizing, and can thus be safely used on sensitive samples or electronics, as well as the human body. One of the most powerful analytical techniques available to date in this spectral range is the so-called THz Time-Domain Spectroscopy (THz-TDS). This technology makes use of broadband THz pulses (almost single-cycle in time) generated by means of a femtosecond laser system (e.g., ytterbium-doped or titanium-sapphire sources). TDS works as a pump-probe system, where an ultrashort laser pulse is used as a variably delayed gating probe to sample the THz transient (in turn generated by a second, coherent pulse). In this way, the THz waveform is reconstructed directly in the time-domain, so that both amplitude and phase are retrieved. This ultimately means that all the information carried by the THz wave is promptly available, enabling a complete characterization of the optical properties of the object under investigation, e.g. its complex refractive index (Jepsen et al., 2011).

1.2 Imaging with terahertz radiation

The unique combination of the THz radiation features described above makes imaging one of the most attractive and explored applications (Mittleman, 2018). As mentioned above, THz can easily pass through many dielectric materials, allowing to reveal inner structures with a good contrast. At the same time, its wavelength is on the scale of hundreds of microns, i.e. shorter than microwaves, so that it still enables to achieve relatively high imaging resolutions (~100 micrometers). When a THz-TDS system is used for imaging, its capabilities of material characterization open the route to multidimensional imaging, combining the reconstruction of the object shape with the extraction of the refractive index (Cunningham et al., 2011), recognition of the presence of unknown objects (Pohl et al., 2016), or extraction of the features of multilayer samples (Redo-Sanchez et al., 2016) (Fig. 1.2(a)). THz imaging represents a useful tool, able to provide complementary information to that obtained with microwaves, IR-ultraviolet (UV), and X-rays images. Examples of imaging applications explored in the last years include security screening (H. B. Liu et al., 2007) (Fig. 1.2(b)), quality and safety check in industry (Duling & Zimdars, 2009; Jansen et al., 2010; Jördens & Koch, 2008), biomedical imaging (Naccache et al., 2017; Q. Sun et al., 2017; X. Yang et al., 2016), and even spectral imaging of paintings and archeological pieces (Abraham et al., 2010; Dong et al., 2017; Koch-Dandolo et al., 2015) (Fig. 1.2(c)).

Since the seminal paper by Hu and Nuss, in 1995 (Hu & Nuss, 1995), the growing interest in the field has fostered the development of a large variety of THz imaging systems. In general, we can sort them into two main categories: THz cameras and techniques based on single-pixel detectors. The obvious advantage of the former is the capacity of capturing images in an almost instantaneous fashion. The low energy of THz photons, though, makes the realization of multipixel sensors based on electronic transitions in semiconductors rather challenging. This is because THz cameras are expected to exhibit a sensitivity high enough to capture images at high frame rates and do so at room temperature, to avoid cumbersome and expensive cooling systems. These requirements pose serious limitations to the realization of these devices. So far, THz cameras are mostly based either on thermal detector arrays, such as micro-bolometers (A. W. M. Lee, Qin, et al., 2006; Nemoto et al., 2016) and pyroelectric sensors (J. Yang et al., 2008a), or field-effect transistors (Al Hadi et al., 2012). The advantage of these types of sensors is their broadband response, but at the cost of recording only the intensity of the THz beam, sacrificing the temporal/spectral information. The other option involves systems based on point detectors. These are generally more sensitive and can enable the detection of the complex amplitude of THz pulses. A major drawback is the typical need of spatially scanning the object pixel-by-pixel to obtain the image, making the acquisition process very long. Such long acquisition time is the main longstanding issue that has hampered the widespread use of THz imaging. In the last years, a great deal of research has arisen with the aim of overcoming this troublesome technological bottleneck, leading to a variety of ingenious solutions (Guerboukha et al., 2018; Zanotto et al., 2020).

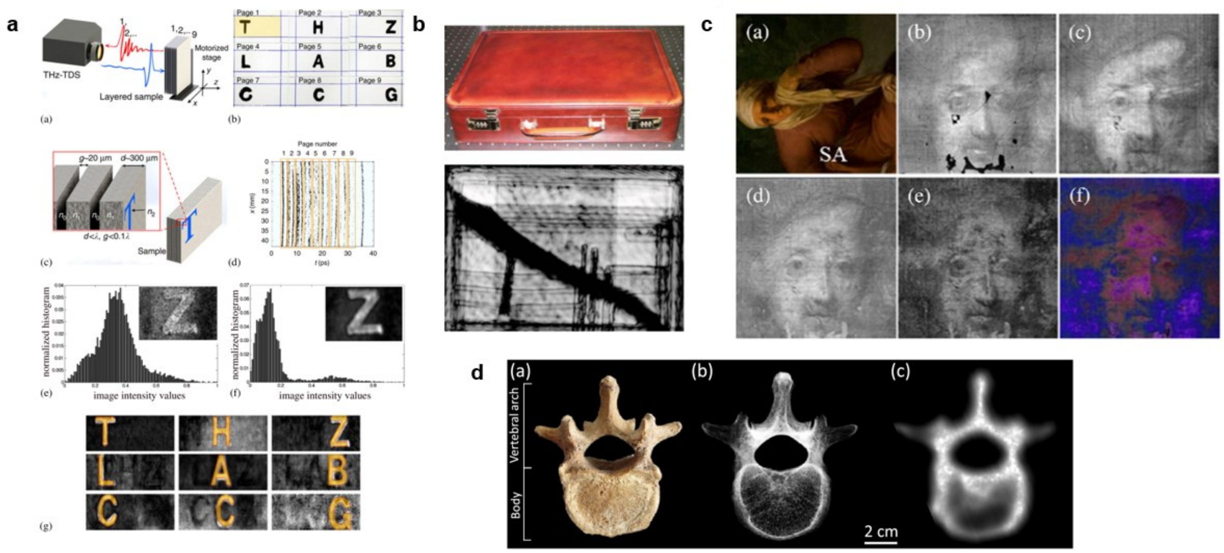

Figure 1.2 | Examples of imaging applications of terahertz radiation. (a) Time-of-flight imaging of a multilayer sample. *Adapted from (Redo-Sanchez et al., 2016) under the https://creativecommons.org/licenses/ license.* (b) Security screening of a suitcase*. Adapted from (Liu, et al., 2007) © 2007 IEEE.* (c) Imaging of hidden layers of a painting. *Adapted with permission from (Koch-Dandolo, et al., 2015) © 2015 The Optical Society.* (d) Imaging of human bones. *Adapted with permission from (Bessou et al., 2012) © 2012 The Optical Society.*

1.3 Making terahertz imaging fast and simple: motivation of this doctoral project and thesis outline

The development of a THz imager working in real-time has been one of the main research goals since the early days of THz research (Wu et al., 1996), and this doctoral project is part of the general effort towards this goal. As mentioned above, most THz imaging systems, and in particular those based on TDS, employ detectors without spatial resolution, i.e. single-pixel detectors. The image reconstruction is therefore typically achieved with a two-dimensional raster-scan of the object. Besides taking a significant amount of time to capture an image (most common experimental systems cannot acquire more than a few pixels/s), this pixel-by-pixel procedure requires bulky mechanical moving parts to displace either the sample or the detection system over the whole imaging area. Furthermore, there exists another significant limitation towards the achievement of fast acquisition times when employing a TDS system. The reconstruction of the THz waveform is usually performed by probing the THz electric field amplitude at different positions along the time window of interest by means of an ultrashort pulse (fs pulse duration). This is carried out by sequentially changing the arrival time of the probe pulse with respect to the THz pulse via a mechanical delay line, which is relatively slow (typically not faster than a few scans/s), further hampering the possibility for real-time operation.

In this thesis work, we have explored the possibility of overcoming the long acquisition time issue related to using a THz-TDS system for imaging with two complementary approaches:

- First, we eliminated the need of the spatial scan by using a single-pixel imaging (SPI) scheme (Gibson et al., 2020) directly implemented in the time domain. SPI is a way to obtain an image by means of a detector with no spatial resolution, i.e. single-pixel, beyond raster scanning. The spatial structure of the object under investigation is retrieved by interrogating it with a series of spatial light patterns and measuring the correlated intensities with a single-pixel detector. Besides avoiding the need of bulky mechanical moving parts to perform the spatial scan, the reason that makes this imaging configuration appealing is that it enables the use of a reduced number of patterns (and, as a result, of measurements), through compressed sensing (CS). CS is a route to reconstruct a good approximation of a signal with fewer measurements than required with conventional sampling schemes (E.J. Candes & Wakin, 2008), enabling faster acquisition (Edgar et al., 2019). Therefore, SPI is a smart way towards reducing the acquisition time in THz imaging and it is also one of the most widely explored (Zanotto et al., 2020).
- Second, we implemented a so-called "single-shot" detection (SSD) technique to avoid the use of a delay line. SSD approaches exploit the possibility of encoding the temporal dimension of the THz pulse into a spatial or spectral dimension of the probe and represent a way to capture the whole THz waveform in a simultaneous fashion. Being the probe pulse typically at visible/IR frequencies, a multipixel detector, like a charge-coupled device (CCD) camera, can be used to retrieve the information it carries. Various SSD techniques have been proposed over the years (Teo et al., 2015). They generally exploit the broadband nature of the ultrashort probe pulse to encode the temporal information into its spectral components (Jiang & Zhang, 1998a), or a tilt in the pulse front of the probe itself to employ its spatial extension for capturing that same temporal information (Kawada et al., 2011). Both time-to-frequency and time-to-space techniques were investigated in this doctoral project, with the latter eventually chosen as the preferred one, since it does not suffer from the degradation of the temporal resolution affecting the former.

The combination of the SPI configuration and the SSD scheme not only allows for a significant reduction in the image acquisition time (more than 90 times faster in our experiments, compared to our same system operating in a standard TDS configuration), but also makes the imaging setup much simpler, just through the use of a spatial light modulator (SLM) and a camera. This arrangement is a promising solution for the development of the next generation of fast, compact, and versatile THz multidimensional imagers, targeting a large variety of scientific and industrial applications.

Below, a brief outline of this thesis is presented.

- In Chapter 2, we first describe the working principle of a standard THz-TDS system and present its basic elements. Afterwards, the procedure to extract the key optical properties of a generic material by employing such a technique is overviewed, with specific reference to its employment for an image reconstruction. Then, examples of notable imaging applications are presented. Finally, some solutions aiming at reducing the acquisition time are reported.
- In Chapter 3, the general SPI approach is introduced, followed by the description of the CS methodology. Thereafter, specific strategies for implementing SPI at THz frequencies are reported, followed by examples of previous THz imaging systems based on SPI. In the last part, we describe the working principle of the SSD techniques applied in this project.
- In Chapter 4, the results related to the first part of this research project are presented and discussed. We first introduce the method we used to spatially modulate the THz beam, and the procedure to obtain the patterns used to put in place the SPI scheme. Afterwards, we present the crucial achievement is the experimental demonstration of how the SPI approach can be successfully coupled to the coherent reconstruction of THz waveforms in the time-domain. Images captured using such a methodology are displayed in the last part of the chapter, using different contrast methods.
- In Chapter 5, the outcomes of the second half of the project are discussed. Here, SSD techniques are coupled to the SPI-based arrangement introduced in Chapter 4. We present both the experimental systems built for the time-to-frequency and time-to-space mapping. Then, we describe the parallelism between the SPI scheme and the phenomenon of light diffraction, which is crucial for the functioning of the arrangement. Finally, examples of image reconstruction using the scanless technique and different contrast methods are presented.
- In Chapter 6, we report some concluding remarks and discuss potential directions for future advancements of the of THz imaging technique developed in this project.

2 IMAGING WITH TERAHERTZ TIME-DOMAIN SPECTROSCOPY

The core experimental system employed in this doctoral project is a THz time-domain spectrometer. It was first developed at the end of the 80s (Van Exter et al., 1989), and it is (to date) one of the most powerful and versatile techniques to exploit the peculiar properties of THz broadband pulses (Jepsen et al., 2011). Moreover, it is also the most employed experimental system for imaging purposes (Wang et al., 2022). THz-TDS is a form of pump-probe technique making use of ultrashort optical pulses (∼100 fs temporal pulse duration, $1/e^2$), typically in the near IR, generated by femtosecond lasers. A sketch of a typical THz-TDS system is shown in Fig. 2.1(a). From here, it can be seen that the source laser beam is split into two lines: one (pump) generates a series of THz pulses, while the other one (probe) is used to measure the THz electric field in the detection part of the setup. Since the laser pulses exhibit a much shorter temporal pulse duration (∼100 fs) when compared to the THz pulses (∼1.5 ps), the former can be employed as an optical gate that allows to perform a temporal sampling of the THz waveform (Fig. 2.1(b)). The probe optical path length can be modified by means of a mechanical delay line (placed before the detection section, as shown in Fig. 2.1(a)), allowing to retrieve information on the THz field amplitude at different temporal positions, and finally resulting in the coherent reconstruction of the temporal profile of the THz electric field. In the following sections, the key elements of this experimental setup will be presented in more detail.

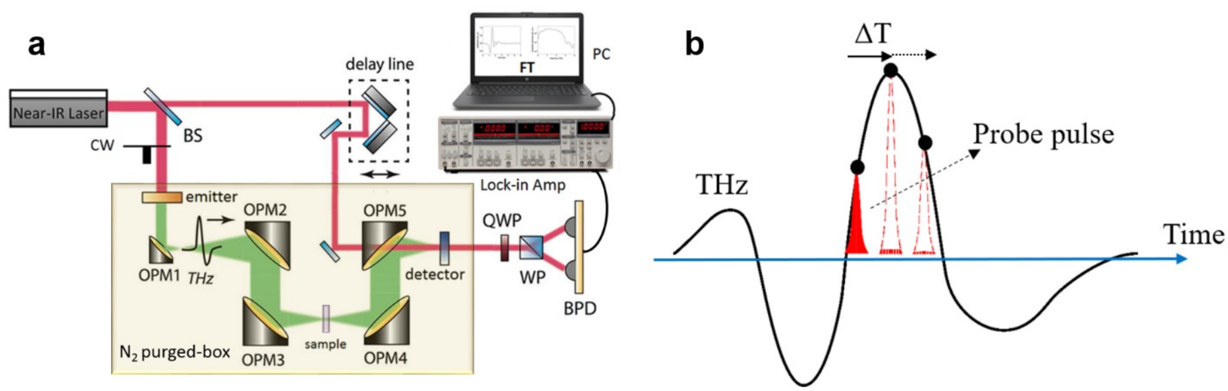

Figure 2.1 | Illustration of THz-TDS setup. (a) Example of THz-TDS experimental setup. (b) Schematic of the coherent detection mechanism, based on a variably delayed probe pulse.

2.1 The femtosecond laser source

The light source in a TDS system is a femtosecond laser, which emits a train of ultrashort pulses (with a temporal pulse duration ranging from tens to hundreds of femtoseconds), typically in the near-IR band. Depending on the THz generation technique employed, the laser source can be either an oscillator producing pulses with energy content of a few nJ and repetition rate in the MHz range, or an amplified laser, the pulses of which typically have a few mJ in energy, at the price of lower repetition rates (commonly of a few kHz). The laser sources used in this work are based on two different gain media, which are among the most widespread for ultrashort pulse generation. The first is titanium-doped aluminum oxide (also known as Ti:sapphire), emitting light with a central wavelength of around 800 nm in wavelength, and the other is an ytterbium-doped crystal (Yb-doped potassium gadolinium tungstate, Yb:KGW), emitting at 1030 nm.

2.2 Generation and detection of terahertz waves

The femtosecond laser is the source of light used to operate the whole THz spectrometer system, but such light lies in the IR region and must be converted into THz radiation. A vast assortment of generation and detection techniques have been developed over the last three decades, with efficiencies and sensitivities progressively improved over the years.

Generally speaking, THz radiation can be generated as a continuous-wave (CW) or in the form of broadband pulses. CW generation can be achieved with a variety of techniques based for example on photo-mixing (Safian et al., 2019) or frequency multiplication of microwaves (Siles et al., 2018), and is beyond the scope of this thesis. On the other side, the generation of broadband THz pulses, based on the use of femtosecond lasers, is generally accomplished by exploiting two different mechanisms: the first exploits the generation of transient photocurrents in semiconductors (e.g. GaAs); the second relies on the nonlinear optical response of bound electrons occurring in nonlinear electro-optic (EO) crystals (e.g. ZnTe). The former method relies upon the use of photoconductive antennas (PCA) and will not be discussed here. An overview on the topic can be found in (Hafez et al., 2016). As for the generation in nonlinear crystals, this is the main generation technique employed throughout the doctoral project and, as such, its main features will be presented in section 2.2.1.

Techniques for THz wave detection have also experienced a rapid technological boost in the past decades and can be generally divided in two main categories: incoherent or coherent techniques. Those belonging to the first class are mostly used in combination with CW sources and are based on thermal effects, where radiation energy is converted into heat to perform the measurement. Typical detectors of this type are bolometers, pyroelectric detectors and Golay cells (Lewis, 2019). On the other side, we have detectors that allow to coherently measure the THz electric field and are generally employed in combination with pulsed sources. As in the case of THz generation, transient photocurrents or the electronic response of nonlinear crystals can be exploited for the detection of

THz pulses. The latter will be presented in section 2.2.2, as it is the one employed throughout this doctoral project.

2.2.1 Terahertz generation in nonlinear crystals

When light interacts with matter, a primary source of optical phenomena is the electron response to the applied EM field. Electrons indeed move under the EM force and the accelerated motion generates new radiation. In most daily life phenomena, these induced motions are very small, so that, e.g., bound electrons are not displaced far from their equilibrium position. Under these conditions, electron oscillations are approximately proportional to the applied electric field. This is called the *linear regime* and, for bound electrons, can be described by the Lorentz model, where the electrons behave as harmonic oscillators (Y.-S. Lee, 2009). In this situation, the polarization (i.e. the density of dipoles describing the electron motion) induced by the external field, $E(t) = E_0 e^{-i\omega_{opt}t}$, can be written as:

$$P(t) = \varepsilon_0 \chi E_0 e^{-i\omega_{opt}t} \propto E(t) \tag{2.1}$$

The induced polarization oscillates at the same frequency, ω_{opt}, of the external field and the susceptibility, χ, does not depend on the strength of the field itself. Light reflection and refraction at the interface between two materials are well-known examples of linear phenomena.

If the applied external electric field is strong, then the electron motion can be large enough to deviate from the linear regime and, as a result, the optical properties become dependent upon the strength of the field itself. The induced polarization can be rewritten in a perturbative fashion since *nonlinear components* are always much smaller than the linear one (Boyd, 2007):

$$P(t) = \varepsilon_0 [\chi^{(1)} + \chi^{(2)} E(t) + \chi^{(3)} E^2(t) + \ldots] E(t) \tag{2.2}$$

Where all quantities are considered as scalars for simplicity, and the polarization depends on the instantaneous value of the external field, which is true only in a lossless and dispersionless medium (i.e. χ does not depend on the frequency of the electric field). Processes that depend upon $P^{(2)}(t) = \varepsilon_0 \chi^{(2)} E^2(t)$ are referred to as second-order nonlinear processes, those depending upon $P^{(3)}(t) = \varepsilon_0 \chi^{(3)} E^3(t)$ are third-order processes and so forth. A rough estimation of the order of magnitude of the nonlinear susceptibility terms can be done as follows: we can expect that, for the second-order correction, $P^{(2)}$, to be of the same order of magnitude of the linear term, $P^{(1)}$, the applied electric field has to be of the order of the atomic electric field strength $E_{at} = e/(4\pi\varepsilon_0 a_0^2) = 5.14 \times 10^{11} V/m$, where $-e$ is the electron charge and $a_0 = 4\pi\varepsilon_0 \hbar^2/me^2$ is the Bohr radius of the hydrogen atom (with m being the electron mass). Under these conditions, $\chi^{(2)}$ is thus of the order of $\chi^{(1)}/E_{at}$. If, as it typically happens in the case of condensed matter, $\chi^{(1)}$ is of the order of unity, we can obtain the following estimation for $\chi^{(2)}$ (and also for $\chi^{(3)}$, following a similar reasoning) (Boyd, 2007):

$$\chi^{(2)} \sim 1/E_{at} \sim 1.94 \times 10^{-12}\, m/V\,, \qquad \chi^{(3)} \sim 1/E_{at}^2 \sim 3.78 \times 10^{-24}\, m^2/V^2 \tag{2.3}$$

This clearly explains why the linear approximation is very accurate to describe most of everyday life phenomena, as very high fields are required for nonlinear processes to become relevant. Another important aspect is that the existence of the individual nonlinear susceptibility terms depends upon the spatial symmetry of the matter system. For example, $\chi^{(2)}$ exists only in non-centrosymmetric systems, which do not display inversion symmetry, whereas $\chi^{(3)}$ is present also in centrosymmetric media, such as gases, liquids, and amorphous materials like glass, which are symmetric under inversion. Such a dependence on symmetries can be ascribed to the vectorial nature of EM fields and the consequent tensorial nature of the electric susceptibility.

The nonlinear process at the basis of THz generation in nonlinear crystals is called Optical Rectification (OR) and is a second-order interaction, which is the reason why it can only occur in specific materials, i.e., those displaying non-centrosymmetric properties. The Lorentzian model of bound electrons can still be used to describe a nonlinear response, if the potential employed to obtain the electron equation of motion is properly adapted. In order to describe the asymmetric landscape of non-centrosymmetric systems, a cubic term can be added to the potential associated with the restoring force (Boyd, 2007):

$$U(x) = \frac{1}{2} m\omega_0^2 x^2 + \frac{1}{3} m\alpha x^3 \tag{2.4}$$

Where m is the electron mass, ω_0 the frequency of the external field and α the parameter to characterize the strength of the nonlinearity. Under these conditions, if the electron motion is sufficiently large, the difference between the positive and negative electron displacements becomes significant, as shown in Fig. 2.2. Such motion can be separated into a linear term and a nonlinear one ($x = x_L + x_{NL}$), with the latter composed of two terms oscillating at distinct frequencies (x_{SHG} at $\omega =$

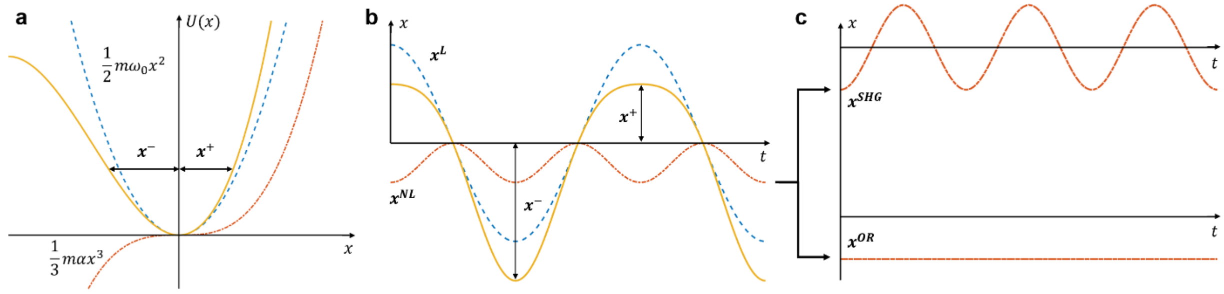

Figure 2.2 | Nonlinear potential and motions. (a) Second-order nonlinear potential. (b) Charge displacement related to the potential in (a). (c) OR and SHG components of the nonlinear motion.

$2\omega_{opt}$ and x_{OR} at $\omega = 0$). One of the key features of nonlinear processes is in fact the generation of fields oscillating at frequencies different from the driving field. More in detail, the equation of motion for the revised Lorentzian model is:

$$\frac{d^2x}{dt^2} + \gamma\frac{dx}{dt} + \omega_0^2 x + \alpha x^2 = -\xi\frac{e}{m}E(t) \tag{2.5}$$

For simplicity we assume a monochromatic wave as the incident field, $E(t) = E_0 e^{-i\omega_{opt}t}$ and ξ represents the coupling strength and ranges between 0 and 1. γ is the damping constant representing the atomic absorption. We can obtain the second-order response by solving Eq. 2.5, and if we seek solutions for the two frequencies $\omega = 2\omega_{opt}$ and $\omega = 0$, we get (Y.-S. Lee, 2009):

$$x_{SHG}(t) = -\alpha\left[\frac{eE_0}{m}\right]^2 \frac{e^{-i2\omega_{opt}t}}{(\omega_0^2 - (2\omega_{opt})^2 - i2\omega_{opt}\gamma)(\omega_0^2 - \omega_{opt}^2 - i\omega_{opt}\gamma)^2} + c.c.$$

(2.6)

$$x_{OR}(t) = -2\alpha\left[\frac{eE_0}{m\omega_0}\right]^2 \frac{1}{(\omega_0^2 - \omega_{opt}^2)^2 + \omega_{opt}^2\gamma^2}$$

Evidently, SHG corresponds to a field oscillating at $\omega = 2\omega_{opt}$ and OR to a DC-field at $\omega = 0$. As we shall see, OR is the process generating THz radiation under specific conditions. The corresponding bulk polarization becomes:

$$P_{OR}^{(2)} = -Nex_{OR} = 2\alpha\left[\frac{E_0}{m\omega_0}\right]^2 \frac{Ne^3}{(\omega_0^2 - \omega_{opt}^2)^2 + \omega_{opt}^2\gamma^2} = 2\varepsilon_0\chi^{(2)}(0, \omega_{opt}, -\omega_{opt})|E_0|^2 \tag{2.7}$$

Where $\chi^{(2)}(0, \omega_{opt}, -\omega_{opt})$ is the nonlinear susceptibility responsible for the generation of the DC field. It is worth pointing out that the OR polarization is directly proportional to the intensity of the applied electric field.

In order to understand how the OR process (or more precisely, a quasi-OR process) can generate THz radiation, we have to consider the case where the incident field is the one associated with a broadband IR pulse, rather than a monochromatic wave. The time-dependent nature of the quasi-rectified electric field can be ascribed to the fact that in this case the OR process involves the combination of all the frequencies in the spectrum of the optical pulse. The difference between two of these components, $\omega_{opt,1}, \omega_{opt,2}$, will result in a slowly oscillating field ($\omega_{opt,2} - \omega_{opt,1} = \omega_{THz} \ll \omega_{opt,1}, \omega_{opt,2}$, i.e., quasi-rectified field), the frequency of which will be in the range of the spectral bandwidth of the optical pulse, i.e., in the THz range. Considering a fully transparent nonlinear medium, the overall spectral bandwidth of the generated THz pulse will be roughly the inverse of the optical pulse duration, typically $T_0 \sim 100$ fs ($1/T_0 = \omega_{opt,MAX} - \omega_{opt,MIN} \approx \Delta\omega_{THz}$). The second order polarization is directly proportional to the intensity of the applied electric field. As such, if such intensity is time-dependent, the rectified polarization will have the same time dependence. For instance, if we consider a pulse with a gaussian amplitude profile of duration T_0, $E(t) = U_0(t)e^{-i\omega_{opt}t} = U_0 e^{-\frac{t^2}{2T_0{}^2}} e^{-i\omega_{opt}t}$, the polarization will replicate its envelope:

$$P_{OR}^{(2)} \propto |U_0|^2 e^{-\frac{t}{T_0}^2} \tag{2.8}$$

After discussing the induction of a rectified polarization, we shall finally see how the generation of THz radiation occurs in a nonlinear medium. The solution can be inferred directly from Maxwell's equations, considering only transverse currents contributions, since we are interested in the far-field radiative solution. Under these conditions, the radiative electric field is written as (Jackson, 1999):

$$\boldsymbol{E_{rad}} = -\frac{\partial \boldsymbol{A}}{\partial t} \tag{2.9}$$

In turn, the vector potential $\boldsymbol{A}$ can be calculated directly from the current in the material, which in the case of bound electrons is proportional to the first-order time derivative of the (second order) polarization (Greene et al., 1992). The radiated THz electric field is therefore proportional to the second order time derivative of the polarization, which is determined by the envelope of the exciting optical pulse (which can be supposed to be gaussian, see Fig. 2.3):

$$\boldsymbol{E_{THz}} \propto 2\varepsilon_0 \chi^{(2)}(0; \omega_{opt}, -\omega_{opt}) \frac{\partial^2 |\boldsymbol{U_0(t)}|^2}{\partial t^2} \tag{2.10}$$

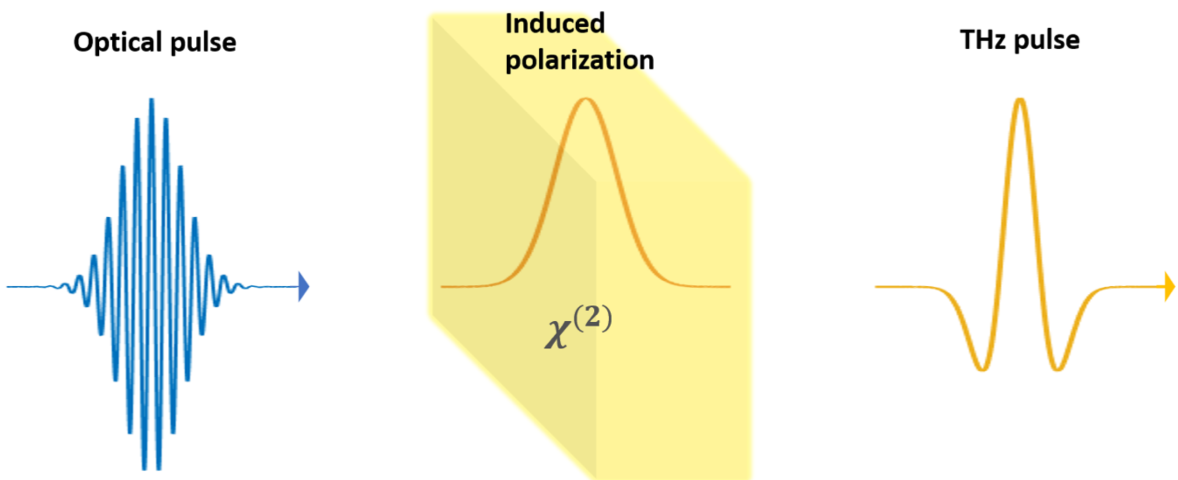

Figure 2.3 | THz generation via OR. Optical (gaussian) pump pulse centered at $\boldsymbol{\omega_{opt}}$; rectified polarization replicating the gaussian envelope; generated THz wave.

If we consider a thin layer of nonlinear material, a propagating optical pulse induces a second-order polarization which in turn will generate a THz electric field. Now, if we think about the nonlinear crystal as a stack of multiple thin layers, the THz electric field generated in the first layer will now be copropagating with the optical field. If the optical and THz pulse travel with the same velocity, the polarization induced in the following layers will generate more THz field, which will add up constructively, resulting in an increase of the amplitude of the THz pulse. Since the conversion efficiency of the process is low ($\sim 10^{-4}$), we can consider the optical pulse as undepleted, so that this amplification process is linear with the propagation distance.

Unfortunately, though, this is typically not the case: the optical and THz pulses propagate at different velocities, due to the material dispersion, which causes a variation of the refractive index at different frequencies. As a result, there is a progressive walk-off of one pulse with respect to the other, which in turn leads to a phase mismatch that hampers an efficient THz generation. It is thus important to choose the proper nonlinear material, where the phase-matching conditions are satisfied for a distance long enough to enable a sizeable THz generation. The specific phase-matching conditions can be derived from the conservation of energy and momentum in the quasi-OR process:

$$\begin{cases} \Delta\omega_{opt} = \omega_2 - \omega_1 = \omega_{THz} \\ \Delta k_{opt} = k_2 - k_1 = k_{THz} \end{cases} \tag{2.11}$$

Where (ω_1, k_1) and (ω_2, k_2) are the frequency and wave vector of two components of the broadband optical pulse, while (ω_{THz}, k_{THz}) are the corresponding quantities of the central component of the THz pulse. By taking the ratio of the two equations above (and introducing differential quantities), we obtain:

$$v_{G,opt} = \frac{\partial \omega_{opt}}{\partial k_{opt}} = \frac{\omega_{THz}}{k_{THz}} = v_{ph,THz} \tag{2.12}$$

where $v_{G,opt}$ and $v_{ph,THz}$ are the group velocity of the pump optical beam and the phase velocity of the THz wave, respectively, which thus need to be equal to ensure phase-matching. From this relation it is possible to define a coherence length, which is the maximum length of the nonlinear medium for an effective optical to THz conversion (Nahata et al., 1996):

$$l_c(\omega_{THz}) = \frac{\pi c}{\omega_{THz}\left|n_{g,opt}(\omega_{opt}) - n_{THz}(\omega_{THz})\right|} \tag{2.13}$$

With the group refractive index of the femtosecond near-infrared laser pulse defined as:

$$n_{g,opt} = n_{opt}(\omega) - \lambda_{opt}\left(\frac{\partial n_{opt}}{\partial \lambda}\right)\Bigg|_{\lambda_{opt}} \tag{2.14}$$

where c is the speed of light in vacuum, ω_{THz} is the THz frequency, $\omega_{opt}(\lambda_{opt})$ the near-IR excitation frequency (wavelength), and n_{THz} and n_{opt} are the refractive index at THz and near-IR frequencies. Clearly, one would want to use a crystal as thick as possible within the limitation posed by the coherence length, so to maximize the emitted THz intensity. A trade-off there exists, though, in the bandwidth achievable for the THz pulse itself. The material is in fact dispersive in the THz range as well, so a longer interaction length limits the phase-matching to a narrower THz bandwidth. This means that, to achieve a larger bandwidth, one has to use a thinner crystal, at the expense of the total intensity of the generated THz pulse. Ideally, the bandwidth of the THz pulse is roughly the inverse of the optical pulse duration, $\frac{1}{\tau} \sim 10$ THz for a ~ 100 fs pulse. But, for ZnTe, for instance, the coherence length becomes very short for frequencies above ~ 3 THz, making it hard to obtain a higher frequency content even with very short pump pulses (Nahata et al., 1996), unless very thin crystals are used (Han & Zhang, 2001). In general, in spectroscopic applications where a larger bandwidth is essential, for instance to extract multiple absorption lines in the spectrum, a thinner EO crystal is preferred, whereas in applications like time-of-flight imaging (see section 2.3.2), where we require multiple pulses produced by, e.g., weakly reflecting interfaces in a multilayer sample, a thicker crystal can be more convenient, in order to maximize the main THz peak amplitude. Another important limitation on the achievable THz bandwidth is posed by the generating crystal absorption in the THz range. This is typically due to the presence of optical phonon resonances, for example, ZnTe has one main phonon absorption at 5.4 THz.

As mentioned above, a second-order process occurs in crystalline materials that do not display inversion symmetry. For a thorough description of a nonlinear crystal optical properties, we need to represent the susceptibility as a tensor $\chi_{ijk}^{(2)}$ and consider the vector nature of electric fields (Y.-S. Lee, 2009):

$$P_i^{(2)}(0) = \sum_{j,k} \varepsilon_0 \chi_{ijk}^{(2)}(0; \omega_{opt}, -\omega_{opt}) E_j(\omega_{opt}) E_k^*(\omega_{opt}) \tag{2.15}$$

The tensor can be rewritten in a compact form $d_{il} = \frac{1}{2}\chi_{ijk}^{(2)}$, since the last two indices are permutable $\chi_{ijk}^{(2)} = \chi_{ikj}^{(2)}$ (Boyd, 2007). Moreover, many crystals commonly used for THz generation are highly symmetric, thus resulting in most of the terms vanishing. Two of these, used in this work, are Zinc Telluride (ZnTe) and Gallium Phosphide (GaP), and both fall in the crystal class $\bar{4}$3m, which have three non-vanishing terms and only an independent one, $d_{14} = d_{25} = d_{36}$. The fields can be conveniently written in a coordinate reference, *(x′,y′,z′)*, where the *(x′,y′)*-plane is on the (110) plane of the crystal, with x' in the direction [-110] (see Fig. 2.4(a)). We can thereby define θ as the angle between the y'-direction (i.e., [001]) of the new coordinates and the polarization vector of the optical pump pulse (Fig. 2.4(b)). The generated THz electric field E_{THz} will also lie in the reference plane *(x′,y′)*, oriented as follows (Blanchard et al., 2011):

$$\begin{pmatrix} E_{THz}^{x'} \\ E_{THz}^{y'} \end{pmatrix} \propto \begin{pmatrix} \sin 2\theta \\ \sin^2 \theta \end{pmatrix} \tag{2.16}$$

The energy associated with such THz field, will thus be proportional to $\mathrm{I}_{THz}(\theta) \propto \sin^4 \theta + \sin^2 \theta$. Which means that the maximum of the irradiated THz field energy will result for an optical pump orientation $\theta = \sqrt{2}$, corresponding to either the [-111] or [1-11] orientations (Fig. 2.4(c)).

Ultimately, an efficient generation of THz pulses requires a material with a sufficiently large nonlinear susceptibility, a coherence length which is long enough to ensure the pulse is constructively amplified, and the lack of absorption resonances in the bandwidth of interest. Furthermore, the proper orientation between the polarization of the incoming pump pulse and the axes of the crystal employed for OR must be carefully considered.

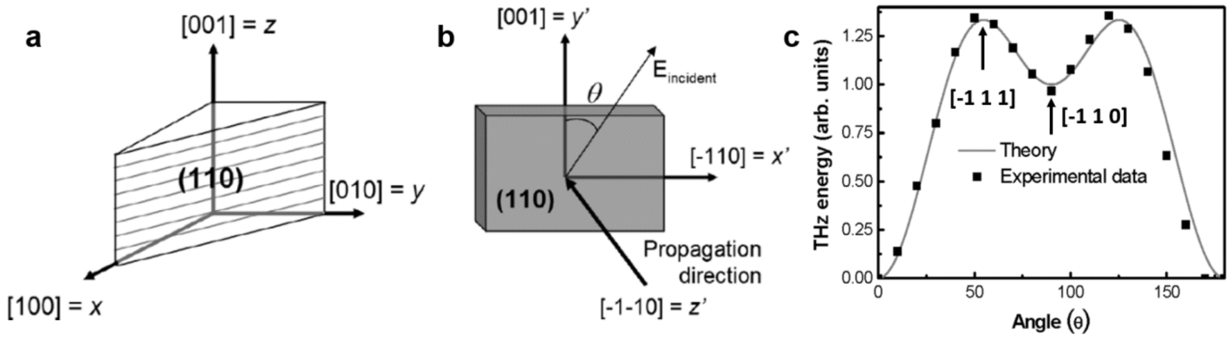

Figure 2.4 | THz generation dependence on crystal orientation. (a) The (110) plane of a crystalline material shown in the (x,y,z) coordinate system. (b) New coordinates (x',y',z') on the (110) plane. A linearly polarized optical wave is normally incident on the (110)-oriented crystal. θ is the angle between the field polarization and the [001] axis. *Adapted from (Blanchard et al., 2011) © 2011 IEEE*. (c) THz radiation intensity vs angle (θ) in ZnTe. *Adapted by permission from Springer, (Y.-S. Lee, 2009) © 2009*

2.2.2 Terahertz detection via electro-optic sampling

The detection of THz pulses in nonlinear crystals relies on the *Pockels effect* in EO materials. This process occurs when a (quasi) DC field is applied to the material inducing a change in the refractive index at visible/IR frequencies. In the case of electro-optic sampling (EOS), the THz wave acts as the quasi-DC field, inducing a slowly changing variation of the refractive index. In phase-matching conditions, the much shorter near-IR pulse copropagating with the THz will experience a constant value of such variation. By delaying the arrival of the probe pulse on the detection crystal, it is possible to extract a temporal map of the amplitude of the THz electric field. The nonlinear polarization related with the Pockels effect is written as (Y.-S. Lee, 2009):

$$P_i^{(2)}(\omega) = 2\sum_{j,k} \varepsilon_0 \chi_{ijk}^{(2)}(\omega;\omega,0)E_j(\omega)E_k^*(0) \tag{2.17}$$

And it is closely connected to the OR process, the coefficients of the susceptibility tensor for a lossless medium being, in fact, the same $\chi_{ijk}^{(2)}(\omega;\omega,0) = \chi_{kji}^{(2)}(0;\omega,-\omega)$, under simple indices and frequencies interchange (Boyd, 2007). The efficiency for both THz generation and detection can thus be inferred by the linear EO coefficient of a material, r_{ijk}, which is directly related to $\chi^{(2)}_{ijk}$, through (Dexheimer, 2008):

$$r_{ijk} = -\frac{4\pi}{n_i^2 n_j^2}\chi^{(2)}_{ijk} \tag{2.18}$$

Where n_i and n_j are the refractive indices expressed in the principal axes of the crystal. It is again possible to introduce a compact notation such that $r_{ijk} \to r_{lk}$, and for crystals like ZnTe and GaP, the only non-zero coefficient is r_{41}.

The change in the refractive index induced by the THz electric field on the EO crystal is measurable as a birefringence effect. We can consider the case of ZnTe and GaP, for instance, with both linearly-polarized optical and THz pulses propagating along the [-1-10] axis of a (110)-cut crystal (Fig. 2.5(a)). In absence of the THz field the crystal is isotropic, therefore the principal axes can be chosen simply as $X = [1\text{-}10]$, and $Y = [001]$. When the THz is present, the nonlinear polarization induced by the Pockels effect causes a rotation of such axes ($X \to X'$, $Y \to Y'$). While the optical probe field propagates through the crystal, its two perpendicular components along the (rotated) principal axes gain a relative phase shift, due to the refractive index difference. Such retardation can be written as:

$$\Delta\phi = \frac{\omega}{c}(n_2 - n_1)d = \frac{\omega n^3 r_{41} E_{THz} d}{2c}\sqrt{1 + 3\cos^2\alpha} \tag{2.19}$$

where n is the refractive index in absence of the THz field, while $n_{1,2}$ are the indices along the principal axes, r_{41} is the relevant EO coefficient of the nonlinear crystal at the probe frequency ω, d is the crystal thickness, α the angle between the THz field and the X-axis.

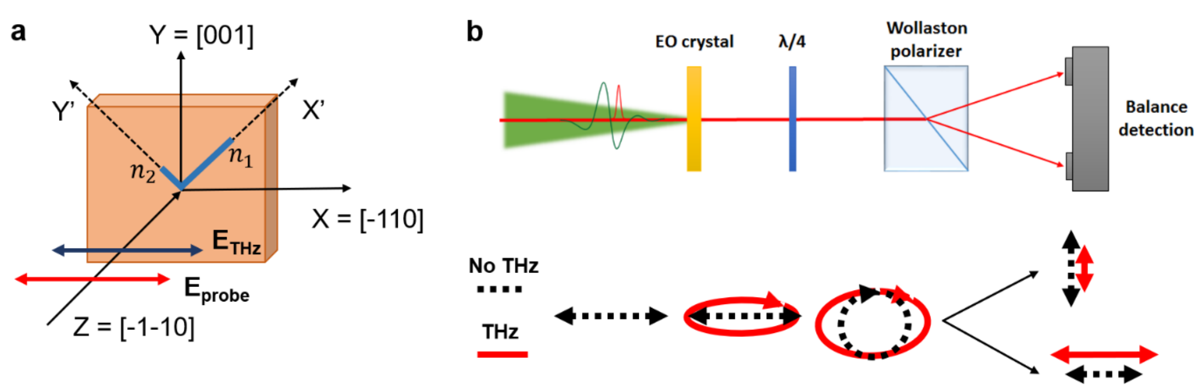

Figure 2.5 | THz detection via EOS. (a) Optical probe pulse and THz pulse incident on a (110)-cut ZnTe. (b) Schematic of the EOS measurement and the respective probe polarization after each optical component.

The maximum of such phase delay is obtained for $\alpha = 0°$, and the maximum of the probe polarization rotation when the angle between the probe itself and the THz, is 0° or 90°, as in Fig. 2.5(a).

The schematic of an EOS measurement is shown in Fig. 2.5(b). The much shorter probe beam is variably delayed in order to sample the longer THz pulse in the time-domain. The probing occurs when the THz beam and the optical probe are spatially overlapped in the crystal, and afterwards, the induced birefringence is measured by a balanced detection system. The probe pulse is elliptically polarized due to the phase retardation induced by the THz field. The ellipticity is maintained even after the propagation through the quarter waveplate, which further induces a $\pi/2$ retardation. The vertical and horizontal linear components of the polarization are separated in a Wollaston prism and finally detected by two balanced photodiodes. The intensities of the two signals can be written as:

$$\begin{aligned} I_1 &= \frac{I_0}{2}[1 - \sin(\Delta\phi)] \\ I_2 &= \frac{I_0}{2}[1 + \sin(\Delta\phi)] \end{aligned} \tag{2.20}$$

where I_0 is the intensity of the optical probe. For a sufficiently low THz electric field $\Delta\phi \ll 1$, so that the intensity modulation becomes directly proportional to the THz electric field amplitude:

$$\frac{\Delta I}{I_0} = \frac{I_1 - I_2}{I_0} = \lim_{\Delta\phi \to 0} \sin\left(\frac{\omega n^3 E_{THz} r_{41} d}{c}\right) \approx \frac{\omega n^3 E_{THz} r_{41} d}{c} \tag{2.21}$$

For high values of the incident THz electric field on the detection crystal, the phase delay between the two polarization components might become larger than $\pi/2$ (i.e., *over-rotation effect*), leading to an inaccurate estimation of the THz electric field value, due to the waveform modulation. The detection bandwidth of EOS is again determined by the phase matching conditions between the THz and the optical probe in the detection crystal, the temporal duration of the probe, and possible absorption of the nonlinear crystal in the THz range (due to, e.g., phonon transitions). To increase the signal-to-noise ratio (SNR) of the measurement, a lock-in amplifier is typically used to selectively amplify the acquired probe signal modulated at a given reference frequency. This is usually implemented by mechanically modulating the THz signal through a chopper wheel.

As mentioned before, EOS allows to coherently resolve the time-dependent THz waveform, thus providing both the amplitude and the phase information of the THz electric field. This detection technique is usually implemented in a THz-TDS measurement, enabling to retrieve, for example, both the refractive index, $n(\omega)$, and absorption coefficient, $\alpha(\omega)$, of a tested sample, as it will be discussed in section 2.3.2.

2.2.3 Nonlinear crystals for terahertz generation and detection

A variety of EO materials have been used for THz generation via OR. Among them are various semiconductors (e.g. ZnTe, ZnSe, GaSe, GaP) and inorganic oxide crystals (e.g. $LiNbO_3$, $LiTaO_3$). Most of these are also the preferred choices for THz sensing via EOS (ZnTe, GaP, GaSe in particular). The EO coefficients of some common materials used for THz generation are reported in Table 2.1.

Table 2.1 | Electro-optic coefficients of some THz emitters. (Blanchard et al., 2011; Dexheimer, 2008)

Material	Electro-optic coefficient (pm/V)
ZnTe	r_{41} = 4.04 (@ 633 nm)
GaP	r_{41} = 0.97 (@ 800 nm)
GaSe	r_{22} = 14.4 (@ 800 nm)
$LiNbO_3$	r_{33} = 30.9 (@ 633 nm) r_{51} = 32.6 (@ 633 nm)
$LiTaO_3$	r_{33} = r_{13} = 30.5 (@ 820 nm)

Zinc telluride (ZnTe) and gallium phosphide (GaP) are two of the most commonly employed, thanks to their fairly good phase matching for pump wavelengths at 800 nm an 1030 nm, respectively (i.e., the emission wavelengths of Ti:Sapphire and Yb-lasers). It is worth noting that the attainable spectral bandwidth is limited by the main phonon absorptions located at 5.4 THz for ZnTe and 11 THz for GaP (Dexheimer, 2008). In addition, the rectified THz pulses cannot typically deliver electric fields greater than ~100 kV/cm, due to multiphoton absorption of the optical pump which causes the saturation of the conversion efficiency for THz at high pump energies, unless large-area crystals are used (Blanchard et al., 2011).

A series of organic crystals (e.g. DAST, DSTMS, OH1, HMQ-T, etc.) have also been studied and provide an efficient and more intense THz generation (P.-J. Kim et al., 2012; Kwon et al., 2008; Pan et al., 1996; Stillhart et al., 2008). DAST, for instance, has an electrooptic coefficient of r_{11} = 47 pm/V at 1.5 µm (r_{11} = 77 pm/V at 800 nm), much higher than ZnTe (4.04 pm/V) and GaP (0.97 pm/V) (Pan et al., 1996), which makes it possible to achieve electric field peaks of few MV/cm (Vicario et al., 2015). Nevertheless, the optimal pump wavelength to meet the phase matching condition usually stands in the range 1.3-1.5 µm for organic crystals, therefore requiring more complex pumping sources, such as an optical parametric amplifier.

One of the most recent additions to the set of organic crystals for THz generation is 2-(4-hydroxy-3-methoxystyryl)-1-methylquinolinium 2,4,6-rimethylbenzenesulfonate (HMQ-TMS) (Jeong et al., 2013; Lu et al., 2015). The advantage of HMQ-TMS, compared to other organic crystals, is its larger OR phase-matching bandwidth, allowing it to be pumped by the emitting wavelengths of widespread laser amplifiers (e.g. 800 nm and 1030 nm), whilst maintaining a high conversion efficiency. Peak fields of some hundreds kV/cm have been demonstrated by our group, by employing an amplified laser source emitting pulses at 1030 nm (Rovere et al., 2018). In the first part of this thesis work, ZnTe crystals were used for both THz generation and detection. ZnTe presents favorable phase-matching conditions at 800 nm, the emission wavelength of the Ti:sapphire regenerative amplified source employed (*Spectra Physics*), producing 150-fs-long pulses, with pulse energy of 2.2 mJ at 1 kHz repetition rate. In the second part, an HMQ-TMS crystal was used for THz generation via an Yb-based laser. In this case, the detection was carried out by means of a GaP crystal, which achieves a good phase-matching condition at 1030 nm, as does HMQ-TMS. The source was a Yb:KGW laser (*Light Conversion*), emitting 170-fs-long pulses centered at 1030 nm with maximum pulse energy of 1 mJ and tunable repetition rate up to 6 kHz.

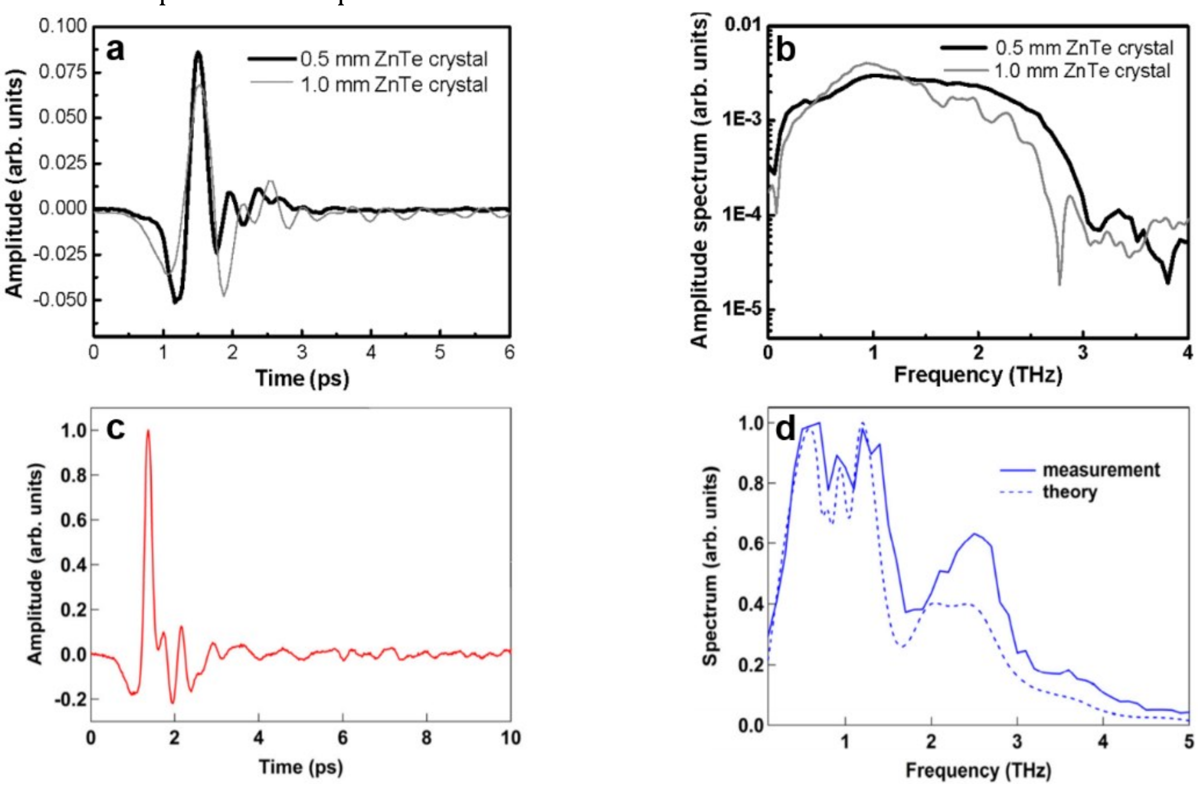

Figure 2.6 | THz waveforms using different nonlinear crystals. Top: (a) THz pulses generated by 0.5-mm- and 1-mm-thick ZnTe crystals and detected via EOS by a 0.5-mm-thick one. (b) Frequency spectrum of the THz waveforms shown in (a). *Adapted from (Blanchard et al., 2011) © 2011 IEEE*. Bottom: (c) THz electric field waveform emitted by a 630-μm-thick HMQ-TMS organic crystal and retrieved using a GaP detection crystal. (d) Measured (solid) and calculated (dashed line) THz emission spectra. *Adapted with permission from (Rovere et al. 2018) © 2018 The Optical Society.*

2.3 Time-domain spectroscopy for imaging purposes

Here, we discuss how TDS enables the extraction of amplitude and phase of an ultrashort THz pulse, and how this ability can be exploited to obtain images. We consider the example of transmission imaging, where a semitransparent object is illuminated by the THz beam (Fig. 2.7(a)). The classical way to retrieve the 2D image is to raster-scan the sample, placed in the Fourier plane of a pair of focusing elements (Fig. 2.7(b)). A temporal THz trace is recorded at each pixel of the scene (Fig. 2.7(c)), such that the result is a three-dimensional data matrix, where the third dimension is time.

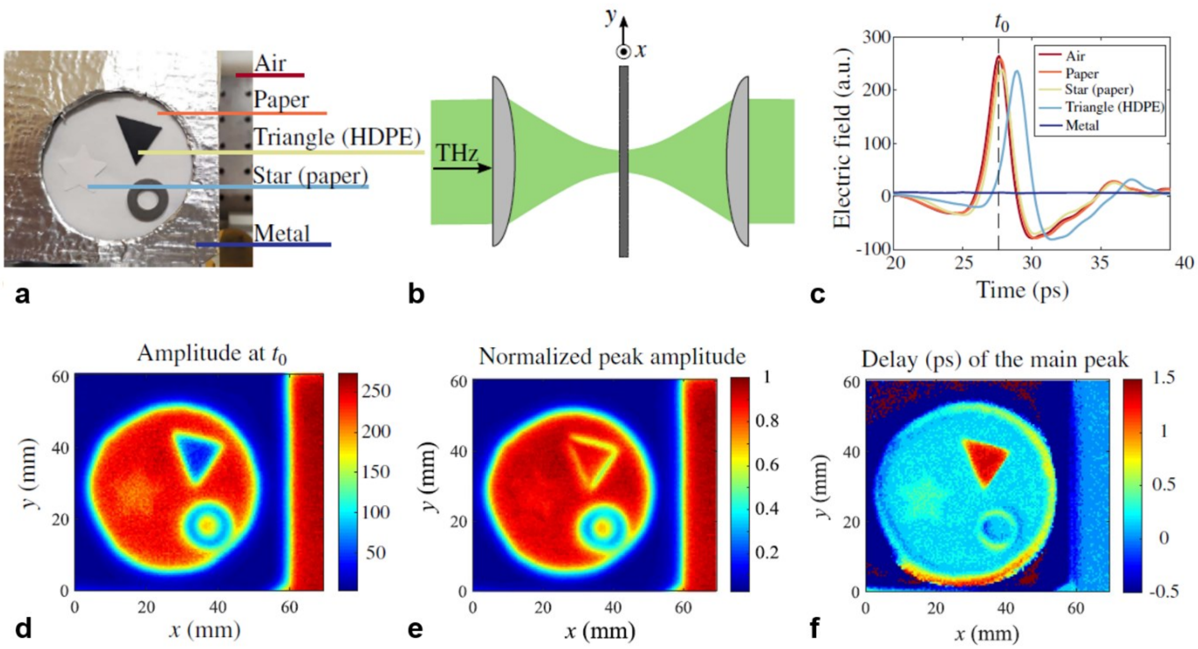

Figure 2.7 | THz imaging techniques. (a) Photograph of the sample, composed of a paper star, a metallic washer, and a HDPE triangle. (b) Schematic of the imaging configuration: the sample was mechanically moved in the (x, y) focal plane of a pair of lenses. (c) THz waveforms measured in air and at the objects positions. (d) Image obtained using the amplitude of the pulses at fixed time t_0. (e) Image obtained with the amplitude of the THz peak. (f) Image obtained using the phase delay of the main peak, related to the reference in air. *Adapted with permission from (Guerboukha et. al, 2018) © 2018 The Optical Society.*

This set of raw data can be used to extract images using different methods, usually chosen in order to enhance the image contrast depending on the targeted application. Examples of different contrast methods are presented in Fig. 2.7. We can use the THz traces directly in the time-domain or by taking their Fourier transform, in order to extract the spectral amplitude and phase. In the former case we can, for instance, visualize the amplitude at fixed time positions (Fig. 2.7(d)), revealing the irradiation dynamics at the picosecond scale, or show the peak of the THz waveform normalized to the peak of a reference sample (Fig. 2.7(e)), revealing details about the absorption, reflection or scattering losses. Otherwise, we can choose to map the time delay of the waveform peak at each pixel, with respect to the reference in air (Fig. 2.7(f)), obtaining the corresponding optical path change and thus information on material refractive index or thickness of the sample. If we perform the Fourier transform, the spectral amplitude can again give a general indication on frequency-dependent losses, and it can reveal material-specific absorption lines. Finally, the spectral phase is related to the optical path of each frequency component of THz radiation.

2.3.1 Transmission and reflection imaging

The ability to coherently reconstruct the THz waveform with TDS enables material characterization, by retrieving the complex refractive index. Let us introduce the Fresnel coefficients for a (p-polarized) THz wave refracted or reflected at the interface between two materials (1,2) with complex refractive index $\tilde{n}_{1,2} = n_{1,2} + ik_{1,2}$:

$$t_{12} = \frac{2\tilde{n}_1}{\tilde{n}_1 + \tilde{n}_2}$$
$$r_{12} = \frac{\tilde{n}_1 - \tilde{n}_2}{\tilde{n}_1 + \tilde{n}_2} \tag{2.22}$$

For simplicity, we have here defined the transmission and reflection coefficients for the case of normal incidence. Note that, in the case of raster-scan imaging, the beam is focused, so the coefficients must be corrected to take into account the non-planar wave front of the beam (Guerboukha et al., 2018). By performing TDS measurements for each one of the pixels, we can obtain a 2D map of the complex refractive index of the material under investigation.

In more detail, here is how TDS spectroscopy enables the extraction of the relevant optical parameters. We start considering a transmission geometry, with a sample of thickness L and refractive index $\tilde{n}_2$, placed between two media respectively with refractive index $\tilde{n}_1$ and $\tilde{n}_3$. We will have to measure one THz waveform transmitted in presence of the sample, $E_s(t)$, and another one without it, $E_{ref}(t)$. The THz waveforms in the time-domain will be then Fourier transformed to obtain $E(\omega) = A(\omega)e^{i\phi(\omega)}$, where $A(\omega)$ and $\phi(\omega)$ are the spectral amplitude and phase respectively. The transmission function will be:

$$T_s(\omega) = \frac{E_s(\omega)}{E_{ref}(\omega)} = \frac{t_{12}P_2t_{23}}{t_{13}P_1}FP_{123} \tag{2.23}$$

Where t_{ab} is the Fresnel coefficient for transmission between medium a and b, as defined in Eq. (2.22), $P_a = e^{-\frac{i\tilde{n}_a\omega L}{c}}$ is the propagation coefficient in a medium of thickness L and refractive index $\tilde{n}_a$, and the Fabry-Perot coefficient, due to the internal reflections in the sample, is defined as $FP_{abc} = \sum_{k=0}^{\infty}\{r_{bc}{P_b}^2 r_{ba}\}^k$. All of these coefficients depend on the angular frequency ω. The Fabry-Perot term is easily simplified to $FP = 1$, if the sample is optically-thick, so that the time echoes due to the secondary reflections are well separated in time, and only the directly transmitted THz pulse (corresponding to $k = 0$ in the summation) is recorded. This condition is commonly encountered: for example, even a relatively thin layer ($d = 500$ μm) of a semiconductor like silicon ($n = 3.42$), introduces a delay between two echoes $\Delta t = 2nd/c \approx 11$ ps, which makes it possible to discard all the secondary reflections. Furthermore, if the sample ($\tilde{n}_2 = \tilde{n} = n - ik$) is in air ($\tilde{n}_3 = \tilde{n}_1 = 1$), Eq. (2.23) further simplifies into:

$$T_s(\omega) = \frac{t_{12}P_2t_{21}}{P_1} = \frac{4\tilde{n}(\omega)}{(1+\tilde{n}(\omega))^2} e^{-\frac{i\omega L}{c}(n(\omega)-1)} e^{-\frac{\omega L}{c}k(\omega)} \tag{2.24}$$

From this equation we can obtain the expression for the real ($n(\omega)$) and imaginary ($k(\omega)$) parts of the refractive index:

$$\begin{aligned} n(\omega) &= \frac{c}{\omega L}\left\{\arg\left[\frac{(\tilde{n}(\omega)+1)^2}{4\tilde{n}(\omega)}T_s(\omega)\right]\right\} + 1 \\ k(\omega) &= -\frac{c}{\omega L}\log\left[\left|\frac{(\tilde{n}(\omega)+1)^2}{4\tilde{n}(\omega)}T_s(\omega)\right|\right] \end{aligned} \tag{2.25}$$

Where arg (z) is the phase of the complex number z. Eq. (2.25) can be solved with iterative methods by assigning an initial value (n_0, k_0) to the refractive index (for example by assuming $(\tilde{n}(\omega)+1)^2/4\tilde{n}(\omega) = 1$), and recalculating the solution until it converges to a fixed point (Guerboukha et al., 2018).

The complementary approach is reflection imaging, that we can perform by illuminating the sample with the THz beam and then recording its reflection pixel by pixel. An example is a sample with refractive index $\tilde{n}_3$, placed behind a window of thickness L and refractive index $\tilde{n}_2$, and immersed in a third medium (such as air) with index $\tilde{n}_1$. This configuration is used, for instance, to characterize liquids inside plastic bottles (Jepsen et al., 2007). If the window is thick enough, so that one can separate its front and back reflection traces in the time domain, the reflection function R_s is extracted by dividing the reflection $E_s(\omega)$ from the window/sample interface, by $E_{ref}(\omega)$ from the air/window interface. Moreover, if we discard the Fabry-Perot term, we get:

$$R_s(\omega) = \frac{E_s(\omega)}{E_{ref}(\omega)} = \frac{t_{12}r_{23}t_{21}{P_2}^2}{r_{12}} = \frac{4\tilde{n}_2\tilde{n}_1(\tilde{n}_2 - \tilde{n}_3)(\tilde{n}_1 + \tilde{n}_2)}{(\tilde{n}_1 - \tilde{n}_2)(\tilde{n}_2 + \tilde{n}_3)(\tilde{n}_1 + \tilde{n}_2)} e^{-2\frac{i\omega L}{c}(\tilde{n}_2 - 1)} \tag{2.26}$$

Assuming $\tilde{n}_1 = 1$ for air, and $\tilde{n}_2 = \tilde{n}_w$ as the known refractive index of the window, we can write:

$$C = \frac{E_s}{E_{ref}} \frac{(1 - {\tilde{n}_w}^2)}{4\tilde{n}_w} e^{2\frac{i\omega L}{c}(\tilde{n}_w - 1)} = \frac{\tilde{n}_w - \tilde{n}_3}{\tilde{n}_w + \tilde{n}_3} \tag{2.27}$$

And we can find an analytical solution for $\tilde{n}_3$:

$$\tilde{n}_3(\omega) = \left[\frac{1 - C(\omega)}{1 + C(\omega)}\right] \tilde{n}_w(\omega) \tag{2.28}$$

When a sample is strongly absorbing, the reflection geometry is clearly superior to the transmission one, as it minimizes signal loss. For example, since liquid water is strongly absorbing in the THz spectral range, many THz biomedical applications rely on a reflection geometry (S. Fan et al., 2014).

2.3.2 Time-of-flight imaging

Time-of-flight (TOF) (or THz pulsed imaging, TPI) relates to the mapping of the arrival times of THz pulses at the detector. The temporal delay between the pulses reveals the internal structure of the sample. Most commonly, a reflection geometry is used for TOF, so that the reflection from the front surface can be directly used as reference, without the need of a second acquisition. Nevertheless, a transmission geometry, whose alignment is typically easier, can also be used. Already in the early days of THz imaging, TOF was demonstrated by imaging the internal structure of a 3.5 inch floppy disk (Mittleman et al., 1996). In a TOF measurement, the optical path travelled by the THz pulse is directly related to the delay, Δt, accumulated by such pulse. Assuming a refractive index n constant over the relevant THz frequency bandwidth, one can use the time delay between the pulse reflected by the sample surface and the one reflected by a sample internal interface to measure the distance d between the two surfaces:

$$d = \frac{c\Delta t}{2n} \tag{2.29}$$

In a similar manner, in a transmission geometry, the distance traveled by the pulse through the sample can be obtained by calculating the relative delay accumulated by such pulse with respect to a reference one, measured without the sample (i.e., propagating in air, $n_a = 1$):

$$d = \frac{c\Delta t}{(n - n_a)} = \frac{c\Delta t}{(n - 1)} \tag{2.30}$$

An example of a practical application of TOF imaging is the quality check of tablets coatings in the pharmaceutical industry (Haaser et al., 2013; Zeitler et al., 2010). Coating materials are typically opaque to visible/IR but semi-transparent at THz, allowing for non-destructive imaging. The same general idea was also employed to evaluate other tablets properties, such as hardness, density (May et al., 2013), and porosity (Bawuah et al., 2014). In addition, THz-TOF was also used to check the thickness uniformity of automobile exterior covering films (Su et al., 2014).

2.4 Examples of terahertz imaging applications

A large assortment of potential applications has been proposed over the last twenty years of development of THz imaging technologies (Mittleman, 2018). The fields of interest are the most diverse: we present a few of them here, to underline the importance that THz have gained in the broad scientific community.

One typical feature of EM radiation in the far-IR band is that it is strongly absorbed by water. This represents an asset for certain applications, since for example it offers a high sensitivity in the detection of even modest variations in the concentration of moisture, or a limitation for others, due to a limited penetration depth, restraining its use for the inspection of water solutions. Absorption of liquid water is due to a combination of effects, but in the THz region it is dominated by the reorientation of permanent and induced dipole moments (Thrane et al., 1995). The first measurement of liquid water absorption using a THz-TDS system was performed in a reflection geometry (Thrane et al., 1995), and subsequently confirmed by transmission measurements (Mittleman et al., 1996), and molecular dynamics simulations (Nuss, 1996). One example of application, proposed since the early days of THz imaging (Mittleman et al., 1996), is the monitoring of water content in living plants. The interest in the topic kept growing in more recent years (Castro-Camus et al., 2022; Jansen et al., 2010), particularly due to the increased occurrence and severity of droughts across many regions worldwide, caused by global warming (Browne et al., 2020). The use of THz is especially beneficial because it is inherently nondestructive, and can be carried out *in* vivo, even with repeated measurements on the same tissue, without damaging it (Gente et al., 2018). One recent example is the work by Castro-Camus and coworkers (Singh et al., 2020), which has provided insights on the mechanisms some desert plants such as agaves exploit to resist drought conditions. In a previous study, they showed (using THz-TDS) how agave fructans, a type of sugar produced by these plants, is able to form large hydration shells (Morales-Hernández et al., 2019). Then, they employed THz-TDS to obtain a 3D map of the Agave leaves, and displayed how the carbohydrate-rich inner regions are much more hydrated than the outer vascular tissue layer (Fig. 2.8). This way, they proved that fructans are at the basis of agaves' exceptional capacity of water retention.

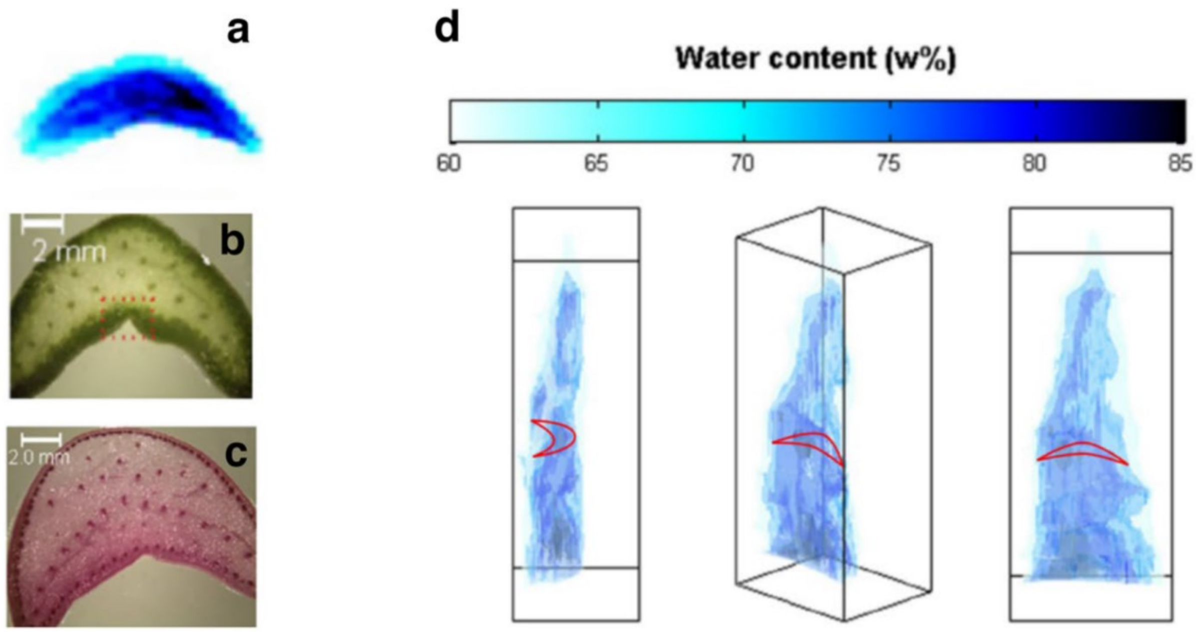

Figure 2.8 | THz imaging of water content. *(a) Cross-section of water-content image of an agave leaf obtained via THz imaging. We can see a high hydration core surrounded by a lower hydration layer. (b) Optical microscope image of a cross-section of an agave leaf where the inner hydrenchyma (white) and the outer chlorenchyma (green) are visible and correlate with the image in (a). (c) Periodic acid-Schiff (PAS) staining of the agave leaf revealing the presence of carbohydrates. (d) 3D water-content image of the entire agave leaf from 3 perspectives showing the outer low-hydration, and inner high hydration regions. Adapted from (Castro-Camus et al. 2022) under the https://creativecommons.org/licenses/by/4.0/ license.*

The possibility of contactless measurements of water content can also be exploited for medical imaging. Again, the non-ionizing nature of THz is a great advantage, making it safe to use even if lengthy exposures are needed. One example is the assessment of tissue burns, using a reflection geometry, performed by monitoring the hydration dynamics in the post-burn caused by edema (Bajwa et al., 2017; Tewari et al., 2019). The initial water depletion at the burn site, minutes after the injury, causes a reduction of the terahertz reflection at the cutaneous surface. Nevertheless, the following inflammatory response produces an accumulation of water over the next few hours, with a related reflection increase. This effect also allows evaluating the severity of burns, since it is more pronounced in third degree burns, affecting a thicker layer of skin, than in first- or second-degree ones. It is worth noting that in the case of burns, an additional contrast mechanism can be exploited. Various skin structures, both at the surface and underneath in the tissue volume, have a characteristic size of the order of the THz wavelength. The concentration (i.e., number/unit of volume) of these structures changes in burns (typically more severe wounds lead to lower concentrations of discrete structures), yielding a contrast mechanism due to light scattering, and that can be employed in addition to the hydration changes (Arbab et al., 2013). Other examples of medical imaging uses of THz, based on control of moisture level, include the (early) diagnosis of the diabetes foot syndrome (Hernandez-Cardoso et al., 2022), which cause dehydration of feet skin, and the non-contact monitoring of water content in the cornea, which is an important indicator of eye health, and can potentially be used as a diagnosis and checkup tool for various vision-impairing conditions (Bennett et al., 2012; Ozheredov et al., 2018).

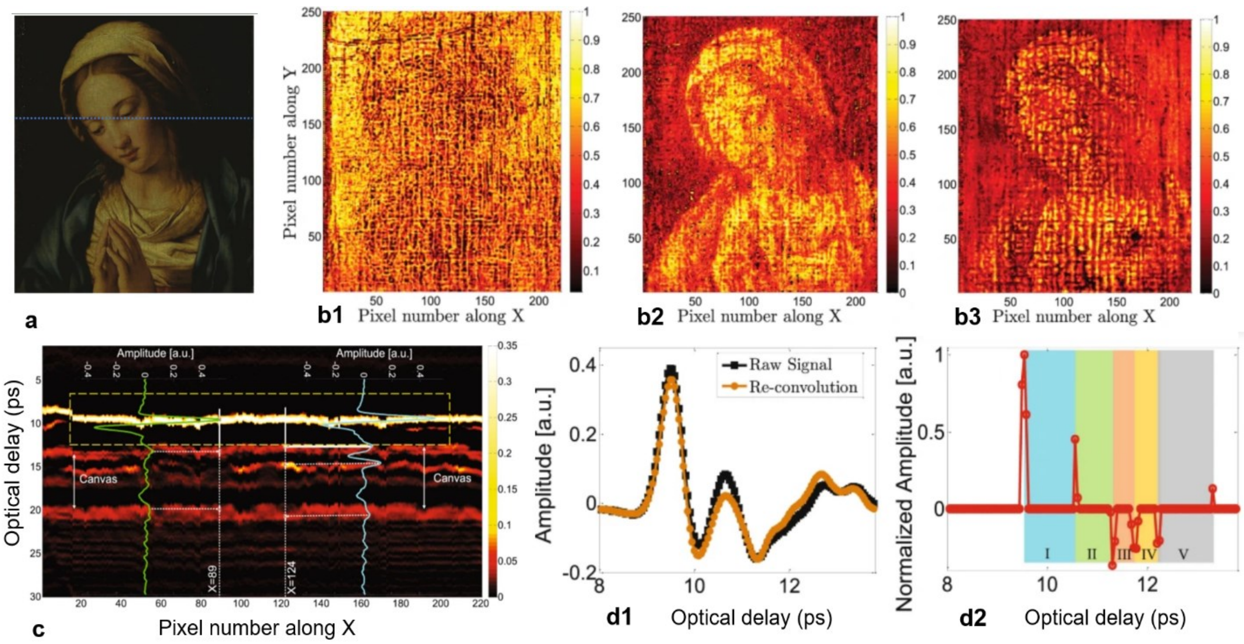

Figure 2.9 | THz imaging of a painting. *(a) Visible photo of the Madonna in preghiera painting (the dashed line corresponds to the cross-section used for the B-scan in (c)). (b) Images of layers reconstructed from some of the peaks deconvolved from the first reflected pulse, (b1) surface varnish, (b2) pictorial layer, (b3) underpainting layer. (c) THz B-scan (2D presentation displayed as a cross-sectional view of the painting) based on the amplitude of raw signals corresponding to the cross-section in (a), with two typical THz reflected signals. (d) Typical THz reflected signals and the sparsity-based deconvolved signals, (d1) examples of raw signals (black) and signals reconstructed after sparse-deconvolution, (d2) corresponding sparsity-based deconvolution signals. Adapted from (Dong et al. 2017) under the https://creativecommons.org/licenses/by/4.0/ license.*

A very different area of research where THz imaging has found an interesting application is that of artworks and historical artifacts conservation. X-ray and IR imaging are routinely employed as analytical tools by archeologists and historians, so the availability of an additional contactless, non-destructive solution has attracted a lot of attention. Pioneering studies were conducted by K. Fukunaga and coworkers, who demonstrated how THz spectroscopy was able to discern and identify different pigments and binders in various paint layers (Fukunaga et al., 2007). This first work inspired a great deal of activity (Cosentino, 2016), and perhaps one of the most exciting findings is that THz imaging can unveil hidden layers in ancient paintings by using tomographic TOF methods (Koch-Dandolo et al., 2015, 2016). A further development of this application makes use of a deconvolution algorithm which enables to achieve sub-wavelength and sub-pulse-width depth resolution (Dong et al., 2016, 2017) (Fig. 2.9). Very thin layers ($< 50\mu m$) in the paints are smaller than the wavelengths contained in the THz pulse spectrum, thus producing overlapping echoes in the first cycle of the reflected THz field trace. The algorithm exploits the sparsity of the THz time-domain impulse response, in order to resolve the overlapped echoes and characterize in great detail the painting stratigraphy. The approach can potentially find use also in other contexts where nondestructive depth-resolved imaging is needed.

2.5 Speeding up the acquisition process

As mentioned in the introduction, one longstanding limitation of THz-TDS-based imaging systems is the long acquisition time typically required for the image capture. This slowness is essentially due to two reasons, related to the characteristics of the detection scheme.

First, detection in THz-TDS systems is typically single-pixel, because the setup complexity and limited SNR make it very challenging to build an array of sensors. In this condition, the common approach is based on scanning the whole area of the object one pixel at a time (raster scan), by shifting the object itself or the detection system. This mechanism is inherently slow. Firstly, because a full time-domain measurement is required for each pixel, leading to a linear increase of the acquisition time with the number of pixels. Secondly, the mechanical displacement of the sample further adds up time to the total measurement duration. One way to reduce the displacement time is to replace the sample movement with a mechanical steering of the THz beam. This approach can result in a significant improvement of the acquisition speed, and it has been explored using mainly two different techniques: oscillating mirrors with an *f*-theta scanning lens and Gregorian reflectors. The *f*-theta lens is designed to deliver a flat image plane for a range of input angle of incidence (as opposed to a spherical lens which images inputs with different angles along a spherical surface), and it was combined with two flat mirrors mounted on a two-axis galvanometer, to steer the THz beam in two dimensions (Katletz et al., 2011). With this technique, the capture of a 2D 100 mm × 100 mm image was obtained in 1-2 minutes (at a fixed time position along the THz waveform). In the second case, a Gregorian reflector system was used in a reflection geometry to mechanically scan a sample with a THz beam (Cooper et al., 2011). The authors could reconstruct a 50 cm × 50 cm image at 1 frame/s, using a CW THz emitter centered at 0.675 THz (therefore not enabling phase extraction).

The other speed limiting factor in TDS-based systems is the need of an additional scan in the time-domain to reconstruct the THz waveform. This is commonly achieved using a mechanical delay line, that changes the length of the probe beam optical path with respect to the THz pulse path, in order to measure the THz field amplitude at different time positions. The speed limitation of traditional optical delay lines based on mechanical translation stages is essentially due to their interrupted back-and-forth linear movement. Furthermore, every temporal point needs to be individually acquired, and for each of them, a certain integration time is required to achieve a sufficient SNR. For instance, considering measurement systems like the one we used (e.g., employing a lock-in amplifier coupled to an amplified laser source featuring repetition rates in the kHz range, for THz generation/detection) the integration time for a single sampling point is usually not lower than $\sim$100 ms. If we consider a temporal window of $\Delta t = 40$ ps (which makes it possible to obtain a spectral resolution of $1/\Delta t = 25$ GHz), and a time step $\delta t = 0.05$ ps (corresponding to a spectral bandwidth $1/2\delta t = 10$ THz), the number of sampling points is $n = 800$. If to this we add the time required for the delay line movement, the resulting acquisition times are of the order of 1-2 min/scan, for the whole waveform. In recent years, fast delay lines have been developed to address the shortfall related to the linear mechanical movement. Examples are rotary delay lines exploiting uninterrupted movements, through the use of reflectors or prisms (reaching rates up to respectively 400 Hz (G. J. Kim et al., 2008) and 800 Hz (Probst et al., 2014)). Other implementations seek to avoid the mechanical displacement and its many shortcomings, by exploiting acousto-optical delay lines (rates up to 34 kHz) (Schubert et al., 2013), or all-optical configurations, like the asynchronous optical sampling (ASOPS) (Yasui et al., 2005), and the optical sampling by laser cavity tuning (OSCAT) (Wilk et al., 2011). In ASOPS two lasers with slightly different repetition rates ($f_1 < f_2$) are used, such that the relative time delay between the two pulse trains will mimic a linear ramp from 0 to $\Delta t = 1/f_1$. In OSCAT, the variable delay between pump and probe is introduced by tuning the laser repetition rate, making it possible to use a pulse and a successive one from the same train, respectively in the emitter and detector side. With ASOPS it is possible to acquire hundreds of picoseconds-long scans, while OSCAT-based systems can usually achieve tens of picoseconds-long windows, both implementations usually work at sampling rates of hundreds of Hz.

Despite these impressive achievements, the use of mechanical beam steering and fast mechanical delay lines both still present an inherent limitation to widespread use: the presence of (often bulky) moving parts, which require complex electronics to be controlled and synchronized, and are prone to failure. As for all-optical delay lines, they are an optimal solution, but can be very expensive, requiring either the use of two sources, or the precise tuning of the repetition rate of the laser sources employed. The alternative options to reduce the acquisition time, as well as the complexity of TDS-based imaging systems, rely, on the spatial side, on computational imaging schemes to avoid the raster-scan, and on the temporal side, on “single-shot” THz detection configurations, which eliminate the need for a delay line. The use of these alternative approaches to THz imaging will be discussed in Chapter 3.

3 NOVEL APPROACHES TO TERAHERTZ IMAGING

This chapter is partially adapted from: L. Zanotto, R. Piccoli, J. Dong, R. Morandotti, and L. Razzari, "Single-pixel terahertz imaging: a review", Opto-Electronic Advances, 2020, 3(9): 09200012

This chapter will introduce the different approaches employed throughout this doctoral project as viable solutions to reduce complexity and acquisition time of TDS-based THz imaging systems. As already mentioned in chapter 1 and 2, there are two causes of the slowness of such experimental arrangements: the need of a pixel-by-pixel scan in the spatial domain, and that of a temporal one to capture the waveform in the time-domain. As the issue is twofold, so is the proposed solution. In section 3.1 the single-pixel imaging (SPI) technique, used to avoid the spatial raster-scan is presented, followed, in section 3.2, by a review of the state-of-the-art of its application at THz frequencies. In section 3.3, single-shot detection (SSD) techniques are introduced, as methods to avoid the scan in the time-domain, traditionally carried out by means of a mechanical delay line.

3.1 Imaging with single-pixel detectors

Starting in the 70s, the great progress of electronics led to the development of digital imaging: thanks to CCDs it became possible to transduce an optical image directly in electronic format, while the computational power of microprocessors enabled digital processing. It was in the 90s, though, that the imaging community started to fully acknowledge the solutions brought about by electronics as a fundamental shift in the general approach: optics and electronics were no longer considered as independent and their respective processing capabilities could be optimized through concurrent design (Mait et al., 2018). Computation had become an integral part of imaging and the new branch of computational imaging was born.

In the context of THz imaging, where the necessity of raster-scanning the sample under test strongly hampers the potential for its widespread use, computational imaging represents a natural solution, allowing processing power to overcome the limitations posed by the hardware. Specifically, one of the computational schemes most suited to meeting the strict requirements of THz radiation is the SPI technique.

The idea of capturing an image with a single photodetector was first demonstrated in the work titled "Dual photography" by Sen and coworkers (Sen et al., 2005). In the proposed imaging scheme, a series of multi-pixel light patterns is used to interrogate the object under investigation, while a single-pixel detector records the transmitted or reflected light. The core idea is to measure the magnitude of the correlation between the patterns and the object shape, which will be then reflected in the detector's readings. The information about the object spatial distribution is embedded in the patterns shape, with the detector outputs being used as weights for the corresponding patterns in the image reconstruction process. Soon after this first demonstration, the group of Duarte proposed SPI as a method to implement the concept of compressed sensing (CS) for imaging purposes (Duarte et al., 2008). CS generally describes the conditions under which it is possible to reconstruct a signal from un under-sampled dataset (E.J. Candes & Wakin, 2008). In the specific case of SPI, this refers to the possibility of capturing an image by using a number of patterns smaller than the number of image pixels. The combination of these two ideas proved very useful in all contexts where silicon-based sensing technology is not suitable and detector arrays are unavailable or very expensive, like in the IR or deep UV (Edgar et al., 2019). In the last decade, the flexibility of SPI has fostered a great deal of research work, leading to the development of single-pixel cameras operating across the EM spectrum. Examples of applications span from X-ray imaging (Greenberg et al., 2014), IR and visible microscopy (Radwell et al., 2014), a telescopic system (W. K. Yu et al., 2014), and even a compressive Light Detection and Ranging (LiDAR) device (Gong et al., 2016).

3.1.1 The single-pixel imaging concept

The SPI measurement process can be put into a mathematical framework, which properly describes its working principle. The object transmission/reflection function is a $n \times n$ square matrix, $T(x,y)$, corresponding to an image with n^2 pixels. The set of interrogating patterns will be composed of n^2 masks with size $n \times n$, $\{P_i(x,y,)\}_{i=1\dots n^2}$, and the detector readings will be collected in a n^2-element vector W. The measurement process can therefore be described by the following equation:

$$W_i = \sum_{x,y} P_i(x,y)T(x,y) \tag{3.1}$$

The i^{th} detector output, W_i, results from the summation over every (x,y) position (i.e., the image pixels), of the product between the i^{th} pattern P_i, and the object transmission (or reflection) function T. A schematic of the process is shown in Fig. 3.1. It is possible to rewrite Eq. (3.1) in a more compact fashion, by placing the columns of T one next to the other to form a n^2–element vector. Similarly, each of the n^2 patterns $\{P_i(x,y,)\}_{i=1\dots n^2}$ can be also reshaped into a n^2–element vector by stacking the

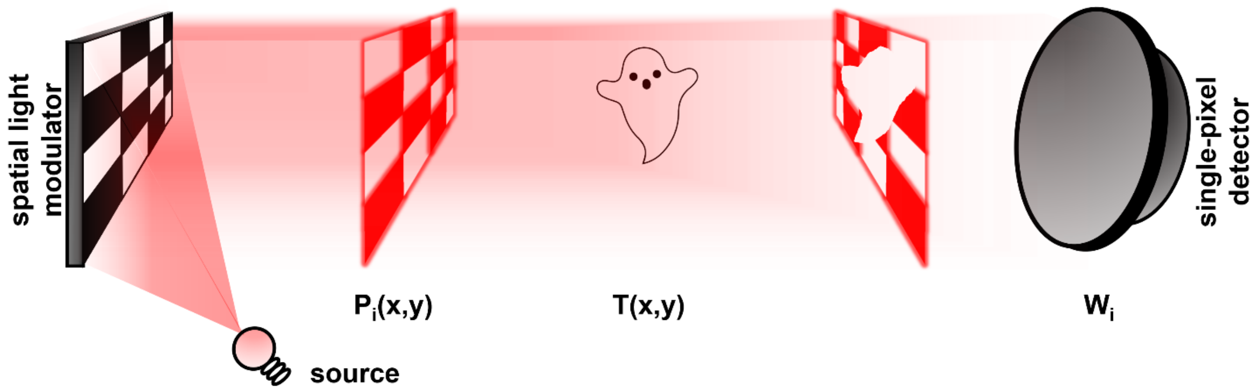

Figure 3.1 | Schematic of the SPI approach. The light from the source is modulated by means of a spatial light modulator, into the pattern $\mathbf{P_i}(\mathbf{x}, \mathbf{y})$. The patterns interrogate the object T(x,y), and the resulting light is acquired by the single-pixel detector, whose readings are collected into the vector W_i.

columns one next to the other, and subsequently the set of vectors can be regrouped into a $n^2 \times n^2$ matrix $\boldsymbol{P}$. In this way, the measurement process can be seen as a matrix-vector multiplication. The knowledge of the pattern matrix $\boldsymbol{P}$ and the measurement vector W enable the retrieval of the vector T (i.e., the image of the object), by simply inverting a linear system of equations:

$$W = \boldsymbol{P}T \qquad (3.2)$$

In general, finding the solution to this problem requires the dimension of vector W to be equal to that of vector T, which in terms of measurements means that the number of (linearly independent) patterns must be equal to the number of pixels in the image. A straightforward choice for the matrix $\boldsymbol{P}$ is represented by the identity matrix, whose corresponding patterns have each only one illuminated pixel, as shown in Figs. 3.2 (a-b). Equivalent in principle to the raster-scan technique, this choice is clearly very poor in terms of SNR, since for every illumination pattern a very weak light intensity ($1/n^2$ times lower than the input) is available. Evidently, the choice of a pattern set ensuring a good performance while possibly limiting the number of measurements (in combination with CS) is crucial to make SPI appealing for real-world applications. Two of the most studied bases are the sets obtained from (i) a Hadamard matrix (Stantchev et al., 2017) (shown in Fig. 3.2 (c)), which is composed of binary patterns, all displaying 50% transmission (Fig. 3.2 (d)), and guarantees an optimal SNR (Harwit & Sloan, 1979), and (ii) the Fourier set, constituted of gray-scale patterns made up with combinations of sinusoidal wavelets, which shows good efficiency when operating in CS conditions (Z. Zhang et al., 2015, 2017).

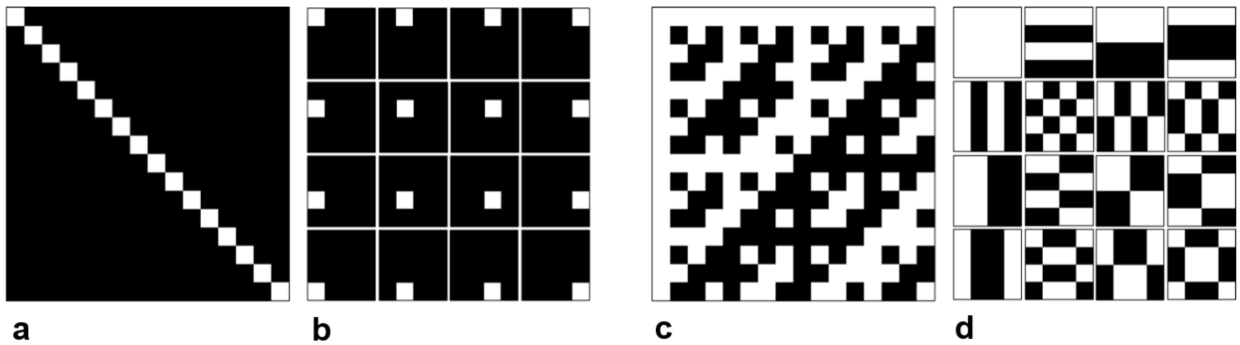

Figure 3.2 | Examples of patterns sets. (a) 16 × 16 identity matrix P and (b) the corresponding series of 16 (n^2), 4 × 4 spatial masks $\{H_i(x,y,)\}_{i=1...16}$ obtained from it; (c) 16 × 16 Hadamard matrix P and (d) corresponding set of 16, 4 × 4 spatial masks $\{H_i(x,y,)\}_{i=1...16}$.

One of the fundamental steps to set up a single-pixel camera is to shape the light beam into spatial patterns. This is typically achieved using a Spatial Light Modulator (SLM). Various types of SLMs exist and are readily available in the market. An example worth mentioning is the class of Liquid-Crystal Devices (LCDs), which make it possible to control both amplitude and phase of the incident light. In the field of SPI, the most commonly used SLM is the Digital Micromirror Device (DMD), developed by Texas Instruments (Texas Instruments, n.d.) and typically used in projector devices. A DMD is composed of hundreds of thousands of metallic mirrors (constituting the DMD 'pixels'), the side length of which is typically ~10 μm. Each one of the mirrors is electrostatically controlled to tilt of ±12° with respect to the plane of the array, so that the illuminating light is reflected in different direction according to the mirror's orientation. The DMD can thus be programmed into binary masks, where a mirror with positive tilt corresponds to a "1" of the mask and a negative one to a "0". The effective pixel size of the pattern can be controlled by grouping together neighboring mirrors. The major advantages of the DMD technology are the very broadband response, and the high modulation rate achievable (> 22 kHz). The latter is usually the bottleneck for the acquisition time of a single-pixel camera, making DMDs the preferred choice in many applications.

3.1.2 Compressed sensing theory

As mentioned earlier, one of the main advantages of the SPI scheme is the related possibility of applying the so-called CS theory, which tackles the problem of solving an undetermined inverse problem where the unknown variables are more than the available data points. Such situation is usually encountered when one wants to estimate data values at temporal/spatial frequencies higher than those available from the sampling equipment (Stern, 2016). In the specific case of SPI, this means retrieving an image with a number of patterns that is smaller than the total number of pixels making up the image. Images are generally "compressible" under certain representations (Duarte et al., 2008). The compressibility of an image is related to the concept of "sparsity", which directly connects to the number of non-zero entries in the vector representing the image. An image is K-sparse if the number of non-zero coefficients in a certain representation is equal to K. Sparsity is already used, for instance, in JPEG (Joint Photographic Experts Group) compression to reduce the size of digital images stored in hard drives. In such case, the compression is applied after the image is acquired via a digital camera by discarding all quasi-zero coefficients corresponding to high-spatial frequency components in the Discrete Cosine representation (which express a signal in terms of a finite number of cosine functions with variable frequency) (E.J. Candes & Wakin, 2008). In CS though, the compression is employed during the acquisition process so to enable the reconstruction of the image with an "incomplete" set of measurements. In this situation, the problem presented in Eq. (3.2) exhibits infinite solutions (i.e., it is undetermined). Nevertheless, it is possible to apply a pseudo-inversion method to retrieve the image. Numerous strategies have been developed to pursue such a reconstruction and the field is still an open subject of research (Edgar et al., 2019; Gibson et al., 2020). The traditional approach, first proposed by Candès and Tao (E.J. Candes & Wakin, 2008; Emmanuel J. Candes & Tao, 2006), relies on using a sensing basis which is incoherent with the spatial features of the image. This means that the distribution of "illuminated" pixels of each pattern has a low correlation with the object spatial shape. The easiest way to achieve this condition is to use pseudo-random bases. Subsequently, an iterative optimization procedure enables the retrieval of the image. Typically, these kinds of optimization algorithms are based on minimizing quantities like the l_1-norm, (defined as $\|\boldsymbol{S}\|_1 = \sum_k^{n^2} |S_k|$, with $\boldsymbol{S}$ a n^2-element vector), and it is demonstrated that the reconstruction is correct when the number of samples is $m \geq C \cdot K \log(N/K)$, where K is the sparsity, N the number of pixels in the image, and C is a proportionality constant (Candès et al., 2006; Donoho, 2006). Such algorithms usually provide a high-fidelity reconstruction of the image, but they can become quite demanding in terms of computational burden. Alternative methods make use of sampling bases that are not incoherent with the spatial distribution of the image, like the Hadamard, Fourier or wavelet matrices. In these cases, a subset of the basis must be chosen and the image is retrieved using a fast algorithm (Bian et al., 2018). This is generally preferable when the application needs fast reconstruction, but it does not require very high resolutions. Clearly, in such scenario, it is important to choose a basis subset that properly samples the object spatial features. This can be done adaptively or with prior information about the object (Edgar et al., 2019).

3.2 Single-pixel imaging at terahertz frequencies

In the context of THz imaging, SPI has been extensively explored as a valuable scheme over the last years, due to its abovementioned advantages. The related opportunity of CS image capture represents an efficient way to successfully overcome the long acquisition time issue, without the need of resorting to complex mechanical parts to make up for the lack of multipixel detectors. Even so, its implementation in this specific frequency range presents some challenges, particularly regarding the approach to obtain the spatial modulation of the interrogating beam. In the following sections, various SPI-based solutions for THz systems will be presented.

3.2.1 Terahertz modulation techniques

As mentioned previously, a crucial feature of the SPI technique is the use of a series of multi-pixelated light patterns to illuminate the object under investigation. To this end, the spatial modulation of the incident light beam is required. SLMs are widespread tools to produce patterned beams, but typically operate at visible/IR frequencies. Unfortunately, there are no commercial SLMs currently available to directly modulate an incident THz beam. This has made the quest for effective methods to pattern the THz light one of the core experimental challenges in the field. A variety of solutions have been proposed in the last years and can generally be sorted in two categories depending on whether it is the THz beam to be directly modulated, or a patterned illumination is used for the generation/detection of THz radiation in nonlinear crystals.

Direct modulation of the THz beam

The first solution proposed for THz spatial modulation made use of metallic binary masks shaped into a series of patterns (employed to perform the image reconstruction) (Chan et al., 2008). These masks were then placed on the propagation path of the THz beam, acting as binary amplitude modulators. Physical metallic masks offer an optimal modulation depth, being truly binary. The drawback is clearly the lack of flexibility as a set of metallic masks has a fixed series of patterns, and the need to mechanically slide them into the THz path, thus limiting the achievable patterning speed. One improved implementation of this type made use of a metallic spinning disk with a series of engraved patterns, in order to increase the acquisition speed (H. Shen et al., 2012).

Some implementations of THz SLMs have also been explored in the last years. A metamaterial-based SLM was successfully employed to reconstruct a 64-pixel image of a metallic cross (Watts et al., 2014). The pixels of this SLM were constituted of metamaterial absorbers cells, yielding an almost unitary absorption at a specific frequency. The application of a reverse bias voltage to a dielectric layer underneath the absorbers enables the tuning of both the real and imaginary part of the dielectric function. In this way, an electrically controlled modulation of the absorption can be produced in real-time. Another recent example is a micro-mirror-based SLM, operating in the range 0.97-2.28 THz (Jan Kappa et al., 2019). With a mirror lateral size of several hundred micrometers, this device is compatible with diffraction at THz wavelengths. The main limitation of this device is the relatively narrow bandwidth where it provides a sufficiently large modulation contrast (larger than 0.5 between 0.97 and 2.28 THz, and consistently beyond 0.6 only between 1 and 1.5 THz).

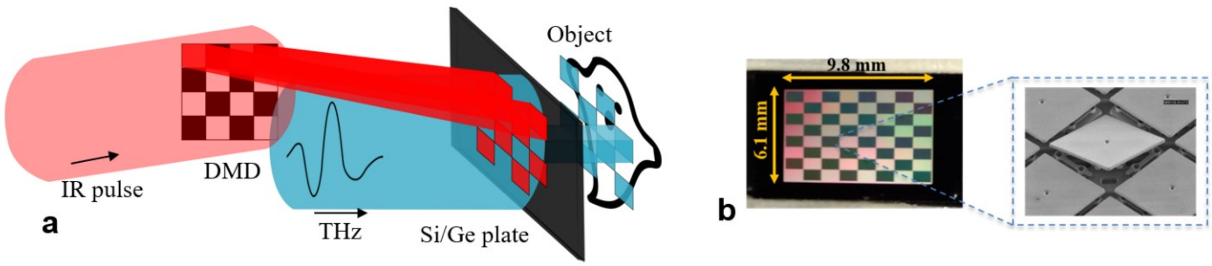

Figure 3.3 | The photo-modulation mechanism. (a) The IR beam is modulated by the DMD and then illuminates the semiconductor plate, locally generating free carriers that block THz transmission. (b) Photo of the DMD chip and microscope image of the micromirrors.

The modulation technique that has recently become the most widespread in the field is the one based on carrier photo-excitation in semiconductors. A visible/near-IR beam (often obtained as a fraction of the pump beam used for THz generation) is first modulated with a standard SLM, and then shined onto the surface of a semiconductor (Fig. 3.3(a)). In Fig. 3.3(b) we see a photo of a DMD chip, the most widespread type of SLM used for SPI. In THz implementations, this is the device is typically used to modulate the IR light. This light then illuminates the semiconductor, and in doing so induces an above-bandgap excitation, which results in the generation of free carriers in the illuminated regions. Semiconductors are generally transparent to THz radiation because the energy of THz photons (a few meV) is lower than the semiconductor bandgaps (~1 eV). In the illuminated areas, though, the presence of a layer of free carriers at the surface makes them behave like Drude metals, leading to absorption/reflection of the incident THz pulse. Therefore, such local illumination operates has an amplitude mask allowing to transfer the pattern shape from the optical beam to the THz wave with great flexibility. The first demonstration of such an optical modulation method was reported by Chen (Q. Chen et al., 2000), as a mean to perform near-field imaging. The authors modulated only the center of a focused THz beam, directly on the surface of a sample made of GaAs, so to increase the spatial resolution beyond the diffraction limit. The same technique was then applied for THz beam steering and imaging, with an incoherent illumination form a projector exploited as photo-modulating light (Busch et al., 2012). In this case, a 64 × 64-pixel image of a metallic cross was obtained by utilizing a series of masks with only one illuminated pixel. The first study exploiting multiplexed masks for SPI eventually appeared in 2013 (Shrekenhamer et al., 2013). The authors acquired images of metallic objects with increasing resolution, showing the superiority of multiplexed masks with respect to masks with a single illuminated pixel. The flexibility and relative ease of implementation of this modulating technique have attracted the interest of the scientific community and a variety of studies have investigated different solutions for its further improvement. A modulation depth (the ratio of the transmitted THz power while the semiconductor window is completely illuminated to the one without any illumination) of 20 dB was achieved with incoherent white-light illumination from a projector (A. Kannegulla et al., 2014). This is a convenient arrangement since it avoids the need of an amplified laser, but can have limitations in the effective pattern resolution, due to carriers drifting within the semiconductor (Akash Kannegulla et al., 2015). Another example of the effectiveness of the technique is represented by the reconstruction of the spatial map of a THz beam front and the possibility of tracking moving objects (Augustin et al., 2015). Interestingly, germanium (Ge) replaced silicon (Si) as the material for photo-modulation, since the lower bandgap of the former allowed for the use of less illuminating power. Another recent work (She et al., 2019) proved the possibility of realizing "Fourier pattern" sets at THz frequencies. In this study, a Si plate covered with a graphene monolayer was used as a photo-modulator. Fourier patterns could be obtained as 8-bit gray-scale masks (i.e., masks where the intensity in each pixel can exhibit 256 different values, instead of just the 2 values of basic binary masks). These can be generated on the laser beam as a series of temporal dithering patterns (sequence of rapidly changing binary patterns which combined create a single gray-scale mask) using an SLM. The density of the generated photo-carriers will vary with the local laser intensity, resulting in the THz beam to be also modulated in 8-bit patterns. CS reconstruction was then demonstrated with a compression factor down to 1.6% and a reasonable SNR, proving the effectiveness of the Fourier set in terms of compressibility. Finally, a novel technique for efficient THz modulation, based on THz total internal reflection (TIR) in a Si prism, was presented (Stantchev et al., 2020). The modulation was attained by altering the total internal reflection condition for the THz beam (which entered the prism from one of its other faces), by illuminating one face of the prism with a visible CW source. With the use of an SLM featuring a high switching rate to modulate the CW source and a fast PCA-based TDS system, the authors captured 32 × 32-pixel THz peak-field-amplitude images at a notable rate of 6 frames/s.

The above described all-optical modulation technique still represents the most widespread and used method for THz SPI, thanks to its flexibility, ease of implementation, and efficiency. This approach was the one chosen for this thesis project, and the physics behind its working principle will be presented in more detail in section 4.2.2.

Patterning of the optical beam used for THz generation/detection

Alternative solutions have been explored to spatially modulate the THz beam during the generation or detection processes. In one study (Zhao et al., 2019), a collimated probe beam was employed to sample the collimated THz beam in a ZnTe crystal via EOS. The probe beam was patterned beforehand, by means of a standard SLM. With this approach, the THz beam was probed directly with the spatial patterns after its interaction with the object, without the need of an actual THz modulation. The authors tested different series of patterns, obtained good CS reconstruction, and also attained subwavelength resolution of ~60 μm by placing the object in close proximity to the detection crystal. A drawback of this technique is that a collimated THz beam needs to be probed, requiring higher peak field amplitudes to achieve sufficient SNRs. Another technique, first proposed in a theoretical study (Olivieri et al., 2018) and then implemented experimentally (Olivieri et al., 2020), exploited a spatially-modulated pump beam for THz generation via OR in a ZnTe crystal. With this method, which was named *time-resolved nonlinear ghost imaging*, the nonlinear generation process produces a THz beam already shaped into the patterns needed for imaging. The authors pointed out the advantages of the technique in controlling the propagation of the patterned THz beam, especially considering the strong spatiotemporal coupling effect arising when spatially modulating an ultrashort THz pulse at a subwavelength scale. Indeed, in the case of extremely localized sources, the THz field spatial and temporal coordinates are coupled along propagation and the typical image reconstruction performed at fixed-time slices of the transmitted field becomes severely affected by errors and artifacts. The shortcoming associated with this technique is mainly a more complex arrangement. For example, it requires a grating to correct the tilt introduced by the use of the DMD to pattern the THz generation beam, and, for near-field applications, the sample must be placed in contact to the generation crystal itself.

3.2.2 Previous implementations of single-pixel terahertz imaging

The use of SPI for THz applications has been widely explored in the last fifteen years. A lot of work has focused on improving the spatial modulation technique, as reported in the previous sections. In the following, we list some implementations of SPI in contexts where THz-TDS imaging is typically employed. These mostly consist of proof-of-principle studies, aimed at demonstrating the efficiency of the technique in view of future applications.

Amplitude, phase and hyperspectral imaging in the far-field

In the first application of SPI at THz frequencies with metallic masks (Chan et al., 2008), Chan and collaborators demonstrated the possibility of reconstructing images in the far-field, using two different contrast methods: spectral amplitude and phase. In the amplitude-only measurements, they imaged a metallic object, by using CS and showing the reconstruction of a 1024-pixel image with only 300 patterns (compression ratio of ~30%). In the second case, the 1024-pixel image of a rectangle of Teflon (transparent to THz radiation) was obtained through 400 phase measurements, at the specific frequency of 0.1 THz. Another example of a phase-sensitive implementation was achieved by Saqueb and coworkers (Saqueb & Sertel, 2016). They used intensity-only measurements, and exploited an algorithm called *Phaselift* to retrieve the phase. The core idea of this experiment was the application of a series of complex-valued masks, thus modulating both amplitude and phase of a specific frequency component (0.69 THz). This possibility is offered by the photo-modulation, since the layer of carriers generated on the Si surface induces a phase shift in addition to the amplitude modulation, due to the change of the complex refractive index of the material. These first two works presented two different ways to enable phase-contrast imaging. In another paper, Inverse Fresnel Diffraction (IFD) was also proposed to reconstruct the compressed image of a metallic object (Shang et al., 2019).

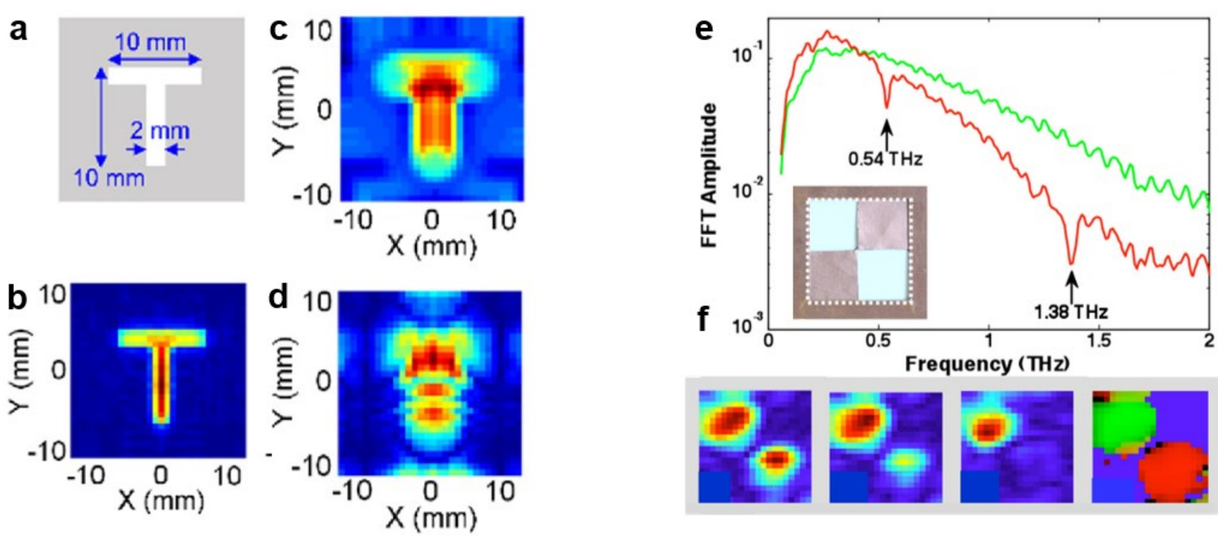

Figure 3.4 | Examples of far-field SPI imaging. (left) Far-field reconstruction of a metallic object with Inverse Fresnel Diffraction (IFD): (a) metallic T-shaped sample; (b) image reconstructed using the IFD algorithm; (c) peak amplitude image, and (d) spectral image at 0.3 THz, before reconstruction with IFD. *Adapted with permission from (Shang et al., 2019) © 2019 The Optical Society.* (right) Hyperspectral imaging for spectroscopic recognition: (e) THz spectra of polyethylene (green trace) and lactose (red) and photo of the sample (polyethylene at the upper-left side, lactose at the bottom-right and copper in the rest of the surface). (f) Spectral images of the sample shown in the inset of (e): the first three images (left to right) are reconstructed at 0.50 THz, 0.54 THz, 1.38 THz, respectively, while the last is an RGB map of the regions with different absorption features (lactose in red, polyethylene in green, copper in blue). *Reprinted from (Y. C. Shen et al., 2009) with the permission of AIP Publishing.*

The aim of the study, which again represents a far-field imaging implementation, was to show how the IFD allows for the correction of the diffraction effect when the patterned THz beam propagates for a certain distance before interrogating the sample (Fig. 3.4(a)).

Another powerful capability of THz imaging is the spectral recognition of substances. The first use of SPI for spectroscopic recognition (Y. C. Shen et al., 2009), reported the analysis of a composite material made of polyethylene and lactose. The change in absorption at specific frequencies in the spectrum enabled the identification of the regions where lactose (featuring two main absorption lines at 0.54 THz and 1.38 THz) was present (Fig. 3.4(b)). CS reconstruction was also applied, showing the image formation with only 10% of the total number of masks.

Near-field imaging

A series of studies have been devoted to applying SPI in near-field conditions, so to improve the achievable spatial resolution for imaging. The wavelength of THz radiation typically limits the resolution in the far-field to hundreds of microns, and the opportunity to go beyond such constraint is of great interest for practical applications. A series of publications by Stantchev and collaborators explores different aspects and applications of near-field THz imaging. They reported the capture of the image of a metallic cartwheel and a circuit board, achieving resolutions down to 100 μm (~$\lambda/4$), at first (Stantchev et al., 2016). Afterwards, they further improved the resolution by addressing the key limitation, which is the thickness of the Si-based modulator. The image of the same cartwheel was obtained with a 9 μm resolution, employing thin Si wafers (with thickness down to 6 μm), directly supporting the object to be imaged (Stantchev et al., 2017) (Fig. 3.5(a)). The same group also investigated the conductivity of a graphene monolayer, deposited on the surface of the Si modulator, and produced conductivity maps with a 75 μm resolution (Hornett et al., 2016). Finally, they performed a hyperspectral study of the permittivity of a cartilage sample with subwavelength thickness (Stantchev et al., 2018). The resolution limit was pushed even further, down to $\lambda/100$ (4.5 μm), by Chen and coworkers (S.-C. Chen et al., 2019), by using a photo-modulation setup featuring a thin film of vanadium dioxide (VO_2) with a thickness of only 180 nm.

Aside from improving the spatial resolution, the other challenge in THz near-field SPI is represented by the time-domain waveform reconstruction. Olivieri and colleagues showed the retrieval of the temporal THz waveform, for each image pixel of subwavelength lateral size (down to 125 μm), while imaging a plant leaf (Olivieri et al., 2020) (Fig. 3.5(b)). In this case, the authors performed near-field SPI by directly patterning the optical beam used to pump the THz generation crystal. They also established a theoretical framework to describe these conditions (Olivieri et al., 2018), providing evidence that spatiotemporal coupling effects must be considered to properly reconstruct the image with sub-wavelength resolution, and providing a method (named "space-time refocusing") to achieve such reconstruction.

Alternative SPI implementations

Beside the two main research lines described in the previous sub-sections, other intriguing studies have investigated different implementations and applications of THz SPI. For instance, a two-dimensional THz tomographic SPI-based system was established (Mohr et al., 2018). For this type of imaging, multiple images of semi-transparent objects are captured in transmission, with variable orientation of the object. Thereafter, a reconstruction algorithm allows combining the images, thus retrieving the object inner features.

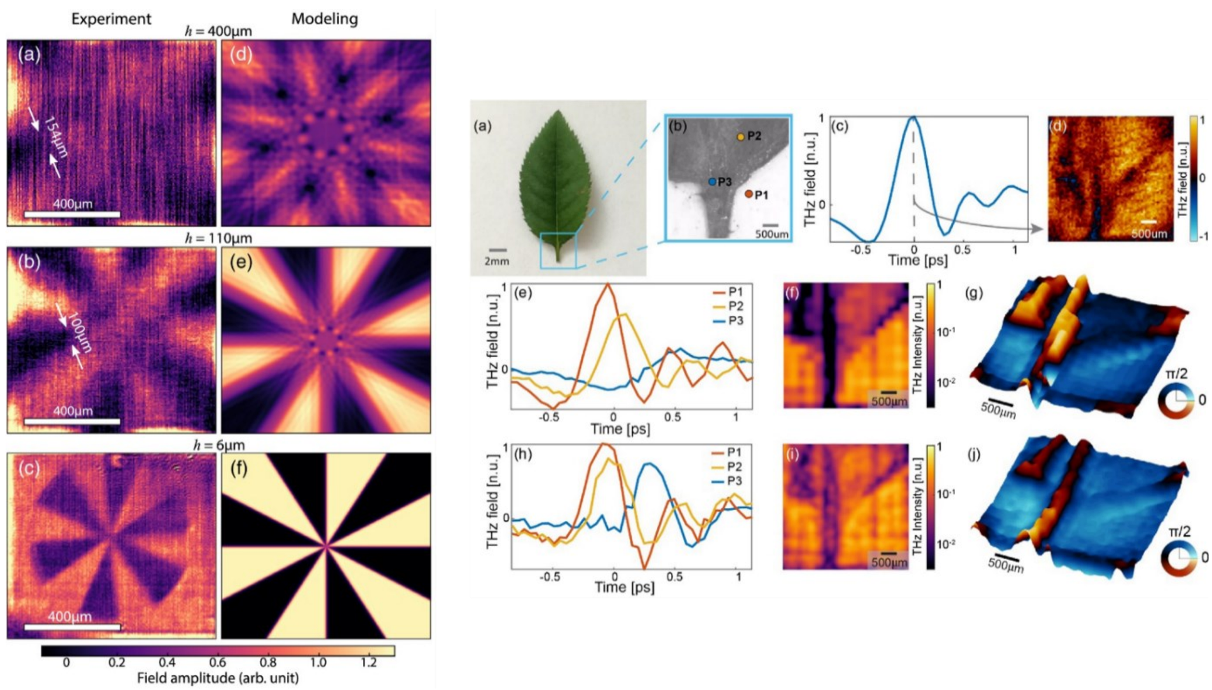

Figure 3.5 | Examples of near-field imaging. (left) THz near-field imaging of a metallic cartwheel. The images present the comparison between the experimental results and numerical modeling, for Si modulators with decreasing thickness (400 μm (a), (d), 110 μm (b), (e), 6 μm (c), (f)). As can be clearly seen, only the 6μm-thick Si wafer allows to resolve the central region with smaller features. *Adapted with permission from (Stantchev et al., 2017) © 2017 The Optical Society*. (right) Hyperspectral image of a leaf: (a) Optical image of the leaf; (b) microscope image; (c) temporal waveform of the THz field transmitted through the leaf; (d) fixed-time reconstruction (128 × 128 -pixels); (e) local temporal response of the fresh leaf in the points indicated in (b); (f) hyperspectral image of a fresh leaf at 1.5 THz (16 × 16 -pixels); (g) phase image of the fresh leaf, obtained without phase unwrapping of the experimental data; (h)–(j) same as the previous panel for a dried leaf (32 × 32 -pixels image). All the images correspond to a field of view of 4mm×4mm. *Reprinted with permission from (Olivieri et al., 2020) © 2020 The Optical Society*.

Another work (Saqueb & Sertel, 2018) made use of a single-bit sensor (i.e., featuring only two value states), as detector to read only the "sign" (positive or negative) of the difference between the variation of the optical probe intensity, produced by the probe's interaction with a THz beam modulated into a certain pattern and its complementary. They showed how this information is sufficient to achieve the image reconstruction. The same group also presented another THz compressive imaging approach, by employing multiple sensors used to record the THz intensity in multiple points of the Fourier space (Saqueb & Sertel, 2019). The advantage of this approach is that the number of required masks (and the related acquisition time) decreases linearly with the increase in the number of sensors.

Finally, it is worth mentioning that even a spintronic THz emitter array (STEA), has been proposed as a viable approach to perform THz SPI. Such emitters exploit the spin-polarized current induced in a ferromagnetic material after illumination from a femtosecond laser to generate THz radiation (Seifert et al., 2016). One of the advantages of this generation technique is the gapless and wide frequency-band readily available (0.3-30 THz), thanks to the absence of detrimental optical phonon modes. In the STEA (S. C. Chen et al., 2020), every element of the array acts as an individual emitter, which can be independently programmed by photo-excitation, so that patterned THz light can be directly generated. Such approach was tested to achieve super-resolution in near-field conditions, by exploiting the array elements size of only $6.5 \times 6.5\ \mu m^2$ and placing the sample only 150 nm after the source.

A general objective of THz SPI is to obtain multidimensional images at THz frequencies with a reduced acquisition time. This means gathering additional information from the object under investigation, being it in the spectral or temporal domain, beyond its spatial characteristics. Nevertheless, most of the works reported above presented results of image reconstruction based on the extraction of only a fraction of the information that THz-TDS can provide (e.g., field amplitude, frequency spectrum or phase).

When a raster-scan of the object is performed in a traditional THz-TDS-based system, both amplitude and phase are available simultaneously, thanks to the capture of the temporal waveform related to each pixel. This makes it possible to fully harvest the information on the sample under investigation. The complete reconstruction of few-cycle THz pulses in the time-domain (at each pixel position) is therefore paramount to prove that the SPI paradigm can be effectively and conveniently employed for THz applications. The first part of this doctoral project was dedicated to demonstrating that this time-domain reconstruction can be accomplished at THz frequencies. The detailed description of the experimental work and related results are presented in Chapter 4.

3.3 Recording terahertz waves without a delay line

As mentioned previously, the other noteworthy factor severely limiting the speed of TDS measurements, even beyond the context of imaging, is the long acquisition time usually required to perform the temporal scan of the THz pulse. We recall that, in TDS systems, the IR probe pulse operates as an optical gate, which is variably delayed in order to sequentially sample the THz electric field at different temporal positions, typically by employing a mechanical delay line. This process is generally rather slow and cumbersome, especially when targeting multidimensional THz measurements, like imaging, which results in a further increase of the total acquisition time with the number of time points and the number of other scanned dimensions.

In the last twenty years, several SSD techniques have been explored as ways to simultaneously capture the whole THz waveform in the time-domain while overcoming the shortfalls of conventional EOS-based systems. In the following sections, an overview of these methodologies is given, with a particular emphasis on those utilized in this doctoral project (i.e., time-to-frequency and time-to-space mapping).

3.3.1 Single-shot detection of terahertz waves

SSD techniques have been originally developed as a response to the need of recording non-repeating events. The traditional multi-shot EOS scanning approach is indeed incompatible with the observation of the dynamics of rapidly varying irreversible phenomena. However, SSD acquisition, used in combination with averaging, can also be an effective way to significantly reduce the time required for multidimensional THz measurements, while preserving SNR levels comparable to those obtained in traditional EOS schemes. A detection scheme of this sort has to recover the entire THz waveform, in principle within a single laser shot, while ensuring a temporal window long enough to deliver the desired resolution in the THz frequency spectrum (since the frequency resolution is inversely proportional to the size of the temporal window). Furthermore, for the approach to be effective, it is expected that the SNR of the THz trace retrieved by means of the SSD technique is comparable to that obtained by using a traditional scanning method (Teo et al., 2015). It is important to note that, even if widely used, under averaging conditions the term single-shot is not accurate: as a matter of fact, multiple shots are usually recorded during the experimental measurement since this results in a significant increase of the SNR level. Nonetheless, the techniques still in principle captures the whole THz temporal trace by exploiting just a single laser shot.

SSD techniques are generally based on mapping the temporal dimension of the THz pulse onto one dimension of the probe pulse. In this way, even though one of the available dimensions is sacrificed for the task, the temporal information about the detected THz beam can be simultaneously recorded while acquiring a single IR probe beam. Three broad classes can be defined, depending on which dimension is allocated to store the THz temporal information: time-to-frequency mapping, time-to-space mapping, and time-to-angle mapping. We start by briefly introducing the latter, as it has not been employed in this work, and afterwards we will discuss the other two more extensively. The time-to-angle encoding technique is built around a complementary pair of transmission-mode echelons, which are optics resembling glass stairways (K. Y. Kim et al., 2007). When the probe beam propagates through a pair of a thin and a thick echelon, it emerges as an array of tiny “beamlets”, with incremental delays to one another. The beamlets are all focused to the same spot at the detection crystal, where they arrive with delays proportional to the incidence angle. They separate after the crystal and are spatially resolved at distinct regions of a 2D detector array at the image plane. This technique is generally easy to implement, as it requires a minimal modification of the standard TDS system. Furthermore, it does not suffer from serious limitations in the available temporal window, degradation of the temporal resolution, or waveform distortions (Teo et al., 2015). For these reasons, it has sparked interest in the THz community, even recently for a combined THz-Raman spectroscopy system (Duchi et al., 2021). A limit of this method is its lack of flexibility, since the echelons can only provide a fixed time window/resolution, which cannot be adapted to potentially variable experimental needs. Moreover, echelons are not widespread optics, and are often custom-made. For these reasons, this approach was not pursued in this work. The first approach explored in this doctoral project was the time-to-frequency mapping, which is based on temporally stretching the probe pulse, so that its (temporally-spread) frequency components can sample different temporal portions of the THz pulse. This technique will be introduced in section 3.3.2. The second method exploits a spatially-spread readout pulse, so that separate spatial points overlap with the THz at different times. Its characteristics and working principle will be described in section 3.3.3.

In section 3.3.4, the acquisition method based on near-zero transmission is presented. This scheme is required to enable an efficient detection of the THz amplitude in the case where a differential measurement (via a balanced photodetection method, such as the one employed in traditional EOS schemes) can be complex to implement. This is the case when using SSD techniques, where the simultaneous recording of multi-value readout signals is required. The reason is that lock-in amplifiers, which are highly needed to achieve an effective differential measurement, do not typically have multiple acquisition channels, and thus cannot be used to simultaneously read the THz temporal waveform.

3.3.2 Time-to-frequency encoding

The first demonstration of the time-to-frequency method dates back to the early days of THz technology (Jiang & Zhang, 1998b), and was followed by a good deal of work aimed at improving its effectiveness. A relevant example is the implementation of a dynamic subtraction technique, with the goal of increasing the achievable SNR level (Jiang et al., 2000). This technique relies on the introduction of a linear frequency chirp to the probe pulse, by means of a couple of diffraction gratings (Fig 3.6(a)). In a linearly chirped pulse, the frequency components are incrementally delayed relative to each other. In this way, the components arrive at the detection crystal at different times and each of them samples a different temporal position of the THz waveform (Jiang & Zhang, 1998a) (Fig 3.6(b)). The different polarization modifications of the probe "colors" induced by the THz pulse in the EOS detection crystal are then converted into intensity modulations through a linear polarizer, and eventually measured with a spectrometer.

Mathematically, we can consider a gaussian pulse, $u_0(t) = e^{-\frac{t^2}{T_0{}^2}-i\omega_0 t}$, where T_0 is the original (Fourier-limited) duration of the probe pulse, and ω_0 its central frequency. After it has been stretched by the grating system, the chirped pulse can be written as:

$$u_c(t) = e^{-\frac{t^2}{T_c{}^2}-i\alpha t^2-i\omega_0 t} \tag{3.3}$$

Where α is the chirp rate and T_c is the chirped pulse duration. In case of linear chirp (as it happens when a grating system is used), α is a constant, and the instantaneous frequency is directly proportional to the time delay:

$$\omega(t) = \omega_0 + 2\alpha t \tag{3.4}$$

The technique is relatively simple to implement but has a significant drawback. Indeed, it features a very limited temporal resolution, which is essentially constrained by the bandwidth (i.e., the Fourier-limited temporal duration) of the readout signal (i.e., the probe pulse). Under typical operating conditions it can be shown that $\alpha \approx 1/T_0 T_c$, while the resolution is well approximated by $\Delta T^2 \approx 1/\alpha$ (F. G. Sun et al., 1998). The maximum achievable resolution is then given by:

$$\Delta T = \sqrt{T_0 T_c} \tag{3.5}$$

On one side, we need T_c to be at least $T_c \sim T_{THz}$, with T_{THz} the duration of the THz pulse, in order to "cover" the whole THz waveform. T_{THz} has typically a duration of 1-2 ps, but can be longer in presence of dispersive materials. On the other hand, the retrieved THz pulse will be distorted if the temporal resolution, ΔT, is too low to sample a few-cycle THz pulse, whose typical period is $\sim$1 ps. The bottleneck is ultimately the duration of the transform-limited pulse, T_o, which is set by the laser employed in the measurement. As an example, we can consider the working conditions of our system, where the Ti:Sapphire laser has a transform-limited pulse duration of $T_0 = 150$ fs. Considering that $T_{THz} \sim 1.5$ ps, the temporal resolution results $\Delta T \sim 0.47$ ps, which is too low to provide an accurate reconstruction of the THz waveform. Sources emitting shorter transform-limited pulses (of the order of tens of fs) do exist, but would still not be sufficient to obtain high temporal resolutions.

Alternative solutions to overcome this issue include the use of broadband probe pulses coupled with a higher chirp rate ($\Delta T^2 \approx 1/\alpha$, i.e., higher chirp rates lead to better resolutions), the utilization of a white-light continuum for the readout pulse, or interferometric techniques to deconvolve the time-to-frequency map (K. Y. Kim et al., 2006). These options come at a cost of, respectively, a generally lower conversion efficiency in THz generation when using shorter pulses, larger group velocity mismatch between probe and THz when using white light, or a more complex scheme for interferometric implementations.

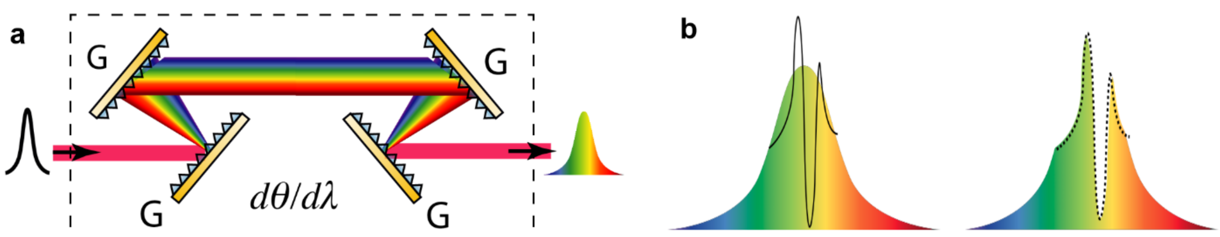

Figure 3.6 | Time-to-frequency encoding. (a) The grating system used to temporally stretch the probe pulse, by introducing a linear chirp (usually only 2 gratings are used, with the pulse bouncing twice on each of them). (b) The chirped pulse superimposed to the THz wave (left), and the modulated pulse, where separate frequencies (colors) sample different times of the THz waveform (right).

3.3.3 Time-to-space encoding

Another possible SSD configuration is the time-to-space mapping. The technique is based on tilting the IR probe pulse front, so that the transverse profile of the optical readout samples the THz field at different temporal positions in a simultaneous fashion, when they spatially overlap in the detection crystal. The modulated probe is then recorded by means of a detector array, such that the captured probe image corresponds to an instantaneous picture of the THz waveform itself. The pulse front tilt can be achieved either in a non-collinear (Shan et al., 2000) detection geometry, or by introducing a dispersive element (Kawada et al., 2011) in the probe beam path. As opposed to the time-to-frequency mapping, the time-to-space one does not suffer from the limitation in the achievable temporal resolution, as well as offer more flexibility in the overall available time window. As we will prove in chapter 5, it is also an optimal option to be coupled to an SPI-based system. Thanks to these advantages, it is the technique that was successfully employed in this research work.

We will describe the working principle of the time-to-space mapping in the following. A key device is a dispersive element (usually a prism or a grating), which spatially spreads the different frequency components within the broadband probe pulse. The beam then propagates through a 4-f system and reaches the detection crystal. If the appropriate imaging conditions are met (i.e., the detection crystal is located at a distance equal to the sum of the focal lengths of the two lenses), an image of the probe front is formed at the detection crystal position (Fig. 3.7(a)). The readout image is additionally scaled by the magnification provided by the 4-f, that is the ratio between the focal lengths of the two lenses, and the probe pulse front will be tilted by an angle that is determined by the employed dispersion optics (e.g., prism or transmission/reflection grating). The derivation of the mathematical expression linking the probe pulse front tilt to the dispersion induced by the dispersive element is described in (Bor & Rácz, 1985). Such equation is independent from the specific dispersion element used (Hebling, 1996), and can be written as:

$$\tan\gamma_0 = \bar{\lambda}\frac{d\epsilon}{d\lambda} \tag{3.6}$$

where γ_0 is the angle between the pulse front and the phase front, i.e., the tilt angle, $\bar{\lambda}$ is the mean wavelength and $d\epsilon/d\lambda$ is the angular dispersion. This latter parameter is very important and directly related to the grating parameter d, i.e., the number of grating lines per millimeter, and the diffraction angle β, as:

$$\frac{d\epsilon}{d\lambda} = \frac{1}{d\cos\beta} \tag{3.7}$$

The 4-f system images the tilted pulse onto the detection crystal with a magnification, M, determined by the lenses' focal lengths, resulting in a scaled tilt angle, $\tan\gamma = \frac{1}{M}\tan\gamma_0$. The resulting temporal window T that can be recorded in a single shot is determined as a function of the probe beam diameter σ at the detection position ($\sigma = M\sigma_0$, where σ_0 is the beam diameter at the grating position), and the tilt angle (c is the speed of light) as:

$$T = \frac{\sigma \tan \gamma}{c} = \frac{\bar{\lambda}\ \sigma_0}{c\ d \cos \beta} \tag{3.8}$$

Eq. 3.8 shows that the size of the available temporal window, T, is directly determined by the diameter of the beam at the detection plane and by the tilt angle at the crystal position. In turn, if we look at the last term on the right of Eq. 3.8, we see that ultimately the temporal window depends upon the grating parameter and the angle of diffraction from the grating. The probe diameter has to be properly chosen considering the extension of the THz beam on the detection crystal, in order to enable an accurate sampling (as it will be explained by the analysis reported in section 5.2.2). The magnification of the 4-f is thus used to control the beam size to this end. Varying the magnification has no influence on the temporal window though, as the diffracted angle and the diameter dependences upon it mutually cancel out. This leaves us with the grating parameter as a way to ultimately adjust the tilt angle (and therefore the temporal window). Though, the extension of the temporal window is also coupled to the achievable temporal resolution, for the following reason. The recording of the probe is performed by a multipixel detector (usually a camera), which captures the probe after it has sampled the THz beam in the detection crystal (Fig. 3.7(b)). Here, another 4-f system is needed to bring the probe from the crystal to the multipixel detector, and make sure its profile is properly imaged. The temporal resolution of the measurement is ultimately linked to the spatial resolution of the detector, because the temporal profile of the THz waveform is captured along a spatial direction of the detector itself (X-axis in Fig. 3.7(b)). Nonetheless, the tilt angle and the magnification of the 4-f system can be used to adjust the actual temporal resolution. First, we can

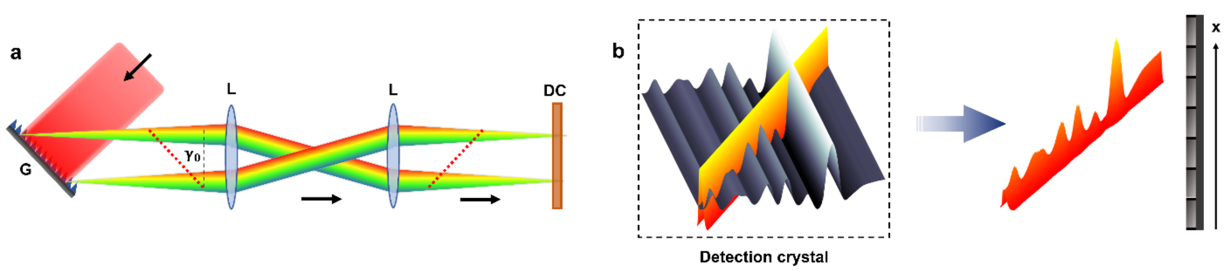

Figure 3.7 | Time-to-space encoding. (a) A diffraction grating (G) spatially separates the frequency components, and a 4-f system (lenses, L) is used to produce an image of the probe pulse front at the detection crystal (DC). The diffraction angle varies for different frequencies, resulting in their separation (prior to their proper recombination at the crystal position). The non-specular reflection caused by the grating thus ultimately results in the pulse front tilt (with an angle $\boldsymbol{\gamma_0}$). (b) The tilted probe pulse overlapped with the THz waveform on the detection crystal (left), and the modulated probe eventually read by a multipixel detector. The latter reproduce in space the temporal shape of the THz waveform.

choose the 4-f magnification so to maximize the extension of the beam on the detector (i.e., to cover its whole X-axis length), this also increases the resolution by spreading the waveform over a larger number of pixels. Once this is fixed, though, the only variable we are left with is again the tilt angle, which means that we are only allowed to adjust temporal window and resolution as coupled variables. The tilt has a sort of "zoom-out" effect: the larger it gets, the longer the temporal window (i.e., the field-of-view), but at the expense of a reduced resolution, and vice-versa.

3.3.4 Near-zero transmission detection

The detection of THz radiation in a TDS system can exploit free-space EOS in a nonlinear crystal. The underlying mechanism is the generation of a birefringence by the THz electric field, proportional to the amplitude of the field itself, and was described in section 2.2.2. A linearly polarized probe pulse propagating through the crystal in coincidence with the THz pulse will experience the induced birefringence and its polarization state will become slightly elliptical. The standard detection configuration is based on a differential measurement of the two orthogonal polarization components, after a quarter-wave plate and a Wollaston prism. Such difference is directly proportional to the incoming THz electric-field amplitude.

Balanced photodetection is not straightforwardly advantageous for most SSD implementations, since they require a multi-pixel detector to simultaneously record the whole THz waveform. Using two multi-pixel detector to acquire positive and negative components could be an option, but reaching an accurate balancing of such configuration is not easy. Moreover, it is not straightforward to use a lock-in amplifier in extracting a signal from a noisy background, because of the complexity and cost associated with the implementation of such a multi-channel lock-in measurement.

In order to detect the weak modulation produced by the THz pulse on the probe in a non-differential fashion, it is crucial to minimize the readout background noise, due to the laser intensity fluctuations. The solution is to use a near-zero optical transmission scheme (Jiang et al., 1999), where a linear polarizer is placed after the detection crystal with its axis almost perpendicular to the polarization direction of the linearly polarized probe (Fig. 3.8(a)). Under these conditions, the intensity transmitted through the polarizer is close to zero, thus significantly reducing the background noise. When the THz field is present, the probe polarization state gets modified and the component of the probe field parallel to the analyzer axis is transmitted, producing a change in the measured intensity. When used in an SSD setup, the probe detector can be a camera or a spectrometer, whose pixels record a variable intensity corresponding to different levels of induced birefringence, which in turn depend upon the strength of the THz electric field for a particular temporal position.

The issue arising when working in these conditions is that the intensity variation at the detector, after the polarizer, is no longer linearly proportional to the polarization change induced by the THz electric field (as it was in the case of a balanced detection). The mathematical relation can be written as (Jiang et al., 1999):

$$I = I_0[\eta + \sin^2(\Gamma_0 + \Gamma)] \tag{3.9}$$

Where I_0 is the input intensity, η is a scattering contribution in the crystal (which is very small, $\eta \ll 1$), Γ_0 is the optical phase bias contribution term due to the optical elements in the system (from, e.g., strain-induced and residual birefringence), and Γ is the THz-induced contribution. The optical bias is typically small. In the case of a small THz-induced modulation, so that $|\Gamma_0 + \Gamma| \ll 1$, Eq. 3.9 can be rewritten as:

$$I \approx I_0[\eta + (\Gamma_0 + \Gamma)^2] \tag{3.10}$$

Since the THz field is proportional to the Γ term, this equation tells us that the photodetector output has a nonlinear (quadratic, in the case of Eq. 3.10) dependence on the THz field. It is possible to avoid distortions in the THz waveform extraction by using a quadratic calibration (Kawada et al., 2011; Usami et al., 2002), or exploiting an optimal optical bias point (Jiang et al., 1999). These kinds of corrections are usually required when targeting spectroscopic measurements, where resonances at precise positions in the frequency spectrum need to be evaluated. The proof-of-principle measurements carried out in this project were based on the extraction of the temporal delay between

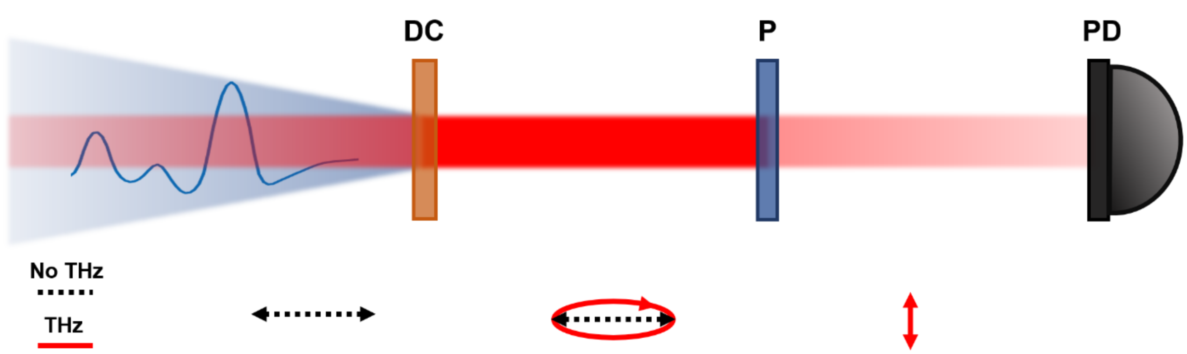

Figure 3.8 | The near-zero transmission detection configuration. (In displaying the probe polarization states after the optical elements, for simplicity we assumed $\boldsymbol{\eta}, \boldsymbol{\Gamma_0} = \mathbf{0}$ and a perfectly crossed polarizer). The IR readout probes the THz pulse in the EO crystal (DC), then propagates through a polarizer (P), whose optical axis is almost perpendicular to the probe polarization, and it is eventually measured by a photodetector (PD). When the THz signal is present, the transmission is changed because of the modified probe polarization state.

the peaks of well separated THz pulses, therefore such procedures were not implemented.

SSD techniques have been explored over the last twenty years, and even applied, to some extent, for THz imaging purposes (Jiang & Zhang, 1998a). However, no attempt has been made, so far, to employ a combination of the SPI scheme and an SSD configuration. In the second part of this doctoral project, we have coupled the two approaches into a TDS-based THz imaging system. With this arrangement, we successfully demonstrated how it is possible to retain the powerful capabilities of coherent detection of TDS at the same time avoiding the use of any bulky moving part, and so reducing both system complexity and acquisition time. These results will be presented in Chapter 5.

4 TIME-DOMAIN TERAHERTZ COMPRESSIVE IMAGING

This chapter is partially adapted from: L. Zanotto, R. Piccoli, J. Dong, D. Caraffini, R. Morandotti, and L. Razzari, "Time-domain terahertz compressive imaging", Opt. Express 28, 3795-3802 (2020)

In this chapter, the results related to the first part of the doctoral project are presented. Here, the main goal to be achieved was to experimentally prove that the SPI approach could be applied to a typical THz-TDS-based imaging system, while still preserving the ability to coherently detect arbitrary THz pulses, which is inherent to TDS.

As previously mentioned, the foremost strength of THz-TDS resides in the direct sampling of the electric field amplitude in the time-domain, which yields the reconstruction of the temporal waveform of few-cycle THz pulses (where one cycle means one complete temporal oscillation of the electric field). Once again, this implies that both the amplitude and phase information associated with a generic THz pulse can be retrieved by employing the THz-TDS scheme. This marks the difference between TDS and most detection devices based on photo-/thermo-electric effects, typically employed in the IR/visible range (e.g., photodiodes, CCDs, pyro-detectors), where only the light intensity can be measured. In the context of traditional TDS imaging, the raster-scan of an object enables the capture of a THz temporal trace for each pixel of the image, with the related possibility to extract the complete local optical properties, without recurring to the cumbersome Kramers-Kronig relations (Jackson, 1999). This allows for the retrieval of multi-dimensional images, combining the 2D spatial shape of the sample with time, phase or spectral information.

In the case of SPI, the working principle is somehow different. The recorded THz temporal waveforms do not correspond to specific pixels in the image, but are the combination of the simultaneous contributions from all the "white" pixels (i.e., the areas where there is no illumination on the semiconductor photo-modulator and the THz wave is transmitted) of the patterns used in the structured illumination process. Therefore, in order to prove that the technique yields an outcome equivalent to the traditional raster-scan, it is necessary to demonstrate that, starting from the THz waveforms recorded for each pattern, it is possible to reconstruct those corresponding to each pixel. In what follows, we experimentally demonstrate this key result. Moreover, we also show some examples of images reconstructed by using different pieces of information extracted from the same time-domain data, depending on the type of sample analyzed.

4.1 Single-pixel imaging reconstruction in time-domain

The well-established SPI paradigm is based on the measurement of the correlation between the patterns and object spatial shape. This is typically obtained by recording the total intensity of the transmitted (reflected) light using a single-pixel detector. We can recall the SPI problem of Eq. (3.2):

$$W = \boldsymbol{P}T$$

Here, the detector readings, collected in the vector W, are real and positive values corresponding to the light intensity reaching the detector. In the case of TDS though, the detector is sensitive to the electric field, the value of which can be either positive or negative, and the detector output is a series of amplitude values sampled at different time instants. As a result, the electric field read by the detector is the superposition of the fields transmitted (reflected) by the "white" pixels of the pattern, after the interaction with the object under test. Since such superposition is linear, the solution of the SPI problem yields the field value related to each pixel. A schematic of the working principle is depicted in Fig. 4.1. Mathematically, Eq. (3.2) can be rewritten by substituting the vectors W and T with their time-dependent versions, $W(t)$ and $T(t)$, containing respectively the electric field readings of the detector and the electric field waveforms corresponding to each pixel position:

$$W(t) = \boldsymbol{P}T(t) \tag{4.1}$$

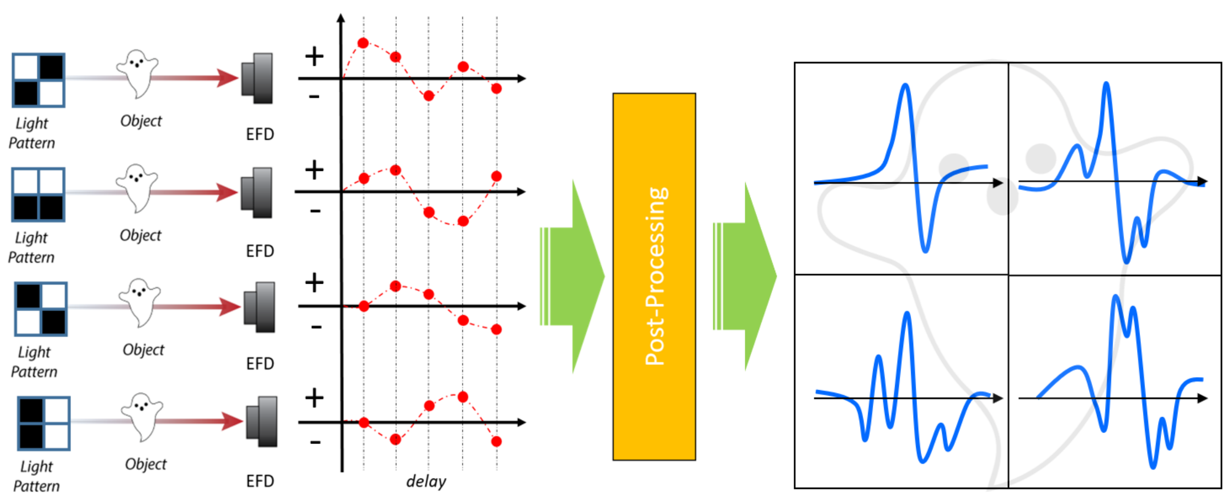

Figure 4.1 | Schematic of the time-domain SPI technique. On the left, the measurement process, with a series of waveforms acquired by an electric-field-sensitive detector (EFD) for each of the illuminating patterns. On the right, the waveforms related to each pixel of the image, reconstructed in post-processing by solving Eq. 4.1.

By sequentially solving the linear system of Eq. (4.1) for each temporal point, it is then possible to retrieve the THz electric field temporal waveforms for each spatial point of the scene. The experimental proof needed to verify this concept represents one of the core results of this thesis.

4.2 Experimental implementation

4.2.1 Experimental setup

The employed experimental setup is a modified version of a traditional THz-TDS system (Fig. 4.2(a)). An amplified Ti:Sapphire laser (800 nm, 150 fs pulse duration, 2 mJ at 1 kHz repetition rate) is split into three beams: pump (48% of total laser power), probe (4%) and pattern generator (48%). The pump beam is used to produce THz pulses via OR in a 1-mm-thick ZnTe crystal. We blocked the residual pump light, transmitted by the OR crystal, by means of a piece of Teflon (which does not absorb THz light), located behind the crystal itself. The THz beam is first enlarged (6 times) by means of a series of gold off-axis parabolic (OAP) mirrors, propagates through a 500-μm-thick Si plate (undoped, 5000 Ω cm) used for spatial modulation, and then passes through the sample. Finally, the THz waveform is recorded via EOS in another 1-mm-thick ZnTe crystal, by means of the probe beam. This latter has a collimated diameter of 8 mm and was focused, by means of a lens with 200 mm focal length, at the detection crystal plane, with a resulting beam spot of ~ 25 μm. The THz beam was also focused, by an OAP mirror of 50.8 mm focal length, from a ~ 48 mm collimated diameter to a ~ 400

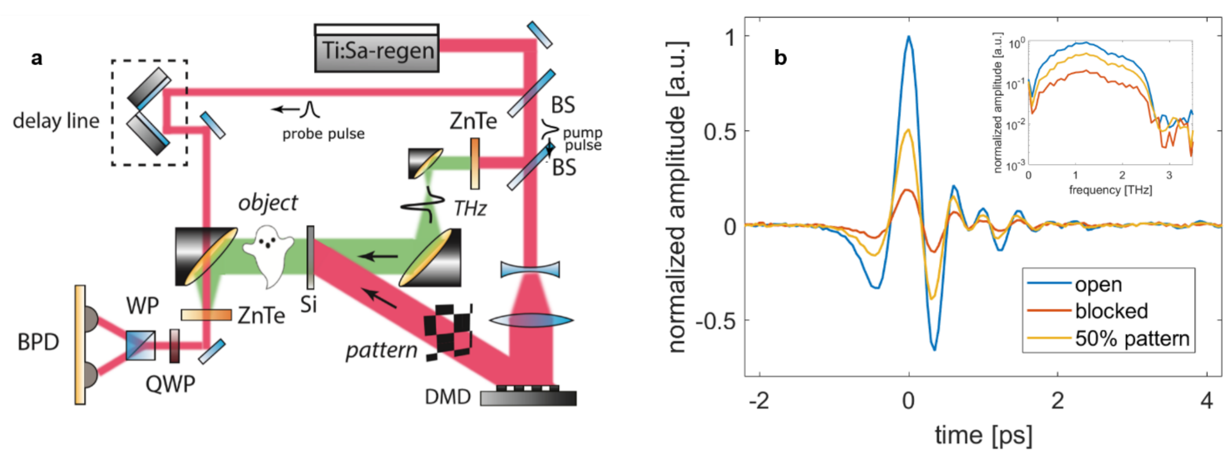

Figure 4.2 | The SPI THz-TDS system. (a) Illustration of the experimental setup: modified version of a THz-TDS system. The beam from the fs-laser is split into three lines (BS-beam splitter), one generates the THz pulse in a ZnTe crystal, one is used as a probe in the EOS crystal (ZnTe), and the last one is employed for THz modulation (after being patterned with the DMD). The signal is recorded by two balanced photodiodes, after the probe has propagated through a quarter-wave plate (QWP) and a Wollaston prism (WP) (as explained in section 2.2.2). (b) Examples of THz waveforms captured without any sample, with variable modulating IR intensities: no light (blue), fully illuminated window (red), 50% illuminated window; the inset shows the spectral amplitudes corresponding to the temporal waveforms.

μm focused one (to be noted that the imaging window is actually smaller than the collimated THz beam diameter, resulting in an even bigger focused spot). With this arrangement, the area of the THz beam sampled by the probe is much smaller than the THz spot, so that an actual "point detection" was achieved (more details on the subject will be presented in section 5.2.1). The spatial modulation of the THz beam is achieved by carrier photo-excitation in a Si plate. First, the IR pattern generation beam is modulated by means of a digital DMD (LightCrafter4500, Texas Instruments). Thereafter, the modulated IR beam illuminates the surface of the Si plate, thereby exciting electrons to the conduction band. The generated free carriers locally block the transmission of the THz light, thus transferring the pattern spatial distribution from the IR beam to the THz one. By applying this technique, we were able to achieve a modulation depth of about 85% (peak of the THz pulse) with an IR pulse energy of ~140 μJ incident on the Si plate. There are two reasons why, despite almost 1 mJ of energy is deployed for pattern generation, only ~ 15% of it is actually available. The first is that the DMD chip has a rectangular shape while the laser beam is circular so part of the energy is inevitably lost because of this shape mismatch. The second is that the DMD is composed of $\sim 10^6$ micromirrors of 7.6 μm pitch, which results in it behaving like a 2D diffraction grating. The device is designed such that the 1^{st} diffraction order is the one to be used to project the patterns, but part of the light is actually distributed to all other orders of diffraction, included the zeroth (i.e., specular reflection). By adjusting the angle of incidence, it is possible to maximize the energy transferred to the 1st order, but it is physically impossible to eliminate all diffraction-related losses. Some THz temporal waveforms recorded without any sample and under variable illumination conditions are presented in Fig. 4.2(b): the blue line is the THz waveform retrieved without any IR illumination, the red one with the window fully illuminated (i.e., the whole THz beam is in principle blocked), the orange line is instead obtained when one of the Hadamard patterns was projected (i.e., 50% of the window blocked). The limited power available for THz modulation set a higher limit on the size of the window, since the larger the window, the higher is the power required to obtain reasonable modulation depth (80-90% of the THz peak). At the same time, the minimum size of the pattern pixels is bounded by diffraction. In fact, while the pattern propagates from the modulation window to the object under investigation, it undergoes diffraction broadening, which becomes more pronounced the smaller the pixel size. An estimation of the minimal pixel size that avoids detrimental diffraction effects can be done using the Rayleigh range, $z_R \approx {x_{pix}}^2/\lambda$, defined as the propagation distance z_R from an aperture x_{pix} at a which a beam cross-sectional area is doubled. In our configuration, we placed the objects right behind the Si window used for THz modulation. In this way, we minimized the distance between the pattern generation plane and the object to a value of $d \approx 0.5$ mm (the Si thickness), hence the minimum pixel size is set to $x_{pix} \geq \sqrt{d\lambda} \approx 0.4$ mm, with $\lambda = 300$ μm @ 1 THz. Considering the available laser power for THz modulation and the calculated pixel diffraction constraint, while targeting a reasonable acquisition time $\Delta t_{scan} \times N_{pixels} \approx 2 \text{ min} \times N_{pixels}$, we finally set the scene dimension to 1.6 × 1 cm^2, divided into a maximum number of 16 × 16 pixels (with a size of 1 mm × 0.625 mm).

4.2.2 Photo-modulation in semiconductors

The modulation technique applied in this thesis work relies on photo-excitation of charges in semiconductors. A comprehensive study on the main material parameters to be considered for an effective application of THz light photo-induced modulation has been carried out for Si, Ge, and gallium arsenide in (Akash Kannegulla et al., 2015). In this doctoral project, both Si and Ge were used, in combination with an 800-nm or a 1030-nm source, respectively.

In the following, an overview on the mechanism that allows for free-carrier generation on the surface of a semiconductor by means of an intense laser beam is provided. Under normal conditions, undoped (and unexcited) Si and Ge are both transparent at THz frequencies, showing an almost dispersion-less refractive index and minimal absorption. We recall here the Drude permittivity for a metal, which can be used to describe a photo-excited semiconductor (Ashcroft & Mermin, 1976):

$$\varepsilon(\omega) = \varepsilon_b + \frac{i\,\omega_p^2}{\omega\left(\frac{1}{\tau_s} - i\omega\right)} = \varepsilon_b + \frac{iNe^2}{\varepsilon_0 m_{eff}\,\omega\left(\frac{1}{\tau_s} - i\omega\right)} \tag{4.2}$$

Where N is the density of charged carriers, e the electron charge, m_{eff} the electron effective mass and τ_s the average carrier scattering time, ε_b the background permittivity. The main parameter of interest to evaluate the efficiency of the photo-induced modulation is the number of carriers N generated in the semiconductor. If the photon energy $\hbar\omega$ of the pump light is high enough to overcome the semiconductor bandgap, electrons are excited from the valence to the conduction band, and are thus free to move inside the medium. The bandgap of Si is 1.1 eV, so that light at 800 nm (1.55 eV) can effectively excite electrons in the conduction band. In the case of pump light at 1030 nm (1.20 eV) though, the number of excited carriers in Si is found not to be high enough to provide a good modulation depth following typical femtosecond pulse excitation, so Ge, the bandgap of which is 0.66 eV, had to be used. The depth profiles of the generated carrier concentrations are reported in Fig. 4.3(a). After the recombination time, electrons eventually decay back to the ground state. Electrons population at time t after photo-excitation can be calculated as $N(t) = N(0)e^{-t/\tau_c}$, where τ_c is the carrier recombination time. In the case of Si, $\tau_c = 25$ µs (Gaubas & Vanhellemont, 2007) and considering the repetition period of the laser we employed (1 ms), the photo-excited carriers have time to relax back to the ground state before the next exciting pulse arrives on the semiconductor. In the case of Ge, τ_c is longer, ~1 ms (H. Y. Fan et al., 1954), nonetheless the Yb-laser repetition period in our experiment was 4 ms, again long enough for the recombination to happen before the following pulse arrival. With both arrangements then, cumulative effects can be neglected. Furthermore, the THz pulse was set to arrive a few picoseconds after the optical pulse excitation, thus experiencing maximum modulation (since the time is too short for carriers to recombine before the pulse arrival). With this in mind, we can assume that the number of carriers is equal to that generated by a single exciting pulse and stays constant during the THz pulse propagation. The key parameter to be determined to estimate the carrier density is the volume occupied by the carriers themselves. This depends on the penetration depth of the exciting light, the illuminated area of the semiconductor, and the carrier mean displacement. The latter is calculated via $< x^2 >= 6Dt$, where $D = \frac{\mu k_B T}{e}$ is the diffusion coefficient, μ is the carrier mobility, $T = 298$ K the temperature, e the electron charge, and k_B the Boltzmann constant. The mobilities are, for Si, $\mu_e = 1350$ cm^2/Vs, whereas for Ge, $\mu_e = 3600$ cm^2/Vs (Kittel, 2005). Assuming the THz pulse arrives ~10 ps after the photo-excitation (the relative retardation can be easily controlled with a delay line along the photo-exciting beam path), this time period is sufficiently long to allow for thermalization and cooling of hot charges, but short enough to minimize carrier trapping and/or recombination, which occurs on nanosecond time scales (Hendry et al., 2007). We can make the following considerations:

- The penetration depth of the 800 nm pump light for Si is $d \sim 11$ µm (see Fig. 4.3(a)), and the calculated carrier displacement for electrons is $s = \sqrt{< x^2 >} = 477$ nm. The latter is therefore negligible compared to the former and we can calculate the carrier density simply as:

$$N_{Si} = \frac{I(1-R)}{2\hbar\omega A d} \tag{4.3}$$

  where I is the incident intensity, R is the reflectivity of Si at the pump wavelength (ω), A the area of excitation and d the penetration depth.

- The 1030 nm light penetration depth for Ge is much smaller $d \sim 500$ nm (again Fig. 4.3(a)), in fact of the same order of the mean electron displacement $s = 767$ nm (which is in turn larger due to higher mobility). While the carriers are much more concentrated compared to the case where Si is employed, the dependence of the carrier density on the carrier drift is more relevant. The density can be estimated as:

$$N_{Ge} = \frac{I(1-R)}{2\hbar\omega A(d+s)} \tag{4.4}$$

- A lateral drift (parallel to the semiconductor surface) can cause the smearing and broadening of the spatial features when transferring the optical pattern to the THz beam. Though, considering that a pattern pixel in the experiments performed throughout this doctoral project has a typical size of hundreds of microns, a displacement of ≤ 1 μm can be safely neglected, and thus pattern broadening can be considered to be negligible for both Si and Ge.

At this point, we can calculate the values of N for the specific experimental conditions used in this work (illumination pulse energy of ~ 90 μJ/cm^2, at 800 nm for Si and at 1030 nm for Ge). The scattering time can be obtained from the carrier mobility and the effective mass as $\tau_c = m_{\text{eff}}\mu_{\text{eff}}/e$ (Ulbricht et al., 2011). The values are shown in Table 4.1.

Table 4.1 | Optical parameters for Si and Ge. *The effective mass is given as a fraction of the free electron mass, $\mathbf{m_e} = \mathbf{9.1 \times 10^{-31}}$ **kg**. [1](Dai et al., 2004), [2](Green, 1990), [3](Kaplunov et al., 2019), [4](Akash Kannegulla et al., 2015).

	n (1 THz)	k (1 THz)	Eff. mass (× m_e)*	Scatt. time (fs)	N (#/m^3)
Si	3.42[1]	0.0001[1]	0.26[2]	211	$\sim 10^{23}$
Ge	4.00[3]	0.007[3]	0.12[4]	266	$\sim 10^{24}$

We can thus proceed to the calculation of the Drude electric permittivity of the photo-excited layer. The results are plotted in Fig. 4.3(b), where on the x-axis we have the frequency normalized to the plasma frequency of the Drude metal. For both Si and Ge, the plasma frequency ($\sim$ 57 THz and $\sim$ 227 THz respectively) is well beyond the bandwidth of the THz radiation generated via OR in our systems ($\sim$ 2.5 THz), ensuring that the free charges generated in the two semiconductors effectively screen the incoming radiation. Furthermore, the real part of the permittivity is negative, which is the typical characteristic of a metallic behaviour (Ashcroft & Mermin, 1976).

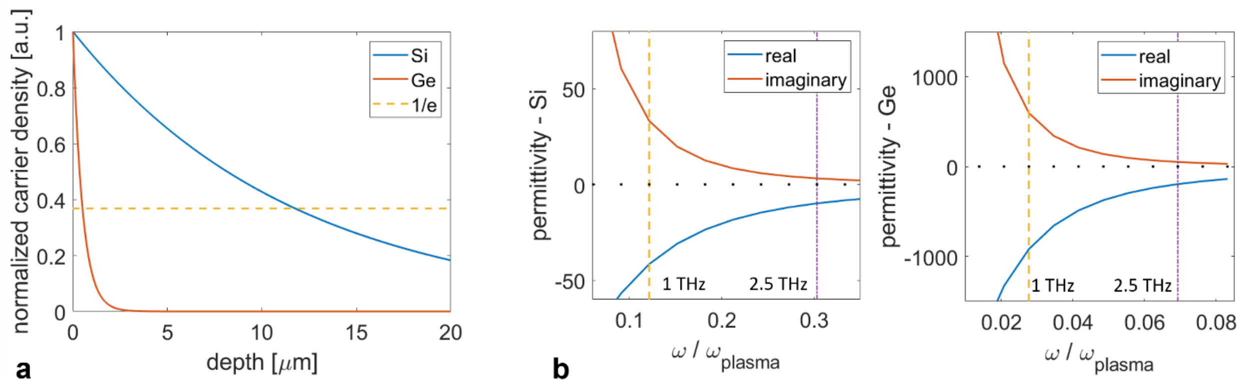

Figure 4.3 | Photo-excited semiconductors parameters. (a) Generated carrier density in Si and Ge, as a function of the depth (inside the semiconductor) from the illuminated surface. The dotted line shows the level at which the density of carriers falls to the value of $1/e$ and roughly corresponds to the penetration depth of the photo-exciting light. (b) Si and Ge electric permittivity calculated with the Drude model. In both cases, the plasma frequency is well above the bandwidth of interest $\sim \mathbf{2.5\ THz}$.

4.2.3 Hadamard patterns construction and Cake-cutting ordering

The set of patterns employed throughout this project is the one obtained from a so-called Hadamard matrix. This is a square matrix composed of $+1$ and -1 values, whose rows (and columns) are orthogonal to one another. If rows (or columns) of the array are exchanged, the orthogonality of the matrix is preserved (Pratt et al., 1969). The lowest order Hadamard matrix is of order two:

$$H_2 = \begin{bmatrix} 1 & 1 \\ 1 & -1 \end{bmatrix} \tag{4.5}$$

The easiest way to construct Hadamard matrices of higher order is by putting together lower order matrices (Pratt et al., 1969):

$$H_{2N} = \begin{bmatrix} H_N & H_N \\ H_N & -H_N \end{bmatrix} \tag{4.6}$$

The matrix obtained combining Hadamard matrices of order N will thus be of order $2N$. This procedure can be iterated to get Hadamard matrices of an order which is a power of 2 ($N = 2^n$). The sequence of rows (and columns) produced by this method is called the “natural ordering” (Fig. 4.4(a)). In the present work, the Hadamard matrix construction was carried out by means of a built-in Matlab® function.

A frequency interpretation can be given to the Hadamard matrix: along each of its rows, the frequency corresponds to the number of changes in sign. With this frequency interpretation, we can consider the rows to be equivalent to rectangular waves ranging between ± 1 with a subperiod of $1/N$ units.

Therefore, in the context of imaging, the Hadamard matrix merely performs the decomposition of an image by a set of rectangular waveforms rather than, for instance, the sine-cosine waveforms associated with the Fourier transform (Pratt et al., 1969). Half of the entries of each row and column are $+1$ and the other half -1 (except those corresponding to the zero frequency, first row and column in Fig. 4.4(a)). This yields one of the most useful properties associated with the Hadamard decomposition, which is that it guarantees an optimal SNR (Harwit & Sloan, 1979). Each of the patterns composing the set used for the SPI acquisition was obtained from a single different row of the Hadamard matrix (the n^{th} row corresponds to the n^{th} pattern). The procedure is shown in Fig. 4.4: a row from a N-order Hadamard matrix (Fig. 4.4(a)) is separated in $\sqrt{N}$ segments (each containing $\sqrt{N}$ elements), which are then flipped and stacked together (Fig. 4.4(b)), to form a $\sqrt{N}$-order pattern (Fig. 4.4(c)).

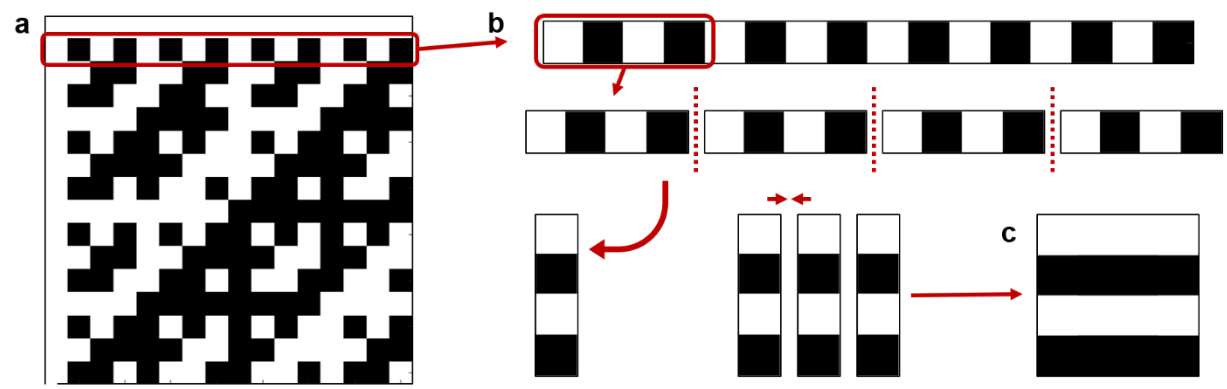

Figure 4.4 | The Hadamard patterns building procedure. (a) Hadamard matrix of order 16, in the "natural ordering", built following the procedure presented in the text (using a Matlab built-in routine). (b) Methodology to construct the set of patterns of order 4, from the rows of the matrix in (a). (c) Example of an order-4 pattern obtained from the 2nd row of (a).

In order to implement a fast CS reconstruction, we used the Hadamard set ordered in a "cake-cutting" (CC) sequence (W.-K. Yu, 2019). This ordering ensures that the most significant patterns are always displayed first, leading to a more accurate reconstruction with lower sampling ratios and at a lower computational cost. The CC sequence is based on considering the number of connected blocks (i.e., areas where all pixels have the same value, see Fig. 4.5(b,d)) in each of the 2D patterns of the set, and reordering them in a sequence with incremental number of blocks. The number of blocks can be seen as a 2D analogous of the change-of-sign frequency introduced earlier for each row of the Hadamard matrix: the higher the number of blocks, the higher the frequencies sampled by the pattern. Most natural images are sparse under a certain representation (see Chapter 3.1.2), and such sparsity results in high spatial frequencies having low (or zero) significance in the process of image reconstruction. Evidently, by ordering the set according to an incremental number of blocks, we will be always illuminating the object with the most significant subset first, eventually discarding the non-important ones. This enables a prompt reduction of the acquisition time, while minimizing the computational burden, since no minimization algorithm is needed in post-processing. In Fig. 4.5, we show the naturally ordered Hadamard matrix (Fig. 4.5(a)), and its corresponding set of 2D pattern (Fig. 4.5(b)), as well as the CC ordered matrix (Fig. 4.5(c)), and its patterns (Fig. 4.5(d)). As we can see, the number of connected blocks increases in the CC ordering while it has an arbitrary distribution in the natural sequence.

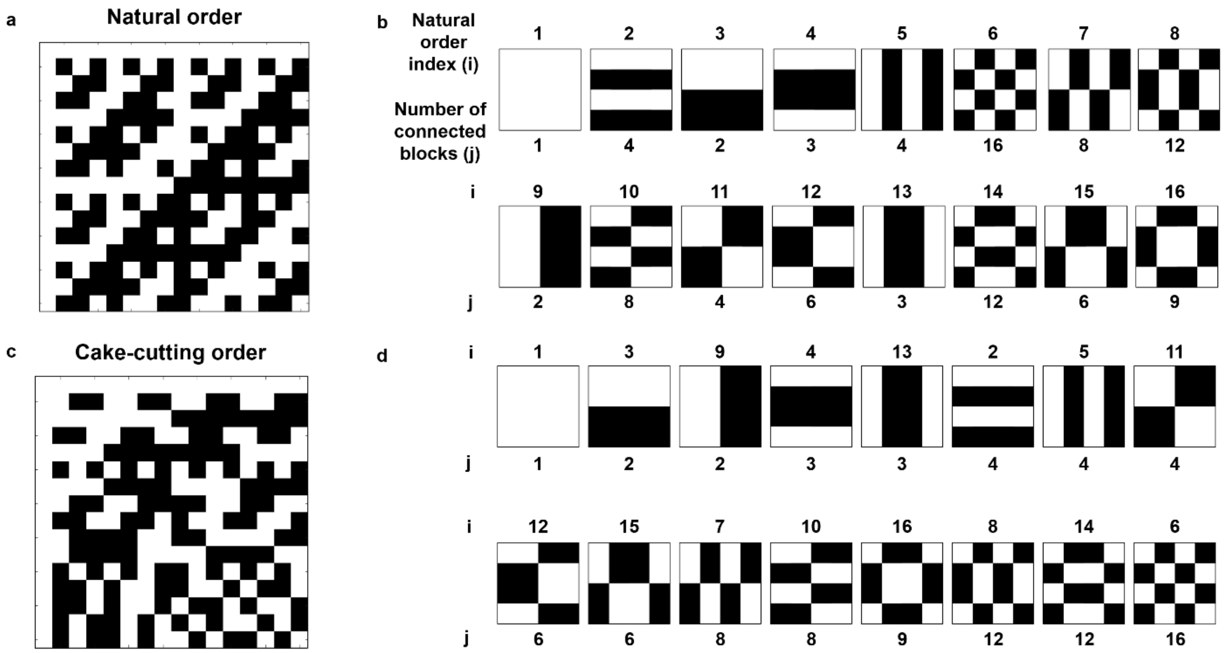

Figure 4.5 | Different ordering of Hadamard matrices. (a) Hadamard matrix of order 16 in the "natural ordering" sequence. (b) Set of patterns assembled from the rows of (a). (c) Hadamard matrix of order 16 in the CC sequence. (d) Set of patterns assembled from the rows of (c). "i" represents the natural ordering index, and "j" the number of connected blocks for each of the patterns. As we can see, the CC ordering exhibit incremental "j" values, which corresponds to increasing the pattern spatial frequency.

In our implementation at THz frequencies, we used binary amplitude modulation (1 or 0) which is straightforward to achieve using the carrier photoexcitation technique. This means that the patterns will exhibit either 0 or 1 values, rather than ± 1 composing the actual Hadamard set. The (0,1)-set can be used directly as is for the reconstruction, but it is also possible to shine alternatively a pattern and its "complementary" version, where the 0s and 1s are inverted:

$$H_+ = \begin{bmatrix} 1 & 1 \\ 1 & 0 \end{bmatrix}, \qquad H_- = \begin{bmatrix} 0 & 0 \\ 0 & 1 \end{bmatrix} \tag{4.7}$$

Evidently, the original Hadamard matrix can be obtained from the difference between the two, $H = H_+ - H_-$. Therefore, subtracting the set of measurements produced by positive and negative illumination, $W_+ = H_+T$, $W_- = H_-T$, will result in a dataset corresponding to a true Hadamard encoding:

$$W_+ - W_- = (H_+ - H_-)T = HT \quad (4.8)$$

This procedure comes at the cost of doubling the number of patterns one has to employ in the measurement process, but if the two complementary patterns are projected one after the other, this can eliminate sources of unwanted noise, particularly from low-frequency source fluctuations (Stantchev et al., 2016). Both the single pattern series approach ((0,1)-patterns only) and the double one ((0,1) + (1,0) patterns) were explored throughout this doctoral project, with the second one eventually employed when it resulted in more accurate image reconstruction.

We can finally briefly discuss the type of algorithm used for SPI reconstruction throughout this project. As explained previously, we chose to use a standard ordering of the series of interrogating patterns, so that the most significant ones are displayed first (i.e., those exhibiting lower spatial frequencies). In this way, the sample interrogation was performed directly with a pattern set which was highly coherent with the spatial features and the reconstruction could be carried out with a simple non-iterative algorithm, as described in (Bian et al., 2018). This type of algorithm makes it possible to minimize the computational burden required for the reconstruction.

4.2.4 Test-bed samples

For this experiment, we made use of two different semitransparent samples, in order to show imaging reconstruction exploiting different contrast methods. Optical pictures of the two samples, captured with a standard digital camera, are shown in Fig. 4.6. The first (Fig. 4.6(a)) was made of

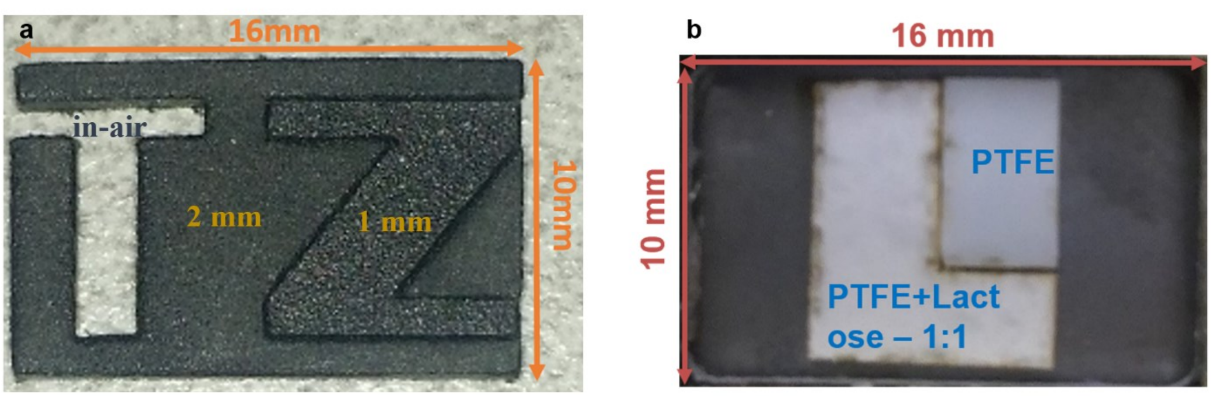

Figure 4.6 | Test-bed samples. (a) HDPE three-layer sample for TOF imaging: letter "T" in-air, letter "Z" 1 mm-thick, outer region 2 mm-thick. (b) Composite sample: L-shaped pellet made of 1:1 mixture of Teflon (PTFE) and Lactose, for spectral recognition, and rectangular pellet made of Teflon as a reference.

high-density polyethylene (HDPE, refractive index n = 1.54 and negligible absorption @ 0.5-2.5 THz (Naftaly & Miles, 2007)), fabricated via CNC (computer numerical control) machining (Hubs.com). The choice of HDPE was dictated mainly by its relatively high refractive index (compared, for instance, to Teflon), whilst maintaining almost zero absorption in the THz range. This made it possible to have sufficient temporal separation between the THz pulses produced by different layers, while avoiding having a sample too thick, for which diffraction effects could become relevant leading to image degradation. The sample had a rectangular shape with a size of 1.6 cm × 1 cm, in order to cover all the imaging window, and was 2 mm thick. The letters "TZ" were carved onto the surface with different thicknesses. In particular, the "T" was 2-mm-deep (i.e., in-air), while the "Z" was 1 mm deep. This sample was used to capture THz-peak-field-amplitude, and TOF images, by extracting different pieces of information from the same raw data (i.e., the temporal waveforms for each pixel). The second sample (Fig. 4.6(b)) was a composite one, made of a 1:1 mixture of Teflon and Lactose powders, compressed to form a ∼ 0.7 mm-thick pellet. Teflon (PTFE, refractive index n = 1.45 and negligible absorption @ 0.5-2.5 THz (Cunningham et al., 2011)) played the role of binding material, and Alpha-Lactose monohydrate, which features a clear absorption line at 1.38 THz (Brown et al., 2007; K. Li et al., 2020), was used to prove the possibility of performing hyperspectral imaging. The L-shaped composite sample was placed next to a rectangular pellet made of Teflon only and of the same thickness, used as a reference. Teflon was chosen, in this case, as it can be easily purchased as a powder and thus employed to prepare tailored mixtures with other chemicals, producing pellets suitable for spectroscopic measurements.

4.3 Experimental results

As mentioned above, the main result achieved in the first half of this doctoral project is the demonstration of the indirect reconstruction of temporal waveforms related to each pixel, starting from those recorded while shining the object with the patterned light modulated by the DMD.

In Fig. 4.7(b) we can see three examples of measured THz waveforms, acquired under illumination of the Si-plate with specific patterns (Fig. 4.7(a)), while imaging the HDPE sample of Fig. 4.6(a). These traces show a series of THz pulses in time, due to the contributions from the portions of the THz beam that passed through the sample at spatial positions with different HDPE thicknesses, and thus arriving at different times. In Fig. 4.7(c), we show the THz traces reconstructed for some specific pixel of the image (displayed in Fig. 4.7(d)), by solving Eq. (4.1). These waveforms clearly correspond to single few-cycle THz pulses, proving that the SPI approach can extract the local time-domain information from the convoluted data collected for each pattern. Moreover, we note that these pulses appear at time instants matching the time delays introduced by the different thickness values of the sample for the specific pixel positions. This means that the SPI technique can be applied for imaging purposes while preserving the full capability of TDS to retrieve complete time-domain data (in other words, amplitude and phase information). Fig 4.7 shows the data obtained from analyzing the sample under test with an 8 × 8 pixel image, which allows to clearly distinguish the waveforms with a decent electric field SNR for the single pixels (~25 in average, intrinsically limited by the low THz field amplitude passing through each pixel).

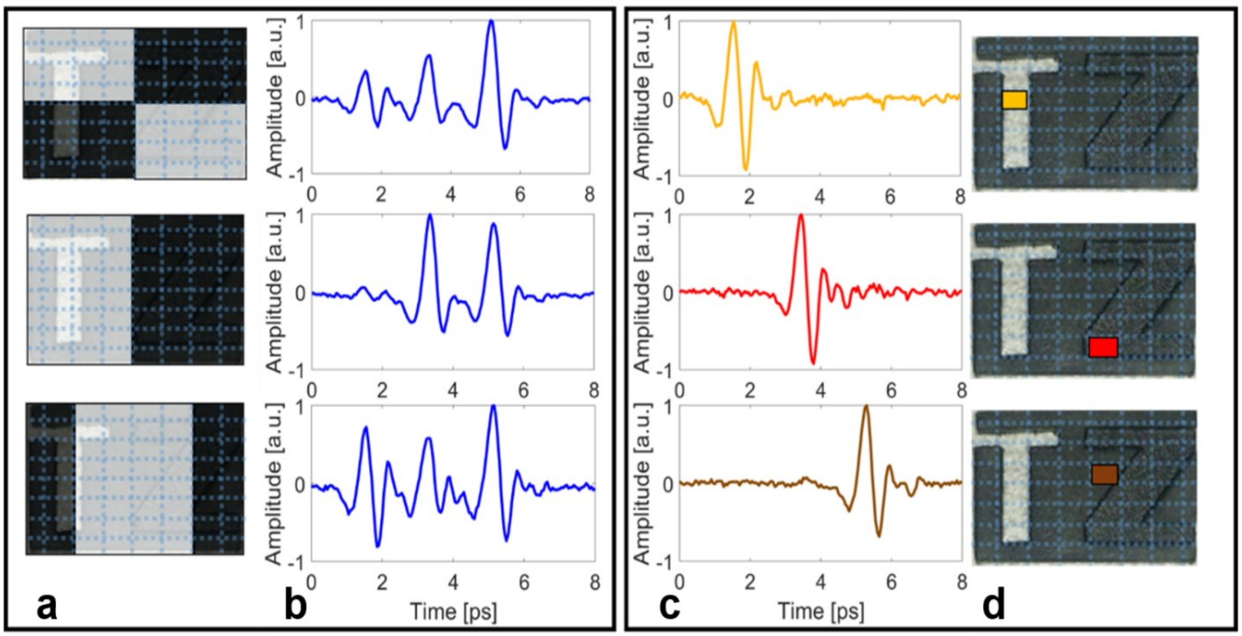

Figure 4.7 | Time-domain reconstruction of THz waveforms with SPI. (a) examples of three 8×8 Hadamard patterns; (b) detector output for the patterns in (a). The THz waveforms are multi-pulse, due to THz waves arriving at variable times after passing through the sample at different positions. (c) THz electric field reconstructed in time, at three selected pixel positions, marked in (d). The THz waves are clearly single-pulse, demonstrating that the SPI approach preserves the coherent detection ability of THz-TDS. *Adapted with permission from (Zanotto et al. 2020) © 2020 The Optical Society.*

In the following, we present a series of images of the samples, relying on different methods to display the contrast. It is important to underline that, for all the images, the same type of raw data (i.e. time-domain traces) are extracted from the measurements as well as the subsequent reconstruction process. Then, depending on the nature of the sample and the kind of information to be shown, the image contrast method is chosen. This is a clear proof of the flexibility of the time-domain SPI approach, and its potentially broad range of application in the context of THz imaging.

4.3.1 Fixed-time amplitude images of semitransparent objects

In the case of semitransparent objects, as for example our HDPE sample, different contrast methods can be chosen. One possibility is to show the electric field amplitude recorded at specific temporal positions. the variable thickness within the HDPE sample produces a spatially-dependent temporal delay for the incoming THz beam. Therefore, if one observes the electric field amplitude at a fixed time position, t_0, it will be maximum for those pixels where the delay corresponds to the chosen t_0, and almost zero elsewhere.

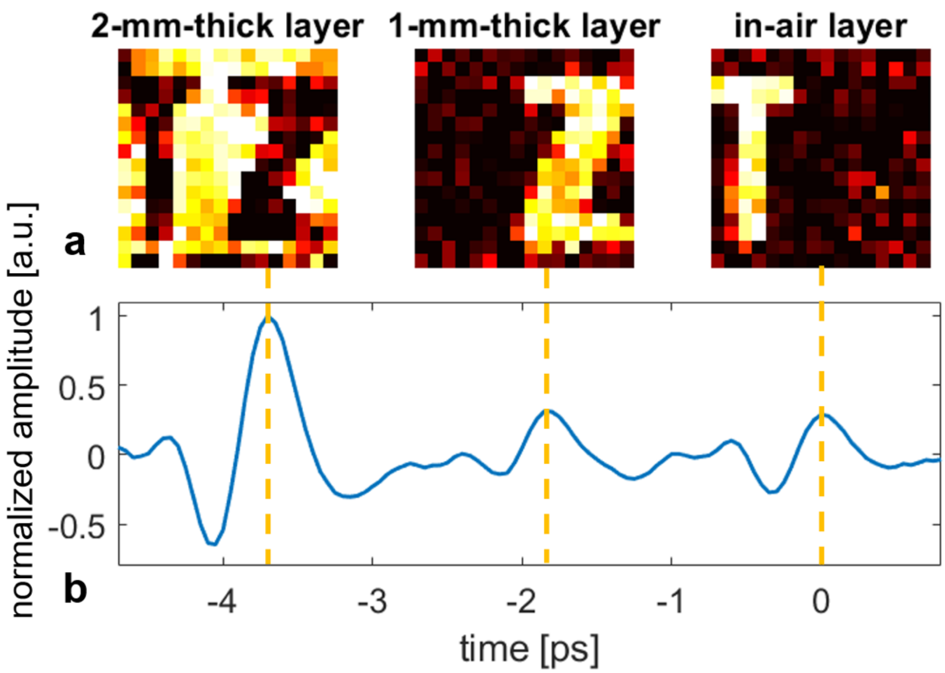

Figure 4.8 | Fixed-time amplitude imaging. (a) images captured at three different time instants, corresponding to the main peaks of the THz wave, shown in (b). The three peaks correspond to the three layers with variable thickness of the sample: "T" in-air, "Z" 1 mm, outer region 2 mm.

This technique allows to clearly recognize the presence of areas with different thicknesses in a sample. In Fig. 4.8(a), we display three 16 × 16 frames captured at times corresponding to the three main peaks of the waveform shown in Fig. 4.8(b) (a representative waveform detected for one of the employed patterns). The frames clearly show the three areas with different thickness: "T" in-air, "Z" 1 mm-thick, outer region 2 mm-thick. One could notice some deviations in the expected amplitude levels at some pixels in the three plots. This has potentially two causes. The first is scattering, which mostly occur at the boundary between the sample regions featuring different thicknesses and leads to reduced transmission. Additionally, some of the bright pixels of the patterns could happen to illuminate a sample region where two different thickness levels are present. Hence, because of the different time delays introduced by the two layers, the transmitted light will be distributed between two THz pulses arriving at different times in the coherent detection. As a result, the pixels at the borders will once again exhibit a reduced transmission in the fixed-time amplitude map. Such issue could be partially improved by increasing the resolution of the imaging patterns. There were essentially two factors that limited the resolution that could be achieved in our experimental conditions (and have been discussed in section 4.2.1). First, the minimum distance between the modulation plane and the sample, set by the thickness of the Si-plate used for modulation (500 μm), does not allow us to have pixel smaller than $\sim$400 μm. This is due to diffraction effects, that would cause the degradation of the reconstructed image. Second, the acquisition time, still long due to the slowness of the delay line and limited repetition rate of the laser, hampered the possibility of acquiring measurements requiring more than a few hundred patterns.

4.3.2 Time-of-flight images

Another useful way of extracting information from semitransparent materials relies on the retrieval of the time delays of the THz pulse with respect to a reference, at each spatial position. This procedure allows to estimate the thickness (or the refractive index) of a sample. Such technique is called time-of-flight (TOF) and has been described in section 2.3.2. In Fig. 4.9(a), we can see examples of THz traces recovered for three of the pixels of the image in Fig. 4.9(b), along with the reference pulse (dashed blue line). By calculating the time delay between the peaks of the THz pulses, we can obtain the local thickness of the sample (featuring a refractive index of 1.54). The obtained values are used to reconstruct the 256-pixel thickness map shown in Fig. 4.9(b). The same image can also be conveniently displayed as a real 3D image, to visualize all three spatial dimensions (Fig. 4.10).

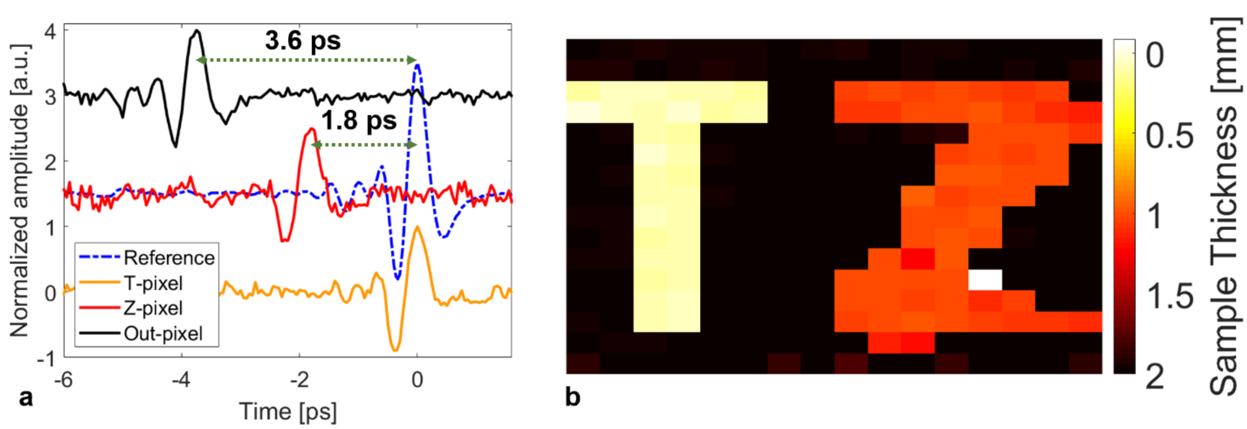

Figure 4.9 | Time-of-flight imaging. (a) Examples of THz pulses reconstructed for three of the pixels in (b), and their delay relative to a reference pulse, captured without the sample. (b) 256-pixel reconstructed image of the local thickness of the HDPE sample described in the text. The thickness is retrieved with the relative time delay of the THz pulses at each spatial position, considering the refractive index of HDPE (n=1.54).

As we can see from the plots shown in Figs. 4.9 and 4.10, the quality of the image reconstruction is quite accurate. In particular, the thickness of the three layers can be clearly distinguished. As discussed earlier, some pixels along the margins of the "Z", especially across the slanted portions, fail to represent the correct thickness, and this is most probably due to the limited resolution offered by the 16 × 16 patterns (1 mm horizontal, and 0.625 mm vertical). This leads to the light from one pixel being partially transmitted through two neighboring areas, but the delay calculated for the pixel displays exclusively one of the two thicknesses (relative to the largest transmitted THz peak amplitude).

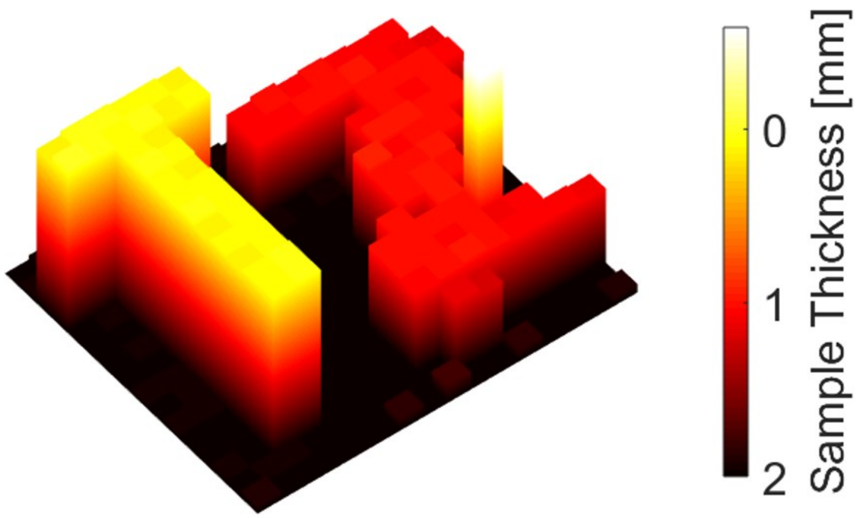

Figure 4.10 | 3D version of the image displayed in Fig. 4.9(b). *Reprinted with permission from (Zanotto et al. 2020) © 2020 The Optical Society.*

4.3.3 Compressed sensing reconstruction

As a proof-of-principle, we also performed a CS reconstruction of the TOF image, in order to show that the image recovery is possible even with a number of measurements smaller than the number of pixels. This is one of the main advantages provided by the SPI paradigm, and a crucial one when one seeks to target practical applications in the THz range, as explained in chapter 3. The algorithm applied is a standard non-iterative one (Bian et al., 2018). Based on the fact that the SPI measurements represent the correlation between the modulation patterns and the target scene, the object can be reconstructed by correlating the modulation patterns with the corresponding measurements (Basano & Ottonello, 2007). The reconstruction algorithm is a weighed summation of modulation patterns, $P_i(x, y)$, with weights being the corresponding measurements, W_i (Bian et al., 2018):

$$T(x,y) = \frac{1}{m}\sum_{i=1}^{m}(W_i - \{W_i\})P_i(x,y) = \{W_i P_i(x,y)\} - \{W_i\}\{P_i(x,y)\} \tag{4.9}$$

Where $\{\cdot\}$ is the ensemble average in terms of i. Since each pattern carries some information about every pixel of the scene, even with an incomplete pattern set the method yields a complete image. The smaller the number of patterns used, though, the less accurate the final reconstruction will be. The results are shown in Fig. 4.11, where we also present a comparison between the CS reconstruction obtained by using the Hadamard patterns in the natural order (Fig. 4.11(a)), and with the CC order (Fig. 4.11(b)). As we can see in Fig. 4.11(a), the natural sequence does not allow to achieve high compression ratios: at 75% the image is already quite degraded. At 50% we can notice the phenomenon called "aliasing", for which the loss of information due to under-sampling leads to the formation of replicas of portions of the image (in this case a large part of the "T", and two corners of the "Z"), while other features are completely lost. In turn, in Fig. 4.11(b), we can see how using the CC ordering, we can safely reduce the number of measurements. The procedure results in the loss of some details of the image, but the shape of the letters is still recognizable even with only 25% of the

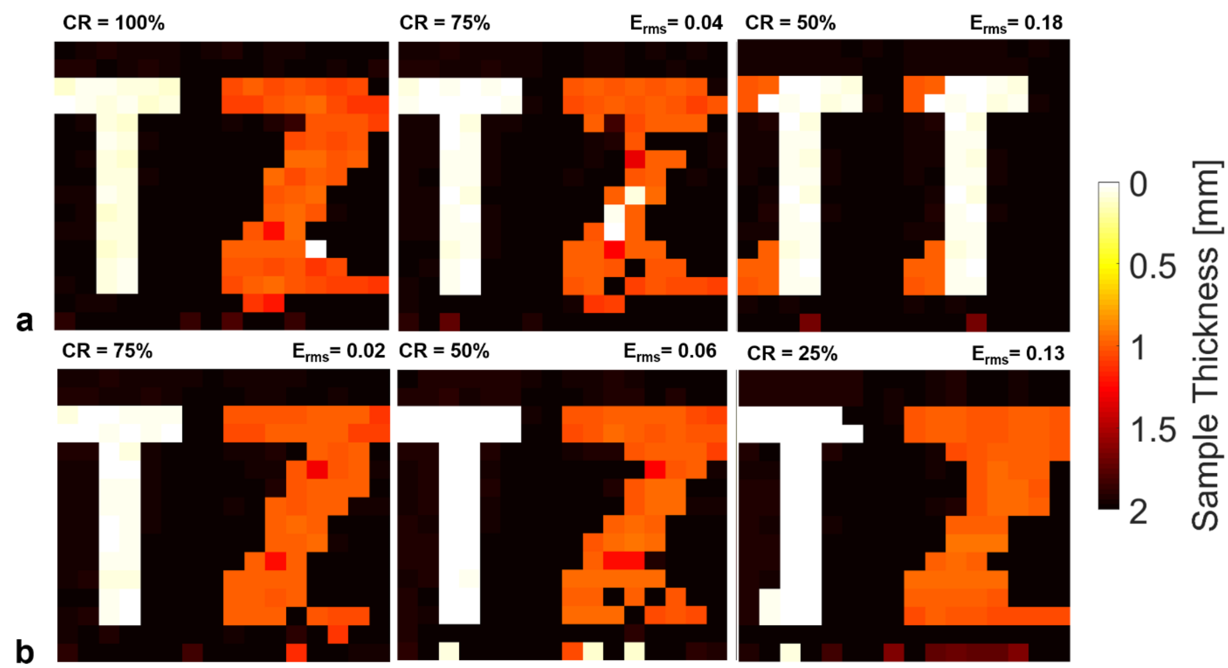

Figure 4.11 | CS-TOF reconstruction. 256-pixel images of the local thickness of the HDPE sample described in the text. As above, the thickness is retrieved by extracting the relative time delay of the THz pulses at each spatial position. Each image is recovered with variable compression ratio (CR, number of measurements/number of pixels). (a) reconstruction using the Hadamard set in the "natural sequence", left to right: CR=100%, CR=75%, CR=50%. (b) reconstruction using the Hadamard set in the CC sequence, left to right: CR=75%, CR=50%, CR=25%. The Root Mean Squared Error (E_{RMS}) is calculated averaging the error (i.e., the difference between the peak amplitude of the compressed reconstruction and that of the corresponding pixel with no compression) over all the pixels in the image.

total number of patterns, and it is still possible to extract the thickness at each spatial position. The fact that the "Z" letter in the image is more affected by compression than the "T" is likely due to the pattern ordering chosen for the Hadamard set (as described in section 4.2.2). Indeed, by following this order, the spatial frequency content of each pattern increases progressively as the number of patterns increases. Therefore, a significant compression factor exploiting only the first subset of patterns (i.e., containing low spatial frequencies) is likely to degrade more the quality of oblique edges, which would require higher resolution to be properly resolved. A measure of the degradation can be obtained by calculating the Root Mean Squared Error (E_{RMS}) for the image, computed by averaging the square of the error, calculated as the difference between the peak amplitude of the compressed reconstruction and that obtained without any compression, over all the pixels in the image.

4.3.4 Hyperspectral images

Finally, we used our system to also prove the possibility of performing spectral recognition of chemical compounds. In this context, the contrast method applied is based on showing the relative absorption at specific frequencies, with respect to a reference pulse. To this end, we realized the sample shown in Fig. 4.6(b). The idea is to obtain a map of the spectral absorption at specific frequencies. The presence of lactose will be revealed by the strong resonance at ~1.38 THz. We reconstructed 8 × 8-pixel images using two distinct contrast methods, to show how different information can be extracted from the same sample. In Fig. 4.12(a), we see a TOF image, showing the delay between the time-domain pulses at each pixel and a reference pulse, similarly to what we did in Fig. 4.9. In this image, we can clearly distinguish the central rectangular area of the sample from the two sides, where no sample was present, and the beam propagated in air. We can also note that the sample area has basically a uniform thickness (a slight difference between the L-shaped area, containing lactose, and the smaller rectangular pellet made of Teflon can somehow be seen, due to a small refractive index variation caused by the presence of lactose, as well as a minor thickness discrepancy). In Fig. 4.12(b-c), we instead display spectral images by post-selecting the transmission at ~1 THz (Fig. 4.12(b)), and in correspondence of the lactose absorption line, at ~1.38 THz (Fig. 4.12(c)). The spectra used to retrieve these images are obtained by Fourier transforming the time-domain data provided by the SPI reconstruction for each individual pixel of the image.

Examples of such spectra for some selected pixels of Fig. 4.12(c) are shown in Fig. 4.12(d). The transmission is then calculated simply as the ratio between the spectral amplitude of the sample traces with respect to the reference ones, collected without the sample, $T(\omega) = E_{\text{sample}}(\omega)/E_{\text{ref}}(\omega)$.

No clear features are visible for the spectral image at 1 THz, because none of the two portions of the sample have an absorption line at this frequency, nor, needless to say, does the air. Conversely, in Fig. 4.12(c) we observe that the L-shaped portion, made of the Teflon/lactose mixture, results clearly darker overall, while again, the Teflon rectangle shows no significant discrepancy from the rest of the imaging window. The uneven absorption among different pixels within the L-shaped section is probably due to the Lactose inhomogeneous spatial distribution within the mixture.

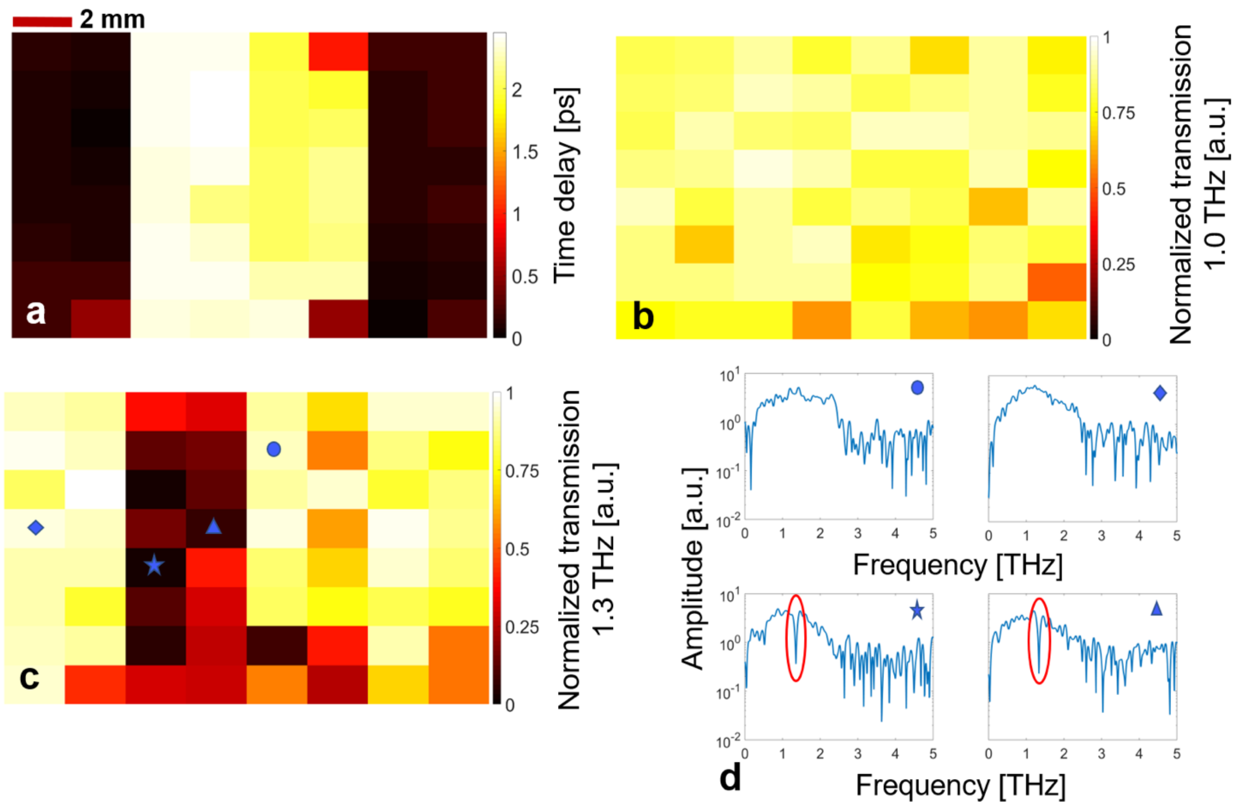

Figure 4.12 | Hyperspectral imaging. Imaging of a sample containing a chemical featuring a spectral absorption line in the THz range (see Fig. 4.3(b)). (a) 64-pixel TOF image: the central rectangular area (yellow) correspond to the sample, and is clearly discernable from the rest of the in-air area (dark brown). The L-shaped mixture containing lactose, and the smaller rectangular portion made of PTFE only are barely distinguishable. (b,c) 64-pixel spectral images: (b) spectral transmission around 1 THz; (c) spectral transmission around 1.38 THz. No feature is present in (b), because neither any portion of the sample, nor air significantly absorb at 1 THz. The L-shaped pellet appears in (c), thanks to the lactose absorbption at 1.38 THz. (d) examples of THz spectra of four selected pixels (indicated in (c)), obtained by direct Fourier-transformation of the time-domain THz waveforms reconstructed at each pixel position: for the pixels where lactose is present, the absorption line at 1.38 THz is clearly visible. *Adapted with permission from (Zanotto et al. 2020) © 2020 The Optical Society.*

4.3.5 Discussion and conclusions

Here, we can make some considerations regarding the acquisition time, which is one of the driving reasons to employ SPI. For the image with the highest resolution (16 × 16, 256 pixels), the current acquisition time was about 10 hours (similar to what would result with a traditional raster-scan). The application of CS would already reduce such acquisition time significantly, since the use of only

25% of the patterns already yields a decent reconstruction. The main limitation is the slow delay line employed in our system, along with the need of relatively long integration at each point of the time window, due to the limited repetition rate of our laser (1 kHz). These two elements combined result in a 2.5-minute-long acquisition for the 8-ps temporal scan needed for each pattern. Higher-repetition rate laser sources, coupled with readily available fast delay lines performing multiple scans per second, and a specifically customized DMD/lock-in software interface would directly reduce such time to few minutes. In any case, the two key advantages of the time-domain SPI scheme proposed here are the following: i) it avoids the use of complex and bulky motorized mechanical systems necessary to perform raster-scan, and ii) it allows for the implementation of CS algorithms.

Summarizing, we have demonstrated an appropriate reconstruction of the THz electric field waveform in the time-domain at each spatial position of the object image, without the need of mechanical raster-scanning. We have exploited this capability to retrieve images featuring various contrast methods, including fixed-time amplitude, TOF and hyper-spectral images. This demonstrates the flexibility of the applied SPI technique in retrieving far-field images in multiple dimensions. Moreover, we have shown that CS algorithms can be also implemented, potentially leading to a significant reduction of the overall acquisition time.

5 TERAHERTZ IMAGING WITH A SINGLE-SHOT DETECTION TECHNIQUE

This chapter is partially adapted from: L. Zanotto, G. Balistreri, A. Rovere, O-P. Kwong, R. Morandotti, R. Piccoli, and L. Razzari, "Terahertz scanless hypertemporal imaging" arXiv:2209.11646 (2022)

In this chapter, the results related to the second half of the doctoral project are presented. Here, the main goal was the combination of the THz-SPI imaging system developed in the first part of the project (see Chapter 4), with a so-called single-shot detection (SSD) technique. As explained in Chapter 3, SSD techniques are THz acquisition approaches that enable the simultaneous capture of a whole THz waveform in the time-domain, in principle within a single laser shot, thus significantly reducing the acquisition time usually required to perform the temporal scanning of the THz pulse by employing a mechanical delay line. As already mentioned in the previous chapters, the need for the temporal scan is one of the main factors severely limiting the acquisition speed of current TDS-based THz imaging systems.

The SSD techniques employed throughout this doctoral project are the so-called time-to-frequency and time-to-space mapping. Their working principles have been introduced in Chapter 3. In the following sections, we present the experimental setups built to exploit both methods into our SPI-based THz imaging system. The time-to-frequency arrangement and related results will be discussed in section 5.1, while the time-to-space one in section 5.2. At the end of section 5.2, we will summarize the main findings from these experimental characterizations and highlight their relevance for the advancement of current THz imaging systems.

5.1 Time-to-frequency configuration

The first technique we tested was the time-to-frequency method, which is relatively easy to implement. Despite the shortcomings related to the limited temporal resolution (as mentioned in section 3.3.1), we achieved the SPI reconstruction of the THz electric-field waveforms in the time-domain, although with some distortions (see below in section 5.1.2).

5.1.1 Experimental setup

The experimental system used for this attempt, shown in Fig. 5.1(a), was a modified version of that already employed in the previous experimental characterization and described in section 4.2.1. The beam from the amplified Ti:Sapphire laser is split into three lines: pump, probe and pattern generator. The pump beam is used to generate THz pulses via OR in a ZnTe crystal, while the pattern generator beam is used to reshape the THz beam via the photo-modulation technique described in Section 4.2.2, by using a DMD. The main difference, compared to the setup presented in chapter 4, involves the need of temporally stretching the probe beam. The way to achieve such temporal stretch is based on introducing a linear frequency chirp, i.e., incrementally delaying the different frequency components of the optical pulse. The chirp is introduced by means of a couple of diffraction gratings (in Fig. 5.1(a) we display 4 gratings for clarity, but in the actual experiment we used two and had the beam bouncing twice on each of them) along the beam path: the first bounce on the grating is used to spatially spread the frequency components of the broadband pulse, the second collimates the beam, the third brings the frequency components back together, and the fourth collimates the beam again. The chirp rate can be adjusted by changing the separation between the two gratings, as the longer the distance, the larger will be the spread in the frequency content. After this process, a quadratic phase is maintained, which will result in a longer temporal pulse. The probe beam then samples the THz waveform when they overlap in the detection ZnTe crystal, subsequently propagates through the linear polarizer (oriented in near-zero conditions, see Section 3.3.4) and illuminates the spectrometer, where it is eventually recorded. The actual THz waveform is not directly measured by the spectrometer acquisition. The readout is, in fact, the probe frequency spectrum, modulated by the THz wave. It is necessary to capture a background probe spectrum too, in absence of THz modulation. Examples of the probe spectrum recorded with and without the THz pulse are illustrated in Fig. 5.1(b). The waveform is then obtained by subtracting the background probe from the probe modulated by the THz beam. To realize the mapping between time and

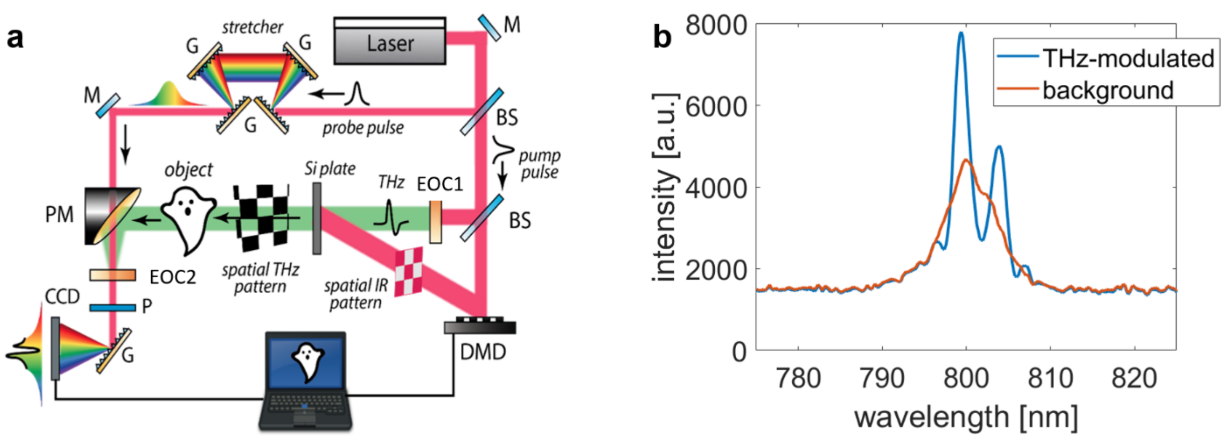

Figure 5.1 | The time-to-frequency imaging setup. (a) Schematic of the experimental setup: SPI-based THz-TDS, with time-to-frequency mapping. The beam from the fs-laser (Ti:Sapphire, Spectra Physics) is split into three lines (BS-beam splitter), one generates the THz pulse in a ZnTe crystal (EOC1), one is used as probe in a second ZnTe crystal (EOC2), and the last one is employed for THz modulation (after being patterned with the DMD). A linear temporal chirp is introduced in the probe pulse by means of a system of gratings (G). The signal is recorded by a spectrometer (G + CCD), after the probe has propagated through a polarizer (P). (b) The probe pulse acquired by the spectrometer when the THz is present (blue), and without it (red).

frequency (wavelength), the peak of the THz waveform is shifted along the probe spectrum, by sequentially changing the relative delay between the THz and probe pulses, using a mechanical delay line. In doing so, we obtain, through a fitting procedure (Fig. 5.2(a)), a time/wavelength calibration value of 0.214 ps/nm. We note that this calibration does not give the actual achievable time resolution, because of the limitation linked to the probe pulse bandwidth, as discussed in Section 3.3.2. Considering that the pulse duration of our laser is $T_0 = 0.150$ ps, and the related bandwidth $\sim$14 nm, the calibration yields a chirped pulse duration $T_c \approx 3$ ps, leading to a temporal resolution of $\Delta T \approx 0.67$ ps (see Eq. 3.5).

5.1.2 Experimental results

We carried out some imaging tests of simple objects using only 4×4-pixel Hadamard patterns for illumination. We were able to retrieve the time-domain waveforms at every pixel, even though the SNR of the measurement (calculated at the peak of the THz wave) was just ~ 30 (the SNR obtained with a standard delay-line-based acquisition was ~ 150). Furthermore, the limitation on the achievable temporal resolution leads to a distortion of the measured THz waveforms. As we can see in Fig. 5.2(b), the THz waveform recorded using the time-to-frequency mapping (red line) displays a second peak, which is most likely a copy of the main peak visible in the trace captured with the standard technique. Such replica is clearly an artifact introduced by the acquisition approach. Moreover, the oscillations following the main peak are clearly distorted in the SSD acquisition. The reason of both these distortions is most probably the low time resolution (0.67 ps), which is well

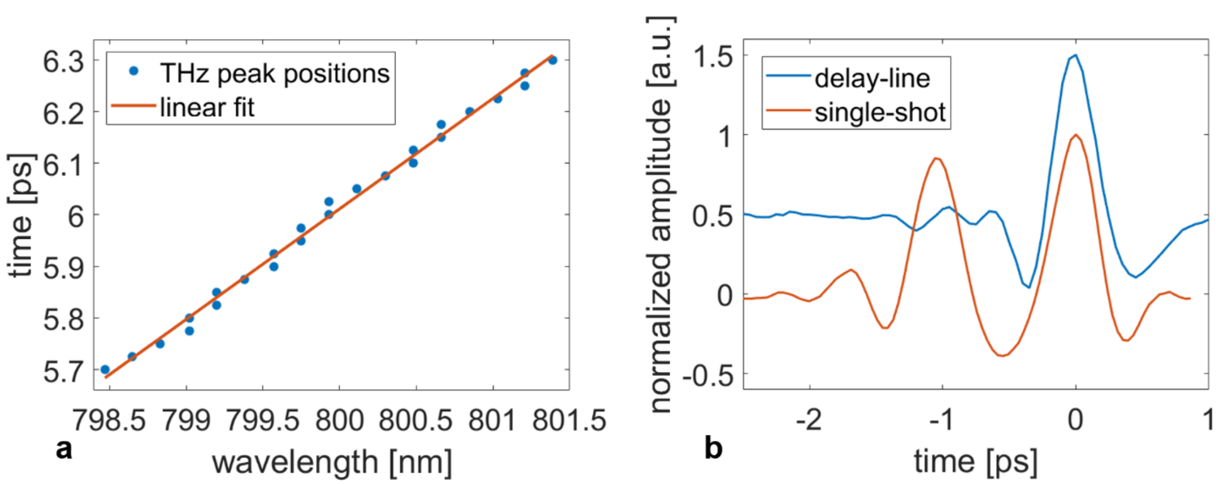

Figure 5.2 | Time-to-frequency THz waveform reconstruction. (a) Time VS wavelength calibration: the value extracted from the linear fit is 214.1 fs/nm. (b) THz waveform reconstructed with the traditional EOS, featuring a delay line (blue), and using the time-to-frequency mapping, SSD configuration (red) (the blue waveform is shifted vertically for clarity). The red trace is clearly distorted, compared to the blue one, as a replica of the main pulse appears around -1 ps. This is likely due to the low temporal resolution provided by this SSD method.

beyond the Nyquist limit ($\Delta t_N = T_{THz}/2 = 0.5$ ps @ 1 THz). Similar issues, where SSD-based measurements result in distorted waveforms exhibiting replicas of the same pulse, are reported in literature (Murakami et al., 2008).

Nonetheless, we still managed to achieve the reconstruction of the spatial shape of a simple L-shaped object made of aluminum foil (Fig. 5.3(a,b)), and the TOF reconstruction of a L-shaped Teflon sample (Fig. 5.3(c,d)). The imaging window had, in this case, an area of 1.2 × 0.8 cm^2, divided into 4 × 4 pixels. The image in Fig. 5.3(b) was obtained by integrating the intensity of the THz temporal waveforms of each pixel. As for the one in Fig. 5.3(d), it was reconstructed considering the time delay of the main THz peak with respect to a reference pulse, and calculating the local thickness by considering the refractive of Teflon ($n = 1.45$ @ 1 THz).

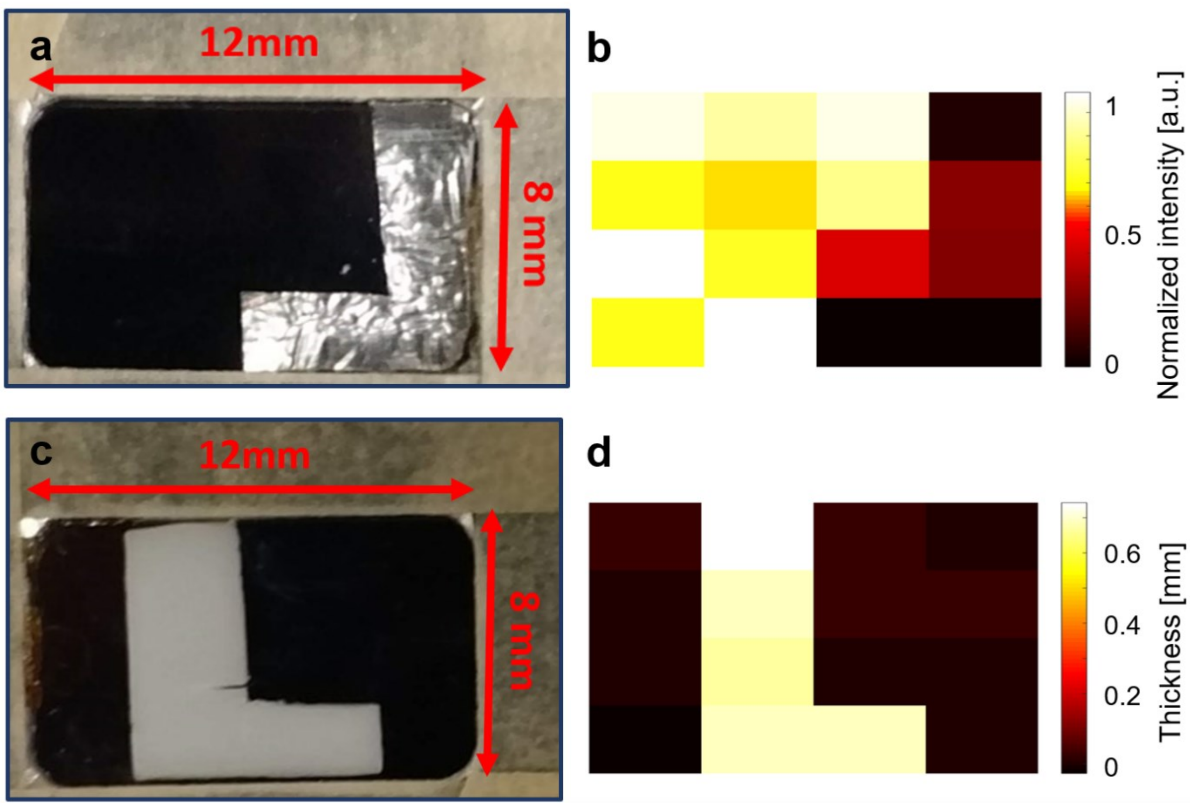

Figure 5.3 | Imaging with time-to-frequency mapping. Images retrieved using the time-to-frequency mapping technique. (a) Opaque L-shaped sample, made of aluminum foil. (b) 4 × 4-pixel image, reconstructed using the transmitted THz intensity as the contrast method. (c) Semitransparent L-shaped sample, made of Teflon (n = 1.45 @ 1 THz). (d) 4 × 4-pixel TOF image, obtained by considering the delay of the THz peak at each pixel, with respect to a reference pulse.

5.2 Time-to-space configuration

The SSD scheme delivering the best performance in our operating conditions was the time-to-space mapping and, as such, it was chosen for the final experimental arrangement. The core feature of this implementation is the use of a probe beam with a tilted front, in order to perform the THz detection with the time-to-space mapping (see Section 3.3.3). The tilt is introduced by means of a grating, and the pulse profile after the grating needs to be imaged onto the detection crystal. It is thus crucial that the probe itself and the THz beam spatially overlap at the detection crystal with appropriate respective sizes. In the following, we will show that the diffraction undergone by a light beam propagating in free space allows to naturally meet the SPI working conditions. The theoretical investigation of such parallelism is presented in section 5.2.1. Furthermore, simulations of the propagation of the diffracted THz patterns have been carried out, in order to obtain the specific parameters of our experimental conditions, as discussed in section 5.2.2. The experimental setup employed for our proof-of-principle characterization, together with the results obtained from it are then shown and discussed in sections 5.2.3 and 5.2.4.

5.2.1 Capturing images after diffraction

In this paragraph we will explore a very interesting property of the SPI scheme, which is particularly useful for the experimental arrangement based on the time-to-space SSD technique. We can start by recalling once again the summation presented in Eq. (3.1):

$$W_i = \sum_{x,y} P_i(x,y)T(x,y,\omega) = E(\omega)\sum_{x,y} P_i(x,y)T'(x,y,\omega) \tag{5.1}$$

In which we have separated the incident THz field $E(\omega)$ from the object transmission $T'(x,y,\omega)$. A crucial information given by this equation is that each value recorded by the detector and collected in the vector W results from the contribution of all the pixels of the patterned beam. These values carry information about the correlation between patterns and the object spatial distribution, and are used as weights in the summation that yields the image reconstruction.

In the Huygens-Fresnel picture of diffraction, the complex field amplitude of a light beam after free-space propagation can also be seen as a summation of spherical waves generated at the source plane (Fig. 5.4(a)) (Goodman, 1996). The field value at a certain position (x,y) at the detection plane, after propagation for a distance z, is the result of contributions from all the points at the source plane (ξ,η). Techniques such as coherent diffraction imaging and ptychography (Dierolf et al., 2010; Faulkner &

Rodenburg, 2004; Thibault et al., 2008), as well as digital holography (Osten et al., 2014; Schnars & Jüptner, 2002) are based on the solution of the diffraction integral. In this way, it is possible to retrieve the image of an object by probing amplitude and phase of the EM field after propagation. In general, in these cases, the field has to be sampled at different positions at the detection plane to collect the information on the spatial distribution of the object. If a structured illumination is used (as it happens in the case of SPI) though, only one measurement of the correlation between the patterns and the object spatial shape is needed. This can be accomplished by simply probing one point only at the detection plane. Diffraction automatically performs the spatial integration that brings to a single point such correlation information, naturally delivering the operating conditions of SPI. Typically, a focusing element would be employed to concentrate the energy of the propagating beam and obtain a better image contrast, but this is not strictly necessary: simple free-space propagation would be enough to perform an SPI measurement.

We can prove the validity of this concept by considering the propagation of a patterned beam under the Huygens-Fresnel principle, starting from the Rayleigh-Sommerfeld diffraction solution (Goodman, 1996). If U_1 and U_2 are the electric field distributions in the source and observation planes, respectively, we can write:

$$U_2(x, y) = \frac{1}{i\lambda} \iint\limits_{\Sigma} U_1(\xi, \eta) \frac{\exp{(ikr)}}{r} \cos\theta \, d\xi d\eta \tag{5.2}$$

Where λ is the optical wavelength, k is the wavenumber, $r = \sqrt{(x-\xi)^2 + (y-\eta)^2 + z^2}$ the distance between a position in the source plane and a position in the observation plane. (ξ, η) are the variables in the source coordinate systems and (x, y) those in the observation one, z the distance between the source and observation planes and Σ is the source area. To simplify Eq. 5.2, we can make use of the so-called Fresnel approximation. We start by expanding r in a Taylor series, $r = \sqrt{(x-\xi)^2 + (y-\eta)^2 + z^2} \approx z\left[1 + \frac{1}{2}\left(\frac{x-\xi}{z}\right)^2 + \frac{1}{2}\left(\frac{y-\eta}{z}\right)^2 + \cdots\right]$. If $z \gg |x-\xi|$ and $|y-\eta|$, we can then consider up to the second-order term in the exponential on the right side of Eq. 5.2, and just the first order term ($r \approx z$) for the denominator. By setting $\cos\theta \approx 1$, after some rearrangements we obtain (Goodman, 1996):

$$U_2(x, y) = \frac{e^{ikz}}{i\lambda z} \exp\left[\frac{ik(x^2+y^2)}{2z}\right] \iint\limits_{\Sigma} U_1(\xi, \eta) e^{\frac{ik}{2z}(\xi^2+\eta^2)} e^{-\frac{ik}{z}(x\xi+y\eta)} d\xi d\eta \tag{5.3}$$

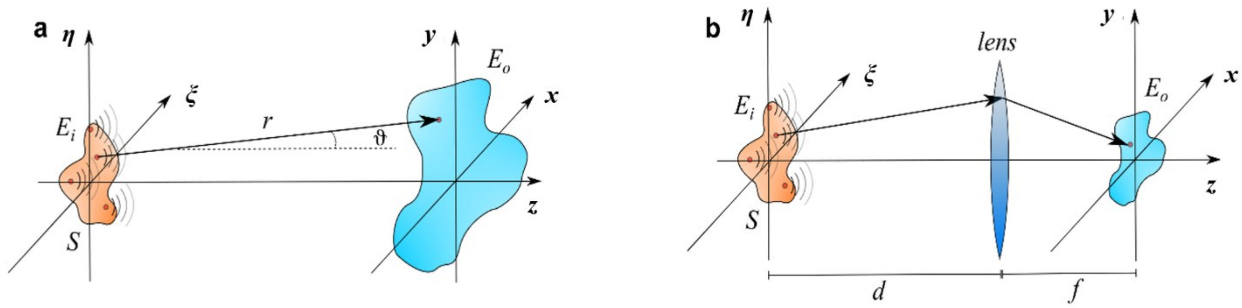

Figure 5.4 | The Huygens-Fresnel principle. (a) Schematic of the Huygens principle of diffraction. (b) A lens creates the same conditions of Fraunhofer diffraction but with higher energy concentration.

Moreover, if we are in far-field conditions (Goodman, 1996), i.e., $z \gg \frac{k({D_x}^2+{D_y}^2)}{2}$ (which at 1 THz, $\lambda =$ 300 μm is easily satisfied in normal lab working environment: $z \gg 5$ mm for a sample with a typical feature size of $D_x \times D_y = 0.5 \times 0.5$ mm), the expression can be further simplified as the Fraunhofer integral:

$$U_2(x,y) = \frac{e^{ikz}}{i\lambda z} \exp\left[\frac{ik(x^2+y^2)}{2z}\right] \iint_{\Sigma} U_1(\xi,\eta) e^{\frac{2\pi i}{\lambda z}(x\xi+y\eta)} d\xi d\eta \tag{5.4}$$

Where the integral is simply the 2D Fourier transform of the input field, if we define the spatial frequencies as $\nu_x = x/\lambda z$ and $\nu_y = y/\lambda z$. The field amplitude and phase at (x,y) are thus directly related to amplitude and phase of the Fourier spectrum at $\left(\frac{x}{\lambda z},\frac{y}{\lambda z}\right)$. Now the input field in the case of SPI can be written as the product between the pattern distribution $P_n(\xi,\eta)$, the transmission function of the object $T(\xi,\eta,\omega)$, and the THz field $E(\omega)$. Here, for simplicity, we can consider the patterns to be purely real (amplitude modulation) and independent from the frequency ω. We note though, that all the considerations can be extended to the most general case where all the entities involved (i.e., patterns and object) are complex-valued. The single-pixel detector reading at the center of the field distribution $(x = y = 0)$ becomes:

$$W_n(\omega) = \frac{\omega e^{i\frac{\omega}{c}z}}{i2\pi cz} E(\omega) \iint_{\Sigma} P_n(\xi,\eta) T(\xi,\eta,\omega) d\xi d\eta \tag{5.5}$$

The integral in this expression is the average value (i.e., the DC-component of the Fourier transform) of the product between the pattern distribution and the object transfer function. The choice of the DC-component is a matter of convenience, since the mathematical expression is less complex, and the central spot is typically the brightest, offering a better experimental performance. In principle, it would be possible to use the value of the field at another point of the plane, since such value would be the result of an integration over all the points on the source plane as well. By comparing Eq. (5.5) and (5.1), it can be clearly seen that they are equivalent in the case of a pixelated image. As such, simple free-space propagation of a light beam after illuminating the object naturally creates the conditions to perform an SPI measurement via a point detection. Such interesting property underlies the functioning of various SPI-based arrangements. Some examples are systems for lens-free diffractive imaging at visible and IR frequencies (Horisaki, Matsui, & Tanida, 2017; Horisaki, Matsui, Egami, et al., 2017), digital holography (Clemente et al., 2012, 2013; Martínez-León et al., 2017), and ptychography, where the phase is extracted from intensity-only measurements (M. Li et al., 2021).

In order to avoid operating in the far-field at long distances from the object, it is convenient to insert a focusing element (e.g., a thin lens) in the path between the object and the detector. In particular, we can place a lens of focal length *f* at a certain distance *d* from the object and place the detector in the focal plane of the lens (Fig. 5.4(b)). After some steps from the Fresnel expression, Eq. 5.3, we reach the following expression for the output field in the focal plane of the lens:

$$U_2(x,y) = \frac{e^{ik(d+f)}}{i\lambda f} exp\left[\frac{ik(1-\frac{d}{f}(x^2+y^2)}{2f}\right] \iint_{\Sigma} U_1(\xi,\eta) e^{\frac{2\pi i}{\lambda f}(x\xi+y\eta)} d\xi d\eta \tag{5.6}$$

The last integral corresponds again to taking the 2D Fourier transform of the input field U_1. Thus, the amplitude and phase of the light at coordinates (*x,y*) are directly related to the amplitude and phase of the input spatial spectrum, this time calculated at the spatial frequencies $\left(\frac{x}{\lambda f}, \frac{y}{\lambda f}\right)$. We can now make some considerations:

- for the special case $d = f$ the quadratic phase factor preceding the integral vanishes (i.e., the phase curvature disappears), thus leaving in the focal plane of the lens exactly the Fourier transform of the input field. This is the well-known $f - f$ configuration. However, if we only probe the center of the output distribution ($x = y = 0$) this phase factor is irrelevant for any value of *d*.
- the role of the lens is essentially to "collect energy". The intensity of the far-field distribution after free-space propagation decreases as $1/z^2$, while the intensity in the focal plane of the lens is fixed by the focal length as $1/f^2$.

We can finally analyze the situation in which the Fresnel approximation (Eq. 5.3) does not hold true. We can start again considering the general expression in Eq. (5.2) and write explicitly the various terms in order to find the electric field U_2 at the coordinate ($x = y = 0$):

$$r = \sqrt{z^2 + \xi^2 + \eta^2}$$
$$\cos\theta = \frac{z}{r} \tag{5.7}$$

substituting into Eq. (5.2), we get:

$$U_2(0,0,z,\omega) = \frac{z}{i\lambda} \iint_{\Sigma} U_1(\xi,\eta) \frac{\exp\left(ik\sqrt{z^2 + \xi^2 + \eta^2}\right)}{|z^2 + \xi^2 + \eta^2|} d\xi d\eta \tag{5.8}$$

as usual, $U_1(\xi,\eta) = T(\xi,\eta,\omega)P(\xi,\eta)E(\omega)$ (where we dropped the n index for the pattern P). So far, we have assumed real-value patterns (i.e., amplitude modulation). However, since the output electric field quantity recorded via coherent detection (e.g., electro-optic sampling) is intrinsically a complex quantity (i.e., amplitude and phase), we can also drop the assumption that the patterns must be real-value qualities: they can have both amplitude $p(\xi,\eta)$ and phase $\phi(\xi,\eta)$, so that we can write more generally $\tilde{P}(\xi,\eta) = p(\xi,\eta)\exp[i\phi(\xi,\eta)]$. Therefore, the term in the integral can be written as:

$$U_2(0,0,z,\omega) = \frac{z}{i\lambda} E(\omega) \iint_{\Sigma} \tilde{P}(\xi,\eta) T(\xi,\eta,\omega) \frac{\exp\left(ik\sqrt{z^2 + \xi^2 + \eta^2}\right)}{|z^2 + \xi^2 + \eta^2|} d\xi d\eta \tag{5.9}$$

In the end, SPI works even in the most general case of the Huygens principle. Somehow, it is actually the commonly-unwanted diffraction that enables the correct functioning of the technique under the appropriate point detection conditions. However, if the Fraunhofer conditions are not met, the inverse problem of Eq. (5.1) is not as straightforward to solve because of the presence of the extra diffractive term (Eqs. (5.8) and (5.9)), which needs to be accounted for.

5.2.2 Theoretical investigation of patterned beam free-space propagation

In the experimental system we have arranged, the THz pulse is focused on the detection crystal with the goal of improving the SNR by spatially concentrating most of the energy, and the detection occurs at the Fourier plane of the focusing element. In traditional TDS setups, the optical probe pulse is typically focused too (diameter of tens of microns), so to increase the modulation induced by the THz pulse, and therefore probes only the zero-frequency (DC-element) of the 2D spatial Fourier transformation performed by the focusing element. In the case of a THz-TDS using a time-to-space mapping technique, the probe is instead an image of the pulse on the grating plane, and thus much larger (in our configuration, the calculated diameter is ~1 mm). The probe energy is not integrated, but different spatial points along the probe pulse front sample variable time portions of the THz pulse. It is thus crucial to make sure that the probe and THz beam have appropriate matching sizes and spatially overlap at the detection crystal position. Separate spatial points of the readout beam should all sample the DC-element of the THz, so that their outputs can be consistently used to retrieve the temporal waveform.

We performed simulations of the pattern propagation from the pattern generation plane to the detection crystal plane, also considering the OAP mirror employed to focus the THz beam. The simulations are based on the Rayleigh-Sommerfeld diffraction solution (Goodman, 1996), introduced in Section 5.2.1. Eq. (5.2) can be rewritten as a convolution integral:

$$U_2(x,y) = \iint_{\Sigma} U_1(\xi,\eta) h(x-\xi, y-\eta) d\xi d\eta \tag{5.10}$$

by considering $\cos\theta = 1$, and the Impulse Response $h = \frac{z}{i\lambda} \frac{\exp{(ikr_{12})}}{r_{12}}$, with $r_{12} = \sqrt{z^2 + (x-\xi)^2 + (y-\eta)^2}$. Eq. (5.10) can be evaluated thanks to the Fourier convolution theorem (Voelz, 2011):

$$U_2(x,y) = \mathcal{F}^{-1}\{\mathcal{F}\{U_1(x,y)\mathcal{F}\{h(x,y)\}\} = \mathcal{F}^{-1}\{\mathcal{F}\{U_1(x,y)\}H(f_x,f_y)\} \tag{5.11}$$

Where $H(\nu_x,\nu_y) = \exp\left[ikz\sqrt{1-(\lambda\nu_x)^2-(\lambda\nu_y)^2}\right]$ is the Transfer Function, and (ν_x,ν_y) are the variables in the Fourier space. The only requirement for the use of this solution is that we limit the analysis to scalar diffraction and that $r \gg \lambda$ (Voelz, 2011). This transfer function is used to simulate the free-space propagation of the beam from the sample to the OAP. Afterwards, we approximated such OAP as a thin lens and simulated the formation of a diffraction pattern at the focal plane. We considered U_2 as the beam impinging on the lens, and using Eq. 5.6, with $d = 0$, we extract the focal plane distribution U_3:

$$U_3(x',y') = \frac{e^{ikf}}{i\lambda f} \exp\left[\frac{ik(x'^2+y'^2)}{2f}\right] \iint_{\Sigma} U_2(x,y)P(x,y)e^{-\frac{2\pi i}{\lambda f}(xx'+yy')}dxdy \tag{5.12}$$

Where $P(x, y)$ is the pupil function of the lens, and (x', y') the variables in the focal plane.

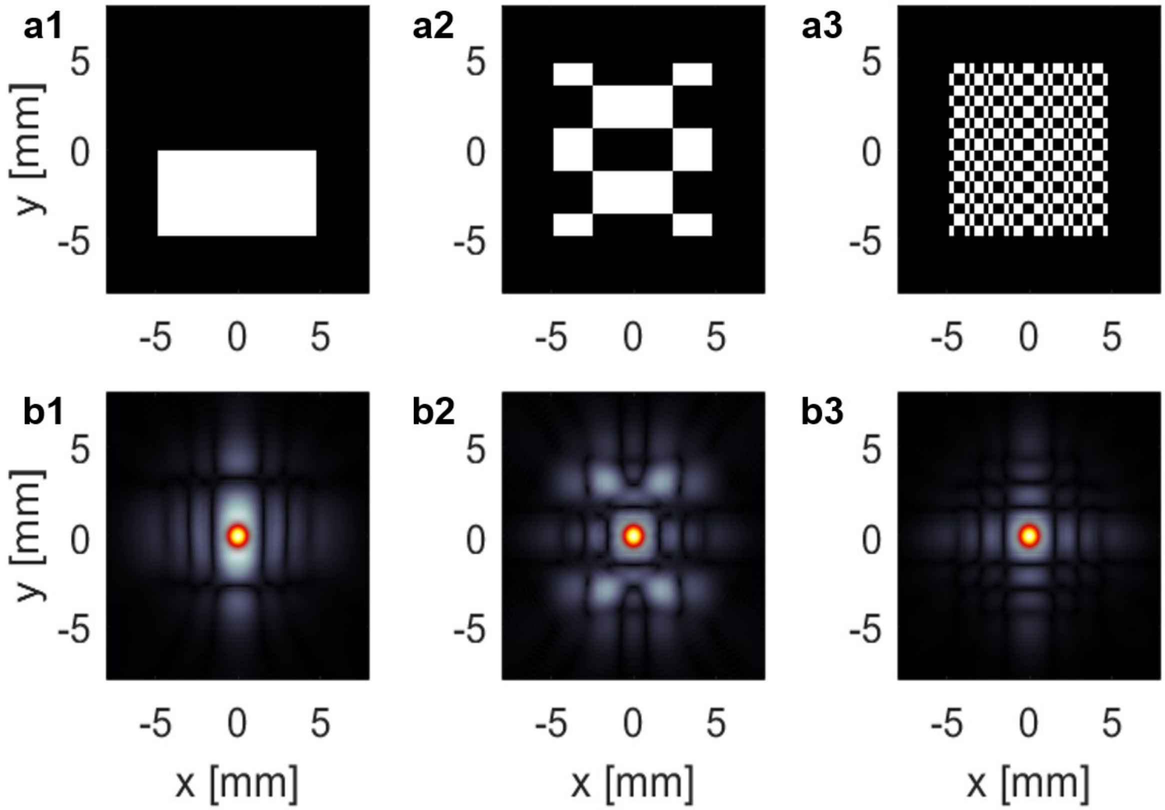

Figure 5.5 | Numerical simulations of pattern propagation. (a1,a2,a3) Examples of three 32 × 32 Hadamard patterns at the object plane. (b1,b2,b3) the corresponding series of diffracted patterns at the detection plane, after free propagation (~**20** cm, as in our experimental conditions), and focusing by an OAP mirror (diameter = 2", focal length = 2"). The central red spot shown in the bottom row images correspond to the-probe beam size. The simulations were carried out with Matlab©.

Examples of some patterns are shown in Fig. 5.5(a1-a3), along with their relative spatial shape at the detection crystal position in Fig. 5.5(b1-b3). As it can be seen from these latter, as well as from the 1D profiles shown in Fig. 5.6, the central spot of the propagated patterns (the DC-component) has a lateral size $\geq$ 1 mm thus larger than the size of the probe at the detection crystal, for our experimental configuration. In these conditions, we are assured that every point along the probe pulse front interrogates the THz beam within its DC-component. In this way, the SPI conditions described in Section 3.1.1 are met, enabling the image reconstruction.

5.2.3 Experimental setup

The setup used for the time-to-space mapping experiments is shown in Fig. 5.7(a). As one can see, the setup is similar to that employed in the experiments presented in the previous sections (see Section 4.2.1), but it features different elements. The first difference lies in the laser source employed,

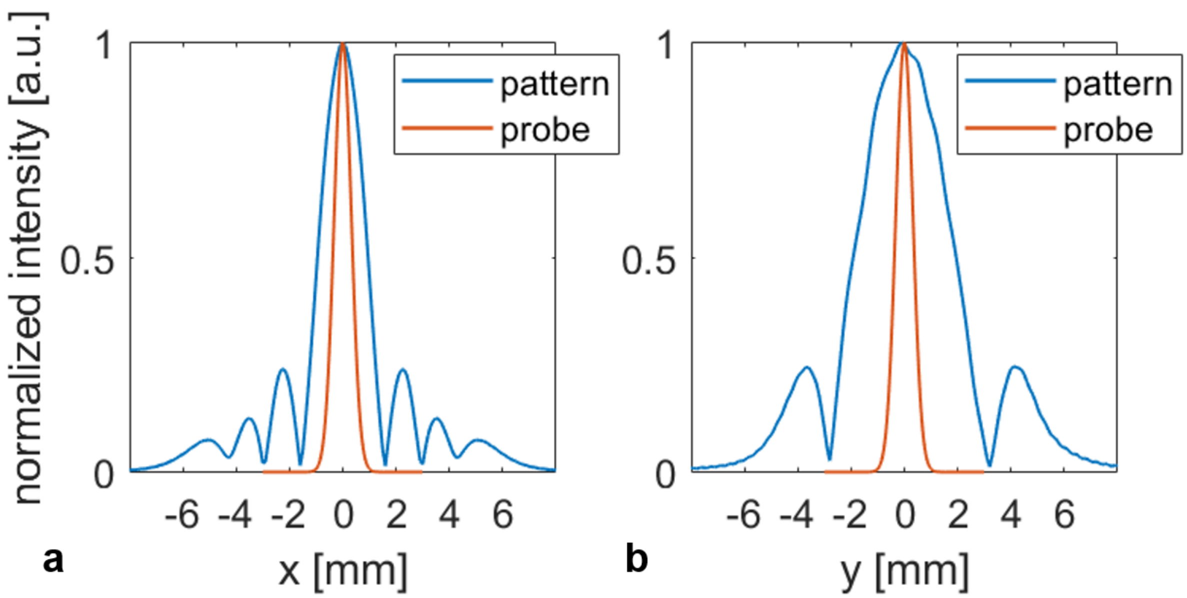

Figure 5.6 | 1D profiles of the diffracted pattern. Same pattern as in Fig. 5.5(b1) (blue) and probe beam (orange), at the detection crystal. (a) x-direction profile. (b) y-direction profile.

an amplified Yb laser (1030 nm, 170 fs pulse duration, 1 mJ at 250 Hz repetition rate). Again, the beam is split into three beams (pump, probe, pattern beams), first by means of a 4:96 wedge window and then via a 50:50 beam splitter on the 96% path side. The pump beam generates the THz pulses via OR in a 300-μm-thick HMQ-TMS organic crystal, which can be pumped collinearly using radiation at around 1 μm. After some magnifying optical elements, the THz beam propagates through a 125-μm-thick Ge plate (undoped, resistivity > 40 Ωcm) used for spatial modulation, and eventually passes through the sample (with a 10 mm × 10 mm size). Finally, free-space EOS is carried out via a 3-mm-thick GaP crystal, where the THz and probe beams are spatially overlapped. The pattern generation is realized using the photo-modulation technique described in Section 4.2.2, by employing a DMD and a Ge plate in place of a Si one, in order to maximize the carrier generation at the laser source wavelength. As mentioned in section 4.2.2, the Si plate had to be replaced with a Ge one, because the photon energy at the wavelength of the laser source (1.2 eV, 1030 nm) is barely sufficient to overcome the Si bandgap (1.1 eV) and thus does not generate enough free carriers, while can easily do so in the case of Ge (0.66 eV). The modulation depth achieved in this case was around 95% (peak amplitude of the THz pulse).

To implement the time-to-space SSD scheme described above, a reflection grating (1200 grooves/mm) is placed along the probe beam path, followed by a 4-f system (50 cm and 10 cm focal lengths). As a result of this, the probe beam incident on the EO detection crystal exhibits a reduced size (~1 mm in diameter, $1/e^2$), because of the 1/5 demagnification factor introduced by the 4-f

system, and a tilted wave front (tilt angle of 81°), because of the angular dispersion induced by the reflection grating. After probing the THz pulse, the probe beam is magnified by a second 4-f system (5 and 50 cm focal lengths, i.e., 10× magnification factor), propagates through a linear polarizer (part of the near-zero transmission detection scheme) and finally reaches the recording InGaAs camera (Xeva 320 Series, Xenics). The spatial probe pulse front is thus imaged by the camera and its intensity variations reveal the THz waveform temporal shape. An example of images taken by the camera, with and without THz modulation, are shown in Fig. 5.7(b,c). The image of the THz-modulated probe (Fig. 5.7(b)) clearly exhibits vertical stripes which correspond to the temporal oscillations of the THz pulse, sampled by different spatial portions of the probe when they overlap on the detection crystal. The image without THz in Fig. 5.7(c) simply shows the probe beam profile and it is used as a background. The THz waveform is extracted by first subtracting the image of the background probe from the one modulated by the THz, and then dividing by the background: $\Gamma = (I_{THz} - I_{bg})/I_{bg}$ (Fig 5.7(d)). We divide the signal by the background after subtraction in order to properly account for the spatial shape of the probe pulse.

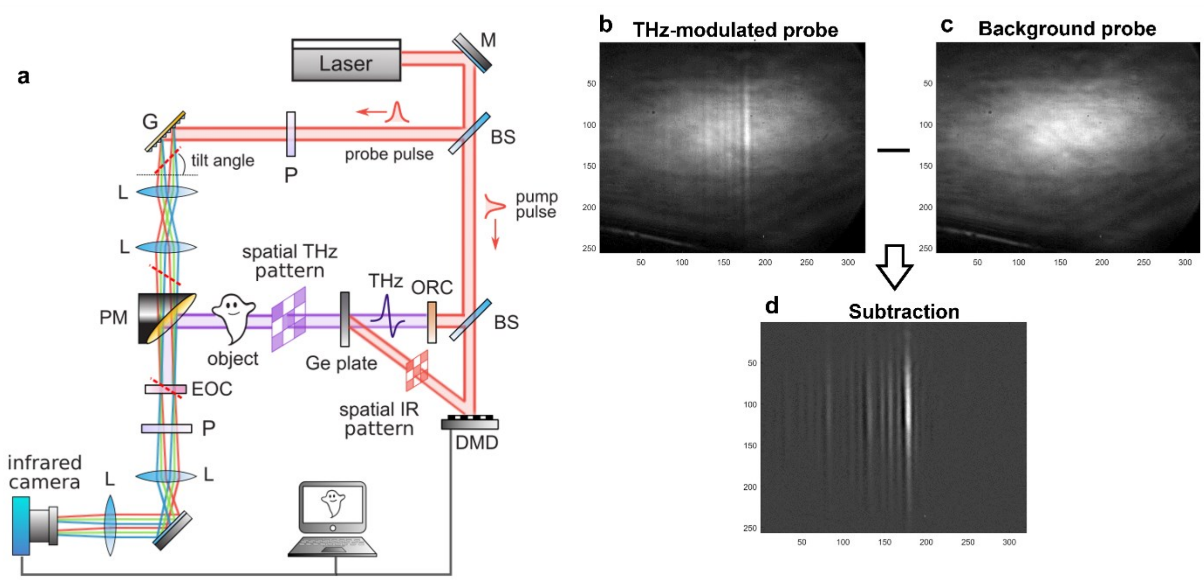

Figure 5.7 | The time-to-space imaging setup. (a) Schematic of the experimental setup: SPI-based THz-TDS, with time-to-space mapping. The laser beam is split into two lines (pump and probe) using a beam splitter (BS). The pump pulse is split again: one line generates THz radiation via optical rectification in an organic crystal (ORC, HMQ-TMS), the other is spatially modulated using a DMD, and then employed for THz modulation in a Ge wafer; the patterned THz beam interrogates the sample and then reaches the detection crystal (EOC2, GaP). The probe line goes through a polarizer (P) and then hits a grating (G), which tilts the pulse front; two lenses (L) form a 4-f system that images the probe beam onto the detection crystal (EOC, GaP). After detection, a second 4-f system takes the THz-modulated probe pulse to the recording camera (InGaAs), after it has propagated through a polarizer (P). (b) Probe pulse acquired by the camera after it has been modulated by the THz pulse. (c) Background probe when THz is not present. (d) Subtraction (normalized) of (c) from (b), resulting in the actual THz waveform.

By considering the parameters of the employed grating (i.e., 1200 lines/mm) and an incident angle of 72° (diffracted angle 16°), the expected available time window provided by the probe is ~19 ps (calculated by using Eq. (3.8)). The effective time window extracted for our experimental system and available for the measurements was ~15 ps, narrower than the expected one since the extremities of the probe spatial profile are not intense enough to be used. Such temporal window was sufficiently wide to acquire the THz pulse replicas transmitted through the multilayered samples we employed, each of them typically separated by a ~1.8 ps delay. We temporally calibrated our system using a mechanical delay line, to change the probe optical path and check the corresponding shift of the temporal position of the THz pulse peak on the camera (Fig. 5.8(a)). The temporal resolution obtained in our experimental conditions was 68.7 fs/pixel. This resolution is clearly much better than that provided by the time-to-frequency mapping (which we recall here was 670 fs), as is the overall time window available for the measurement (15 ps vs 3 ps). Finally, it is also worth underlining that we can exploit the 2D geometry of the camera sensor to increase the SNR of the measurement. The temporal information regarding the THz waveform is captured along the *X*-axis of the camera, while the series of rows along the *Y*-axis of the camera are simply replicas of the same THz pulse. As a consequence, by integrating the THz pulse along the *Y*-axis, it is possible to increase the SNR (from ~140 to ~200 in our measurements, with SNR defined as the ratio of the THz peak electric field and the standard deviation of the electric field measured before the arrival of the THz pulse). In Fig. 5.8(b) we report the rectangular area of the camera sensor used for the integration (80 lines, hence 2.4 mm considering the size of the camera pixel of 30 μm), and the waveform obtained after integration (the waveform is already temporally calibrated using the fit in Fig. 5.8(a)).

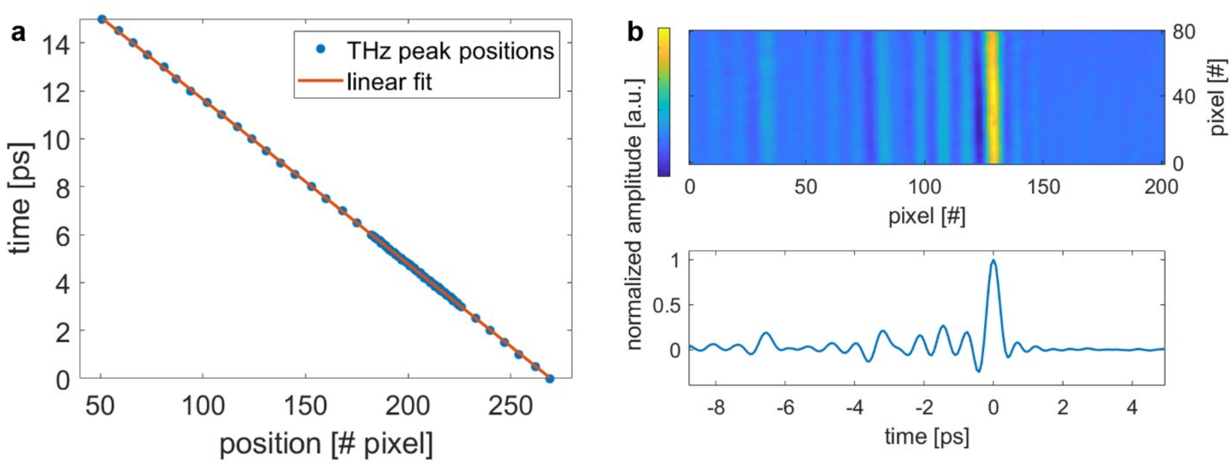

Figure 5.8 | Time-to-space THz waveform reconstruction. (a) Time vs space (pixel) calibration: the value obtained from the linear fit is 68.7 fs/pixel. (b) THz waveform reconstruction. (top) Portion of the area extracted from the images recorded by the camera and corrected by subtracting and dividing the modulated probe by the background; (bottom) THz waveform reconstructed by integrating along the columns of the image above.

Furthermore, in Fig. 5.9(a) we show the comparison between a THz waveform measured using the traditional EOS acquisition scheme (featuring two balanced photodiodes (PDs), and a delay line to sample the time-domain (see Section 2.2.2)) and the SSD technique based on the time-to-space mapping. We can see that this latter (red line) reasonably reproduces the main oscillations recorded in the former (blue line). There are deviations, mostly in the negative lobes, where the oscillations displayed by the SSD-reconstructed trace are typically smaller than those captured with the standard technique. Such deviations are ascribed to the fact that the modulation of the probe pulse recorded using the near-zero transmission scheme (described in Section 3.3.4) have a quadratic relation to the THz amplitude, as opposed to the linear one found for the standard technique. Such distortions can be accounted for and corrected (Kawada et al., 2011). In our measurements, though, we were mostly interested in the values of the peak amplitude of the THz pulses, as well as the time delays between different pulses, and these quantities are hardly affected by such deviations, so we could safely disregard them. Finally, in Fig. 5.9(b) we display a comparison between three waveforms recorded with the SSD method under variable modulating optical light intensity. When there is no illumination, the THz is maximally transmitted (blue line). With maximum illumination on the Ge plate, the transmission drops to $\sim 5\%$ (peak amplitude, red line). The yellow line shows instead a typical THz waveform under illumination with a typical Hadamard pattern covering 50% of the area.

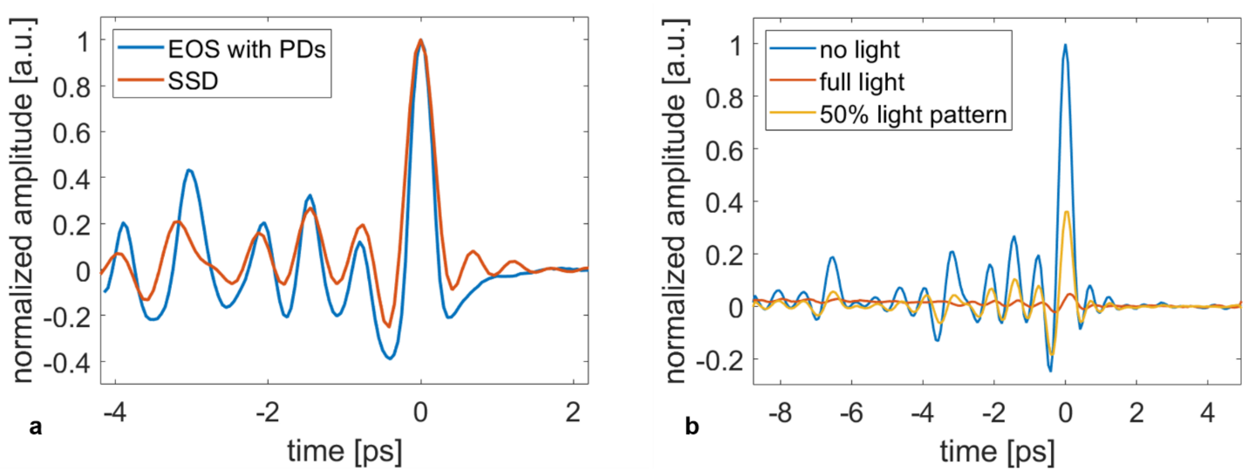

Figure 5.9 | Time-to-space waveform reconstruction. (a) THz waveforms measured in the time-domain, using the standard EOS acquisition arrangement with balanced photodiodes (PDs) (blue line), and the time-to-space SSD technique (red line). (b) Examples of THz waveforms under different levels of IR modulating illumination on the Ge plate (blue, no IR light – red, window fully illuminated – yellow, 50% illuminating pattern.

5.2.4 Test-bed samples

We employed two samples made of high-density polyethylene (HDPE), which has a refractive index of 1.54 and negligible absorption ($\alpha \leq 1$ cm^{-1}) @ 0.5-2.5 THz (Naftaly & Miles, 2007). Sample (1) (Fig.

(5.10(a)) has the letters T-H-Z engraved, with three different thicknesses (T – 1 mm, H and Z – 2 mm, outside area – 3 mm), while sample (2) (Fig. 5.10(b)) the letters I-N-R-S, again with three different levels (I and N – in air, R and S – 1 mm, outside area – 2 mm). The samples were again fabricated by CNC machining (Hubs.com). We chose to investigate these two samples made with the same material as a way to compare the performances of the technique with objects exhibiting different spatial features. For example, the "THz" sample has mostly vertical and horizontal edges, and only slanted ones in the "Z" letter, while the "INRS" sample has a richer set of features, including curves along the "R" and "S". Moreover, the latter sample features some in-air portions, which lack two material interfaces, thus increasing the expected transmission.

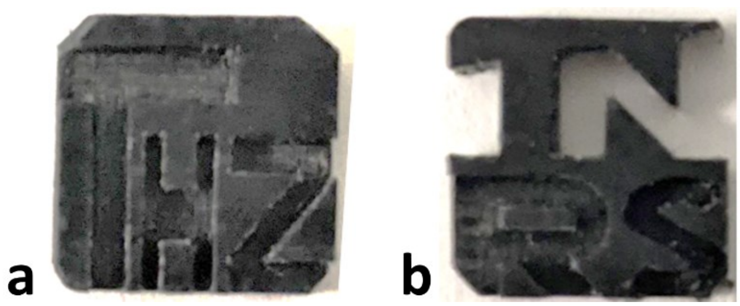

Figure 5.10 | Test-bed samples. (a) Sample (1), high-density polyethylene (HDPE) with T-H-Z letters engraved. The letters have three different thicknesses: T – 1 mm, H and Z – 2 mm, outside area – 3 mm. (b) Sample (2), HDPE with I-N-R-S letters engraved. The letters have three different thicknesses: I, N – in-air, R, S – 1 mm, outside area – 2 mm.

5.2.5 Experimental results

Here we present the results obtained by combining the SSD time-to-space mapping and the SPI techniques by means of the experimental setup shown in Fig. 5.7(a). The raw data are the THz waveforms reconstructed in the time-domain, for each image pixel, as described in Section 4.2. We display images of the two samples, employing different contrast methods, to prove the versatility of this imaging technique in reconstructing multidimensional images, of interest for THz technologies applications.

Fixed-time amplitude images

We first reconstructed images considering the THz field amplitude at various fixed time positions. In Figs. 5.11 and 5.12, we see 16 × 16 and 32 × 32 images, obtained respectively for the sample (1) and (2). The contrast is provided as the normalized field amplitude, extracted from the temporal waveforms retrieved at each pixel position through the SPI inversion. Each of the frames displayed in Fig. 5.11(a,b) and 5.12(a,b) exhibits the amplitude at fixed temporal positions along the waveforms, which correspond to the peaks of the THz pulse replicas, as shown in Fig. 5.11(c) and 5.12(c). These latter report the THz waveforms recorded while the first pattern of the Hadamard series was illuminating the sample (i.e., the pattern where THz radiation was transmitted everywhere). Analogous reconstructions can be carried out for every position within the temporal window: we chose to present the peaks here because they clearly show the characteristics of each of the three layers featured in the two samples.

As we can see, the images featuring 16 × 16 pixels (Fig. 5.11(a) and 5.12(a)) fail to capture some of the smaller features of the letters. This is especially true for slanted edges, and even more for those with a curvature as it occurs in the "R" and "S" of Fig. 5.12(a). The reason is obviously the low

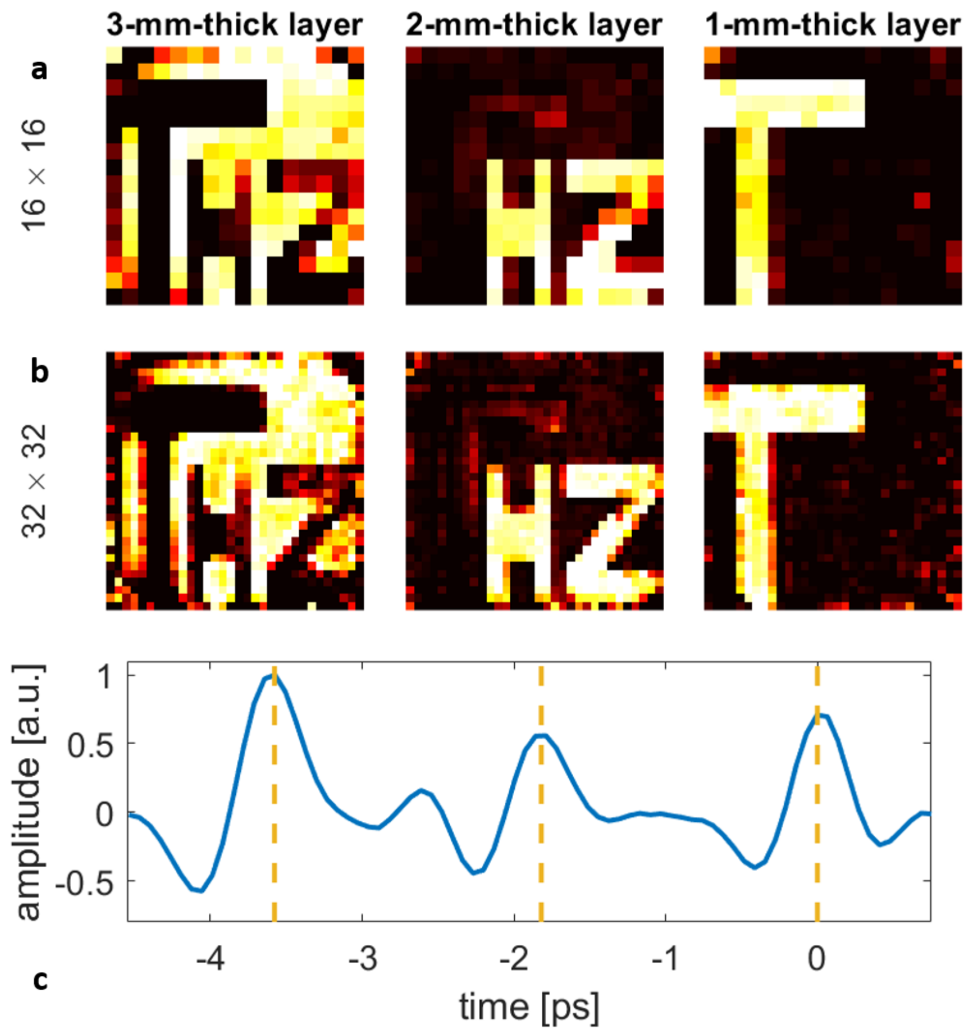

Figure 5.11 | Fixed-time amplitude imaging. (a) 16 × 16 images and (b) 32 × 32 images of sample (1), reconstructed considering the electric field amplitude at the time positions corresponding to the three different peaks of the THz waveform (c).

resolution of these images (pixel size 625 μm). The 32 × 32 pixels images in Fig. 5.11(b) and 5.12(b) exhibit better fidelity, thanks to the higher resolution of 312.5 μm (pixel size). In this case, while the letters are generally better resolved, we see that some pixels along the edges display reduced transmission (for instance along the vertical boundary of the "T" or the "N"). As opposed to the 16 × 16 case, this is probably due to diffraction effects. The pixel size is in this case of the same scale of the central wavelength (300 μm @ 1 THz), which means that while the patterns propagate through the Ge layer and the (optically thick) sample, they undergo diffraction modifications, which result in a less accurate sampling of the letter boundaries. The Rayleigh range can give us an estimation of the distance after which the diffraction effects become significant: for our pixel size, such distance is, $z_R = x_{pix}^2/\lambda \approx 0.3$ mm. One precaution, which helped limit diffraction detrimental effects, was the use of a thin Ge window, thinner than z_R with the sample directly in contact with it.

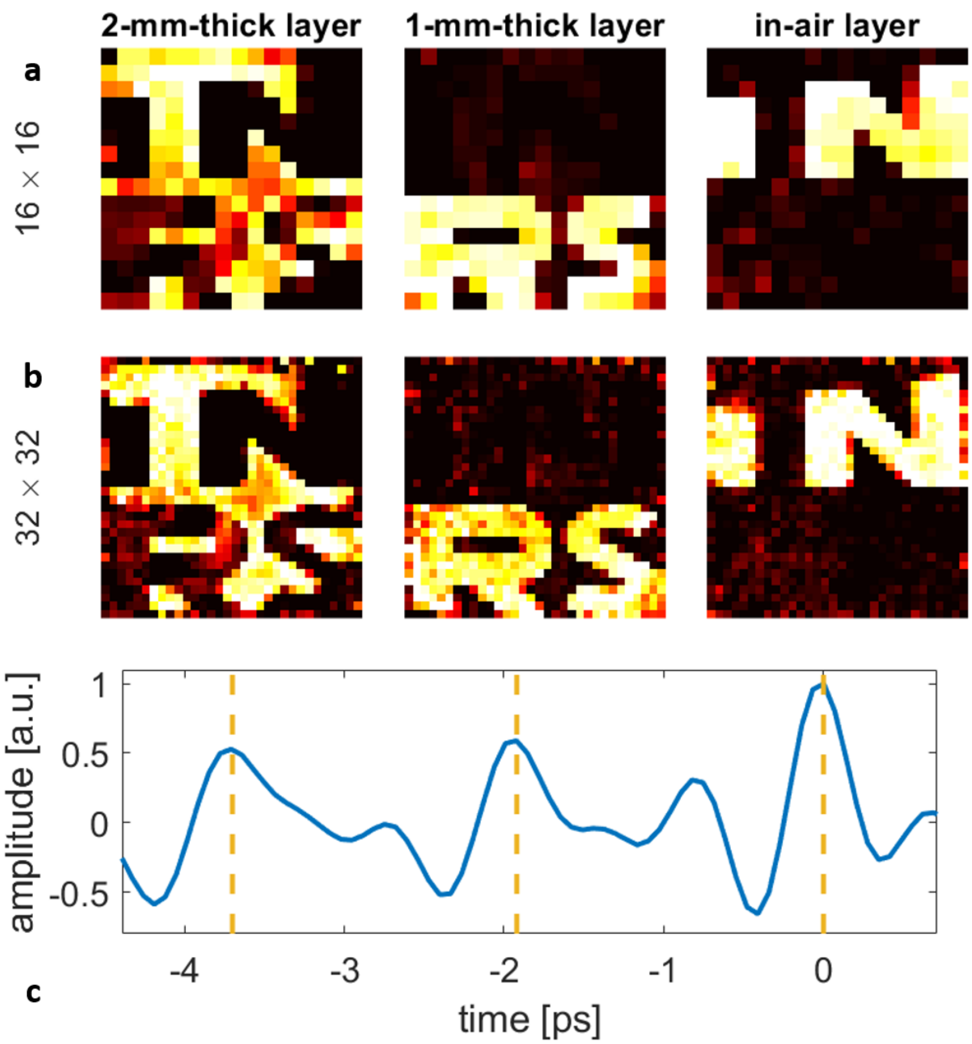

Figure 5.12 | Fixed-time amplitude imaging. (a) 16 × 16 images and (b) 32 × 32 images of sample (2), reconstructed considering the electric field amplitude at the time positions corresponding to the three different peaks of the THz waveform (c).

We simulated the propagation of a patterned THz beam through Ge layers of variable thickness to find a proper compromise for our operating conditions (10 mm × 10 mm window size, with 312.5 µm pixel size). In Fig. 5.13 we display the simulations results for thickness from 50 µm up to 500 µm. As we can see, for a Ge thickness up to 125 µm, the diffraction modifications are negligible. Therefore, we decided to use a 125 µm-thick window, which was cheaper to fabricate and less fragile when compared to even thinner wafers. Evidently, since the samples are optically thick (thickness $\gg \lambda$), the propagation of the patterned beam through them can itself result in the degradation of the pattern's shape with consequent detrimental results in the reconstruction. The fact that the reconstruction does not seem to be strongly affected by this is probably to be ascribed to the extent of the typical features of the samples, which are generally bigger than the image pixel's size. This means that most of the information is captured by patterns with bigger features, which are less subject to detrimental diffraction effects.

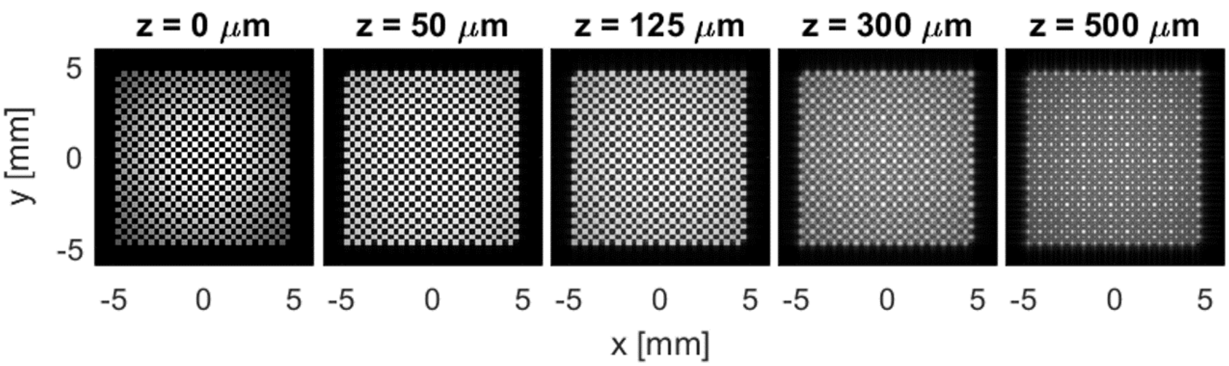

Figure 5.13 | Pattern propagation through a Ge wafer. Evolution of a 32 × 32 pattern propagating through a wafer made of Ge. Up to 125 µm, the pattern is almost identical to the one at the generation plane (z = 0). Beyond 300 µm, diffraction effects start to become relevant.

Compressed sensing reconstruction

The same images displayed above are also reproduced through the application of a standard CS algorithm. As mentioned earlier, this enables reconstructing the images using a number of patterns smaller than the number of pixels (1024 for the 32 × 32 images). The algorithm is a simple non-iterative one, which requires a minimum computational power (Bian et al., 2018). This type of algorithms works optimally in combination with a series of patterns ordered with incremental spatial frequencies, as it happens for the CC ordering of the Hadamard patterns applied for these measurements (W.-K. Yu, 2019).

As shown in Fig. 5.14, even with only 25% of the patterns (compression ratio, CR = number of patterns used/number of pixels), it is still possible to retrieve a good approximation of the spatial features of the three layers. On the other hand, we see that if the compressing ratio is reduced down to 10%, then in the reconstruction the letters “H” and “Z” start getting blurred, especially along the Z slanted profiles. Interestingly, we can barely notice any difference between the reconstructions with CR = 100% and those with CR = 65%, showing how a large subset of patterns (at least 35% of them) does not add key information to the reconstruction, proving the effectiveness of Hadamard masks in sampling sparse images.

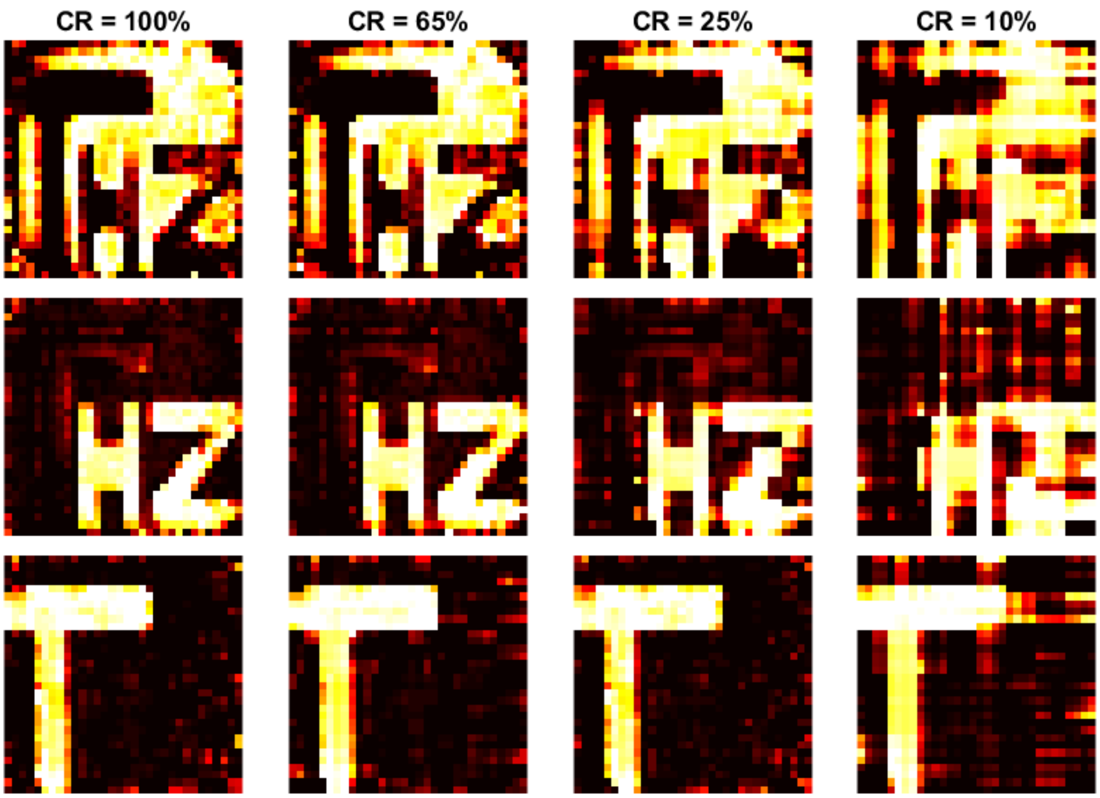

Figure 5.14 | CS imaging. 32 × 32 images of sample (1) reconstructed considering the amplitude at different time positions (as in fig. 5.11), and with a decreasing compressive ratio (CR) (from left to right), 100% - 65% - 25% - 10%.

Better compression ratios could be potentially achieved by using different pattern sets (Z. Zhang et al., 2017) or more advanced reconstruction algorithms (Bian et al., 2018). These solutions have been proved to be effective at optical frequencies but are not always straightforward to implement in the THz range, due to the limitations posed by the photo-modulation technique, for instance considering the complexity in generating non-binary patterns. Innovative methods for THz modulation, potentially more flexible, have been introduced in recent years (W. Li et al., 2022; Watts et al., 2014). These methods are still in their infancy, and need further development to become widespread, but could represent viable solutions in the future.

Time-of-flight images

The other contrast method we applied in the image reconstruction was based on a TOF approach, as described in Section 2.3.2. In this way, we obtained images where the pixel color is related to the time delay experienced by the THz pulse while propagating through a specific spatial position of the sample. With the knowledge of the HDPE group refractive index, it is possible to extract the relative thicknesses of the different layers from the delays between the different THz pulse replicas. Our samples were designed with a relative difference in thickness, between each layer, of 1 mm. Considering the group refractive index of HDPE (n = 1.54), such thickness, d, leads to an expected delay of $\Delta t = d(n-1)/c = 1.8$ ps, between each layer.

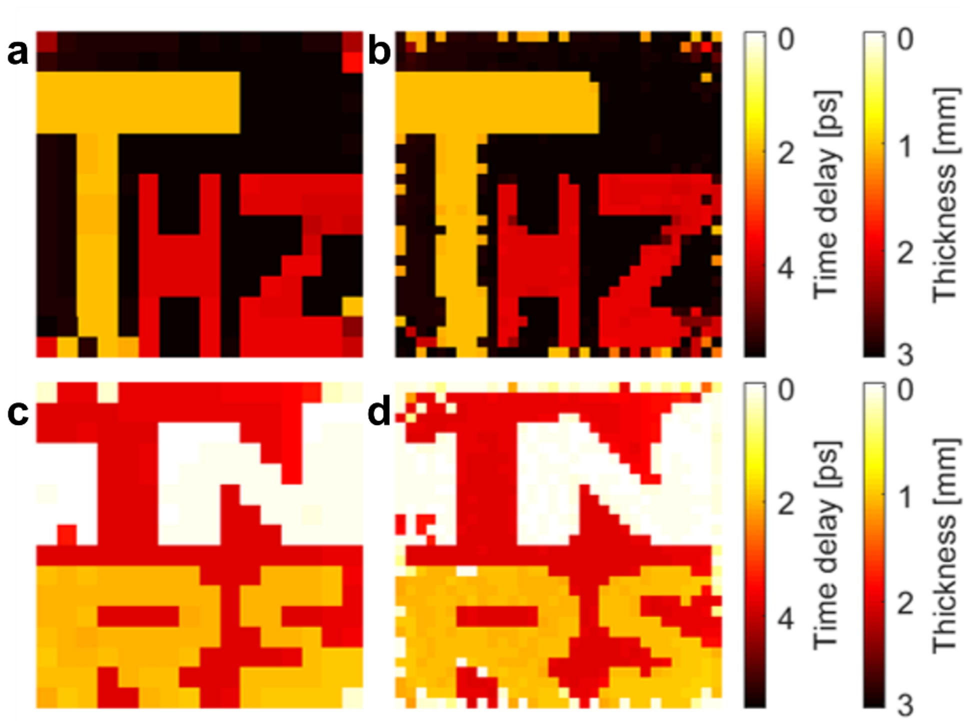

Figure 5.15 | TOF imaging. (top) sample (1); (a) 16 × 16 and (b) 32 × 32 pixels images reconstructed considering the delay between the time position of the THz pulse in air and the pulses retrieved at each pixel position. (bottom) sample (2); (c) 16 × 16 and (d) 32 × 32 pixels images reconstructed considering the delay between the time position of the THz pulse in air and the pulses retrieved at each pixel position.

In Fig. 5.15, we present both 16 × 16 and 32 × 32 images. The TOF reconstruction of 16 × 16 images is accurate and allows to discern the letters at each layer, although the limited resolution (625 μm) does not enable to properly resolve some of the smallest features at the edges, which is more evident for the letter "Z" in the first sample (Fig. 5.15(a)) and the letters "R" and "S" in the second sample (Fig. 5.15(c)). In the 32 × 32 images (Fig. 5.15(b,d)), we can once again observe that the increased spatial resolution allows to better show the smallest spatial features in the sample, thus enhancing the reconstruction fidelity. On the other hand, we notice that some of the pixels, especially those located at the edges of the letters, or at the borders of the sample, fail to represent the proper time delay. This may be ascribed once again to diffraction effects. Furthermore, we note once again that the time delay is calculated as the retardation between the THz peak, reconstructed at each pixel, and a reference pulse. The algorithm locates the maximum of the amplitude within the temporal window and uses its position to extract the delay. At the edges of the letters and at the external rim of the samples, some pixels can happen to be partially within areas with different thickness, which results in the waveforms corresponding to those pixels having multiple pulses. The algorithm chooses the higher one, which can happen to be the first or the second (probably due to noise fluctuations), leading to alternate colors, for example along the vertical border of the “T” in Fig. 5.15(b).

5.2.6 Discussion and conclusions

We can make some final considerations regarding the acquisition time for our system, and specifically compare its performance to that of the setup presented in chapter 4. By employing the combination of SSD and SPI techniques, the acquisition of a 32 × 32 image (i.e., 1024 patterns) still required a relatively long time (~40 min), mainly due to the need of a relatively long average for each frame captured by the camera (0.5 sec) and the acquisition of multiple (5) frames for each pattern, in order to achieve a sufficiently high SNR level (in our experiments ~200 for the THz waveforms acquired for each pattern). Nevertheless, we note that, by employing a system with a mechanical delay line, acquiring the same image (i.e., same number of patterns and temporal window, as well as comparable SNR) would have required ~40 hours. Therefore, this represents already a dramatic improvement between the two configurations, clearly showing the superiority of the SSD+SPI methodology. Furthermore, a key bottleneck constraining a further speeding up of the process is the limited repetition rate of our THz source (i.e., 250 Hz). The only other two elements that can potentially limit the acquisition speed in the system are the DMD, the refreshing rate of which can go up to 2 kHz (and in newer systems can also reach 20 kHz), and the camera, which could in principle acquire images at 1000 fps. With laser systems operating at repetition rates in the MHz range, and photoconductive antennas (PCA) for THz generation, the same SNR could be obtained by capturing ms-long frames, thus potentially bringing the acquisition time of the whole image down to few seconds. Moreover, the application of CS algorithms can further reduce such time, by limiting the number of patterns to a small fraction of the full set.

In conclusion, in the second part of this project, we have studied a configuration for multidimensional THz imaging, which combines the SPI scheme with an SSD technique. We implemented and tested both time-to-frequency and time-to-space detection configurations, and we proved the superiority of the latter in terms of achievable temporal resolution, width of temporal window, and ultimately accuracy in the THz pulse waveform reconstruction. We then demonstrated how the THz single-point coherent detection can consistently be used in combination with the time-to-space mapping (by properly leveraging diffraction), to enable the retrieval of multidimensional images, combining the extraction of the 2D space distribution of the object, with time/phase information. This implementation enables to achieve fast imaging without the need for complex electronics and any mechanical moving part, without information loss with respect to a traditional THz-TDS system. Because of this, it could represent an appealing solution for the future generation of THz imagers, targeting a variety of real-world applications.

6 CONCLUSIONS AND PERSPECTIVES

To summarize the results of the research work presented in this thesis, we start by recalling the main requirements that a THz imaging system based on TDS should have. On one side, it is critical to preserve the capability of coherent detection, which is typically provided by the temporal scan of the THz electric field, and makes this spectroscopy technique unique in its ability of material properties extraction (Jepsen et al., 2011). On the other, with THz imaging technologies progressively shifting from laboratory-based systems to commercial products, it is important for a THz imager to be fast, and possibly simple and inexpensive. In this research project, we developed an approach to THz imaging that could be a powerful tool to realize devices combining these two requirements.

- In the first half of the project, we demonstrated how the SPI scheme is an ideal solution to be coupled with TDS-based setups which rely on detectors without spatial resolution. SPI makes it possible to retrieve an image with an under-sampled measurement, while at the same time reconstructing the dataset in the time-domain that enables multidimensional operation. Moreover, an SPI-based system does not rely on mechanical moving parts to scan the sample, making the arrangement much less complex.
- In the second half, we coupled the SPI-based implementation to an SSD technique. This latter addresses the problem of the long temporal scan used to reconstruct the THz waveform in the time-domain, by providing an approach able to capture such waveform at once. The combination of SPI and SSD allows to further reduce the acquisition time, since both the spatial and temporal scans are avoided. Furthermore, the complexity of the imaging system is also greatly reduced, since the only two critical devices needed, beyond the laser source, are an SLM and a standard camera.

While the proof-of-principle experimental system we built does not deliver real-time operation, it addresses key shortcomings of traditional TDS-based THz imaging systems.

In the introduction to this thesis, we have given a perspective on the reasons underlying the interest of the scientific community in developing THz technologies. The potential for the use of THz radiation, for a wide variety of applications, spanning from telecommunications and security to quality control, medical diagnostics and many others, is impressive. The existing challenges are various, but the efforts carried out in the last thirty years have already provided solutions to many of the issues the pioneers of THz research were facing. The development of increasingly more powerful sources and more sensitive detectors brought us to a stage in which we are routinely able to control and utilize THz radiation. Now, the next step has a lot to do with developing THz devices which meet the standards of commercial products to expand their real-world use.

In the case of the SPI-based imaging system presented in this thesis work, we showed how it is possible to build a device that is simple and retain all the main capabilities of THz-TDS. From this point on, the primary research efforts must be directed toward optimizing some aspects which can enable actual fast and possibly cost-effective imaging.

The first is the refinement of the spatial modulation of the THz beam needed to carry out the SPI. One possibility, in this sense, is the amelioration of the semiconductor photo-excitation technique. Innovative approaches such as the one exploiting total internal reflection in the photo-excited semiconductor (X. Liu et al., 2016), could deliver better modulation depths with lower illuminating power. Other examples similarly aiming at improving the modulation efficiency are, for instance, the use of composite materials, like graphene (Z. Chen et al., 2018; Wen et al., 2014) or polymers (B. Zhang et al., 2014) deposited on Si. Beyond this, a lot of work has been put into the development of THz-SLMs, capable of directly modulating a THz beam. These are either based on metamaterials (W. Li et al., 2022; Shi et al., 2015; Watts et al., 2014) or micromirrors (J. Kappa et al., 2019). Clearly, this sort of systems would make the implementation of an SPI-based arrangement much easier, as the THz waves could be modulated in a more flexible and controllable way. Moreover, the availability of these devices would be beneficial beyond the context of THz SPI, as tools to easily manipulate THz light, in ways analogous to what is done in the IR/visible range.

The second critical aspect has to deal with the detection scheme, which should ensure there is no significant loss of the relevant information, compared to traditional systems. In this sense, one important step is the optimization of the way SPI is implemented in the imaging system. This can be done, on the hardware side, by improving the spatial modulation, as discussed above, and on the computational side by testing different, potentially more effective, pattern sets (She et al., 2019), and more advanced CS reconstruction algorithms (Bian et al., 2018). The other key point is the refinement of the scanless detection technique, which we saw is crucial to enable fast acquisition of data readily available for multidimensional imaging. SSD techniques, like those applied in this work, or other methods like the compressed acquisition of the THz waveform presented in (Zhao et al., 2021), are still relatively new. Because of this, it is important to make sure that they deliver a performance (in terms, for instance, of SNR level, spatial resolution, spectral resolution, or other parameters) comparable to traditional systems. Improvements in this sense can be achieved, for instance, by optimizing the synchronization between THz modulator and acquisition device (e.g., camera), and implementing a dynamic subtraction acquisition (to improve the SNR, by acquiring a reference measurement after every THz-modulated one, (Jiang et al., 2000)).

Once such performance requirements are met, the next key step is the coupling of the imaging system with high-repetition-rates laser sources. The use of this type of sources would allow for a substantial reduction in the measurement time, by dramatically increasing the data acquisition rates. Moreover, most of TDS systems are limited to laboratory environments due to their complexity, but with new compact fiber laser sources coupled to PCAs for THz generation, the possibility of building more "portable" devices is becoming more realistic. If a compact imaging system, like the one we presented, could be directly combined with such sources, this would promptly translate into the availability of a THz imager which could be fast, simple and cost-effective. A device of this type could significantly help the ongoing process of taking THz technology out of the labs and toward real-world applications.

SOMMAIRE RÉCAPITULATIF

A. Introduction

A.1. Introduction aux ondes térahertz

La force électromagnétique (EM) est l'interaction sous-jacente à la base de la grande majorité des phénomènes naturels. Cette force peut être décrite en termes de champs EM, qui se propagent à la fois dans l'espace et dans le temps, transférant ainsi de l'énergie et des informations (Maxwell, 1865). Lors de leur propagation, ces champs se comportent comme des ondes oscillantes et l'une de leurs caractéristiques fondamentales est la fréquence, qui donne une information quantitative sur la vitesse à laquelle une onde oscille dans le temps.

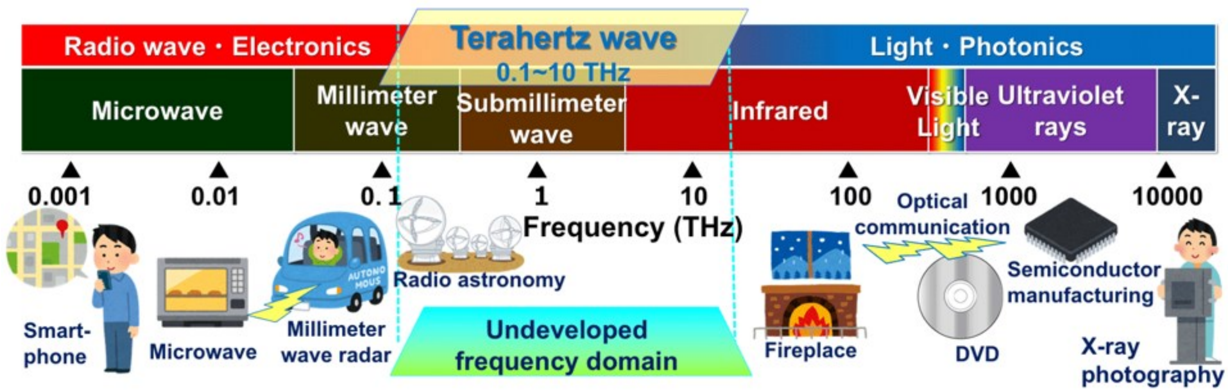

Figure A.1 | La gamme de fréquences THz. *Adaptée de l'Institut national des technologies de l'information et des communications.*

La partie du spectre EM d'intérêt pour cette thèse de doctorat est celle avec des fréquences allant de 0,1 à 10 THz (Fig. A.1), communément appelée « rayonnement térahertz » (THz). Les micro-ondes, lesquelles se trouvent du côté des longueurs d'onde plus longues, peuvent être générées et détectées par des charges oscillantes dans des antennes régulières, tandis que l'infrarouge (IR) et la lumière visible, situés du côté des longueurs d'onde plus courtes sont couramment générées et détectées avec excitation des transitions électroniques (par exemple, dans les semi-conducteurs). L'histoire scientifique du THz est relativement courte, car les technologies efficaces pour générer et détecter ce type de rayonnement ont seulement étés développé à partir des années 80 (Mourou et al., 1981). Ensuite, le développement de systèmes laser capables d'émettre des impulsions ultracourtes à l'échelle de la femtoseconde, menait finalement au développement des premiers dispositifs de spectroscopie THz ultrarapide (Gao et al., 1995).

L'accessibilité de sources et de détecteurs de rayonnement THz a rapidement suscité l'intérêt d'explorer davantage ses propriétés intrigantes et leur potentiel pour des applications pratiques. Par exemple, la plupart des matériaux non conducteurs (tels que les semi-conducteurs, les plastiques et les papiers), ainsi que les liquides non polaires, sont transparents aux ondes THz. Cela les rend utiles, par exemple, pour l'inspection non invasive de systèmes multicomposants (Stoik et al., 2008). De plus, de nombreux gaz (Jacobsen et al., 1996), des composés inorganiques (Grischkowsky et al., 1990) et organiques (Parrott & Zeitler, 2015), ainsi que des molécules biologiques (Baxter & Guglietta, 2011), présentent des excitations collectives (par exemple, des phonons), ou des modes de rotation/vibration aux fréquences THz, qui peuvent être détectés à l'aide de mesures spectroscopiques. Cela permet d'utiliser le THz pour révéler la présence des substances, comme des explosifs (Y. C. Shen et al., 2005). De plus, grâce à la faible énergie de ses photons (~ meV), le rayonnement THz est pratiquement non ionisant, et peut donc être utilisé en toute sécurité sur des échantillons sensibles ou de l'électronique, ainsi que sur le corps humain. L'une des techniques d'analyse les plus puissantes disponibles à ce jour dans cette gamme spectrale est la spectroscopie de domaine temporel THz (THz-TDS). Cette technologie utilise des impulsions THz à large bande générées au moyen d'un système laser au femtoseconde. Le TDS fonctionne comme un système pompe-sonde, où une impulsion laser ultracourte est utilisée comme sonde de déclenchement à retard variable pour échantillonner le champ THz (à son tour généré par une seconde impulsion laser). De cette manière, la forme d'onde THz est reconstruite directement dans le domaine temporel, de sorte que l'amplitude et la phase sont récupérées. Cela signifie finalement que toutes les informations transportées par l'onde THz sont directement disponibles, permettant une caractérisation complète des propriétés optiques de l'objet étudié, par exemple son indice de réfraction complexe (Jepsen et al., 2011).

La combinaison unique des caractéristiques de rayonnement THz fait de l'imagerie l'une des applications les plus attrayantes et les plus explorées (Mittleman, 2018). Comme mentionné ci-dessus, le THz peut facilement traverser de nombreux matériaux diélectriques, permettant de révéler des structures internes avec un bon contraste. Sa longueur d'onde étant de l'ordre des centaines de microns permet également d'atteindre des résolutions d'imagerie relativement élevées (~100 microns). Lorsqu'un système THz-TDS est utilisé pour l'imagerie, ses capacités de caractérisation des matériaux ouvrent la voie à l'imagerie multidimensionnelles. Celle-ci combine la reconstruction de la forme de l'objet avec l'extraction de l'indice de réfraction (Cunningham et al., 2011), la reconnaissance de la présence de substances inconnues (Pohl et al., 2016), ou l'extraction des caractéristiques d'échantillons multicouches (Redo-Sanchez et al., 2016) (Fig. A.2(a)). L'imagerie

THz représente un instrument utile, capable de fournir des informations complémentaires à celles obtenues avec les images micro-ondes, IR-ultraviolet (UV) et rayons X. Parmi les exemples d'applications d'imagerie explorées au cours des dernières années, citons le contrôle de sécurité (H. B. Liu et al., 2007) (Fig. A.2(b)), le contrôle de la qualité et de la sécurité dans l'industrie (Duling & Zimdars, 2009; Jördens & Koch, 2008), l'imagerie biomédicale (Naccache et al., 2017; Q. Sun et al., 2017; X. Yang et al., 2016), ou encore l'imagerie spectrale de peintures et pièces archéologiques (Abraham et al., 2010; Dong et al., 2017; Koch-Dandolo et al., 2016) (Fig. A.2(c)).

Depuis l'article fondateur de Hu et Nuss, en 1995 (Hu & Nuss, 1995), l'intérêt croissant pour le domaine a favorisé le développement d'une grande variété de systèmes d'imagerie THz. De manière générale, on peut les classer en deux catégories : les caméras THz et les techniques basées sur des détecteurs à un pixel. L'avantage évident du premier est la capacité de capturer des images de manière quasi instantanée. La faible énergie des photons THz, cependant, rend la réalisation de capteurs multipixels basés sur des transitions électroniques dans des semi-conducteurs plutôt difficile. Ces exigences posent de sérieuses limitations à la réalisation de ces dispositifs. Jusqu'à présent, les caméras THz sont principalement basées sur des ensembles de détecteurs thermiques (A. W. M. Lee, Williams, et al., 2006; J. Yang et al., 2008b)ou sur des transistors à effet de champ (Al Hadi et al., 2012). Ces types de détecteurs ont une réponse à large bande, mais au prix de n'enregistrer que l'intensité du faisceau THz, sacrifiant l'information temporelle/spectrale. L'autre option implique des systèmes basés sur des détecteurs ponctuels. Ceux-ci sont généralement plus

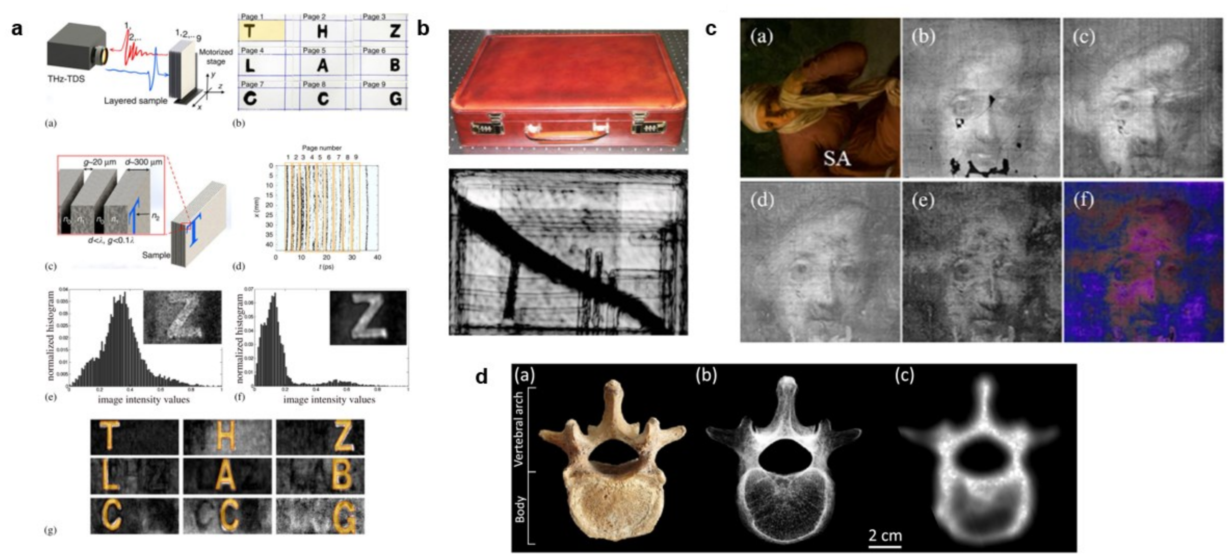

Figure A.2 | Exemples d'applications d'imagerie du rayonnement térahertz. (a) Imagerie par temps de vol d'un échantillon multicouches. *Adaptée de (Redo-Sanchez et al., 2016) sous licence https://creativecommons.org/licenses/* . (b) Contrôle de sécurité d'une valise. *Adaptée de (Liu, et al., 2007) © 2007 IEEE.* (c) Imagerie des couches cachées d'une peinture. *Adaptée avec la permission de (Koch-Dandolo, et al., 2015).* (d) Imagerie d'os humains. *Adaptée avec la permission de (Bessou et al., 2012) © 2015 The Optical Society.*

sensibles et peuvent permettre la détection de l'amplitude complexe des impulsions THz. Un inconvénient majeur est la nécessité typique de balayer spatialement l'objet pixel par pixel pour obtenir l'image, ce qui rend le processus d'acquisition très long. Un temps d'acquisition aussi long est le principal problème qui a entravé l'utilisation généralisée de l'imagerie THz. Au cours des dernières années, de nombreuses recherches ont vu le jour dans le but de surmonter ce goulot d'étranglement technologique, conduisant à une variété de solutions ingénieuses (Guerboukha et al., 2018; Zanotto et al., 2020).

A.2. Rendre l'imagerie térahertz simple et rapide : motivation de ce projet doctoral

Le développement d'un imageur THz fonctionnant en temps réel a été l'un des principaux objectifs depuis le début de la recherche THz (Wu et al., 1996), et ce projet de doctorat fait partie de l'effort général vers cet objectif. Comme mentionné ci-dessus, la plupart des systèmes d'imagerie THz, et en particulier ceux basés sur le TDS, utilisent des détecteurs sans résolution spatiale, c'est-à-dire des détecteurs à un seul pixel. La reconstruction de l'image est donc typiquement réalisée avec un balayage bidimensionnel de l'objet. En plus de prendre beaucoup de temps pour capturer une image (typiquement pas plus de quelques pixels/s), cette procédure nécessite des pièces mobiles mécaniques volumineuses pour déplacer soit l'échantillon, soit le système de détection sur toute la zone d'imagerie. En outre, il existe une autre limitation importante à l'obtention de temps d'acquisition rapides lors de l'utilisation d'un système TDS. La reconstruction de la forme d'onde THz est généralement effectuée en sondant l'amplitude du champ électrique THz à différentes positions le long de la fenêtre temporelle d'intérêt au moyen d'une impulsion ultracourte. Ceci est réalisé en modifiant séquentiellement le temps d'arrivée de l'impulsion de sonde par rapport à l'impulsion THz via une ligne à retard mécanique. Cette dernière est relativement lente (généralement pas plus rapide que quelques balayages/s), entravant davantage la possibilité de fonctionnement en temps réel.

Dans ce travail de thèse, nous avons exploré la possibilité de surmonter le problème de temps d'acquisition chronophage lié à l'utilisation d'un système THz-TDS pour l'imagerie, avec deux approches complémentaires :

- Tout d'abord, nous avons éliminé le besoin du balayage spatial en utilisant un schéma d'imagerie à « pixel unique » (SPI) (Gibson et al., 2020) directement mis en œuvre dans le domaine temporel. Le SPI est un moyen d'obtenir une image en utilisant un détecteur sans résolution spatiale, c'est-à-dire un pixel. La structure spatiale de l'objet étudié est récupérée en le sondant avec une série de motifs lumineux spatiaux et en mesurant les intensités corrélées avec un détecteur à un seul pixel. En plus d'éviter le besoin de pièces mobiles mécaniques volumineuses pour effectuer le balayage spatial, cette configuration d'imagerie permet l'utilisation d'un nombre réduit de motifs (et, par conséquent, de mesures), grâce à la détection compressée (CS). Le CS est une voie pour reconstruire une bonne approximation d'un signal avec moins de mesures que nécessaire avec des schémas d'échantillonnage conventionnels (E.J. Candes & Wakin, 2008), permettant ainsi une acquisition plus rapide. Par conséquent, le SPI est un moyen efficace de réduire le temps d'acquisition en imagerie THz et c'est également l'un des plus explorés (Zanotto et al., 2020).

- Deuxièmement, nous avons mis en place une technique de détection dite « un seul coup » (SSD) pour éviter l'utilisation d'une ligne à retard. Les approches SSD exploitent la possibilité de coder la dimension temporelle de l'impulsion THz dans une dimension spatiale ou spectrale de la sonde et représentent un moyen de capturer l'ensemble de la forme d'onde THz de manière simultanée. Étant donné que l'impulsion de la sonde est généralement à des fréquences visibles/IR, un détecteur multipixels, comme une caméra, peut être utilisé pour récupérer les informations qu'il transporte. Diverses techniques SSD ont étés proposées au fil des ans (Teo et al., 2015). Ils exploitent généralement la nature à large bande de l'impulsion de sonde ultracourte pour coder les informations temporelles dans ses composantes spectrales (Jiang & Zhang, 1998b), ou une inclinaison du front d'impulsion de la sonde elle-même pour utiliser son extension spatiale afin de capturer cette même information temporelle (Kawada et al., 2011). Les techniques fréquence-temps et espace-temps ont été étudiées dans ce projet de doctorat, la dernière étant favorable, car elle ne souffre pas de la dégradation de la résolution temporelle affectant la première.

La combinaison de la configuration SPI et du schéma SSD permet non seulement une réduction significative du temps d'acquisition d'image (plus de 90 fois plus rapide dans nos expériences, par rapport à notre même système fonctionnant dans une configuration TDS standard), mais rend également la configuration d'imagerie beaucoup plus simple, grâce à seule l'utilisation d'un modulateur spatial de lumière (SLM) et d'une caméra. Cet arrangement est une solution prometteuse pour le développement de la prochaine génération d'imageurs multidimensionnels THz rapides, compacts et polyvalents, ciblant une grande variété d'applications scientifiques et industrielles.

B. Imagerie térahertz avec un schéma à « pixel unique »

Dans ce chapitre, les résultats relatifs à la première partie du projet doctoral sont présentés. Ici, l'objectif principal à atteindre était de prouver expérimentalement que l'approche SPI pouvait être appliquée à un système d'imagerie typique basé sur THz-TDS, tout en préservant la capacité de détecter de manière cohérente les impulsions THz, inhérentes au TDS.

B.1. Imagerie avec des détecteurs à un seul pixel

L'idée de capturer une image avec un seul photodétecteur a été démontrée pour la première fois dans le travail intitulé « Dual photography » par Sen et ses collègues (Sen et al., 2005). Dans le schéma d'imagerie proposé, une série de motifs lumineux multipixels est utilisée pour interroger l'objet étudié, tandis qu'un détecteur à un seul pixel enregistre la lumière transmise ou réfléchie. L'idée centrale est de mesurer l'amplitude de la corrélation entre les motifs et la forme de l'objet, qui sera ensuite reflétée dans les lectures du détecteur. Les informations sur la distribution spatiale de l'objet sont intégrées dans la forme des motifs, les lectures du détecteur étant utilisées comme pondérations pour les motifs correspondants dans le processus de reconstruction d'image.

La matrice $n \times n$ qui représente la fonction de transmission (ou réflexion) de l'échantillon, $T(x, y)$, peut être vue comme un vecteur T à n^2 éléments, en plaçant chaque ligne de la matrice l'une à côté de l'autre. La collection de mesures du détecteur correspond à un autre vecteur à n^2 éléments, W. Enfin, la série de n^2 motifs $\{P_i(x,y)\}_{i=1\ldots n^2}$ peut être reformée en n^2 vecteurs de base à n^2 éléments, en concaténant les lignes de chaque motif et en les regroupant dans une matrice $n^2 \times n^2$, $\boldsymbol{P}$. De cette façon, le processus de mesure peut être simplement vu comme une multiplication matrice-vecteur. Ainsi, la connaissance de la matrice $\boldsymbol{P}$ et du vecteur W permet de retrouver la forme de l'objet T, en résolvant un système linéaire d'équations :

$$W = \boldsymbol{P}T \tag{1}$$

Comme mentionné ci-dessus, l'un des avantages de l'imagerie à pixel unique est la possibilité d'appliquer des algorithmes CS. Cela permet une reconstruction beaucoup plus rapide d'un signal en utilisant un ensemble incomplet de mesures (E.J. Candes & Wakin, 2008). Dans le cas particulier du SPI, il s'agit de la possibilité de capter une image en utilisant un nombre de motifs inférieur au nombre de pixels de l'image. En principe, afin d'effectuer l'inversion de matrice de l'Eq. (1), il faut que la dimension du vecteur W soit égale à celle du vecteur T, ce qui revient à effectuer n^2 mesures. Néanmoins, la théorie CS montre que, sous des représentations particulières, il est possible de retrouver la forme de l'objet T avec une bonne approximation en effectuant un nombre m de mesures inférieur au nombre de pixels ($m < n^2$), et en appliquant des algorithmes spécifiques pour exploiter au mieux la « parcimonie » des objets (Duarte et al., 2008).

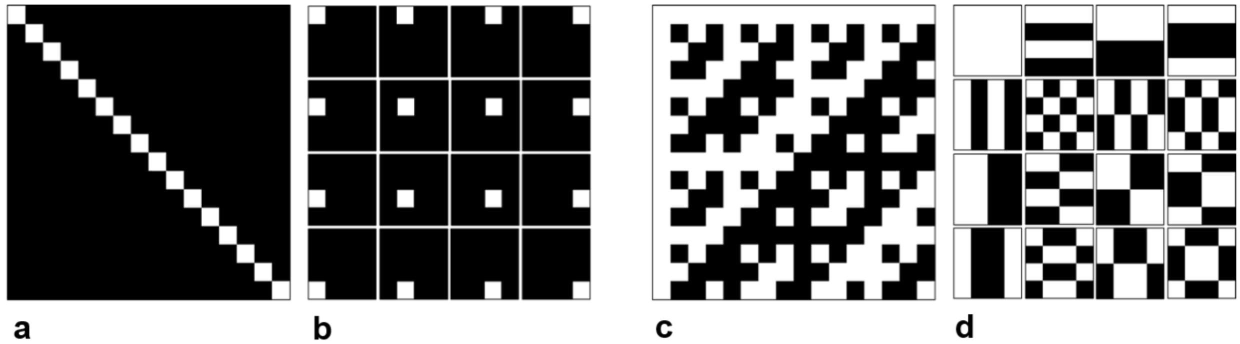

Figure B.1 | Exemples de séries de motifs éclairants. (a) La matrice Identité 16 × 16, *P*, et (b) la série correspondante de 16 ($\boldsymbol{n^2}$), masques spatiaux 4 × 4, $\{\boldsymbol{H_i}(\boldsymbol{x}, \boldsymbol{y},)\}_{\boldsymbol{i=1\ldots n^2}}$, obtenus à partir de celle-ci ; (c) La matrice Hadamard 16 × 16 et (d) l'ensemble correspondant de 16 masques spatiaux 4 × 4.

Il existe une variété de séries de motifs pour mettre en œuvre le schéma SPI. L'une des plus couramment utilisées est celle dérivée de la matrice d'Hadamard, qui s'est avérée bonne pour la maximisation du rapport signal sur bruit (SNR) (Harwit & Sloan, 1979). Dans ce travail, nous avons utilisé une séquence optimisée de l'ensemble Hadamard, surnommé « Coupe du gâteau » (CC) (W.-K. Yu, 2019), dans laquelle le contenu en fréquences spatiales de chaque motif augmente progressivement. En utilisant ce schéma, la plupart des informations liées à l'image seront contenues dans les premiers motifs. Cela permet de diminuer le temps d'acquisition (en réduisant le nombre de mesures nécessaires pour reconstruire l'image), tout en évitant la charge de calcul généralement nécessaire pour les schémas de détection compressée basés sur des ensembles de motifs aléatoires (Edgar et al., 2019). Pour la reconstruction de l'image, nous avons utilisé un algorithme SPI non itératif, tel que rapporté par (Bian et al., 2018).

B.2. Imagerie térahertz compressée dans le domaine du temps

Comme mentionné précédemment, le principal avantage du THz-TDS réside dans l'échantillonnage direct de l'amplitude du champ électrique dans le domaine temporel, ce qui donne la reconstruction de la forme d'onde temporelle d'impulsions THz. Le détecteur, dans ce cas, mesure un champ électrique en fonction du temps (t), avec une amplitude qui peut être positive ou négative à chaque t. Dans le cas d'une configuration SPI, le champ électrique lu par le détecteur est la superposition des champs transmis (réfléchis) par les pixels « blancs » du motif, après l'interaction avec l'objet sous test. Puisqu'une telle superposition est linéaire, la solution du problème SPI donne la valeur de champ liée à chaque pixel.

On peut ainsi réécrire l'Eq. (1), en remplaçant les vecteurs W et T par leurs versions dépendantes du temps $W(t)$ et $T(t)$, représentant l'amplitude de champ électrique évalué par le détecteur et la forme d'onde de champ électrique récupérée à chaque pixel, respectivement :

$$W(t) = \boldsymbol{P}T(t) \quad (2)$$

En résolvant le système linéaire de l'Eq. (2), on peut reconstruire le champ électrique THz en fonction du temps à chaque position spatiale de l'image, ajoutant ainsi une troisième dimension (le temps) aux deux dimensions spatiales.

B.2.1.Configuration expérimentale

La configuration expérimentale est une version modifiée d'un système THz-TDS traditionnel (Fig. B.1 (a)). Un laser Ti:Sapphire amplifié (800 nm, durée d'impulsion de 150 fs, 2 mJ à un taux de répétition de 1 kHz) est divisé en trois faisceaux : pompe (48 % de la puissance laser totale), sonde (4 %) et générateur de motifs (48 %). Le faisceau de pompe est utilisé pour produire des impulsions THz par rectification optique dans un cristal de tellurure de zinc (ZnTe) de 1 mm d'épaisseur. Le faisceau THz est d'abord agrandi, se propage à travers une plaque de silicium (Si) de 500 μm d'épaisseur (non dopée, 5000 Ω cm) utilisée pour la modulation spatiale, puis traverse l'échantillon. Enfin, la forme d'onde THz est enregistrée par échantillonnage électro-optique dans un autre cristal de ZnTe de 1 mm d'épaisseur, par le faisceau de sonde.

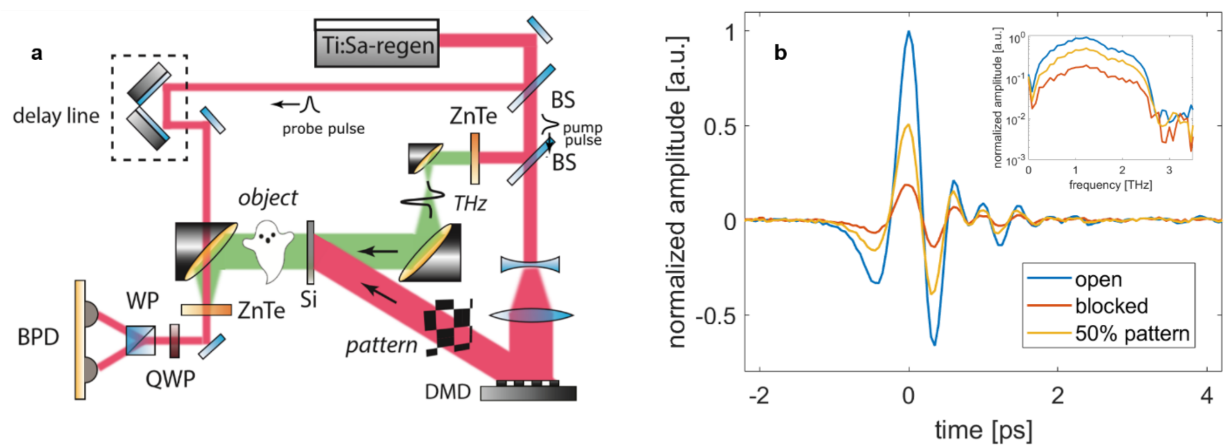

Figure B.2 | Le système TDS SPI. (a) Schéma de la configuration expérimentale : version modifiée d'un système THz-TDS. Le faisceau du laser est divisé en trois lignes (par des séparateurs de faisceau, BS), l'une génère l'impulsion THz dans un cristal ZnTe, l'autre est utilisée comme sonde dans le cristal EOS (ZnTe) et la dernière est utilisée pour la modulation du THz (après avoir été modulée avec le DMD). Le signal est enregistré par deux photodiodes équilibrées, après que la sonde s'est propagée à travers une lame à quart d'onde (QWP) et un prisme de Wollaston (WP). (b) Exemples de formes d'onde THz captées sans échantillon, avec des intensités IR modulantes variables : pas de lumière (bleu), fenêtre entièrement éclairée (rouge), fenêtre éclairée à 50 % (jaune) ; l'encart montre les amplitudes spectrales correspondant aux formes d'onde temporelles.

Pour mettre en œuvre une technique SPI, des motifs spatiaux THz sont nécessaires pour interroger l'échantillon. Les modulateurs spatiaux de lumière couramment utilisés ne conviennent pas à un fonctionnement dans la gamme THz. La solution est de moduler spatialement le faisceau IR au moyen d'un dispositif numérique à micro-miroir (DMD) (LightCrafter4500, Texas Instruments) et d'éclairer la surface de la plaque de Si avec le faisceau modulé. Le Si est normalement transparent dans la gamme THz, mais sous un éclairage laser (avec une énergie photonique supérieure à sa bande interdite), des porteurs libres sont générés localement, empêchant ainsi la transmission de la lumière THz et transférant la distribution spatiale du motif du laser IR au faisceau THz (Shrekenhamer et al., 2013). En appliquant cette technique, nous avons pu atteindre une profondeur de modulation d'environ 85 % (pic de l'impulsion THz) avec une énergie d'impulsion IR d'environ 140 μJ incidente sur la plaque de Si (en Fig. B.1(b) des exemples de formes d'onde obtenues avec différentes intensités de modulation). Compte tenu de la puissance laser disponible pour la modulation THz, de la limite de diffraction du THz sur la taille des pixels (~ 0,4 mm à 1 THz) et du ciblage d'un temps d'acquisition raisonnable, nous avons défini la dimension de la scène à 1,6 × 1 cm^2, divisée en un nombre maximum de 16 × 16 pixels.

B.2.2.Résultats

Le principal résultat obtenu dans la première moitié de ce projet doctoral est la démonstration de la reconstruction indirecte des formes d'onde temporelles liées à chaque pixel, à partir de celles enregistrées en illuminant l'objet avec la lumière à motifs modulée par le DMD. Un échantillon de polyéthylène haute densité (HDPE) (de forme rectangulaire de 1,6 cm × 1 cm et 2 mm d'épaisseur, Fig. B.3(a)), avec des lettres « TZ » gravées (où « T » est de 2 mm de profondeur et "Z" est de 1 mm de profondeur, mesurées à partir de la surface de l'échantillon) a été utilisé. Sur la gauche, nous montrons deux motifs sélectionnés (Fig. B.3(b)) ainsi que les formes d'onde THz correspondantes obtenues lorsqu'ils éclairaient l'objet (Fig. B.3(c)). Dans cette dernière, nous pouvons voir une série d'impulsions THz, dues aux contributions des ondes THz qui sont passées par différentes positions sur l'échantillon, arrivant donc à des moments différents. Sur le côté droit, nous avons les traces THz reconstruites (Fig. B.3(d)) à l'aide de l'Eq. 2 pour trois pixels représentatifs (pour les positions "T", "Z" et "fond", Fig. B.3(e)). La possibilité de récupérer la forme d'onde temporelle à chaque position spatiale donne accès à toute la quantité d'informations que l'on obtiendrait en balayant l'objet, permettant d'effectuer l'imagerie d'objets avec différents mécanismes de contraste. Ensuite, en fonction de la nature de l'échantillon et du type d'informations à afficher, la méthode de contraste d'image est choisie. Ceci est une preuve claire de la flexibilité de l'approche SPI dans le domaine temporel et de son champ d'application potentiellement large dans le contexte de l'imagerie THz.

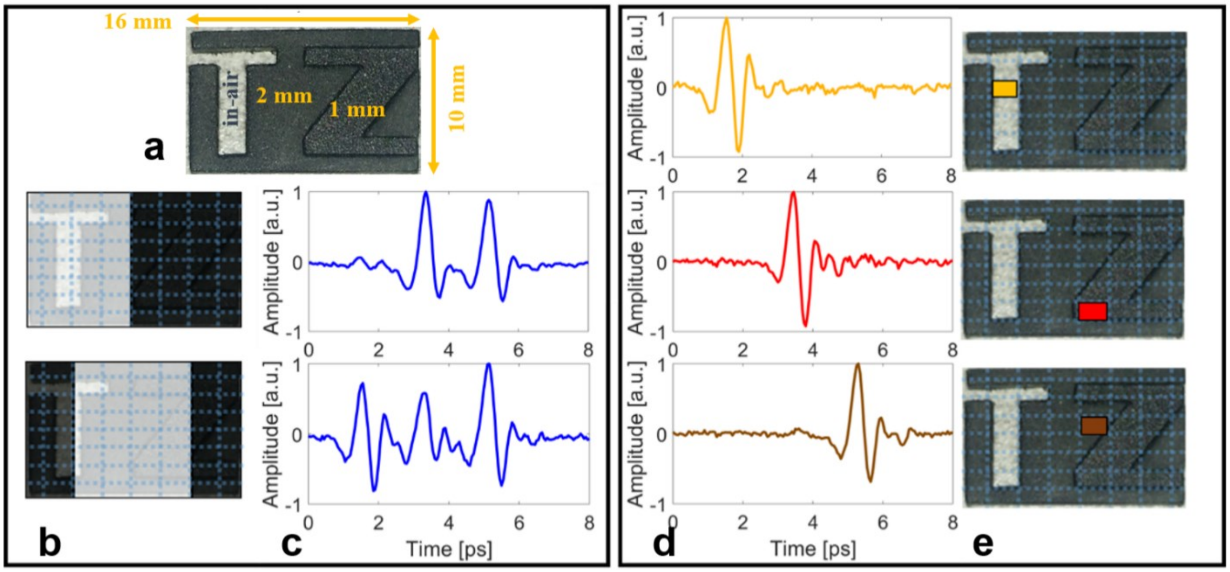

Figure B.3 | Reconstruction dans le domaine temporel des formes d'onde THz avec le SPI. (a) Échantillon utilisé. (b) Exemples de deux motifs Hadamard 8 × 8. (c) signaux détectés pour les motifs en (b). Les formes d'onde THz montrent des impulsions multiples, en raison des ondes THz arrivant à des moments variables après avoir traversé l'échantillon à différentes positions. (d) Champ électrique THz reconstruit dans le temps, à trois pixels sélectionnés, marqués en (e). Les ondes THz sont clairement à impulsion unique, démontrant que l'approche SPI préserve la capacité de détection cohérente du THz-TDS. *Adaptée avec la permission de (Zanotto et al., 2020) © 2020 The Optical Society.*

Images d'amplitude à temps fixes

Dans le cas d'objets semi-transparents, comme notre échantillon HDPE, différentes méthodes de contraste peuvent être choisies. Une possibilité est de montrer l'amplitude du champ électrique enregistrée à des positions temporelles spécifiques. L'épaisseur variable dans l'échantillon HDPE produit un retard temporel dépendant de l'espace pour le faisceau THz entrant. Cette technique permet de reconnaître clairement la présence de zones d'épaisseurs différentes dans un échantillon. Sur la Fig. B.4(a), nous affichons trois images 16 × 16 captées à des moments correspondants aux trois pics principaux de la forme d'onde illustrée sur la Fig. B.4(b) (une forme d'onde représentative détectée pour l'un des motifs employés). Les cadres montrent clairement les trois zones avec des épaisseurs différentes.

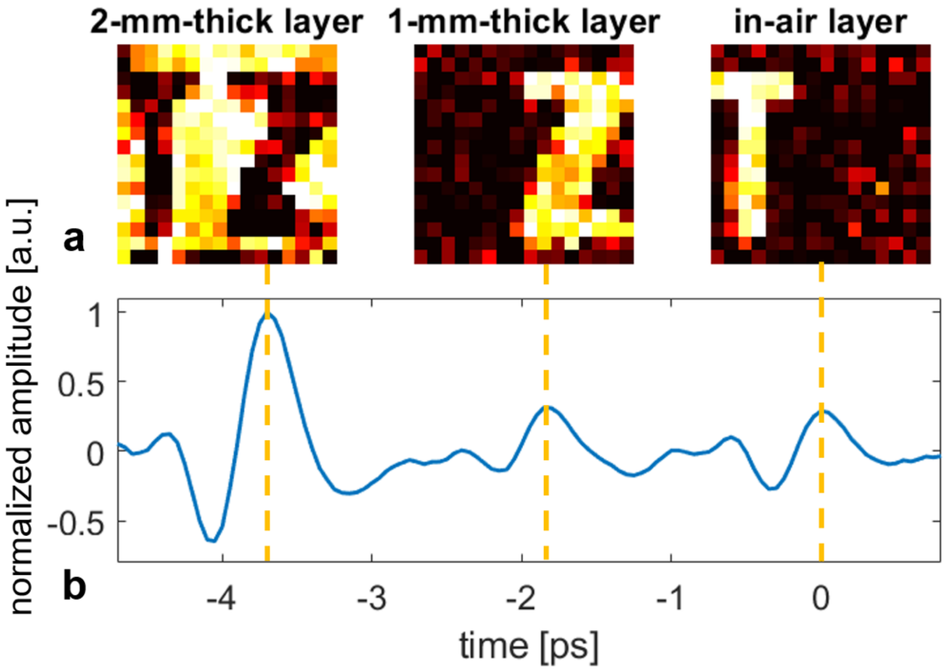

Figure B.4 | Imagerie d'amplitude à temps fixes. (a) Images captées à trois instants différents, correspondants aux principaux pics de l'onde THz, illustrés en (b). Les trois pics correspondents aux trois couches d'épaisseurs variables de l'échantillon : « T » dans l'air, « Z » 1 mm, région externe 2 mm.

On pourrait remarquer quelques écarts dans les niveaux d'amplitude attendus à certains pixels dans les trois tracés. Cela est potentiellement causé par la dispersion, qui se produit principalement à la frontière entre les régions d'échantillon présentant des épaisseurs différentes et conduit à une transmission réduite. Un tel problème pourrait être partiellement amélioré en augmentant la résolution des motifs d'imagerie. Deux raisons limitaient la résolution atteignable dans nos conditions expérimentales. Premièrement, la distance minimale entre le plan de modulation et l'échantillon, fixée par l'épaisseur de la plaque Si utilisée pour la modulation (500 µm), ne nous permet pas d'avoir un pixel inférieur à ~ 400 µm. Ceci est dû aux effets de diffraction, qui provoqueraient la dégradation de l'image reconstruite. Deuxièmement, le temps d'acquisition, encore long du fait de la lenteur de la ligne à retard et de la fréquence de répétition limitée du laser, gênait la possibilité d'acquérir des mesures nécessitant plus de quelques centaines de motifs.

Images de temps de vol

Une autre manière utile d'obtenir des informations de matériaux semi-transparents repose sur la récupération des retards temporels de l'impulsion THz par rapport à une référence, à chaque position spatiale. Cette procédure permet d'estimer l'épaisseur (ou l'indice de réfraction) d'un échantillon. Une telle technique est appelée à temps de vol (TOF). Sur la Fig. B.5(a), nous pouvons voir des exemples de traces THz récupérées pour trois des pixels de l'image de la Fig. B.5(b), ainsi que l'impulsion de référence (ligne bleue pointillée). En calculant le délai entre les pics des impulsions THz, nous pouvons obtenir l'épaisseur locale de l'échantillon (avec un indice de réfraction de 1,54 (Naftaly & Miles, 2007)). Les valeurs obtenues sont utilisées pour reconstruire la carte d'épaisseur de 256 pixels illustrée à la Fig. B.5(b).

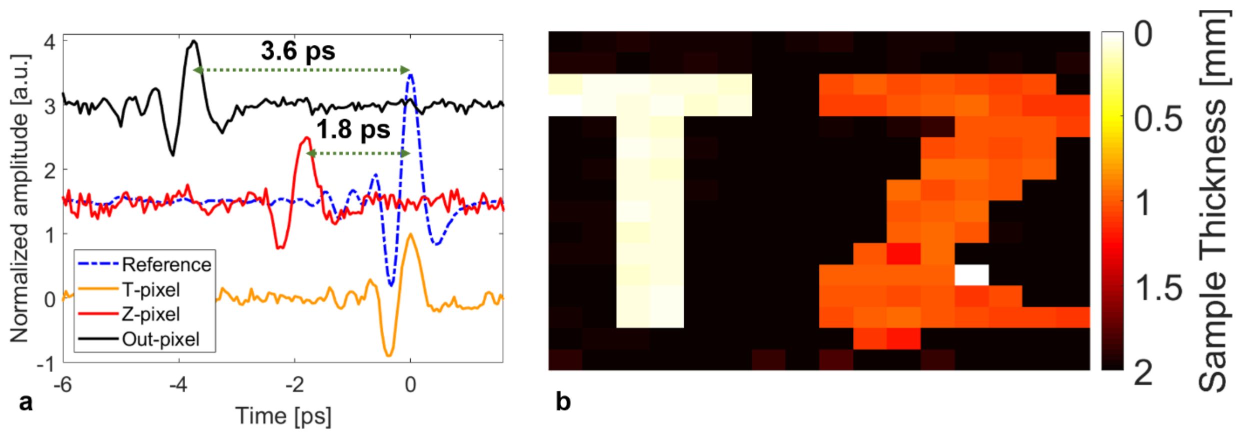

Figure B.5 | Imagerie du temps de vol. (a) Exemples d'impulsions THz reconstruites pour trois des pixels en (b), et leur retard par rapport à une impulsion de référence, captés sans l'échantillon. (b) Image de 256 pixels de l'épaisseur locale de l'échantillon de HDPE, décrit dans le texte. L'épaisseur est récupérée avec le retard relatif des impulsions THz à chaque position spatiale, compte tenu de l'indice de réfraction du HDPE (n = 1,54).

Comme nous pouvons voir sur la Fig. B.5(b), la qualité de la reconstruction de l'image est assez précise. En particulier, l'épaisseur des trois couches peut être clairement distinguée. Comme indiqué précédemment, certains pixels le long des marges du "Z", en particulier sur les parties inclinées, ne représentent pas l'épaisseur correcte, et cela est probablement dû à la résolution limitée offerte par les motifs 16 × 16 (1 mm horizontal, et 0,625 mm verticalement). Certains des pixels brillants des motifs pourraient illuminer une région échantillon où deux niveaux d'épaisseur différents sont présents. Ainsi, du fait des retards temporels différents introduits par les deux couches, la lumière transmise sera répartie entre deux impulsions THz arrivant à des instants différents dans la détection cohérente. Néanmoins, le retard calculé pour le pixel affichant exclusivement l'une des deux épaisseurs (par rapport au plus grand pic d'amplitude THz transmis).

Comme preuve de principe, nous avons également effectué une reconstruction CS de l'image TOF, afin de montrer que la récupération d'image est possible même avec un nombre de mesures inférieur au nombre de pixels. Sur la Fig. B.6, nous pouvons voir comment la procédure CS entraîne la perte de certains détails de l'image, mais la forme des lettres est toujours reconnaissable même avec seulement 25% du nombre total de motifs, et il est toujours possible d'extraire l'épaisseur à chaque position spatiale.

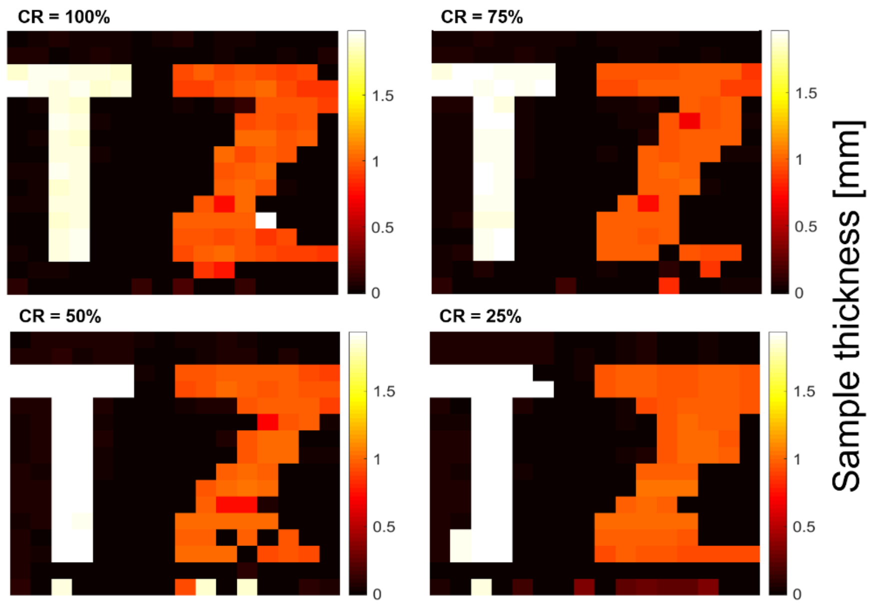

Figure B.6 | Imagerie compressée. Images de l'échantillon de HDPE, avec différents rapports de compression (CR, nombre de motifs/nombre de pixels) : 100% - 75% - 50% - 25%.

Images hyperspectrales

Enfin, nous avons également utilisé notre système pour prouver la possibilité d'effectuer une reconnaissance spectrale de composés chimiques. Dans ce contexte, la méthode de contraste appliquée est basée sur la représentation de l'absorption relative à des fréquences spécifiques, par rapport à une impulsion de référence. À cette fin, nous avons réalisé l'échantillon en Teflon (PTFE) illustré à la Fig. B.7(a). La section avec une forme de « L » contient du lactose incorporé au PTFE. L'idée est d'obtenir une cartographie de l'absorption spectrale à des fréquences spécifiques. La présence de lactose sera révélée par la forte résonance à ~1,38 THz (Brown et al., 2007). Sur la Fig. B.7(b-c) nous affichons des images spectrales en sélectionnant a posteriori la transmission à ~1 THz (Fig. B.7(b)), et en correspondance de la ligne d'absorption du lactose, à ~1,38 THz (Fig. B.7(c)). Les spectres utilisés pour récupérer ces images sont obtenus par transformation de Fourier des données temporelles fournies par la reconstruction SPI pour chaque pixel individuel de l'image. Des exemples de tels spectres pour certains pixels sélectionnés de la Fig. B.7(c) sont montrés sur la Fig. B.7(d).

Aucune caractéristique claire n'est visible pour l'image spectrale à 1 THz, car aucune des deux parties de l'échantillon n'a de ligne d'absorption à cette fréquence, ni, bien entendu, l'air. Inversement, sur la Fig. B.7(c), nous observons que la partie en forme de L, constituée du mélange Téflon/lactose, est nettement plus sombre dans l'ensemble, tandis qu'une fois de plus, le rectangle en Téflon ne présente aucune différence significative par rapport au reste de la fenêtre d'imagerie. L'absorption inégale entre les différents pixels dans la section en forme de « L » est probablement due à la distribution spatiale inhomogène du lactose au sein du mélange.

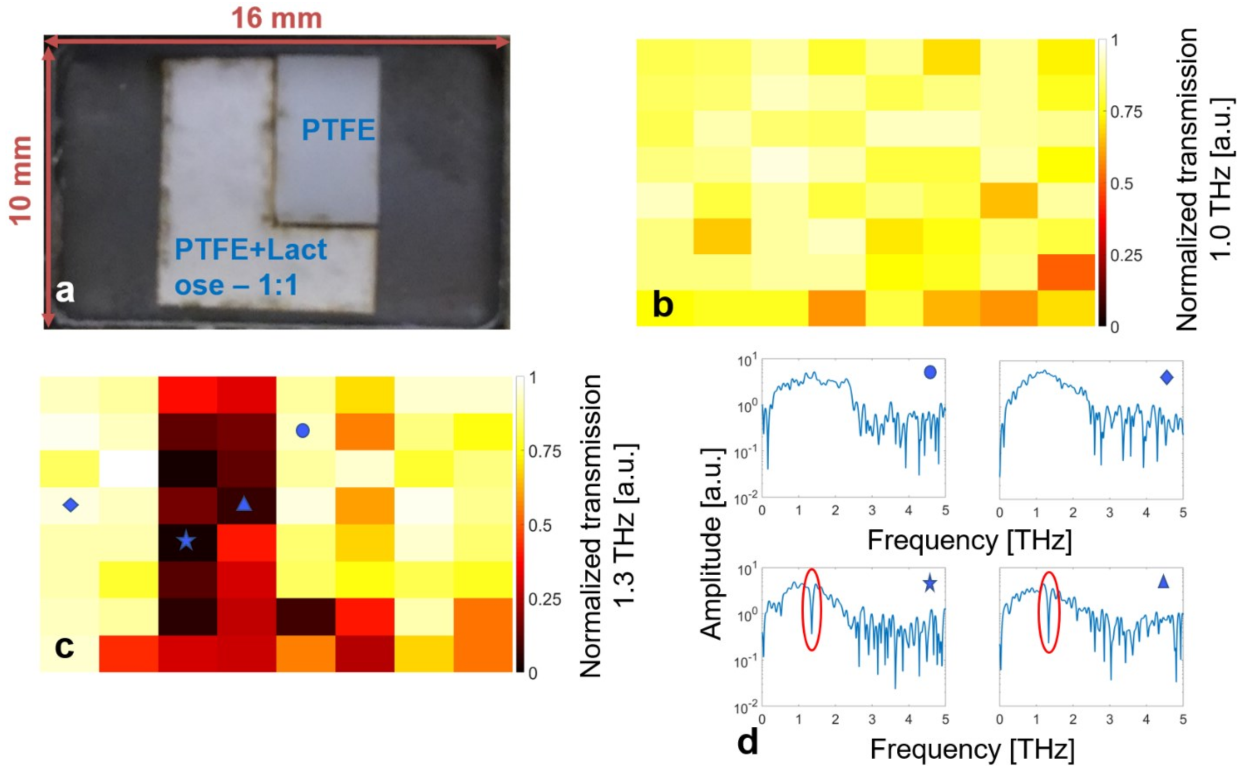

Figure B.7 | Imagerie hyperspectrale. (a) Photo de l'échantillon composé d'une partie en forme de « L » contenant un mélange de lactose et de PTFE, et une portion rectangulaire en PTFE. (b,c) images spectrales 64 pixels : (b) transmission spectrale autour de 1 THz ; (c) transmission spectrale autour de 1,38 THz. Aucune caractéristique n'est présente en (b), car aucune partie de l'échantillon, ni de l'air n'absorbent de manière significative à 1 THz. La pastille en forme de « L » apparaît en (c), grâce à l'absorption du lactose à 1,38 THz. (d) Exemples de spectres THz de quatre pixels sélectionnés (indiqués en (c)), obtenus par transformation de Fourier directe des formes d'onde THz dans le domaine temporel reconstruites à chaque position de pixel : pour les pixels où le lactose est présent, la raie d'absorption à 1,38 THz est clairement visible. *Adaptée avec la permission de (Zanotto et al., 2020) © 2020 The Optical Society.*

B.2.3.Discussion et conclusions

Ici, nous pouvons faire quelques observations concernant le temps d'acquisition, qui est l'une des principales raisons d'utiliser SPI. Pour l'image avec la résolution la plus élevée (16x16, 256 pixels), le temps d'acquisition actuel était encore très long, soit d'environ 10 heures (similaire à ce qui résulterait d'un balayage traditionnel). L'application de CS réduirait déjà ce temps d'acquisition, puisque l'utilisation de seulement 25% des modèles donne déjà une reconstruction décente. La principale limitation est la ligne à retard lente utilisée dans notre système, ainsi que la nécessité d'une intégration relativement longue à chaque point de la fenêtre temporelle, en raison du taux de répétition limité de notre laser (1 kHz). Ces deux éléments combinés se traduisent par une acquisition de 2,5 minutes pour le balayage temporel de 8 ps nécessaire pour chaque motif. Des sources laser à taux de répétition plus élevé, associées à des lignes à retard rapides facilement disponibles effectuant plusieurs balayages par seconde, réduiraient directement ce temps à quelques minutes.

En résumé, nous avons démontré une reconstruction appropriée de la forme d'onde du champ électrique THz dans le domaine temporel à chaque position spatiale de l'image de l'objet, sans nécessiter de balayage spatial mécanique. Nous avons exploité cette capacité pour capter des images présentant diverses méthodes de contraste. Cela démontre la flexibilité de la technique SPI appliquée à la reconstruction d'images en plusieurs dimensions. De plus, nous avons montré que les algorithmes CS peuvent également être mis en œuvre, conduisant potentiellement à une réduction significative du temps d'acquisition global.

C. Imagerie térahertz avec une détection « seul-coup »

Dans ce chapitre, nous présentons les résultats relatifs à la seconde moitié du projet doctoral. Ici, l'objectif principal était la combinaison du système d'imagerie THz SPI développé dans la première partie du projet, avec une technique SSD. Les techniques SSD sont des approches d'acquisition THz qui permettent l'acquisition simultanée d'une forme d'onde THz entière dans le domaine temporel, en principe au sein d'un seul tir laser, réduisant ainsi considérablement le temps d'acquisition. Nous rappelons que, dans les systèmes TDS, l'impulsion de la sonde IR fonctionne comme une porte optique, qui est retardée de manière variable afin d'échantillonner séquentiellement le champ électrique THz à différentes positions temporelles, généralement en utilisant une ligne à retard mécanique. Ce processus est l'un des principaux facteurs limitant sévèrement la vitesse d'acquisition des systèmes d'imagerie THz actuels basés sur TDS.

C.1.Enregistrement des ondes térahertz sans ligne à retard

Au cours des vingt dernières années, plusieurs techniques SSD ont étés explorées. Ces techniques sont généralement basées sur l'étirement de la dimension temporelle de l'impulsion THz sur une dimension de l'impulsion de sonde. De cette manière, les informations temporelles du faisceau THz peuvent être enregistrées simultanément lors de l'acquisition d'une seule impulsion de sonde IR.

La première approche explorée dans ce projet de doctorat était la cartographie fréquence-temps (Jiang & Zhang, 1998b), qui est basée sur l'étirement temporel de l'impulsion de la sonde, de sorte que ses composantes de fréquence (étalées dans le temps) puissent échantillonner différentes portions temporelles de l'impulsion THz. La technique est relativement simple à mettre en œuvre, mais présente un inconvénient important. En effet, la résolution temporelle est très limitée, étant essentiellement contrainte par la bande spectrale (c'est-à-dire la durée temporelle) de l'impulsion de sonde. La résolution maximale réalisable, ΔT, est donnée par (F. G. Sun et al., 1998) :

$$\Delta T = \sqrt{T_0 T_c} \tag{3}$$

Où T_0 est la durée limitée par transformation de Fourier de l'impulsion de sonde, et T_c sa durée étirée. Cette méthode n'a finalement pas été poursuivie, car la reconstruction de la forme d'onde THz était déformée à cause de la basse résolution temporelle.

La méthode utilisée avec succès est la cartographie temps-espace. Ce schéma exploite une impulsion de sonde étalée dans l'espace, de sorte que des points spatiaux séparés se chevauchent avec le THz à des moments différents, sondant donc simultanément ses différentes positions temporelles. Ensuite, l'intensité spatiale de la sonde est capturée avec une caméra, obtenant ainsi une image en principe instantanée de la forme d'onde temporelle THz. L'inclinaison du front de l'impulsion est obtenue au moyen d'un élément dispersif, qui sépare spatialement les différentes composantes de fréquence de l'impulsion de la sonde à large bande, et un système 4-f permettant la formation d'une image du front de la sonde (inclinée) à la position du cristal de détection. La fenêtre temporelle résultante, T, est fonction du diamètre du faisceau de la sonde, σ, à la position de détection, et de l'angle d'inclinaison, γ. L'angle d'inclinaison peut, à son tour, être écrit en termes de longueur d'onde moyenne de la lumière utilisée, $\bar{\lambda}$, le paramètre de réseau, d, la magnification du système 4-f, M, et l'angle de diffraction après le réseau, β (c est la vitesse de la lumière):

$$T = \frac{\sigma \tan \gamma}{c} = \frac{\bar{\lambda}\ \sigma}{c\ M\ d \cos \beta} \tag{4}$$

C.2.Imagerie térahertz avec une détection à cartographie temps-espace

C.2.1.Effet de la diffraction sur un système SPI

Afin d'assurer qu'il est possible de combiner efficacement le schéma SPI et la technique SSD présentée ci-dessus, il est instructif de relier le mécanisme sous-jacent au SPI à la nature ondulatoire de la lumière. Le principe bien connu de Huygens-Fresnel décrit capture la physique derrière la diffraction (Goodman, 1996). Selon ce principe, l'amplitude du champ complexe en un seul point après propagation en espace libre peut être interprétée comme une somme de toutes les ondes sphériques générées en chaque point du plan source. Nous pouvons montrer que le bon fonctionnement de notre arrangement repose strictement sur son existence. Comme mentionné précédemment, grâce à la caractéristique d'éclairage structuré de SPI, nous n'avons besoin que d'une mesure de la corrélation entre les motifs et la forme spatiale de l'objet. La diffraction effectue automatiquement l'intégration spatiale qui amène les informations de corrélation en un seul point, fournissant ainsi naturellement les conditions de travail pour le SPI. De plus, la détection cohérente effectuée aux fréquences THz permet de retrouver la valeur complexe du champ électrique en ce point unique. Ainsi, la reconstruction d'image peut être réalisée même dans le cas le plus général où toutes les entités impliquées (c'est-à-dire les motifs et la transmission/réflexion d'objet) sont à valeurs complexes.

Pour notre implémentation SSD, la diffraction représente aussi un aspect clé. Pour obtenir une « vraie » détection « en un seul point », la taille de la sonde sur le plan du détecteur doit être inférieure à la largeur w du lobe principal du motif THz diffracté au même plan (Goodman, 1996) : $w = \lambda_{THz} z / x_{MAX}$ ($\approx$ 1,5 mm dans notre cas spécifique), où λ_{THz} est la longueur d'onde THz, z est la distance de propagation et x_{MAX} est l'étendue spatiale maximale de l'objet. Ceci est très simple à réaliser en utilisant un faisceau de sonde à des longueurs d'onde IR-visible, environ trois ordres de grandeur plus courtes que celle du rayonnement THz. En gardant la sonde plus petite que cette taille, nous pouvons sacrifier une dimension spatiale pour allouer le domaine temporel (ou, en d'autres termes, utiliser la technique de codage temps-espace), tout en obtenant toujours une reconstruction spatiale complète de l'objet à imager.

C.2.2.Configuration expérimentale

Le dispositif expérimental utilisé pour cette démonstration est illustré à la Fig. C.1(a). Il était similaire à celui utilisé pendant la première partie, sauf que le système de détection a été substitué avec celui basé sur la cartographie temps-espace. De plus, une différente source laser a été utilisée ainsi que d’autres cristaux de génération et de détection. Le faisceau d'un laser Yb amplifié (1030 nm, durée d'impulsion 175 fs, 1 mJ à un taux de répétition de 250 Hz) est divisé en un faisceau de pompe, un faisceau de sonde et un générateur de motifs. Le faisceau de pompe est utilisé pour produire des impulsions THz par rectification optique dans un cristal organique HMQ-TMS (2-(4-hydroxy-3-méthoxystyryl)-1-méthylquinolinium 2,4,6-triméthylbenzènesulfonate) de 300 μm d'épaisseur. Après quelques éléments optiques grossissants, le faisceau THz se propage à travers une plaque de semiconducteur pour la modulation spatiale et finit par traverser l'échantillon (avec une taille de 10 mm × 10 mm). Enfin, l'échantillonnage électro-optique en espace libre est effectué via un cristal de phosphure de gallium (GaP) de 3 mm d'épaisseur, où les faisceaux THz et la sonde sont spatialement superposés. Les motifs spatiaux nécessaires pour utiliser le schéma SPI sont obtenus encore une fois en appliquant la technique de modulation basée sur la photo-excitation d'un semi-conducteur, décrite ci-dessus. La seule différence était dans l'utilisation d'une plaque de germanium (Ge) (125 µm d'épaisseur, non dopée, résistivité > 40 Ω cm), au lieu du Si, pour assurer la génération d'une quantité suffisante de porteurs avec la lumière d'un laser à 1030 nm. En appliquant cette technique, nous obtenons une profondeur de modulation d'environ 90% (amplitude de pic de l'impulsion THz). Pour mettre en œuvre le schéma de détection sans balayage décrit ci-dessus, un réseau de réflexion (1200 rainures/mm) est placé le long du trajet du faisceau de la sonde, suivi d'un système 4-*f*, qui image la sonde sur le cristal de détection de taille réduite (1 mm de diamètre) et à front incliné. Après avoir échantillonné l'impulsion THz, la sonde est agrandie par un second système 4-*f* puis atteint la

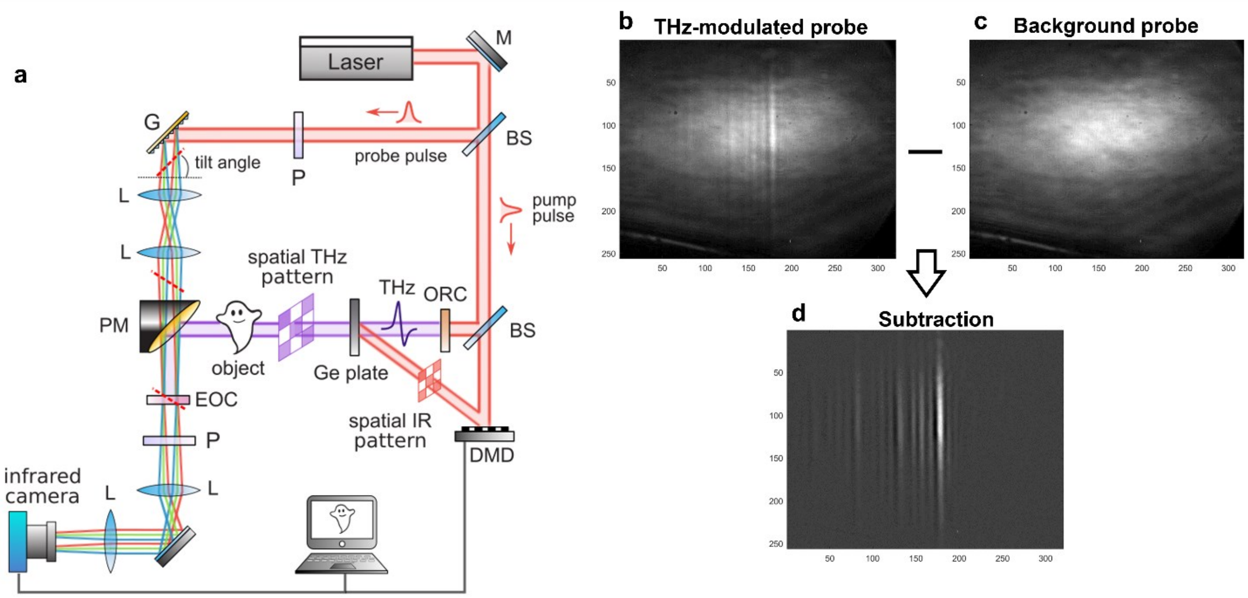

Figure C.1 | Le système d'imagerie THz sans balayage. (a) Montage expérimental. Le faisceau laser est divisé en deux lignes (pompe et sonde) à l'aide d'un séparateur de faisceau (BS). L'impulsion de pompe est alors à nouveau divisée : une ligne génère un rayonnement THz par rectification optique dans un cristal organique (ORC), l'autre est modulée spatialement à l'aide d'un dispositif numérique à micro-miroirs ; le faisceau infrarouge tramé est utilisé pour photo exciter des porteurs dans une plaque Ge, afin de moduler spatialement l'impulsion THz ; ce dernier interroge l'échantillon puis atteint le cristal de détection (EOC). La ligne de sonde traverse un polariseur (P) puis frappe le réseau (G), qui incline le front d'impulsion de la sonde ; deux lentilles (L) forment un système 4-*f* qui image le faisceau de sonde incliné sur le cristal de détection (EOC). Après un tel cristal, un analyseur et un second système 4-*f* acheminent le faisceau sonde modulé THz vers la caméra IR. (b) Exemples d'images enregistrées par la caméra IR : faisceau sonde de fond (à gauche) ; Faisceau de sonde modulé THz (à droite). La région pointillée correspond à la zone en (c). (c) (haut) Portion de la zone extraite des images enregistrées par la caméra et corrigée en soustrayant puis en divisant la sonde modulée par le fond ; (en bas) Forme d'onde THz reconstruite en intégrant l'image ci-dessus le long de la direction verticale.

caméra InGaAs d'enregistrement (Xeva 320 Series, Xenics).

En utilisant le réseau qui fonctionne à un angle d'incidence de 72° (angle diffracté 16°), la fenêtre de temps disponible attendue fournie par la sonde est d'environ 17 ps, ce qui est suffisant pour acquérir correctement les répliques de formes d'onde THz transmises à travers les échantillons multicouches. Nous avons calibré temporellement la détection sans balayage au moyen d'une ligne à retard mécanique, pour changer le chemin optique de la sonde et vérifier le décalage correspondant de la position spatiale du pic d'impulsion THz sur la caméra. La résolution temporelle obtenue dans nos conditions expérimentales était de 68,7 fs/pixel. La Fig. C.1(b) montre des exemples d'images du faisceau de sonde enregistrées par la caméra IR. La forme d'onde est extraite en soustrayant d'abord l'image de la sonde de fond de celle modulée par le THz, puis en divisant le résultat par le fond, pour corriger la forme gaussienne du faisceau de la sonde, $\Gamma = \frac{I_{THz}-I_{bg}}{I_{bg}}$. Sur la Fig. C.1(c), nous montrons un exemple de la portion de la photo utilisée pour la reconstruction, ainsi que la forme d'onde THz réelle obtenue en intégrant le long de la direction verticale pour améliorer le SNR.

C.2.3.Résultats

La reconstruction d'image THz est obtenue grâce à notre algorithme SPI dans le domaine temporel, mis en œuvre en résolvant un problème SPI à chaque point de la fenêtre temporelle, comme expliqué en détail dans la section 2.2. De cette manière, la forme d'onde THz transmise, correspondant à chaque « pixel » d'image peut être obtenue. Pour prouver le potentiel du schéma d'imagerie proposé, , nous montrons la reconstruction d'images 3D d'échantillons multicouches, en affichant le contraste des couches avec différentes méthodes.

Images d'amplitude à temps fixes

Nous avons utilisé deux échantillons de HDPE, lequel possède un indice de réfraction de 1,54 et une absorption négligeable ($\alpha \leq 1$ cm^{-1}) dans l'intervalle 0,5-2,5 THz (Naftaly & Miles, 2007). L'échantillon (1) (Fig. C.2(a)) comporte des lettres T-H-Z gravées avec trois épaisseurs différentes (T - 1 mm, H et Z - 2 mm, zone extérieure - 3 mm), tandis que l'échantillon (2) (Fig. C.2(b)) possède les lettres I-N-R-S (I et N – dans l'air, R et S – 1 mm, zone extérieure – 2 mm). Nous avons d'abord reconstruit des images en considérant l'amplitude du champ THz à différentes positions temporelles fixes.

Dans les Fig. C.2(c-d), nous montrons trois cadres 32 × 32, récupérées en prenant, à chaque pixel, l'amplitude de champ normalisée aux positions temporelles des trois pics des Fig. C.2(e-f). Chaque image montre les caractéristiques spatiales de la couche avec une épaisseur correspondant à ce délai. La résolution dans le plan est dictée par la taille de pixel utilisée pour générer les modèles de modulation (312,5 µm dans ce cas). Nous pouvons voir que la reconstruction reproduit bien la forme de l'objet, à l'exclusion de certaines parties aux extrémités de la lettre et de l'échantillon, ainsi que de certaines caractéristiques plus petites, où les effets de dispersion jouent probablement un rôle dans la réduction de la transmission.

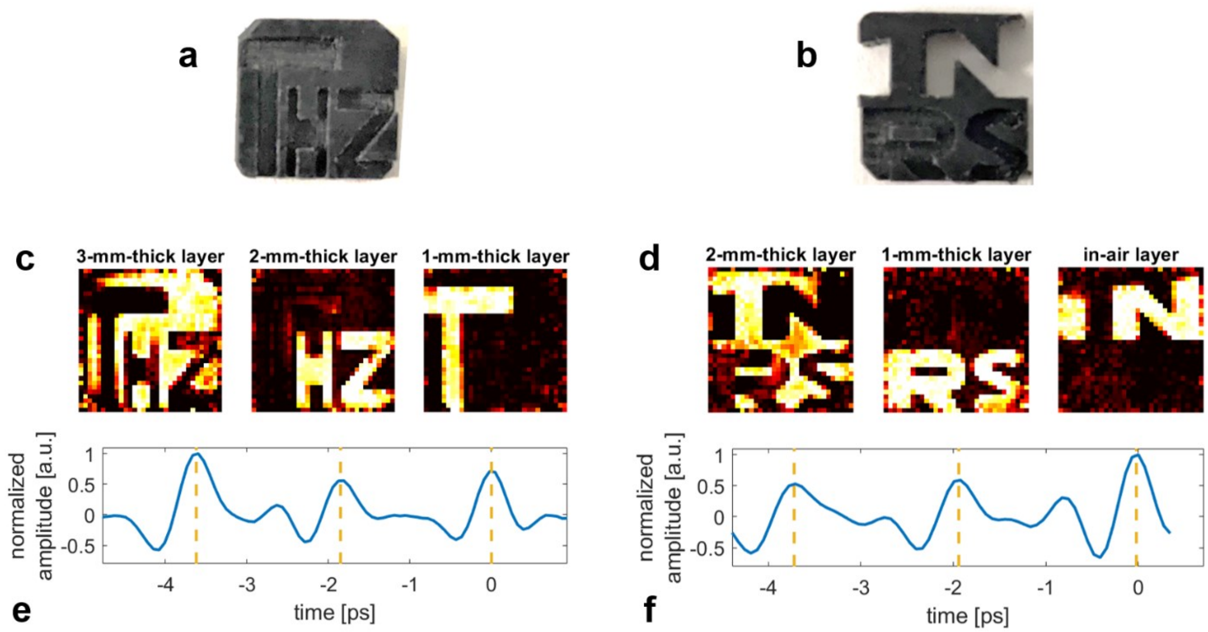

Figure C.2 | Imagerie d'amplitude à temps fixes. (a) échantillon (1), polyéthylène haute densité (HDPE) avec lettres T-H-Z gravées. (b) échantillon (2), HDPE avec lettres I-N-R-S gravées. (c)-(d) Images reconstruites en tenant compte de l'amplitude du champ électrique aux positions temporelles correspondant aux trois pics différents des formes d'onde THz en (e)-(f) respectivement. Les formes d'onde en (e)-(f) sont des exemples de traces THz mesurées avant l'application de la reconstruction SPI. La présence des impulsions multiples dans ces formes d'onde est due à la contribution combinée de tous les pixels "blancs" du motif.

Comme preuve de principe, nous avons également implanté le même algorithme CS décrit ci-dessus, pour reconstruire l'image en utilisant un nombre de motifs inférieur au nombre de pixels (1024 dans ce cas précis). Comme le montre la Fig. C.3, même en utilisant seulement 25 % des motifs, il est toujours possible de récupérer une bonne approximation des caractéristiques spatiales des trois couches. De meilleures compressions pourraient être potentiellement obtenues en utilisant différents ensembles de motifs (She et al., 2019) ou des algorithmes de reconstruction plus avancés (Bian et al., 2018). Ces solutions se sont avérées efficaces aux fréquences optiques, mais ne sont pas toujours simples à mettre en œuvre dans la gamme THz, en raison des limites posées par la technique de photomodulation (par exemple, la complexité de génération de motifs non binaires). Des méthodes innovantes de modulation THz, potentiellement plus flexibles, ont été introduites ces dernières années (W. Li et al., 2022; Watts et al., 2014), mais doivent encore être développées pour devenir des solutions viables.

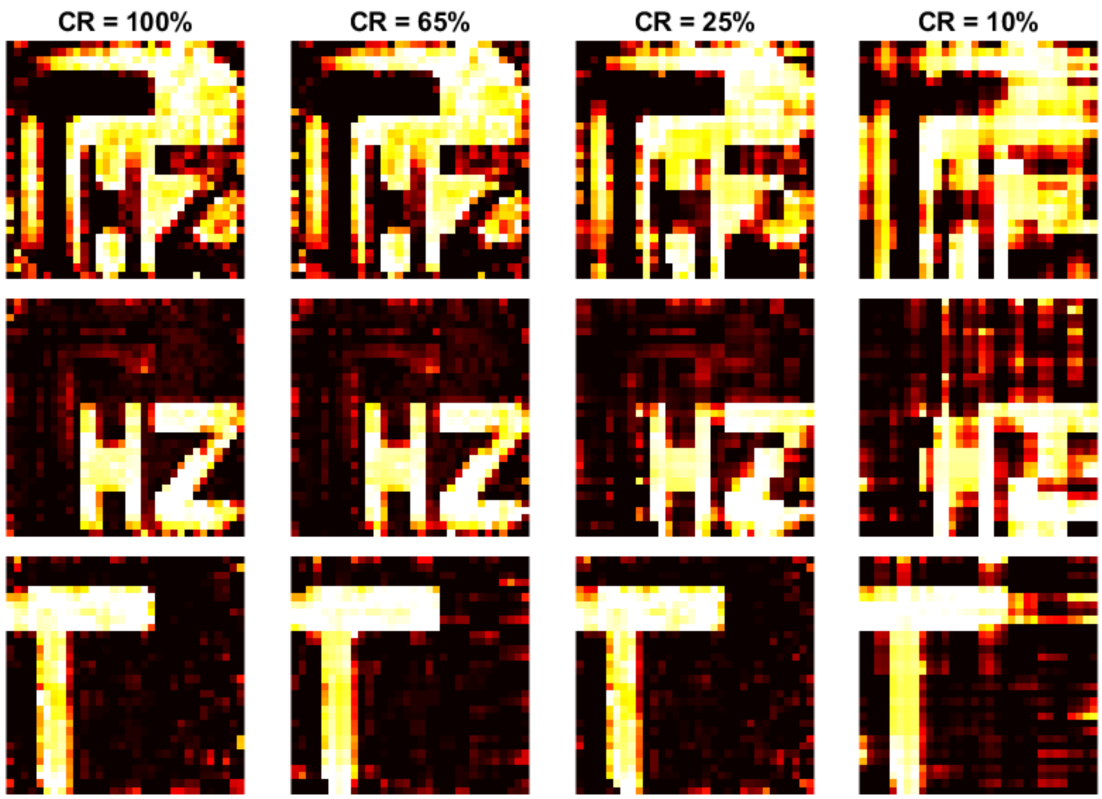

Figure C.3 | Imagerie compressée. Images 32 × 32 de l'échantillon (1) reconstruites en considérant l'amplitude à différentes positions temporelles (comme sur la Fig. C.2), et avec un taux de compression (CR) décroissant (de gauche à droite), 100 % - 65 % - 25 % - 10 %.

Images à temps de vol

Pour les mêmes échantillons, nous avons également mesuré le délai entre une impulsion THz de référence se propageant dans l'air et les impulsions THz récupérées à chaque pixel. Nous avons donc obtenu des images où la couleur du pixel cartographie le retard subi par l'impulsion THz à cette position (d'ailleurs, en considérant l'indice de réfraction du groupe HDPE, il est également possible d'extraire directement les épaisseurs relatives des différentes couches). Sur la Fig. C.4, nous présentons à la fois des images 16 × 16 et 32 × 32 pour les deux échantillons.

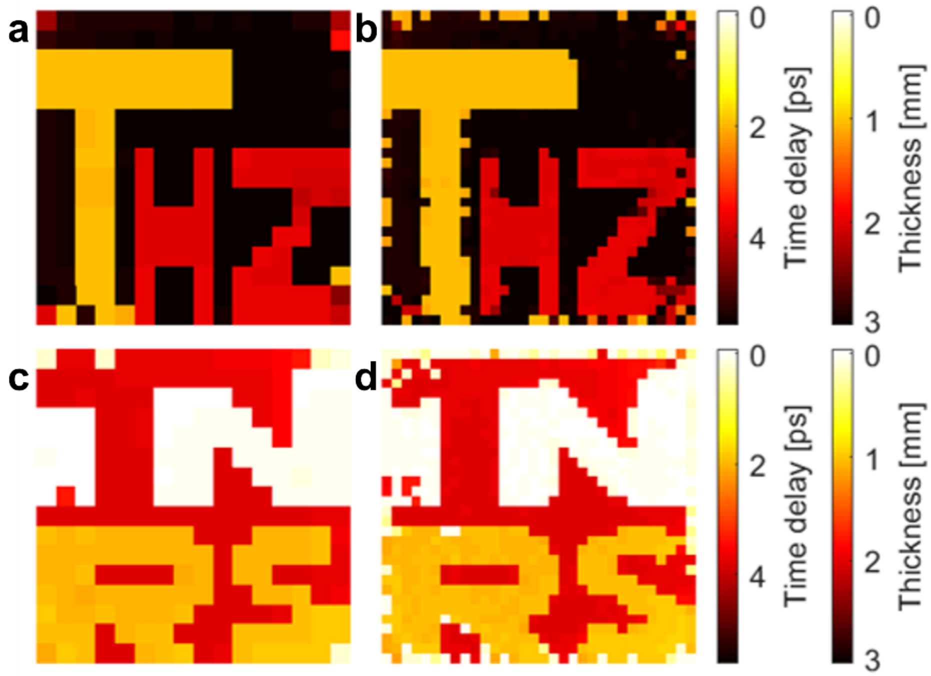

Figure C.4 | Images à temps de vol. (en haut) Images de l'échantillon (1) : (a) images 16 × 16 et (b) 32 × 32 pixels reconstruites en tenant compte du délai entre la position temporelle du pic d'impulsion THz dans l'air et celle des impulsions récupérées à chaque pixel. (en bas) Images de l'échantillon (2) : (a) images 16 × 16 et (b) images 32 × 32 pixels reconstruites de la même manière. Les échelles de couleurs représentent respectivement le retard temporel et l'épaisseur locale des échantillons.

La reconstruction en temps de vol (ToF) des images 16 x 16 est précise et permet de discerner les lettres à chaque couche, bien que la résolution limitée (625 µm) entrave la reconstruction précise des plus petites caractéristiques. Dans les images 32 x 32, la résolution accrue permet clairement de mieux montrer les caractéristiques spatiales nettes, mais nous voyons que certains pixels, principalement sur les bords des lettres et de l'échantillon, ne parviennent pas à représenter le bon délai, probablement en raison de dispersion, mais aussi des effets de diffraction. En effet, la largeur de pixel est dans ce cas de 312,5 µm, donc comparable à la longueur d'onde centrale (300 µm à 1 THz) des impulsions THz. Cela signifie que même après de très courtes distances, le faisceau se propageant subira des modifications de diffraction (distance de Rayleigh ≈ 0,3 mm à 1 THz), qui modifient la distribution spatiale du motif interrogeant l'échantillon, réduisant potentiellement la résolution réelle de l'image reconstruite. Nous l'avons ici limité ces effets en utilisant une tranche mince de Ge (125 µm) afin de réduire la séparation entre la position où le faisceau THz est modulé et l'échantillon.

C.2.4.Discussion et conclusions

On peut, encore une fois, effectuer des observations sur la vitesse d'acquisition de notre système actuel. L'acquisition d'une image 32 × 32 (1024 motifs) nécessite encore beaucoup de temps (~40 min.), principalement en raison de la nécessité d'une moyenne longue pour chaque image captée par la caméra (2,5 s) (notez que l'acquisition de la même image sans la technique SSD prendrait ~40 heures via notre configuration). Une telle acquisition chronophage est nécessaire pour obtenir un SNR suffisant (~200 dans notre configuration) au taux de répétition limité de notre source THz (250 Hz). En utilisant des systèmes laser présentant des taux de répétition dans la gamme MHz, couplés à des antennes photoconductrices pour la génération THz, le même SNR pourrait être obtenu en captant des cadres de ms, ramenant potentiellement le temps d'acquisition de l'image hypertemporelle entière à quelques secondes. De plus, comme indiqué ci-dessus, l'application d'algorithmes CS pourrait réduire davantage le temps nécessaire, en limitant le nombre de motifs à une petite fraction de l'ensemble complet, vers un fonctionnement en temps réel.

En conclusion, la nouvelle configuration que nous avons présentée combine le schéma SPI avec une technique de détection dans le domaine temporel sans balayage, afin d'obtenir une imagerie rapide sans nécessiter d'électronique complexe ou de pièce mobile mécanique. D'un point de vue plus fondamental, nous avons montré que la diffraction joue un rôle crucial dans le fonctionnement de la technique. En particulier, la détection cohérente THz SPI sans balayage mise en œuvre dans ce travail exploite de manière contre-intuitive le cartographie temps-espace au niveau du plan de détection pour récupérer des images multidimensionnelles entières (temps/fréquence, en plus de l'espace), avec la possibilité supplémentaire d'étendre la technique à des motifs et des objets à valeurs complexes sans limitation. En même temps, notre arrangement est rentable et extrêmement simple, ne nécessitant essentiellement, outre la source laser, qu'un DMD et une caméra pour fonctionner, sans présence de dispositif complexe (mécanique ou non) nécessaire pour effectuer les balayages spatio-temporels.

D. Conclusions et perspectives

Pour résumer les résultats des travaux de recherche présentés dans cette thèse, nous commençons par rappeler les principales exigences qu’un système d'imagerie THz basé sur TDS devrait avoir. D'un côté, il est essentiel de préserver la capacité de détection cohérente, qui est généralement fournie par le balayage temporel du champ électrique THz, et rend cette technique de spectroscopie unique dans sa capacité d'extraction des propriétés des matériaux. D'autre part, avec les technologies d'imagerie THz passant progressivement des systèmes de laboratoire aux produits commerciaux, il est important qu'un imageur THz soit rapide, et éventuellement simple et peu coûteux. Dans ce projet de recherche, nous avons développé une approche de l'imagerie THz qui pourrait être un outil puissant pour réaliser des dispositifs combinant ces deux exigences.

- Dans la première moitié du projet, nous avons démontré comment le schéma SPI est une solution idéale à coupler avec des configurations basées sur TDS qui reposent sur des détecteurs sans résolution spatiale. SPI permet de récupérer une image avec une mesure sous-échantillonnée, tout en reconstruisant l'ensemble de données dans le domaine temporel qui permet un fonctionnement multidimensionnel. De plus, un système basé sur SPI ne repose pas sur des pièces mobiles mécaniques pour balayer l'échantillon, ce qui rend l'agencement beaucoup moins complexe.
- Dans la seconde moitié, nous avons couplé l'implémentation basée sur SPI à une technique SSD. Ce dernier résout le problème du long balayage temporel utilisé pour reconstruire la forme d'onde THz dans le domaine temporel, en fournissant une approche capable de capturer une telle forme d'onde à la fois. La combinaison de SPI et SSD permet de réduire davantage le temps d'acquisition, puisque les balayages spatiaux et temporels sont évités. De plus, la complexité du système d'imagerie est également fortement réduite, puisque les deux seuls dispositifs critiques nécessaires, au-delà de la source laser, sont un SLM et une caméra standard.

Bien que le système expérimental que nous avons construit ne fonctionne pas en temps réel, il corrige les principales lacunes des systèmes d'imagerie THz traditionnels basés sur TDS.

Le développement de sources de plus en plus puissantes et de détecteurs plus sensibles nous a amenés à un stade où nous sommes capables de contrôler et d'utiliser le rayonnement THz de façon routinière. Maintenant, la prochaine étape a beaucoup à voir avec le développement d'appareils THz qui répondent aux exigences des produits commerciaux pour étendre leur utilisation dans le monde réel.

Dans le cas du système d'imagerie basé sur SPI présenté dans ce travail de thèse, nous avons montré comment il est possible de construire un dispositif simple et conservant toutes les principales fonctions du THz-TDS. À partir de ce moment, les principaux efforts de recherche doivent être orientés vers l'optimisation de certains aspects qui peuvent permettre une imagerie rapide et éventuellement rentable.

Le premier est le raffinement de la modulation spatiale du faisceau THz nécessaire pour réaliser le SPI. Une possibilité, dans ce sens, est l'amélioration de la technique de photo-excitation dans les semiconducteurs. Des approches innovantes sont celle exploitant la réflexion interne totale dans le semi-conducteur utilisé pour la modulation (X. Liu et al., 2016), or basés sur l'utilisation de matériaux composites, comme le graphène (Cheng et al., 2018; Wen et al., 2014) ou les polymères (B. Zhang et al., 2014) déposé sur Si. Au-delà de cela, beaucoup de travail a été investi dans le développement de THz-SLM, capables de moduler directement un faisceau THz. Ceux-ci sont soit à base de métamatériaux (W. Li et al., 2022 ; Shi et al., 2015 ; Watts et al., 2014) soit de micromiroirs (J. Kappa et al., 2019). Évidemment, ce type de systèmes rendrait la mise en œuvre d'un arrangement basé sur SPI beaucoup plus facile, car les ondes THz pourraient être modulées de manière plus flexible et contrôlable. De plus, la disponibilité de ces dispositifs serait bénéfique au-delà du contexte de THz SPI, en tant qu'outils pour manipuler facilement la lumière THz, de manière analogue à ce qui se fait dans la gamme IR/visible.

Le deuxième aspect critique concerne le schéma de détection, qui doit garantir qu'il n'y a pas de perte significative d'informations par rapport aux systèmes traditionnels. En ce sens, une étape importante est l'optimisation de la façon dont SPI est mis en œuvre dans le système d'imagerie. Cela peut être fait, du côté matériel, en améliorant la modulation spatiale, comme indiqué ci-dessus, et du côté logiciel en testant différents ensembles de motifs potentiellement plus efficaces (She et al., 2019) et des algorithmes de reconstruction CS plus avancés (Bian et al., 2018). L'autre point clé est le raffinement de la technique de détection sans balayage, qui, nous l'avons vu, est cruciale pour permettre une acquisition rapide de données pour permettre l'imagerie multidimensionnelle. Les techniques SSD, comme celles appliquées dans ce travail, ou d'autres méthodes comme l'acquisition compressée de la forme d'onde THz présentée dans (Zhao et al., 2021), sont encore relativement nouvelles. Pour cette raison, il est important de s'assurer qu'ils offrent une performance (en termes, par exemple, de niveau SNR, de résolution spatiale, de résolution spectrale ou d'autres paramètres) comparable aux systèmes traditionnels. Des améliorations dans ce sens peuvent être obtenues, par exemple, en optimisant la synchronisation entre le modulateur THz et le dispositif d'acquisition (par exemple, une caméra), et en mettant en œuvre une acquisition basée sur la soustraction dynamique (pour améliorer le SNR, en acquérant une mesure de référence après chaque mesure du signal modulée par le THz (Jiang et al., 2000)).

Une fois ces exigences de performance seront satisfaites, la prochaine étape clé est le couplage du système d'imagerie avec des sources laser à taux de répétition élevés. L'utilisation de ce type de sources permettrait une réduction substantielle du temps de mesure, en augmentant considérablement les taux d'acquisition des données. De plus, la plupart des systèmes TDS sont limités aux environnements de laboratoire en raison de leur complexité, mais avec de nouvelles sources laser à fibre optique, couplées à des PCA pour la génération THz, la possibilité de construire des dispositifs plus « portables » devient plus réaliste. Si un système d'imagerie compact, comme celui que nous avons présenté, pouvait être directement combiné à de telles sources, cela se traduirait rapidement par la disponibilité d'un imageur THz qui pourrait être rapide, simple et rentable. Un appareil de ce type pourrait contribuer de manière significative au processus en cours de sortir la technologie THz des laboratoires et vers des applications réelles.

REFERENCES

Abraham, E., Younus, A., Delagnes, J. C., & Mounaix, P. (2010). Non-invasive investigation of art paintings by terahertz imaging. *Applied Physics A*, *100*(3), 585–590. https://doi.org/10.1007/s00339-010-5642-z

Al Hadi, R., Sherry, H., Grzyb, J., Zhao, Y., Förster, W., Keller, H. M., Cathelin, A., Kaiser, A., & Pfeiffer, U. R. (2012). A 1 k-pixel video camera for 0.7-1.1 terahertz imaging applications in 65-nm CMOS. *IEEE Journal of Solid-State Circuits*, *47*(12), 2999–3012. https://doi.org/10.1109/JSSC.2012.2217851

Arbab, M. H., Winebrenner, D. P., Dickey, T. C., Chen, A., Klein, M. B., & Mourad, P. D. (2013). Terahertz spectroscopy for the assessment of burn injuries *in vivo*. *Journal of Biomedical Optics*, *18*(7), 077004. https://doi.org/10.1117/1.JBO.18.7.077004

Ashcroft, N. W., & Mermin, N. D. (1976). *Solid state physics*. Harcourt College Publishers.

Augustin, S., Hieronymus, J., Jung, P., & Hübers, H. W. (2015). Compressed Sensing in a Fully Non-Mechanical 350 GHz Imaging Setting. *Journal of Infrared, Millimeter, and Terahertz Waves*, *36*(5), 496–512. https://doi.org/10.1007/s10762-014-0141-5

Auston, D. H. (1975). Picosecond optoelectronic switching and gating in silicon. *Applied Physics Letters*, *26*(3), 101–103. https://doi.org/10.1063/1.88079

Auston, D. H., Johnson, A. M., Smith, P. R., & Bean, J. C. (1980). Picosecond optoelectronic detection, sampling, and correlation measurements in amorphous semiconductors. *Applied Physics Letters*, *37*(4), 371–373. https://doi.org/10.1063/1.91947

Bajwa, N., Sung, S., Ennis, D. B., Fishbein, M. C., Nowroozi, B. N., Ruan, D., MacCabi, A., Alger, J., John, M. A. S., Grundfest, W. S., & Taylor, Z. D. (2017). Terahertz Imaging of Cutaneous Edema: Correlation with Magnetic Resonance Imaging in Burn Wounds. *IEEE Transactions on Biomedical Engineering*, *64*(11), 2682–2694. https://doi.org/10.1109/TBME.2017.2658439

Basano, L., & Ottonello, P. (2007). A conceptual experiment on single-beam coincidence detection with pseudothermal light. *Optics Express*, *15*(19), 12386. https://doi.org/10.1364/oe.15.012386

Bawuah, P., Pierotic Mendia, A., Silfsten, P., Pääkkönen, P., Ervasti, T., Ketolainen, J., Zeitler, J. A., & Peiponen, K. E. (2014). Detection of porosity of pharmaceutical compacts by terahertz radiation transmission and light reflection measurement techniques. *International Journal of Pharmaceutics*, *465*(1–2), 70–76. https://doi.org/10.1016/j.ijpharm.2014.02.011

Baxter, J. B., & Guglietta, G. W. (2011). Terahertz Spectroscopy. *Analytical Chemistry*, *83*(12), 4342–4368. https://doi.org/10.1021/ac200907z

Bennett, D., Taylor, Z., Tewari, P., Sung, S., Maccabi, A., Singh, R., Culjat, M., Grundfest, W., Hubschman, J.-P., & Brown, E. (2012). Assessment of corneal hydration sensing in the terahertz band: *in vivo* results at 100 GHz. *Journal of Biomedical Optics*, *17*(9), 0970081. https://doi.org/10.1117/1.JBO.17.9.097008

Bian, L., Suo, J., Dai, Q., & Chen, F. (2018). Experimental comparison of single-pixel imaging algorithms. *Journal of the Optical Society of America A*, *35*(1), 78. https://doi.org/10.1364/JOSAA.35.000078

Blanchard, F., Sharma, G., Razzari, L., Ropagnol, X., Bandulet, H. C., Vidal, F., Morandotti, R., Kieffer, J. C., Ozaki, T., Tiedje, H., Haugen, H., Reid, M., & Hegmann, F. (2011). Generation of intense terahertz radiation via optical methods. *IEEE Journal on Selected Topics in Quantum Electronics*, *17*(1), 5–16. https://doi.org/10.1109/JSTQE.2010.2047715

Bor, Z., & Rácz, B. (1985). Group velocity dispersion in prisms and its application to pulse compression and travelling-wave excitation. *Optics Communications*, *54*(3), 165–170. https://doi.org/10.1016/0030-4018(85)90284-6

Boyd, R. W. (2007). *Non-linear optics* (Third). Elsevier.

Brown, E. R., Bjarnason, J. E., Fedor, A. M., & Korter, T. M. (2007). On the strong and narrow absorption signature in lactose at 0.53 THz. *Applied Physics Letters*, *90*(6), 061908. https://doi.org/10.1063/1.2437107

Browne, M., Yardimci, N. T., Scoffoni, C., Jarrahi, M., & Sack, L. (2020). Prediction of leaf water potential and relative water content using terahertz radiation spectroscopy. *Plant Direct*, *4*(4), e00197. https://doi.org/10.1002/pld3.197

Busch, S., Scherger, B., Scheller, M., & Koch, M. (2012). Optically controlled terahertz beam steering and imaging. *Optics Letters*, *37*(8), 1391. https://doi.org/10.1364/OL.37.001391

Candès, E. J., Romberg, J., & Tao, T. (2006). Robust uncertainty principles: Exact signal reconstruction from highly incomplete frequency information. *IEEE Transactions on Information Theory*, *52*(2), 489–509. https://doi.org/10.1109/TIT.2005.862083

Candes, E.J., & Wakin, M. B. (2008). An Introduction To Compressive Sampling. *IEEE Signal Processing Magazine*, *25*(2), 21–30. https://doi.org/10.1109/MSP.2007.914731

Candes, Emmanuel J., & Tao, T. (2006). Near-optimal signal recovery from random projections: Universal encoding strategies? *IEEE Transactions on Information Theory*, *52*(12), 5406–5425. https://doi.org/10.1109/TIT.2006.885507

Castro-Camus, E., Koch, M., & Mittleman, D. M. (2022). Recent advances in terahertz imaging: 1999 to 2021. *Applied Physics B: Lasers and Optics*, *128*(1), 12. https://doi.org/10.1007/s00340-021-07732-4

Chan, W. L., Charan, K., Takhar, D., Kelly, K. F., Baraniuk, R. G., & Mittleman, D. M. (2008). A single-pixel terahertz imaging system based on compressed sensing. *Applied Physics Letters*, *93*(12), 121105. https://doi.org/10.1063/1.2989126

Chen, Q., Jiang, Z., Xu, G. X., & Zhang, X.-C. (2000). Near-field terahertz imaging with a dynamic aperture. *Optics Letters*, *25*(15), 1122. https://doi.org/10.1364/ol.25.001122

Chen, S.-C., Du, L.-H., Meng, K., Li, J., Zhai, Z.-H., Shi, Q.-W., Li, Z.-R., & Zhu, L.-G. (2019). Terahertz wave near-field compressive imaging with a spatial resolution of over λ/100. *Optics Letters*, *44*(1), 21. https://doi.org/10.1364/ol.44.000021

Chen, S. C., Feng, Z., Li, J., Tan, W., Du, L. H., Cai, J., Ma, Y., He, K., Ding, H., Zhai, Z. H., Li, Z. R., Qiu, C. W., Zhang, X. C., & Zhu, L. G. (2020). Ghost spintronic THz-emitter-array microscope. *Light: Science and Applications*, *9*(1), 2047–7538. https://doi.org/10.1038/s41377-020-0338-4

Chen, Z., Chen, X., Tao, L., Chen, K., Long, M., Liu, X., Yan, K., Stantchev, R. I., Pickwell-MacPherson, E., & Xu, J. Bin. (2018). Graphene controlled Brewster angle device for ultra broadband terahertz modulation. *Nature Communications*, *9*(1), 1–7. https://doi.org/10.1038/s41467-018-07367-8

Cheng, L., Jin, Z., Ma, Z., Su, F., Zhao, Y., Zhang, Y., Su, T., Sun, Y., Xu, X., Meng, Z., Bian, Y., & Sheng, Z. (2018). Mechanical Terahertz Modulation Based on Single-Layered Graphene. *Advanced Optical Materials*, *6*(7), 1700877. https://doi.org/10.1002/adom.201700877

Clemente, P., Durán, V., Tajahuerce, E., Andrés, P., Climent, V., & Lancis, J. (2013). Compressive holography with a single-pixel detector. *Optics Letters*, *38*(14), 2524. https://doi.org/10.1364/ol.38.002524

Clemente, P., Durán, V., Tajahuerce, E., Torres-Company, V., & Lancis, J. (2012). Single-pixel digital ghost holography. *Physical Review A - Atomic, Molecular, and Optical Physics*, *86*(4), 041803. https://doi.org/10.1103/PhysRevA.86.041803

Cooper, K. B., Dengler, R. J., Llombart, N., Thomas, B., Chattopadhyay, G., & Siegel, P. H. (2011). THz imaging radar for standoff personnel screening. *IEEE Transactions on Terahertz Science and Technology*, *1*(1), 169–182. https://doi.org/10.1109/TTHZ.2011.2159556

Cosentino, A. (2016). Terahertz and Cultural Heritage Science: Examination of Art and Archaeology. *Technologies*, *4*(1), 6. https://doi.org/10.3390/technologies4010006

Cunningham, P. D., Valdes, N. N., Vallejo, F. A., Hayden, L. M., Polishak, B., Zhou, X. H., Luo, J., Jen, A. K. Y., Williams, J. C., & Twieg, R. J. (2011). Broadband terahertz characterization of the refractive index and absorption of some important polymeric and organic electro-optic materials. *Journal of Applied Physics*, *109*(4), 043505-043505–5. https://doi.org/10.1063/1.3549120

Dai, J., Zhang, J., Zhang, W., & Grischkowsky, D. (2004). Terahertz time-domain spectroscopy characterization of the far-infrared absorption and index of refraction of high-resistivity, float-zone silicon. *Journal of the Optical Society of America B*, *21*(7), 1379. https://doi.org/10.1364/JOSAB.21.001379

Dexheimer, S. L. (2008). *Terahertz spectroscopy : principles and applications*. CRC Press/Taylor & Francis.

Dierolf, M., Menzel, A., Thibault, P., Schneider, P., Kewish, C. M., Wepf, R., Bunk, O., & Pfeiffer, F. (2010). Ptychographic X-ray computed tomography at the nanoscale. *Nature*, *467*(7314), 436–439. https://doi.org/10.1038/nature09419

Dong, J., Bianca Jackson, J., Melis, M., Giovanacci, D., Walker, G. C., Locquet, A., Bowen, J. W., & Citrin, D. S. (2016). Terahertz frequency-wavelet domain deconvolution for stratigraphic and subsurface investigation of art painting. *Optics Express*, *24*(23), 26972. https://doi.org/10.1364/oe.24.026972

Dong, J., Locquet, A., Melis, M., & Citrin, D. S. (2017). Global mapping of stratigraphy of an old-master painting using sparsity-based terahertz reflectometry. *Scientific Reports*, *7*(1), 15098. https://doi.org/10.1038/s41598-017-15069-2

Donoho, D. L. (2006). Compressed sensing. *IEEE Transactions on Information Theory*, *52*(4), 1289–1306. https://doi.org/10.1109/TIT.2006.871582

Duarte, M. F., Davenport, M. A., Takbar, D., Laska, J. N., Sun, T., Kelly, K. F., & Baraniuk, R. G. (2008). Single-pixel imaging via compressive sampling: Building simpler, smaller, and less-expensive digital cameras. *IEEE Signal Processing Magazine*, *25*(2), 83–91. https://doi.org/10.1109/MSP.2007.914730

Duchi, M., Shukla, S., Shalit, A., & Hamm, P. (2021). 2D-Raman-THz spectroscopy with single-shot THz detection. *The Journal of Chemical Physics*, *155*(17), 174201. https://doi.org/10.1063/5.0065804

Duling, I., & Zimdars, D. (2009). Revealing hidden defects. *Nature Photonics*, *3*(11), 630–632. https://doi.org/10.1038/nphoton.2009.206

Edgar, M. P., Gibson, G. M., & Padgett, M. J. (2019). Principles and prospects for single-pixel imaging.

Nature Photonics, *13*(1), 13–20. https://doi.org/10.1038/s41566-018-0300-7

Fan, H. Y., Navon, D., & Gebbie, H. (1954). Recombination and trapping of carriers in germanium. *Physica*, *20*(7–12), 855–872. https://doi.org/10.1016/s0031-8914(54)80198-4

Fan, S., He, Y., Ung, B. S., & Pickwell-Macpherson, E. (2014). The growth of biomedical terahertz research. *Journal of Physics D: Applied Physics*, *47*(37), 11. https://doi.org/10.1088/0022-3727/47/37/374009

Faulkner, H. M. L., & Rodenburg, J. M. (2004). Movable aperture lensless transmission microscopy: A novel phase retrieval algorithm. *Physical Review Letters*, *93*(2), 023903. https://doi.org/10.1103/PhysRevLett.93.023903

Fukunaga, K., Ogawa, Y., Hayashi, S., & Hosako, I. (2007). Terahertz spectroscopy for art conservation. *IEICE Electronics Express*, *4*(8), 258–263. https://doi.org/10.1587/elex.4.258

Gao, F., Whitaker, J. F., Liu, Y., Uher, C., Platt, C. E., & Klein, M. V. (1995). Terahertz transmission of a Ba1-xKxBiO3 film probed by coherent time-domain spectroscopy. *Physical Review B*, *52*(5), 3607–3613. https://doi.org/10.1103/PhysRevB.52.3607

Gaubas, E., & Vanhellemont, J. (2007). Comparative Study of Carrier Lifetime Dependence on Dopant Concentration in Silicon and Germanium. *Journal of The Electrochemical Society*, *154*(3), H231. https://doi.org/10.1149/1.2429031

Gente, R., Rehn, A., Probst, T., Stübling, E. M., Camus, E. C., Covarrubias, A. A., Balzer, J. C., & Koch, M. (2018). Outdoor Measurements of Leaf Water Content Using THz Quasi Time-Domain Spectroscopy. In *Journal of Infrared, Millimeter, and Terahertz Waves* (Vol. 39, Issue 10, pp. 943–948). Springer New York LLC. https://doi.org/10.1007/s10762-018-0520-4

Gibson, G. M., Johnson, S. D., & Padgett, M. J. (2020). Single-pixel imaging 12 years on: a review. *Optics Express*, *28*(19), 28190. https://doi.org/10.1364/oe.403195

Gong, W., Zhao, C., Yu, H., Chen, M., Xu, W., & Han, S. (2016). Three-dimensional ghost imaging lidar via sparsity constraint. *Scientific Reports*, *6*(1), 1–6. https://doi.org/10.1038/srep26133

Goodman, J. W. (1996). *Introduction to Fourier Optics* (McGraw-Hill (ed.)).

Green, M. A. (1990). Intrinsic concentration, effective densities of states, and effective mass in silicon. *Journal of Applied Physics*, *67*(6), 2944–2954. https://doi.org/10.1063/1.345414

Greenberg, J., Krishnamurthy, K., & Brady, D. (2014). Compressive single-pixel snapshot x-ray diffraction imaging. *Optics Letters*, *39*(1), 111. https://doi.org/10.1364/ol.39.000111

Greene, B. I., Saeta, P. N., Dykaar, D. R., Schmitt-Rink, S., & Chuang, S. L. (1992). Far-Infrared Light Generation At Semiconductor Surfaces and Its Spectroscopic Applications. *IEEE Journal of Quantum Electronics*, *28*(10), 2302–2312. https://doi.org/10.1109/3.159537

Grischkowsky, D., Keiding, S., van Exter, M., & Fattinger, C. (1990). Far-infrared time-domain spectroscopy with terahertz beams of dielectrics and semiconductors. *Journal of the Optical Society of America B*, *7*(10), 2006. https://doi.org/10.1364/josab.7.002006

Guerboukha, H., Nallappan, K., & Skorobogatiy, M. (2018). Toward real-time terahertz imaging. *Advances in Optics and Photonics*, *10*(4), 843. https://doi.org/10.1364/AOP.10.000843

Haaser, M., Gordon, K. C., Strachan, C. J., & Rades, T. (2013). Terahertz pulsed imaging as an advanced characterisation tool for film coatings - A review. In *International Journal of Pharmaceutics* (Vol. 457, Issue 2, pp. 510–520). Elsevier. https://doi.org/10.1016/j.ijpharm.2013.03.053

Hafez, H. A., Chai, X., Ibrahim, A., Mondal, S., Férachou, D., Ropagnol, X., & Ozaki, T. (2016). Intense terahertz radiation and their applications. In *Journal of Optics (United Kingdom)* (Vol. 18, Issue 9, p. 093004). IOP Publishing Ltd. https://doi.org/10.1088/2040-8978/18/9/093004

Han, P. Y., & Zhang, X. C. (2001). Free-space coherent broadband terahertz time-domain spectroscopy. *Measurement Science and Technology*, *12*(11), 1747–1756. https://doi.org/10.1088/0957-0233/12/11/301

Harwit, M., & Sloan, N. J. A. (1979). *Hadamard transform optics* (1979th ed.). Academic Press.

Hebling, J. (1996). Derivation of the pulse front tilt caused by angular dispersion. *Optical and Quantum Electronics*, *28*(12), 1759–1763. https://doi.org/10.1007/BF00698541

Hendry, E., Koeberg, M., Pijpers, J., & Bonn, M. (2007). Reduction of carrier mobility in semiconductors caused by charge-charge interactions. *Physical Review B*, *75*(23), 233202. https://doi.org/10.1103/PhysRevB.75.233202

Hernandez-Cardoso, G. G., Amador-Medina, L. F., Gutierrez-Torres, G., Reyes-Reyes, E. S., Benavides Martínez, C. A., Cardona Espinoza, C., Arce Cruz, J., Salas-Gutierrez, I., Murillo-Ortíz, B. O., & Castro-Camus, E. (2022). Terahertz imaging demonstrates its diagnostic potential and reveals a relationship between cutaneous dehydration and neuropathy for diabetic foot syndrome patients. *Scientific Reports*, *12*(1), 3110. https://doi.org/10.1038/s41598-022-06996-w

Horisaki, R., Matsui, H., Egami, R., & Tanida, J. (2017). Single-pixel compressive diffractive imaging. *Applied Optics*, *56*(5), 1353. https://doi.org/10.1364/ao.56.001353

Horisaki, R., Matsui, H., & Tanida, J. (2017). Single-pixel compressive diffractive imaging with structured illumination. *Applied Optics*, *56*(14), 4085. https://doi.org/10.1364/ao.56.004085

Hornett, S. M., Stantchev, R. I., Vardaki, M. Z., Beckerleg, C., & Hendry, E. (2016). Subwavelength Terahertz Imaging of Graphene Photoconductivity. *Nano Letters*, *16*(11), 7019–7024. https://doi.org/10.1021/acs.nanolett.6b03168

Hu, B. B., & Nuss, M. C. (1995). Imaging with terahertz waves. *Optics Letters*, *20*(16), 1716. https://doi.org/10.1364/ol.20.001716

Jackson, J. D. (1999). *Classical Electrodynamics*. Jonh Wiley & Sons.

Jacobsen, R. H., Mittleman, D. M., & Nuss, M. C. (1996). Chemical recognition of gases and gas mixtures with terahertz waves. *Optics Letters*, *21*(24), 2011. https://doi.org/10.1364/OL.21.002011

Jansen, C., Wietzke, S., Peters, O., Scheller, M., Vieweg, N., Salhi, M., Krumbholz, N., Jördens, C., Hochrein, T., & Koch, M. (2010). Terahertz imaging: Applications and perspectives. *Applied Optics*, *49*(19), E48–E57. https://doi.org/10.1364/AO.49.000E48

Jeong, J. H., Kang, B. J., Kim, J. S., Jazbinsek, M., Lee, S. H., Lee, S. C., Baek, I. H., Yun, H., Kim, J., Lee, Y. S., Lee, J. H., Kim, J. H., Rotermund, F., & Kwon, O. P. (2013). High-power broadband organic THz generator. *Scientific Reports*, *3*(1), 1–8. https://doi.org/10.1038/srep03200

Jepsen, P. U., Cooke, D. G., & Koch, M. (2011). Terahertz spectroscopy and imaging - Modern techniques and applications. *Laser & Photonics Reviews*, *5*(1), 124–166. https://doi.org/10.1002/lpor.201000011

Jepsen, P. U., Møller, U., & Merbold, H. (2007). Investigation of aqueous alcohol and sugar solutions with reflection terahertz time-domain spectroscopy. *Optics Express*, *15*(22), 14717. https://doi.org/10.1364/oe.15.014717

Jiang, Z., Sun, F. G., Chen, Q., & Zhang, X. C. (1999). Electro-optic sampling near zero optical transmission point. *Applied Physics Letters*, *74*(9), 1191–1193.

https://doi.org/10.1063/1.123495

Jiang, Z., Xu, X. G., & Zhang, X.-C. (2000). Improvement of terahertz imaging with a dynamic subtraction technique. *Applied Optics*, *39*(17), 2982. https://doi.org/10.1364/ao.39.002982

Jiang, Z., & Zhang, X.-C. (1998a). Single-shot spatiotemporal terahertz field imaging. *Optics Letters*, *23*(14), 1114. https://doi.org/10.1364/OL.23.001114

Jiang, Z., & Zhang, X. C. (1998b). Electro-optic measurement of THz field pulses with a chirped optical beam. *Applied Physics Letters*, *72*(16), 1945–1947. https://doi.org/10.1063/1.121231

Jördens, C., & Koch, M. (2008). Detection of foreign bodies in chocolate with pulsed terahertz spectroscopy. *Optical Engineering*, *47*(3), 037003. https://doi.org/10.1117/1.2896597

Kannegulla, A., Jiang, Z., Rahman, S. M., Shams, M. I. B., Fay, P., Xing, H. G., Cheng, L.-J., & Liu, L. (2014). Coded-Aperture Imaging Using Photo-Induced Reconfigurable Aperture Arrays for Mapping Terahertz Beams. *IEEE Transactions on Terahertz Science and Technology*, *4*(3), 321–327. https://doi.org/10.1109/TTHZ.2014.2307163

Kannegulla, Akash, Shams, M. I. Bin, Liu, L., & Cheng, L.-J. (2015). Photo-induced spatial modulation of THz waves: opportunities and limitations. *Optics Express*, *23*(25), 32098. https://doi.org/10.1364/oe.23.032098

Kaplunov, I. A., Kolesnikov, A. I., Kropotov, G. I., & Rogalin, V. E. (2019). Optical Properties of Single-Crystal Germanium in the THz Range. *Optics and Spectroscopy*, *126*(3), 191–194. https://doi.org/10.1134/S0030400X19030093

Kappa, J., Sokoluk, D., Klingel, S., Shemelya, C., Oesterschulze, E., & Rahm, M. (2019). Terahertz Spatial Light Modulator Based on an Electrostatically Tunable Array of Large Micromirrors. *International Conference on Infrared, Millimeter, and Terahertz Waves, IRMMW-THz*, *2019-Septe*. https://doi.org/10.1109/IRMMW-THz.2019.8874286

Kappa, Jan, Sokoluk, D., Klingel, S., Shemelya, C., Oesterschulze, E., & Rahm, M. (2019). Electrically Reconfigurable Micromirror Array for Direct Spatial Light Modulation of Terahertz Waves over a Bandwidth Wider Than 1 THz. *Scientific Reports*, *9*(1), 2597. https://doi.org/10.1038/s41598-019-39152-y

Katletz, S., Pfleger, M., Pühringer, H., Vieweg, N., Scherger, B., Heinen, B., Koch, M., & Wiesauer, K. (2011). Efficient terahertz en-face imaging. *Optics Express*, *19*(23), 23042. https://doi.org/10.1364/oe.19.023042

Kawada, Y., Yasuda, T., Nakanishi, A., Akiyama, K., & Takahashi, H. (2011). Single-shot terahertz spectroscopy using pulse-front tilting of an ultra-short probe pulse. *Optics Express*, *19*(12), 11228. https://doi.org/10.1364/oe.19.011228

Kim, G. J., Jeon, S. G., Kim, J. Il, & Jin, Y. S. (2008). High speed scanning of terahertz pulse by a rotary optical delay line. *Review of Scientific Instruments*, *79*(10), 106102. https://doi.org/10.1063/1.2995763

Kim, K. Y., Yellampalle, B., Rodriguez, G., Averitt, R. D., Taylor, A. J., & Glownia, J. H. (2006). Single-shot, interferometric, high-resolution, terahertz field diagnostic. *Applied Physics Letters*, *88*(4), 1–3. https://doi.org/10.1063/1.2168897

Kim, K. Y., Yellampalle, B., Taylor, A. J., Rodriguez, G., & Glownia, J. H. (2007). Single-shot terahertz pulse characterization via two-dimensional electro-optic imaging with dual echelons. *Optics Letters*, *32*(14), 1968. https://doi.org/10.1364/ol.32.001968

Kim, P.-J., Jeong, J.-H., Jazbinsek, M., Choi, S.-B., Baek, I.-H., Kim, J.-T., Rotermund, F., Yun, H., Lee, Y. S., Günter, P., & Kwon, O.-P. (2012). Highly Efficient Organic THz Generator Pumped at Near-Infrared: Quinolinium Single Crystals. *Advanced Functional Materials*, *22*(1), 200–209. https://doi.org/10.1002/adfm.201101458

Kittel, C. (2005). Introduction to Solid State Physics. In *Physics Bulletin* (Eighth, Vol. 37, Issue 11). John Wiley and Sons Inc. https://doi.org/10.1088/0031-9112/37/11/034

Koch-Dandolo, C. L., Filtenborg, T., Fukunaga, K., Skou-Hansen, J., & Jepsen, P. U. (2015). Reflection terahertz time-domain imaging for analysis of an 18th century neoclassical easel painting. *Applied Optics*, *54*(16), 5123. https://doi.org/10.1364/AO.54.005123

Koch-Dandolo, C. L., Picollo, M., Cucci, C., & Jepsen, P. U. (2016). Fra Angelico's painting technique revealed by terahertz time-domain imaging (THz-TDI). *Applied Physics A: Materials Science and Processing*, *122*(10), 1–8. https://doi.org/10.1007/s00339-016-0396-x

Kwon, O.-P., Kwon, S.-J., Jazbinsek, M., Brunner, F. D. J., Seo, J.-I., Hunziker, C., Schneider, A., Yun, H., Lee, Y.-S., & Günter, P. (2008). Organic Phenolic Configurationally Locked Polyene Single Crystals for Electro-optic and Terahertz Wave Applications. *Advanced Functional Materials*, *18*(20), 3242–3250. https://doi.org/10.1002/adfm.200800633

Lee, A. W. M., Qin, Q., Kumar, S., Williams, B. S., Hu, Q., & Reno, J. L. (2006). Real-time terahertz imaging over a standoff distance (>25meters). *Applied Physics Letters*, *89*(14), 141125. https://doi.org/10.1063/1.2360210

Lee, A. W. M., Williams, B. S., Kumar, S., Hu, Q., & Reno, J. L. (2006). Real-time imaging using a 4.3-THz quantum cascade laser and a 320 × 240 microbolometer focal-plane array. *IEEE Photonics Technology Letters*, *18*(13), 1415–1417. https://doi.org/10.1109/LPT.2006.877220

Lee, C. H. (1977). Picosecond optoelectronic switching in GaAs. *Applied Physics Letters*, *30*(2), 84–86. https://doi.org/10.1063/1.89297

Lee, Y.-S. (2009). *Priciples of Terahertz Science and Technology*. Springer.

Lewis, R. A. (2019). A review of terahertz detectors. In *Journal of Physics D: Applied Physics* (Vol. 52, Issue 43, p. 433001). Institute of Physics Publishing. https://doi.org/10.1088/1361-6463/ab31d5

Li, K., Chen, X., Zhang, R., & Pickwell-Macpherson, E. (2020). Classification for glucose and lactose terahertz spectrums based on SVM and DNN methods. *IEEE Transactions on Terahertz Science and Technology*, *10*(6), 617–623. https://doi.org/10.1109/TTHZ.2020.3013819

Li, M., Bian, L., Zheng, G., Maiden, A., Liu, Y., Li, Y., Suo, J., Dai, Q., & Zhang, J. (2021). Single-pixel ptychography. *Optics Letters*, *46*(7), 1624. https://doi.org/10.1364/ol.417039

Li, W., Hu, X., Wu, J., Fan, K., Chen, B., Zhang, C., Hu, W., Cao, X., Jin, B., Lu, Y., Chen, J., & Wu, P. (2022). Dual-color terahertz spatial light modulator for single-pixel imaging. *Light: Science & Applications*, *11*(1), 191. https://doi.org/10.1038/s41377-022-00879-5

Liu, H. B., Zhong, H., Karpowicz, N., Chen, Y., & Zhang, X. C. (2007). Terahertz spectroscopy and imaging for defense and security applications. *Proceedings of the IEEE*, *95*(8), 1514–1527. https://doi.org/10.1109/JPROC.2007.898903

Liu, X., Parrott, E. P. J., Ung, B. S. Y., & Pickwell-MacPherson, E. (2016). Exploiting total internal reflection geometry for efficient optical modulation of terahertz light. *APL Photonics*, *1*(7), 076103. https://doi.org/10.1063/1.4963141

Lu, J., Hwang, H. Y., Li, X., Lee, S.-H., Kwon, O.-P., & Nelson, K. A. (2015). Tunable multi-cycle THz generation in organic crystal HMQ-TMS. *Optics Express*, *23*(17), 22723.

https://doi.org/10.1364/oe.23.022723

Mait, J. N., Euliss, G. W., & Athale, R. A. (2018). Computational imaging. *Advances in Optics and Photonics*, *10*(2), 409. https://doi.org/10.1364/aop.10.000409

Martínez-León, L., Clemente, P., Mori, Y., Climent, V., Lancis, J., & Tajahuerce, E. (2017). Single-pixel digital holography with phase-encoded illumination. *Optics Express*, *25*(5), 4975. https://doi.org/10.1364/oe.25.004975

Maxwell, J. C. (1865). A dynamical theory of the electromagnetic field. *Philosophical Transactions of the Royal Society of London*, *155*, 459–512. https://doi.org/10.1098/rstl.1865.0008

May, R. K., Su, K., Han, L., Zhong, S., Elliott, J. A., Gladden, L. F., Evans, M., Shen, Y., & Zeitler, J. A. (2013). Hardness and density distributions of pharmaceutical tablets measured by terahertz pulsed imaging. *Journal of Pharmaceutical Sciences*, *102*(7), 2179–2186. https://doi.org/10.1002/jps.23560

Mittleman, D. M. (2018). Twenty years of terahertz imaging [Invited]. *Optics Express*, *26*(8), 9417. https://doi.org/10.1364/OE.26.009417

Mittleman, D. M., Jacobsen, R. H., & Nuss, M. C. (1996). T-ray imaging. *IEEE Journal of Selected Topics in Quantum Electronics*, *2*(3), 679–692. https://doi.org/10.1109/2944.571768

Mohr, T., Herdt, A., & Elsässer, W. (2018). 2D tomographic terahertz imaging using a single pixel detector. *Optics Express*, *26*(3), 3353. https://doi.org/10.1364/OE.26.003353

Morales-Hernández, J. A., Singh, A. K., Villanueva-Rodriguez, S. J., & Castro-Camus, E. (2019). Hydration shells of carbohydrate polymers studied by calorimetry and terahertz spectroscopy. *Food Chemistry*, *291*, 94–100. https://doi.org/10.1016/j.foodchem.2019.03.132

Mourou, G., Stancampiano, C. V., Antonetti, A., & Orszag, A. (1981). Picosecond microwave pulses generated with a subpicosecond laser-driven semiconductor switch. *Applied Physics Letters*, *39*(4), 295–296. https://doi.org/10.1063/1.92719

Murakami, H., Shimizu, K., Katsurada, M., & Nashima, S. (2008). Dependence on chirp rate and spectral resolution of the terahertz field pulse waveform measured by electro-optic detection using a chirped optical pulse and a spectrometer and its effect on terahertz spectroscopy. *Journal of Applied Physics*, *104*(10), 103111. https://doi.org/10.1063/1.3021151

Naccache, R., Mazhorova, A., Clerici, M., Piccoli, R., Khorashad, L. K., Govorov, A. O., Razzari, L., Vetrone, F., & Morandotti, R. (2017). Terahertz Thermometry: Combining Hyperspectral Imaging and Temperature Mapping at Terahertz Frequencies. *Laser & Photonics Reviews*, *11*(5), 1600342. https://doi.org/10.1002/lpor.201600342

Naftaly, M., & Miles, R. E. (2007). Terahertz time-domain spectroscopy for material characterization. *Proceedings of the IEEE*, *95*(8), 1658–1665. https://doi.org/10.1109/JPROC.2007.898835

Nahata, A., Weling, A. S., & Heinz, T. F. (1996). A wideband coherent terahertz spectroscopy system using optical rectification and electro-optic sampling. *Applied Physics Letters*, *69*(16), 2321–2323. https://doi.org/10.1063/1.117511

Nemoto, N., Kanda, N., Imai, R., Konishi, K., Miyoshi, M., Kurashina, S., Sasaki, T., Oda, N., & Kuwata-Gonokami, M. (2016). High-Sensitivity and Broadband, Real-Time Terahertz Camera Incorporating a Micro-Bolometer Array with Resonant Cavity Structure. *IEEE Transactions on Terahertz Science and Technology*, *6*(2), 175–182. https://doi.org/10.1109/TTHZ.2015.2508010

Nuss, M. C. (1996). Chemistry is right for T-Ray imaging. *IEEE Circuits and Devices Magazine*, *12*(2), 25–30. https://doi.org/10.1109/101.485909

Olivieri, L., Totero Gongora, J. S., Pasquazi, A., & Peccianti, M. (2018). Time-Resolved Nonlinear Ghost Imaging. *ACS Photonics*, *5*(8), 3379–3388. https://doi.org/10.1021/acsphotonics.8b00653

Olivieri, L., Totero Gongora, J. S., Peters, L., Cecconi, V., Cutrona, A., Tunesi, J., Tucker, R., Pasquazi, A., & Peccianti, M. (2020). Hyperspectral terahertz microscopy via nonlinear ghost-Imaging. *Optica*, *7*(2), 186–191. https://doi.org/10.1364/optica.381035

Osten, W., Faridian, A., Gao, P., Körner, K., Naik, D., Pedrini, G., Singh, A. K., Takeda, M., & Wilke, M. (2014). Recent advances in digital holography [Invited]. *Applied Optics*, *53*(27), G44. https://doi.org/10.1364/ao.53.000g44

Ozheredov, I., Prokopchuk, M., Mischenko, M., Safonova, T., Solyankin, P., Larichev, A., Angeluts, A., Balakin, A., & Shkurinov, A. (2018). In vivo THz sensing of the cornea of the eye. *Laser Physics Letters*, *15*(5), 055601. https://doi.org/10.1088/1612-202X/aaac76

Pan, F., Knöpfle, G., Bosshard, C., Follonier, S., Spreiter, R., Wong, M. S., & Günter, P. (1996). Electro-optic properties of the organic salt 4-N,N-dimethylamino-4′-N′-methyl-stilbazolium tosylate. *Applied Physics Letters*, *69*(1), 13–15. https://doi.org/10.1063/1.118101

Parrott, E. P. J., & Zeitler, J. A. (2015). Terahertz Time-Domain and Low-Frequency Raman Spectroscopy of Organic Materials. *Applied Spectroscopy, Vol. 69, Issue 1, Pp. 1-25*, *69*(1), 1–25. https://www.osapublishing.org/as/abstract.cfm?uri=as-69-1-1

Pohl, A., Deßmann, N., Dutzi, K., & Hübers, H. W. (2016). Identification of Unknown Substances by Terahertz Spectroscopy and Multivariate Data Analysis. *Journal of Infrared, Millimeter, and Terahertz Waves*, *37*(2), 175–188. https://doi.org/10.1007/s10762-015-0217-x

Pratt, W. K., Andrews, H. C., & Kane, J. (1969). Hadamard Transform Image Coding. *Proceedings of the IEEE*, *57*(1), 58–68. https://doi.org/10.1109/PROC.1969.6869

Probst, T., Rehn, A., Busch, S. F., Chatterjee, S., Koch, M., & Scheller, M. (2014). Cost-efficient delay generator for fast terahertz imaging. *Optics Letters*, *39*(16), 4863. https://doi.org/10.1364/ol.39.004863

Radwell, N., Mitchell, K. J., Gibson, G. M., Edgar, M. P., Bowman, R., & Padgett, M. J. (2014). Single-pixel infrared and visible microscope. *Optica*, *1*(5), 285. https://doi.org/10.1364/optica.1.000285

Redo-Sanchez, A., Heshmat, B., Aghasi, A., Naqvi, S., Zhang, M., Romberg, J., & Raskar, R. (2016). Terahertz time-gated spectral imaging for content extraction through layered structures. *Nature Communications*, *7*(1), 1–7. https://doi.org/10.1038/ncomms12665

Rovere, A., Jeong, Y.-G., Piccoli, R., Lee, S.-H., Lee, S.-C., Kwon, O.-P., Jazbinsek, M., Morandotti, R., & Razzari, L. (2018). Generation of high-field terahertz pulses in an HMQ-TMS organic crystal pumped by an ytterbium laser at 1030 nm. *Optics Express*, *26*(3), 2509. https://doi.org/10.1364/oe.26.002509

Safian, R., Ghazi, G., & Mohammadian, N. (2019). Review of photomixing continuous-wave terahertz systems and current application trends in terahertz domain. *Optical Engineering*, *58*(11), 1. https://doi.org/10.1117/1.oe.58.11.110901

Saqueb, S. A. N., & Sertel, K. (2016). Phase-Sensitive Single-Pixel THz Imaging Using Intensity-Only Measurements. *IEEE Transactions on Terahertz Science and Technology*, *6*(6), 810–816. https://doi.org/10.1109/TTHZ.2016.2610760

Saqueb, S. A. N., & Sertel, K. (2018). Compressive Terahertz Imaging Using a Single-Bit Sensor. *IEEE Transactions on Terahertz Science and Technology*, *8*(6), 757–764.

https://doi.org/10.1109/TTHZ.2018.2873967

Saqueb, S. A. N., & Sertel, K. (2019). Multisensor Compressive Sensing for High Frame-Rate Imaging System in the THz Band. *IEEE Transactions on Terahertz Science and Technology*, *9*(5), 520–523. https://doi.org/10.1109/TTHZ.2019.2926618

Schnars, U., & Jüptner, W. P. O. (2002). Digital recording and numerical reconstruction of holograms. *Measurement Science and Technology*, *13*(9), 85–101. https://doi.org/10.1088/0957-0233/13/9/201

Schubert, O., Eisele, M., Crozatier, V., Forget, N., Kaplan, D., & Huber, R. (2013). Rapid-scan acousto-optical delay line with 34 kHz scan rate and 15 as precision. *Optics Letters*, *38*(15), 2907. https://doi.org/10.1364/ol.38.002907

Seifert, T., Jaiswal, S., Martens, U., Hannegan, J., Braun, L., Maldonado, P., Freimuth, F., Kronenberg, A., Henrizi, J., Radu, I., Beaurepaire, E., Mokrousov, Y., Oppeneer, P. M., Jourdan, M., Jakob, G., Turchinovich, D., Hayden, L. M., Wolf, M., Münzenberg, M., … Kampfrath, T. (2016). Efficient metallic spintronic emitters of ultrabroadband terahertz radiation. *Nature Photonics*, *10*(7), 483–488. https://doi.org/10.1038/nphoton.2016.91

Sen, P., Chen, B., Garg, G., Marschner, S. R., Horowitz, M., Levoy, M., & Lensch, H. P. A. (2005). Dual photography. *ACM SIGGRAPH 2005 Papers on - SIGGRAPH '05*, 745. https://doi.org/10.1145/1186822.1073257

Shan, J., Weling, A. S., Knoesel, E., Bartels, L., Bonn, M., Nahata, A., Reider, G. A., & Heinz, T. F. (2000). Single-shot measurement of terahertz electromagnetic pulses by use of electro-optic sampling. *Optics Letters*, *25*(6), 426. https://doi.org/10.1364/OL.25.000426

Shang, Y., Wang, X., Sun, W., Han, P., Ye, J., Feng, S., & Zhang, Y. (2019). Terahertz image reconstruction based on compressed sensing and inverse Fresnel diffraction. *Optics Express*, *27*(10), 14725. https://doi.org/10.1364/oe.27.014725

She, R., Liu, W., Lu, Y., Zhou, Z., & Li, G. (2019). Fourier single-pixel imaging in the terahertz regime. *Applied Physics Letters*, *115*(2), 021101. https://doi.org/10.1063/1.5094728

Shen, H., Gan, L., Newman, N., Dong, Y., Li, C., Huang, Y., & Shen, Y. C. (2012). Spinning disk for compressive imaging. *Optics Letters*, *37*(1), 46. https://doi.org/10.1364/OL.37.000046

Shen, Y. C., Gan, L., Stringer, M., Burnett, A., Tych, K., Shen, H., Cunningham, J. E., Parrott, E. P. J., Zeitler, J. A., Gladden, L. F., Linfield, E. H., & Davies, A. G. (2009). Terahertz pulsed spectroscopic imaging using optimized binary masks. *Applied Physics Letters*, *95*(23), 231112. https://doi.org/10.1063/1.3271030

Shen, Y. C., Lo, T., Taday, P. F., Cole, B. E., Tribe, W. R., & Kemp, M. C. (2005). Detection and identification of explosives using terahertz pulsed spectroscopic imaging. *Applied Physics Letters*, *86*(24), 241116. https://doi.org/10.1063/1.1946192

Shi, S. F., Zeng, B., Han, H. L., Hong, X., Tsai, H. Z., Jung, H. S., Zettl, A., Crommie, M. F., & Wang, F. (2015). Optimizing broadband terahertz modulation with hybrid graphene/metasurface structures. *Nano Letters*, *15*(1), 372–377. https://doi.org/10.1021/nl503670d

Shrekenhamer, D., Watts, C. M., & Padilla, W. J. (2013). Terahertz single pixel imaging with an optically controlled dynamic spatial light modulator. *Optics Express*, *21*(10), 12507. https://doi.org/10.1364/OE.21.012507

Siles, J. V., Cooper, K. B., Lee, C., Lin, R. H., Chattopadhyay, G., & Mehdi, I. (2018). A New Generation of Room-Temperature Frequency-Multiplied Sources with up to 10× Higher Output Power in the

160-GHz-1.6-THz Range. *IEEE Transactions on Terahertz Science and Technology*, *8*(6), 596–604. https://doi.org/10.1109/TTHZ.2018.2876620

Singh, A. K., Pérez-López, A. V., Simpson, J., & Castro-Camus, E. (2020). Three-dimensional water mapping of succulent Agave victoriae-reginae leaves by terahertz imaging. *Scientific Reports*, *10*(1), 1–9. https://doi.org/10.1038/s41598-020-58277-z

Stantchev, R. I., Mansfield, J. C., Edginton, R. S., Hobson, P., Palombo, F., & Hendry, E. (2018). Subwavelength hyperspectral THz studies of articular cartilage. *Scientific Reports*, *8*(1), 6924. https://doi.org/10.1038/s41598-018-25057-9

Stantchev, R. I., Phillips, D. B., Hobson, P., Hornett, S. M., Padgett, M. J., & Hendry, E. (2017). Compressed sensing with near-field THz radiation. *Optica*, *4*(8), 989. https://doi.org/10.1364/OPTICA.4.000989

Stantchev, R. I., Sun, B., Hornett, S. M., Hobson, P. A., Gibson, G. M., Padgett, M. J., & Hendry, E. (2016). Noninvasive, near-field terahertz imaging of hidden objects using a single-pixel detector. *Science Advances*, *2*(6), e1600190. https://doi.org/10.1126/sciadv.1600190

Stantchev, R. I., Yu, X., Blu, T., & Pickwell-MacPherson, E. (2020). Real-time terahertz imaging with a single-pixel detector. *Nature Communications*, *11*(1), 2535. https://doi.org/10.1038/s41467-020-16370-x

Stern, A. (2016). *Optical Compressive Imaging* (2016th ed.). CRC Press/Taylor & Francis.

Stillhart, M., Schneider, A., & Günter, P. (2008). Optical properties of 4-N,N-dimethylamino-4^′-N^′-methyl-stilbazolium 2,4,6-trimethylbenzenesulfonate crystals at terahertz frequencies. *Journal of the Optical Society of America B*, *25*(11), 1914. https://doi.org/10.1364/josab.25.001914

Stoik, C. D., Bohn, M. J., & Blackshire, J. L. (2008). Nondestructive evaluation of aircraft composites using transmissive terahertz time domain spectroscopy. *Optics Express*, *16*(21), 17039. https://doi.org/10.1364/OE.16.017039

Su, K., Shen, Y. C., & Zeitler, J. A. (2014). Terahertz sensor for non-contact thickness and quality measurement of automobile paints of varying complexity. *IEEE Transactions on Terahertz Science and Technology*, *4*(4), 432–439. https://doi.org/10.1109/TTHZ.2014.2325393

Sun, F. G., Jiang, Z., & Zhang, X. C. (1998). Analysis of terahertz pulse measurement with a chirped probe beam. *Applied Physics Letters*, *73*(16), 2233–2235. https://doi.org/10.1063/1.121685

Sun, Q., He, Y., Liu, K., Fan, S., Parrott, E. P. J., & Pickwell-MacPherson, E. (2017). Recent advances in terahertz technology for biomedical applications. In *Quantitative Imaging in Medicine and Surgery* (Vol. 7, Issue 3, pp. 345–355). AME Publishing Company. https://doi.org/10.21037/qims.2017.06.02

Teo, S. M., Ofori-Okai, B. K., Werley, C. A., & Nelson, K. A. (2015). Invited Article: Single-shot THz detection techniques optimized for multidimensional THz spectroscopy. *Review of Scientific Instruments*, *86*(5), 051301. https://doi.org/10.1063/1.4921389

Tewari, P., Garritano, J., Bajwa, N., Sung, S., Huang, H., Wang, D., Grundfest, W., Ennis, D. B., Ruan, D., Brown, E., Dutson, E., Fishbein, M. C., & Taylor, Z. (2019). Methods for registering and calibrating in vivo terahertz images of cutaneous burn wounds. *Biomedical Optics Express*, *10*(1), 322. https://doi.org/10.1364/boe.10.000322

Texas Instruments. (n.d.). *DLP technology*. Retrieved June 25, 2022, from https://www.ti.com/product/DLP4500NIR

Thibault, P., Dierolf, M., Menzel, A., Bunk, O., David, C., & Pfeiffer, F. (2008). High-resolution scanning

X-ray diffraction microscopy. *Science*, *321*(5887), 379–382. https://doi.org/10.1126/science.1158573

Thrane, L., Jacobsen, R. H., Uhd Jepsen, P., & Keiding, S. R. (1995). THz reflection spectroscopy of liquid water. *Chemical Physics Letters*, *240*(4), 330–333. https://doi.org/10.1016/0009-2614(95)00543-D

Ulbricht, R., Hendry, E., Shan, J., Heinz, T. F., & Bonn, M. (2011). Carrier dynamics in semiconductors studied with time-resolved terahertz spectroscopy. *Reviews of Modern Physics*, *83*(2), 543–586. https://doi.org/10.1103/RevModPhys.83.543

Usami, M., Iwamoto, T., Fukasawa, R., Tani, M., Watanabe, M., & Sakai, K. (2002). Development of a THz spectroscopic imaging system. *Physics in Medicine and Biology*, *47*(21), 3749–3753. https://doi.org/10.1088/0031-9155/47/21/311

Van Exter, M., Fattinger, C., & Grischkowsky, D. (1989). High-brightness terahertz beams characterized with an ultrafast detector. *Applied Physics Letters*, *55*(4), 337–339. https://doi.org/10.1063/1.101901

Vicario, C., Jazbinsek, M., Ovchinnikov, A. V., Chefonov, O. V., Ashitkov, S. I., Agranat, M. B., & Hauri, C. P. (2015). High efficiency THz generation in DSTMS, DAST and OH1 pumped by Cr:forsterite laser. *Optics Express*, *23*(4), 4573. https://doi.org/10.1364/oe.23.004573

Voelz, D. (2011). *Computational Fourier Optics a MATLAB Tutorial*. SPIE.

Wang, Q., Xie, L., & Ying, Y. (2022). Overview of imaging methods based on terahertz time-domain spectroscopy. In *Applied Spectroscopy Reviews* (Vol. 57, Issue 3, pp. 249–264). Taylor and Francis Ltd. https://doi.org/10.1080/05704928.2021.1875480

Watts, C. M., Shrekenhamer, D., Montoya, J., Lipworth, G., Hunt, J., Sleasman, T., Krishna, S., Smith, D. R., & Padilla, W. J. (2014). Terahertz compressive imaging with metamaterial spatial light modulators. *Nature Photonics*, *8*(8), 605–609. https://doi.org/10.1038/nphoton.2014.139

Wen, Q. Y., Tian, W., Mao, Q., Chen, Z., Liu, W. W., Yang, Q. H., Sanderson, M., & Zhang, H. W. (2014). Graphene based all-optical spatial terahertz modulator. *Scientific Reports*, *4*(1), 1–5. https://doi.org/10.1038/srep07409

Wilk, R., Hochrein, T., Koch, M., Mei, M., & Holzwarth, R. (2011). Terahertz spectrometer operation by laser repetition frequency tuning. *Journal of the Optical Society of America B*, *28*(4), 592. https://doi.org/10.1364/josab.28.000592

Wu, Q., Hewitt, T. D., & Zhang, X. C. (1996). Two-dimensional electro-optic imaging of THz beams. *Applied Physics Letters*, *69*(8), 1026–1028. https://doi.org/10.1063/1.116920

Yang, J., Zhang, M., & Ruan, S. (2008a). Real-time, continuous-wave terahertz imaging by a pyroelectric camera. *Chinese Optics Letters, Vol. 6, Issue 1, Pp. 29-31*, *6*(1), 29–31.

Yang, J., Zhang, M., & Ruan, S. (2008b). Real-time, continuous-wave terahertz imaging by a pyroelectric camera. *Chinese Optics Letters, Vol. 6, Issue 1, Pp. 29-31*, *6*(1), 29–31. https://opg.optica.org/abstract.cfm?uri=col-6-1-29

Yang, X., Zhao, X., Yang, K., Liu, Y., Liu, Y., Fu, W., & Luo, Y. (2016). Biomedical Applications of Terahertz Spectroscopy and Imaging. *Trends in Biotechnology*, *34*(10), 810–824. https://doi.org/10.1016/J.TIBTECH.2016.04.008

Yasui, T., Saneyoshi, E., & Araki, T. (2005). Asynchronous optical sampling terahertz time-domain spectroscopy for ultrahigh spectral resolution and rapid data acquisition. *Applied Physics Letters*, *87*(6), 061101. https://doi.org/10.1063/1.2008379

Yu, W.-K. (2019). Super Sub-Nyquist Single-Pixel Imaging by Means of Cake-Cutting Hadamard Basis Sort. *Sensors*, *19*(19), 4122. https://doi.org/10.3390/s19194122

Yu, W. K., Liu, X. F., Yao, X. R., Wang, C., Zhai, Y., & Zhai, G. J. (2014). Complementary compressive imaging for the telescopic system. *Scientific Reports*, *4*(1), 1–6. https://doi.org/10.1038/srep05834

Zanotto, L., Piccoli, R., Dong, J. L., Morandotti, R., & Razzari, L. (2020). Single-pixel terahertz imaging: A review. *Opto-Electronic Advances*, *3*(9), 1–15. https://doi.org/10.29026/oea.2020.200012

Zeitler, J. A., Taday, P. F., Newnham, D. A., Pepper, M., Gordon, K. C., & Rades, T. (2010). Terahertz pulsed spectroscopy and imaging in the pharmaceutical setting - a review. *Journal of Pharmacy and Pharmacology*, *59*(2), 209–223. https://doi.org/10.1211/jpp.59.2.0008

Zernike, F., & Berman, P. R. (1966). Erratum: Generation of far infrared as a difference frequency (Physical Review Letters). In *Physical Review Letters* (Vol. 16, Issue 3, p. 117). American Physical Society. https://doi.org/10.1103/PhysRevLett.16.117

Zhang, B., He, T., Shen, J., Hou, Y., Hu, Y., Zang, M., Chen, T., Feng, S., Teng, F., & Qin, L. (2014). Conjugated polymer-based broadband terahertz wave modulator. *Optics Letters*, *39*(21), 6110. https://doi.org/10.1364/ol.39.006110

Zhang, Z., Ma, X., & Zhong, J. (2015). Single-pixel imaging by means of Fourier spectrum acquisition. *Nature Communications*, *6*(1), 1–6. https://doi.org/10.1038/ncomms7225

Zhang, Z., Wang, X., Zheng, G., & Zhong, J. (2017). Hadamard single-pixel imaging versus Fourier single-pixel imaging. *Optics Express*, *25*(16), 19619. https://doi.org/10.1364/oe.25.019619

Zhao, J., Dai, J., Braverman, B., Zhang, X.-C., & Boyd, R. W. (2021). Compressive ultrafast pulse measurement via time-domain single-pixel imaging. *Optica*, *8*(9), 1176. https://doi.org/10.1364/optica.431455

Zhao, J., Yiwen, E., Williams, K., Zhang, X. C., & Boyd, R. W. (2019). Spatial sampling of terahertz fields with sub-wavelength accuracy via probe-beam encoding. *Light: Science and Applications*, *8*(1). https://doi.org/10.1038/s41377-019-0166-6